

Cavity-enhancement of a low-noise single-photon emitter in diamond

Inauguraldissertation

zur
Erlangung der Würde eines Doktors der Philosophie
vorgelegt der
Philosophisch-Naturwissenschaftlichen Fakultät
der Universität Basel

von

Viktoria Yurgens

Basel, 2023

The original document is saved on the University of Basel document server
<http://edoc.unibas.ch>



This work is licensed under a Creative Commons
Attribution-NonCommercial-NoDerivatives 4.0 International License.

The complete text may be reviewed here:

<http://creativecommons.org/licenses/by-nc-nd/4.0/>

Genehmigt von der Philosophisch-Naturwissenschaftlichen Fakultät
auf Antrag von

Erstbetreuer: Prof. Dr. Richard J. Warburton

Zweitbetreuer: Prof. Dr. Patrick Maletinsky

Externe Expertin: Prof. Dr. Lilian Childress

Basel, den 25. April 2023

Prof. Dr. Marcel Mayor
Dekan

*To my parents,
for the never-ending support, love, and belief in me.*

ABSTRACT

With the immense progress demonstrated in recent years in the field of quantum communication, the use of quantum networks in applications ranging from secure communication to distributed quantum computing is within reach. Systems meeting the requirements set for distant, long-lived network nodes are continuously being identified and developed. The nitrogen-vacancy center (NV) in diamond is a solid-state defect fulfilling many of these conditions, one being its spin-state-dependent fluorescence that provides a direct way to distribute entanglement across a quantum network. Further advantages include record-long spin coherence times at low- and room temperature, spin-state control via electric, magnetic, strain and optical fields, and nearby nuclear spins that can be used for the storage and manipulation of quantum states. However, NVs also display a number of limitations related to their photonic properties. An inefficient photon extraction from the diamond host material, a small fraction of coherent emission, a long radiative lifetime as well as broadened optical linewidths in microstructured diamond all impose limitations on experimental implementations of NVs as nodes in a quantum network.

In this work, we address each of the above-mentioned problems. We develop two improved methods for NV formation – laser writing and carbon implantation post-fabrication (IPF) – and show that they result in reduced NV optical linewidths, both in bulk and in microstructured diamond. This indicates a lower charge-noise level and reduced spectral diffusion compared to other approaches. Most importantly, the majority of the created NVs exhibit a linewidth below 150 MHz, implying a minimized need for NV pre-selection and a reduced experimental overhead in spin-photon entanglement operations.

We incorporate diamond platelets with NVs created via carbon IPF into an open microcavity and make use of the Purcell enhancement resulting from tuning the cavity onto resonance with specific NV transitions to increase the coherent photon flux. We successfully operate the system at cryogenic temperatures, achieving high finesse values of up to 7 900 on the diamond, and detect photon count rates under off-resonant excitation four times higher than the current state-of-the-art. For the first time for an NV in diamond, we successfully measure resonance fluorescence with a signal-to-background ratio higher than 1 without relying on temporal filtering. Projecting the current system efficiency to applications relying on two-mode interference would result in entanglement rates increased by more than an order of magnitude. Even higher gains are within reach after reasonable system improvements. The low-charge-noise NVs and the ability to resonantly generate single photons and with high probability establish the NV-cavity platform as an attractive photonic interface, paving the way for faster and more efficient long-distance quantum communication based on defects in diamond.

CONTENTS

Abstract	iv
Contents	v
1. Introduction	1
2. Background	4
2.1. The NV center in diamond	4
2.1.1. Electronic and vibronic structure	5
2.1.2. Optical- and spin properties	8
2.1.3. Formation	14
2.1.4. NVs as quantum network nodes	17
2.1.5. Other color centers in diamond	21
2.1.6. Optically active defects in other materials	23
2.2. Laser writing of defects in diamond	24
2.2.1. Interaction of ultrashort pulses with dielectrics	25
2.2.2. Creation of NVs via laser writing	27
2.2.3. Creation of NVs via laser ablation	28
2.2.4. Laser writing of other defects	29
2.2.5. Minimizing spherical aberrations	29
2.3. Cavity quantum electrodynamics	33
2.3.1. The Jaynes-Cummings model	33
2.3.2. Light-matter interaction including system losses	35
2.3.3. Purcell-enhancement	36
2.3.4. A plano-concave open microcavity	38
3. Laser writing of NVs in diamond using a solid-immersion lens	45
3.1. Summary	45
3.2. Introduction	46
3.3. Experimental setup	46
3.3.1. Solid immersion lens	47
3.3.2. Laser-writing setup	50
3.4. Laser writing of NVs	51
3.4.1. Creation of vacancies	51
3.4.2. Annealing recipe optimization	52
3.4.3. Formation of NVs in bulk diamond	53
3.4.4. Laser writing close to a surface	55
3.5. Linewidth characterization	57
3.5.1. Photoluminescence excitation	57
3.5.2. Power dependence	59
3.5.3. Linewidth statistics	61
3.6. Further characterization of laser-written NVs	62
3.6.1. Time-dependent PLE	62
3.6.2. Transverse train	63

3.7. Towards laser-written NVs in thin structures	65
3.7.1. Linewidths after etching	66
3.7.2. Laser writing into thin structures	67
3.8. Conclusions and outlook	67
4. Low-noise NVs in diamond formed by carbon implantation	70
4.1. Summary	70
4.2. Introduction	71
4.3. Sample preparation	72
4.3.1. Diamond microfabrication	72
4.3.2. Ion implantation	73
4.4. NV characterization	74
4.4.1. Structure thickness determination	75
4.4.2. Photoluminescence excitation	76
4.4.3. Linewidth statistics	77
4.4.4. Linewidth as a function of structure thickness	78
4.5. Conclusions and outlook	80
5. Purcell-enhancement of a low-noise emitter in diamond	81
5.1. Summary	81
5.2. Introduction	81
5.3. Experimental setup	82
5.3.1. Cavity assembly	83
5.3.2. Diamond sample	84
5.3.3. Measurement setup	85
5.4. Cavity characterization	87
5.4.1. Cavity characterization at room temperature	90
5.4.2. Cavity characterization at low temperature	92
5.5. Purcell-enhancement	94
5.5.1. Lifetime measurements	96
5.5.2. Photon autocorrelation measurements	98
5.6. Resonance fluorescence from an NV in a cavity	100
5.6.1. Measurement sequence and laser suppression	100
5.6.2. Resonance fluorescence	102
5.6.3. Power-dependent dynamics	105
5.6.4. Saturation curves and system efficiency	108
5.7. Conclusions and outlook	111
6. Conclusions	112
7. Outlook	114
Appendices	117
A. Simulating the extent of a laser focus via ray tracing	117
A.1. Focusing without a SIL	117
A.2. Focusing with an h-SIL	119

A.3. Focusing with a t-SIL	120
B. The diamond-cavity mode structure	122
B.1. Bare cavity	122
B.2. Cavity with diamond	123
Bibliography	125
Acknowledgements	144
List of publications	147
Curriculum vitae	148

1

INTRODUCTION

In December 1969, a message was successfully sent and received over a four-node network on what can be seen as the eve of the classical internet. The network, called the Advanced Research Projects Agency Network (ARPANET), consisted of four Interface Message Processors, or IMPs, distributed across research institutes in California¹⁻³. Initially conceived to share resources between remote computers, it has since grown into the backbone of the modern world, providing access to knowledge, transferring virtual resources, and enabling communication across borders and continents.

Today, about 50 years later, we are on the eve of the formation of a *quantum* internet. Implementations exchanging quantum information over large distances have been demonstrated⁴⁻¹⁰ and a small-scale multi-node quantum network based on the nitrogen-vacancy center (NV) in diamond has been implemented for the first time^{11,12}. A quantum network, working in parallel with classical networks, will enable new capabilities ranging from secure communication and identification processes to precise clock synchronization and distributed quantum computing.

The basis of any quantum communication is a quantum bit, or qubit, which can not only take a value of 0 or 1 but also be in a superposition of the two. This changes the way information is created, transported, processed, and read out. Connecting two qubits with each other relies on quantum entanglement, which leads to correlations between distant nodes irreproducible with classical bits and networks. The fact that a qubit cannot be copied leads to direct ways of detecting external interference and errors, new means to encrypt data and appealing possibilities such as quantum key distribution¹³.

A qubit can be realized by almost any two-level system. Implementations up to now include superconducting circuits^{14,15}, cold atoms^{16,17}, trapped ions¹⁸⁻²⁰, photons²¹⁻²³, spins in semiconductor quantum dots²⁴⁻²⁶, spins in self-assembled quantum dots²⁷⁻³⁰, and solid-state defects^{31,32}. The state control is realized by means ranging from radio-frequency fields to microwave, magnetic, electric, strain and optical fields. This "zoo" of systems has led to the establishment of the fields of quantum sensing, quantum computing and quantum communication, with immense progress being demonstrated to this day.

The optical interaction of a single emitter and a single photon is a direct way to distribute entanglement across a quantum network over long distances. Through either quantum or classical channels, information can be sent between distant nodes, enabling secure and high-fidelity communication³³. For this to work as intended, matter qubits need to meet a number of requirements on their spin properties, optical properties, charge-state control, creation mechanisms, material engineering and implementation into micro- and nanostructures³⁴. The NV in diamond, a solid-state defect identified in the

1970s and detected as a single center for the first time in 1997³⁵, has shown many of the necessary properties: long spin coherence at low and at room temperature^{36,37}, spin-dependent emission enabling optical spin-state readout³⁸, high quantum efficiency³⁹, charge-state initialization via off-resonant excitation, spin-state control via electric, magnetic, strain and optical fields³⁸, tuning of the emission frequency with electric fields^{40,41}, cycling and non-cycling optical transitions enabling single-shot spin readout^{42,43} as well as nearby nuclear spins that can be used for the storage and processing of quantum states^{44,45}. Additionally, synthetic growth of diamond allows for the creation of isotopically purified samples and controlled incorporation of impurities⁴⁶. Finally, there is a multitude of methods to form NVs in diamond at precise locations, such as ion implantation^{47,48} and the recently developed method of laser writing⁴⁹.

These developments have together led to applications of NVs both in quantum sensing, demonstrating nanoscale resolution and sensitivity in magnetometry⁵⁰, electrometry^{51,52} and thermometry⁵³, and in quantum communication, with long-distance spin-spin entanglement⁵⁴, multi-node distributed quantum networks^{11,12}, and multi-qubit spin registers⁴⁵. Despite exhibiting a lot of advantages for quantum communication, NVs also bear several limitations related to their photonic properties: a low photon extraction out of the diamond host material, a small fraction of coherent emission⁵⁵, a long radiative lifetime^{56,57} and reduced optical coherence in microstructures due to a high sensitivity to charge noise⁵⁸. All of these issues contribute to increased experimental overhead, low coherent photon flux, reduced experiment fidelities, and the need for preselection of NVs for most applications⁵⁹.

Together, these limitations point towards the need for new, or improved, methods of NV creation as well as for photonic solutions to increase the NV coherent photon flux. In this work, we address both aspects: we develop two improved methods for NV formation, and couple the created NVs to the mode of an open microcavity^{58,60–64} in order to increase in the flux of useful photons. The advantage of our system is that it requires minimal diamond fabrication, making it possible to preserve the good, almost bulk-like, optical properties of the NVs as well as to position the emitters far away from surface-related noise sources. We show a strong enhancement of the photons emitted out of the system compared to NVs located in free space, and measure resonance fluorescence in the coupled NV-cavity system. The experiment relies on one of the developed NV creation methods, yielding NVs with narrow optical linewidth at a precise depth within the diamond, with little or no emitter preselection. The microcavity allows full spectral tunability and increases the collection efficiency, coherent photon fraction, and flux of coherent photons, presenting an important step towards a coherent spin-photon interface based on NVs in diamond.

This thesis is divided into several main parts. Chapter 2 is dedicated to motivating and describing the background behind this work, to place it in context with what has already been achieved in the field. Furthermore, it explains important concepts regarding NVs, NV formation methods, and the use of optical cavities to enhance the light-matter interaction between solid-state emitters and photons. The following three Chapters 3, 4 and 5 report on the results achieved in this work. Chapter 3 describes a refined method of creating NV centers in diamond, where a high-power femtosecond laser is used together with a solid immersion lens to create vacancies that subsequently form low-charge-noise NVs. Chapter 4 illustrates a parallel path undertaken to create low-charge-noise NVs,

in which carbon ions are implanted after the creation of the diamond microstructures, preserving good optical properties even in thin diamond. This is the approach chosen for the diamonds used in Chapter 5, where the emission of NVs in a thin diamond platelet is coupled to the mode of a tunable open microcavity in order to enhance the coherent photon flux out of the system. Finally, Chapters 6 and 7 conclude on the results and present future research directions.

2

BACKGROUND

Diamond is a material famous for its hardness, thermal conductivity, optical properties – and, increasingly during the past 20-30 years, its defects. Tetrahedral covalent bonds between its carbon atoms, arranged in a version of a face-centered cubic structure, give a tightly packed and rigid structure, and the substitution or absence of carbon atoms on selected lattice sites leads to electronic states deep within the 5.47 eV wide bandgap^{65,66}. These states, known as color centers, possess appealing spin and optical properties that can be employed for a range of applications in quantum sensing and quantum communication.

2.1 The NV center in diamond

The NV center, a color center in diamond consisting of a substitutional nitrogen atom and a neighboring vacancy, is either formed naturally during the diamond growth (then referred to as a “native” NV), or created by a wide variety of methods afterwards.

Diamond itself has been grown synthetically since 1953⁶⁵. The two main synthesis methods are chemical vapor deposition (CVD) and high-pressure-high-temperature growth (HPHT)^{67,68}. The most common impurity is nitrogen (N), and diamonds are categorized as type-I or type-II depending on whether they contain a nitrogen concentration high enough (>5 ppm) to be detected by IR absorption spectroscopy or not. The categories are divided further depending on the type of impurities: type Ia (aggregated N impurities), type Ib (isolated single N impurities), type IIa (no measurable N or boron impurities), and type IIb (boron impurities). Generally, natural diamonds are of type I, HPHT diamonds of type Ib, and CVD diamonds of type IIa. Single-crystal CVD diamonds with a low nitrogen content can further be classified as optical-grade ($[N] < 5$ ppm) or electronic-grade ($[N] < 5$ ppb, $[B] < 1$ ppb)^{69,70}.

Diamond has a wide transparency window, extending from the deep ultraviolet (wavelength of 225 nm) to radio frequencies (wavelengths $\gg 20$ μm), with a refractive index of approximately 2.4 in the visible range. Oriented along the $\langle 111 \rangle$ crystalline direction in the diamond lattice, the NV has trigonal symmetry and is therefore part of the C_{3v} symmetry group³⁸. It is a deep-level defect, evidenced by sharp emission features^{71,72} (Fig. 2.1a). It is usually found in its neutral charge state⁷³ as NV^0 with an optical zero-phonon line (ZPL) at 575 nm (2.156 eV)⁷⁴ or in its negative charge state^{71,72} as NV^- with ZPLs at 637 nm (1.945 eV, triplet)⁷⁵ and 1042 nm (1.190 eV, singlet)^{76,77}. Both charge states have a broad phonon sideband (PSB) that extends towards longer wavelengths in the emission spectrum.

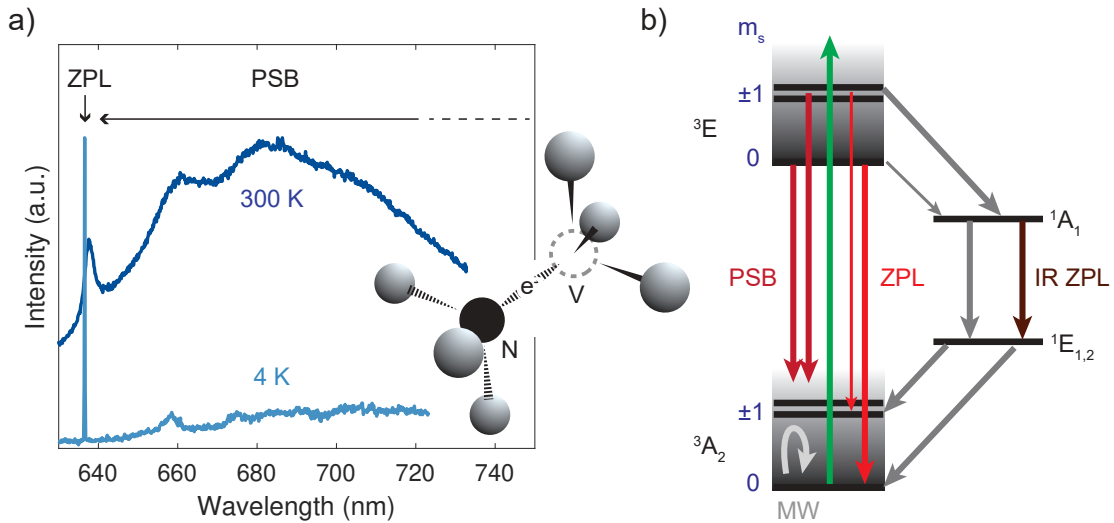


Figure 2.1.: The NV center in diamond. (a) Room- and low-temperature emission spectrum. The room-temperature spectrum was recorded on an ensemble of NVs. Inset: atomic structure, with a substitutional nitrogen atom and a neighboring vacancy oriented along the $\langle 111 \rangle$ direction in the diamond lattice. In order for the NV to be in its negative charge state, an additional electron has to be provided by a nearby donor. (b) Electronic level structure. The spin triplet ground- and excited state are connected via ZPL transitions, and have vibrational quasi-continua that give rise to the PSB. From the excited state, there is a non-zero probability for the NV to deexcite via the singlet levels. Gray arrows indicate non-radiative transitions.

2.1.1 Electronic and vibronic structure

An NV in its neutral charge state has five electrons: three from the dangling bonds of the carbon atoms surrounding the vacancy and two from the nitrogen atom from which the NV is formed. A sixth, giving the defect its negative charge state, typically comes from a nearby N^{71,72}. Therefore, depending on the nitrogen content of the diamond, a different NV charge state dominates: in type-Ib diamond, NV⁻ is the dominant charge state due to the excess of electron donors, while a large variation in the relative NV charge state concentration can be seen in type-IIa diamond with less intrinsic nitrogen⁷⁸.

NV⁻ has a 3A_2 triplet ground state and a 3E triplet excited state, each consisting of the spin sublevels $m_s = 0$ and $m_s = \pm 1$, as well as a 1A_1 and 1E singlet state³⁸. The electronic level structure of an NV⁻ at room temperature is illustrated in Fig. 2.1b. The ground-state zero-field splitting (ZFS) is 2.87-2.88 GHz, arising due to first-order electronic spin-spin interactions^{71,72}, and the excited-state ZFS is 1.42 GHz^{79,80}. Both ZFSs are detectable via optically detected magnetic resonance (ODMR)³⁸. In the excited state, the NV electron configuration results in a permanent electric dipole moment^{38,81,82}.

2.1.1.1 Hyperfine structure

The hyperfine structure of the NV⁻ ground state due to the $I = 1$ ($I = 1/2$) ^{14}N (^{15}N) nuclear spin splits each spin sublevel into three (two) levels. For either isotope, the ground

state spin Hamiltonian can be written as

$$\hat{H}_{gs} = D_{gs} \left[\hat{S}_z^2 - S(S+1)/3 \right] + A_{gs}^{\parallel} \hat{S}_z \hat{I}_z + A_{gs}^{\perp} \left[\hat{S}_x \hat{I}_x + \hat{S}_y \hat{I}_y \right] + P_{gs} \left[\hat{I}_z^2 - I(I+1)/3 \right] \quad (2.1)$$

with D_{gs} being the ZFS, \hat{S}_x , \hat{S}_y and \hat{S}_z the spin operators, P_{gs} the nuclear electric quadrupole parameter (≈ -5.0 MHz for ^{14}N and ≈ 0 for ^{15}N) and A_{gs}^{\parallel} and A_{gs}^{\perp} the axial and non-axial magnetic hyperfine parameters. The values of A_{gs}^{\parallel} and A_{gs}^{\perp} have been measured to lie between 2.1 and 3.7 MHz, but their signs are debated³⁸.

The influence of a static electric field \vec{E} , magnetic field \vec{B} and strain field $\vec{\delta}$ when assumed to be constant over the extent of the NV can be defined as

$$\begin{aligned} \hat{V}_{gs} = & \mu_B g_{gs}^{\parallel} \hat{S}_z B_z + \mu_B g_{gs}^{\perp} (\hat{S}_x B_x + \hat{S}_y B_y) + \mu_N g_N \vec{I} \cdot \vec{B} \\ & + d_{gs}^{\parallel} (E_z + \delta_z) \left[\hat{S}_z^2 - S(S+1)/3 \right] + d_{gs}^{\perp} (E_x + \delta_x) (\hat{S}_y^2 - \hat{S}_x^2) \\ & + d_{gs}^{\perp} (E_y + \delta_y) (\hat{S}_x \hat{S}_y - \hat{S}_y \hat{S}_x) \end{aligned} \quad (2.2)$$

Here, μ_B is the Bohr magneton, μ_N the nuclear magneton, $g_{gs}^{\parallel} = g_{gs}^{\perp} = 2.0028$ the components of the ground-state electronic g-factor tensor^{71,72}, g_N the isotropic nuclear g-factor, and $d_{gs}^{\parallel} = 0.35$ and $d_{gs}^{\perp} = 17$ the components of the ground-state electric dipole moment⁸³.

The hyperfine structure of the excited state can at room temperature be described by

$$\hat{H}_{es}^{RT} = D_{es}^{\parallel} \left[\hat{S}_z^2 - S(S+1)/3 \right] + A_{es}^{\parallel} \hat{S}_z \hat{I}_z + A_{es}^{\perp} \left[\hat{S}_x \hat{I}_x + \hat{S}_y \hat{I}_y \right] + P_{es} \left[\hat{I}_z^2 - I(I+1)/3 \right] \quad (2.3)$$

which is similar to the Hamiltonian in Eq. (2.1) describing the ground state. The modification due to a static electric-, magnetic- or strain field can be expressed by

$$\hat{V}_{es}^{RT} = d_{es}^{\parallel} (E_z + \delta_z) + g_{es}^{RT} \vec{S} \cdot \vec{B} + \zeta (\hat{S}_y^2 - \hat{S}_x^2) \quad (2.4)$$

with g_{es}^{RT} the excited-state electronic g-factor and ζ a strain-dependent parameter³⁸.

At low temperature (<10 K), the excited state ^3E is split into six sublevels, E_1 , E_2 , E_x , E_y , A_1 , and A_2 , by spin-orbit and spin-spin interactions as well as by strain and electric fields⁸². The resulting level structure is shown in Fig. 2.2a and an example spectrum in Fig. 2.2b. $E_{1/2}$ and $A_{1/2}$ correspond to the spin sublevels with $m_s = \pm 1$ and can be addressed via circularly polarized light. $E_{x/y}$ correspond to the spin sublevels with $m_s = 0$ and are addressed by linearly polarized light. The low-temperature fine structure of the excited state can be written as

$$\begin{aligned} \hat{H}_{es}^{LT} = & D_{es}^{\parallel} \left[\hat{S}_z^2 - S(S+1)/3 \right] - \lambda_{es}^{\parallel} \hat{\sigma}_y \otimes \hat{S}_z + D_{es}^{\perp} \left[\hat{\sigma}_z \otimes (\hat{S}_y^2 - \hat{S}_x^2) \right] \\ & + \lambda_{es}^{\perp} \left[\hat{\sigma}_z \otimes (\hat{S}_x \hat{S}_z + \hat{S}_z \hat{S}_x) \right] - \hat{\sigma}_x \otimes (\hat{S}_y \hat{S}_z + \hat{S}_z \hat{S}_y) \end{aligned} \quad (2.5)$$

with $\hat{\sigma}_x$, $\hat{\sigma}_y$ and $\hat{\sigma}_z$ being the standard Pauli matrices, and $D_{es}^{\parallel} = 1.42$ GHz, $D_{es}^{\perp} = 1.55/2$ GHz, $\lambda_{es}^{\parallel} = 5.3$ GHz and $\lambda_{es}^{\perp} = 0.2/\sqrt{2}$ GHz^{38,84}. The influence of an electric,

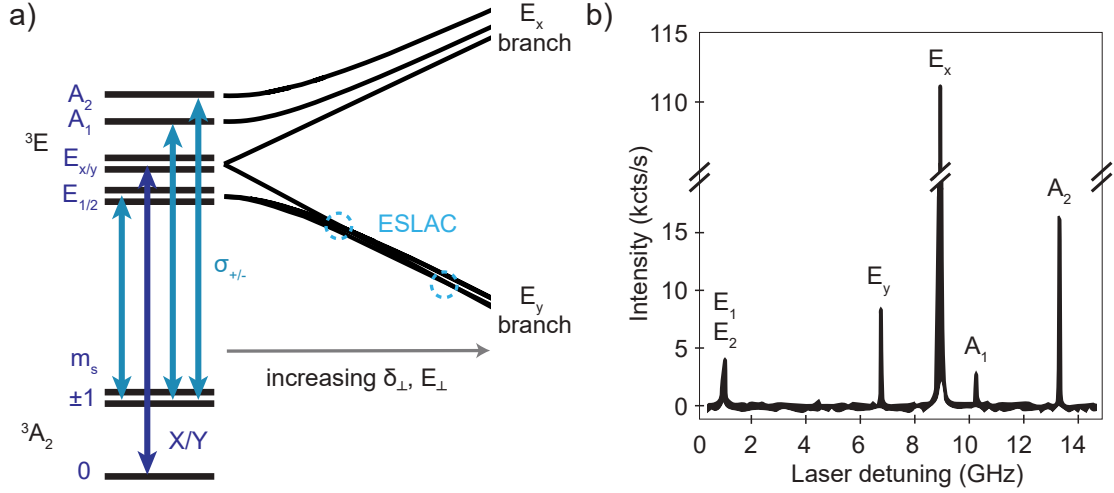


Figure 2.2.: Low-temperature electronic structure. (a) Electronic level structure of NV^- at low temperature. The states $E_{1/2}$ and $A_{1/2}$ can be addressed via circularly polarized light ($\sigma^{+/-}$) and the states $E_{x/y}$ can be addressed by linearly polarized light (X/Y). The excited-state triplet splits up into two orbital branches, E_x and E_y , due to transverse strain- and electric fields, indicated by δ_{\perp} and E_{\perp} . Two ESLACs are indicated. Adapted from Ref. 38. (b) Photoluminescence excitation (PLE) spectrum at low temperature. Adapted from Ref. 43.

magnetic and strain field can be described by

$$\hat{V}_{es}^{LT} = d_{es}^{\parallel}(E_z + \delta_z) + d_{es}^{\perp}(E_x + \delta_x)\hat{\sigma}_z - d_{es}^{\perp}(E_y + \delta_y)\hat{\sigma}_x + \mu_B(l_{es}^{\parallel}\hat{\sigma}_y + g_{es}^{\parallel}\hat{S}_z)B_z + \mu_B g_{es}^{\perp}(\hat{S}_x B_x + \hat{S}_y B_y) \quad (2.6)$$

with $l_{es}^{\parallel} \approx 0.1$ being the orbital magnetic moment, $g_{es}^{\parallel} \approx 2.01$ and $g_{es}^{\perp} \approx 2.01$ the components of the electronic g-factor tensor, and d_{es}^{\parallel} and d_{es}^{\perp} the components of the ${}^3\text{E}$ electric dipole moment (both on the order of 6 kHz m/V)^{38,85}.

Eq. (2.6) demonstrates that a longitudinal strain or electric field along the NV axis leads to a unidirectional shift of the energy levels, while a transverse strain or electric field splits the energy levels in opposite directions. The latter case results in the two orbital branches E_x and E_y . Depending on the exact strain and electric field, the branches undergo a number of excited-state level anti-crossings (ESLACs) that lead to spin-flip transitions as well as an increased probability for inter-system crossing (ISC). ESLACs reduce the optical contrast between spin sublevels⁸⁴ and can be exploited to map the transverse strain and electric fields experienced by an NV⁸⁶.

The conversion from the detailed low-temperature excited-state structure to the single, broad ODMR signature at room temperature occurs due to phonon-induced processes^{87,88}, where the population in a given ${}^3\text{E}$ low-temperature fine structure level is redistributed to other fine structure levels with the same spin projection via spin-conserving phonon transitions. The degree of population redistribution increases with increased phonon transition rates and thus increasing temperature. The room temperature structure can therefore be seen as the average of the low-temperature structure^{38,84}.

The fine structure of NV^0 was experimentally confirmed only recently⁸⁹. It has a ${}^2\text{E}$ ground state, consisting of a pair of doublet states with opposite spin-orbit parity; the degeneracy is lifted by Zeeman interactions under a magnetic field. It further has a ${}^2\text{A}_2$

excited state without spin-orbit structure which is split only by the spin-Zeeman effect. Together, this leads to a fine structure with four spin-conserving transitions under an applied magnetic field. The radiative lifetime of NV^0 is 22 ns⁸⁹.

2.1.1.2 Vibronic structure

The NV emission spectrum (Fig. 2.1a) is generated by the interaction of the NV's electronic and vibrational degrees of freedom. The simplest model to describe these interactions is the Huang-Rhys model⁵⁵. In this model, the quasi-continuum of vibrational modes in the diamond lattice is replaced by a single vibrational mode³⁸. Within the Born-Oppenheimer approximation, the vibrational motion can be described by the potential formed by the state's electronic energy and its dependence on the nuclear coordinates. After a further approximation of this potential by a quadratic function of the nuclear coordinates, the 3A_2 and 3E states can be associated with simple harmonic oscillator states with energy $\hbar\omega(v + 1/2)$ and $\hbar\sqrt{\omega^2 + b}(v + 1/2)$. Here, b is the quadratic electron-vibration coupling parameter and v the vibrational occupation⁹⁰.

Due to the non-zero overlap between the vibrational wavefunctions of the ground and excited state, transitions are allowed between all vibronic levels. The transition rates are proportional to the vibrational Franck-Condon factors. The vibrational degrees of freedom allow for efficient off-resonant excitation of the NV, but also lead to one of the main drawbacks of NVs in applications relying on coherent photons: the large PSB. It is formed due to the non-zero overlap between the lowest vibronic level in the excited state and the higher vibronic levels in the ground state. These transitions, in which photons are emitted with one or several fast-dephasing phonons (coherence lifetime of less than a picosecond⁶¹), are Stokes-shifted with respect to the ZPL in the emission spectrum and encompass the majority of the emission⁵⁵. With an NV Debye-Waller factor of 2.55%⁵⁸, only a fraction of all photons are emitted into the ZPL, corresponding to the transition between the lowest vibronic level in the ground state and the lowest vibronic level in the excited state.

2.1.2 Optical- and spin properties

The excited-state lifetime of NV^- , which is largely temperature-independent, is typically 12 to 14 ns for the spin sublevel $m_s = 0$ and 7 to 8 ns for $m_s = \pm 1$ ^{38,56,57}. Optical transitions between 3A_2 and 3E are spin-conserving⁸⁴, and the difference in emission rate for different spin sublevels leads to spin-state dependent PL that is employed in most NV-related applications.

2.1.2.1 Spin-state-dependent photoluminescence

Without prior spin-polarization and initialization into $m_s = 0$, a bi-exponential fluorescence decay is observed from NV^- due to its spin sublevels having different lifetimes^{38,84,91}. This is in turn due to an NV in $m_s = \pm 1$ having a higher probability (8-9

times) to undergo ISC to the singlet levels compared to $m_s = 0$, and equal probability to decay back to the 3A_2 spin sublevels⁹². The long, ≈ 460 ns lifetime of the singlet state, given mainly by the lifetime of 1A_1 , leads to a reduced fluorescence for $m_s = \pm 1$ and an effective spin polarization. Due to the temperature-dependence of the singlet lifetime (reducing to ≈ 220 ns at room temperature), the degree of spin-polarization decreases with temperature⁹³. It is typically reported to be about 80%^{38,57}.

The first term in Eq. (2.2) indicates that the spin sublevels in the NV^- ground state are split under an applied magnetic field by the Zeeman effect (Fig. 2.3a). Together with the reduction in fluorescence for $m_s = \pm 1$, this leads to a straightforward way to measure magnetic fields with high resolution, forming the basis of NV magnetometry.

Figure 2.3b illustrates how the ODMR signature of an NV changes depending on the magnetic field projection along the NV axis. When sweeping the frequency of an applied microwave (MW) field and monitoring the NV photoluminescence (PL) under off-resonant excitation, dips in the signal are recorded when the MW frequency matches the spacing between the $m_s = 0$ and the $m_s = +1$ spin sublevel or the splitting between the $m_s = 0$ and $m_s = -1$ spin sublevel. The reduced fluorescence is a consequence of the preferential decay of the $m_s = \pm 1$ levels through the singlet manifold. The higher the magnetic field projection B_{NV} along the NV quantization axis, the larger the splitting between the $m_s = -1$ and the $m_s = +1$ spin sublevel, and the wider the splitting between the dips in the ODMR measurement.

The sensitivity in NV magnetometry is defined, among other things, by the distance between the NV and the sensed object. An established method to minimize this distance is to place the NV at the end of a diamond nanopillar, and use this as the tip of an atomic-force microscope^{94,95}. The sensing contrast is further improved by increasing the photon collection efficiency⁹⁶ and optimally orienting the NV with respect to the sample⁹⁷. The technique has been used in nanoscale magnetometry of, among other things, two-dimensional magnets⁹⁸, current flows in two-dimensional materials⁹⁹ and domain walls

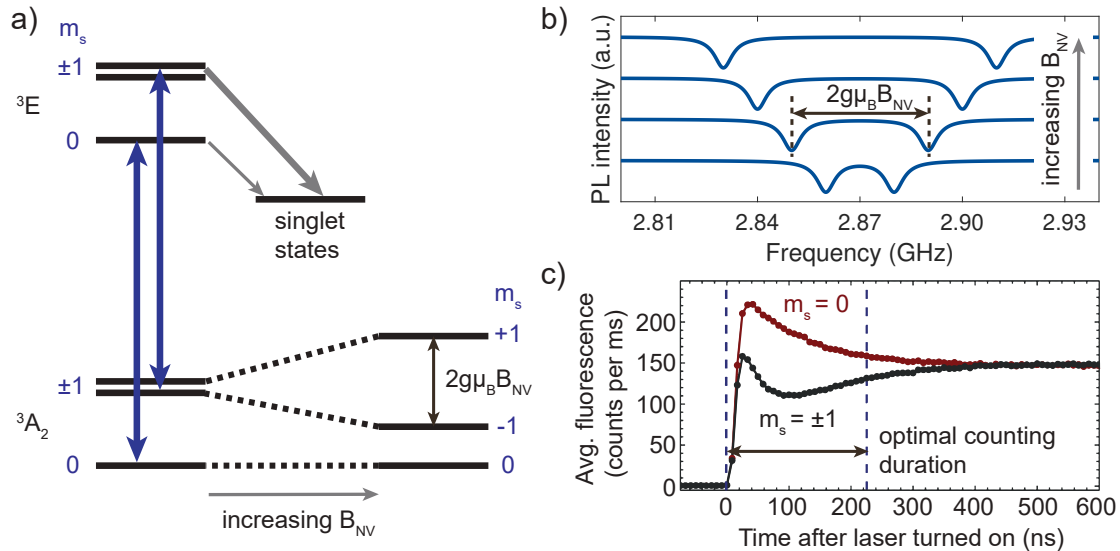


Figure 2.3.: Spin-state dependent PL. (a) The ground-state $m_s = \pm 1$ sublevels split with increasing magnetic field B_{NV} along the NV axis. (b) ODMR signal as a function of increasing B_{NV} . (c) Fluorescence transient upon resonant excitation of an NV in $m_s = \pm 1$ or $m_s = 0$. Adapted from Ref. 92.

in antiferromagnets¹⁰⁰.

Figure 2.3c illustrates that NV fluorescence undergoes different dynamics depending on whether the initial spin state is $m_s = 0$ or $m_s = \pm 1$. It indicates on one hand that more than one cycle is needed to reach a spin-polarized steady-state, and on the other hand that the spin state can be read out optically by choosing an appropriate counting duration¹⁰¹.

2.1.2.2 Optical dynamics and linewidth

The optical dynamics of an NV, governing the conversion between NV^0 and NV^- , are both radiative and non-radiative. The radiative transitions occur between the excited levels of NV^0 and NV^- via the valence and conduction band, leading to photo-conversion processes that are proportional to the square of the optical excitation intensity and independent of the donor and acceptor concentration in the vicinity of the NV¹⁰². Since the non-radiative transitions occur directly between electronic states of NV^0 and NV^- , they correspond to the tunneling between the NV and close-lying electron donors or acceptors, and so their rate depends strongly on the distance between the NV and such donors and acceptors in the lattice¹⁰³.

Both NV^0 and NV^- can be detected as single centers using confocal microscopy, and have both been identified as single photon sources through their photon statistics³⁸. Both charge states can be excited using off-resonant green excitation (typically 532 nm/2.3 eV)¹⁰⁴. Bleaching, photo-conversion between the two charge states, as well as two-photon absorption processes (in particular under resonant excitation) all lead to reduced PL.

In the case of NV^- , two-photon absorption under resonant excitation (Fig. 2.4a) leads to photoionization and conversion into NV^0 . Off-resonant excitation through green illumina-

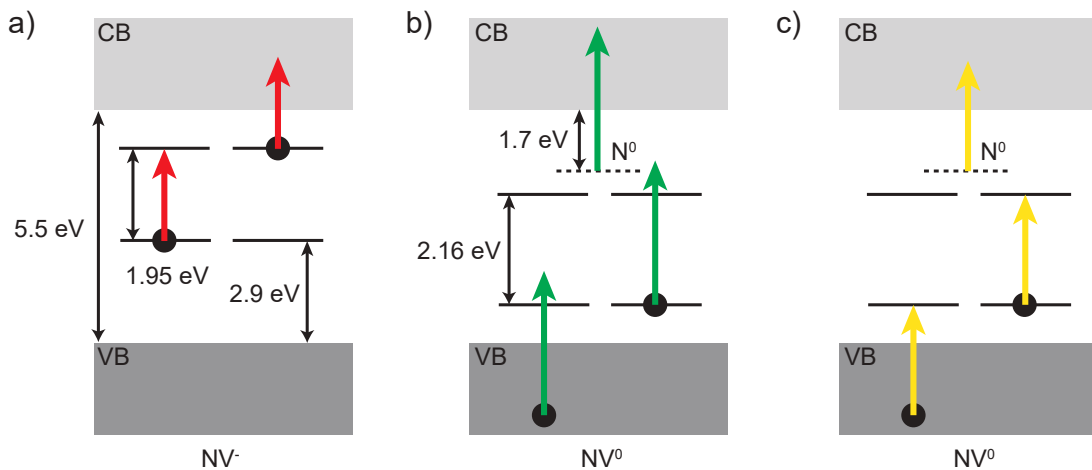


Figure 2.4.: Ionization mechanisms. (a) Resonant excitation of NV^- can lead to a two-photon process, promoting an electron into the conduction band (CB) and converting the NV into its neutral charge state, NV^0 . (b) Off-resonant green excitation (532 nm/2.3 eV) excites NV^0 , restoring the negative charge state of the NV. However, it also excites nearby N^0 , leading to charge noise that affects the spectral stability of the NV. (c) Yellow excitation (575 nm/2.16 eV) resonantly addresses NV^0 , restoring the NV charge state without inducing excessive charge noise.

nation (Fig. 2.4b) restores the negative charge state, but can also ionize NV^- , leading to a balance between the NV^- and NV^0 populations depending on the excitation wavelength, the nitrogen concentration, and the duration and intensity of the illumination^{105,106}. Furthermore, green illumination excites nearby N^0 donors. Due to the permanent electric dipole moment of the NV and the associated first-order sensitivity to electric fields, this change in the charge environment shifts the NV's emission frequency through the DC Stark effect¹⁰⁷. A way to reduce this spectral diffusion, or spectral "jittering", is to resonantly address NV^0 with yellow illumination (575 nm/2.16 eV, Fig. 2.4c), restoring the NV charge state even at low excitation powers¹⁰⁸. Another commonly used approach is probing the state preparation of an NV under resonant excitation and applying a green repump pulse only if the charge resonance check results in a photon count below a given threshold¹⁰⁹. This reduces the effect of spectral jumps induced by the off-resonant repump. Dynamic stabilization of the NV ZPL frequency via Stark tuning has furthermore been reported¹¹⁰.

The most common spectroscopic method for measuring the ZPL linewidth of an NV is photoluminescence excitation (PLE). There, PL in the PSB is recorded as a function of the frequency of the resonant excitation. A lifetime-limited linewidth (Fig. 2.5a, dashed line) in such a measurement gives a Lorentzian emission lineshape with a full-width-half-maximum (FWHM) of $\gamma_0/(2\pi)$:

$$L(f) \propto \frac{\frac{1}{2}(\gamma_0/(2\pi))}{(f - f_0)^2 + (\frac{1}{2}(\gamma_0/(2\pi)))^2} \quad (2.7)$$

where γ_0 is defined by the radiative lifetime τ_0 via $\gamma_0 = 1/\tau_0$.

Until now, only native NVs have shown lifetime-limited linewidths, $\gamma_0/(2\pi) \approx 13$ MHz⁴⁰. Instead, most of the NV ZPL linewidths are broadened by a number of mechanisms. A homogeneously broadened linewidth is a Lorentzian with an increased FWHM, $\Gamma_h/(2\pi) > \gamma_0/(2\pi)$ ¹¹¹, given by non-radiative transitions and interactions with phonons. The linewidth can further be broadened to a width $\Gamma_p/(2\pi) = \Gamma_h/(2\pi) \cdot \sqrt{1 + s_0}$ by the power of the excitation light (Fig. 2.5a, solid line), with $s_0 = I/I_s$ the saturation parameter on resonance, I the laser intensity and I_s the saturation intensity.

Temperature drifts and spectral jumps further result in inhomogeneous broadening of the linewidthⁱ, with a measured FWHM of $\Gamma_{in}/(2\pi) > \Gamma_h/(2\pi)$. A linewidth broadened due to the NV emitting at different frequencies throughout the measurement due to fast spectral jumps is typically described by a Gaussian¹¹¹:

$$G(f) = \frac{1}{\sigma\sqrt{2\pi}} e^{-\frac{((f-f_0)-\mu)^2}{2\sigma^2}} \quad (2.8)$$

with a measured FWHM of $\Gamma_{in,G}/(2\pi) = 2\sqrt{2\ln 2} \cdot \sigma$ (Fig. 2.5b). Including all of the mentioned broadening mechanisms leads to a convolution between a Lorentzian and a Gaussian lineshape,

$$V(f) = \int_{-\infty}^{\infty} G(f')L(f + f_0 - f') df' \quad (2.9)$$

ⁱHere, we refer to *temporal* rather than *spatial* inhomogeneous broadening. The former stems from varying conditions for a single emitter, while the latter can be obtained from an ensemble of nominally identical emitters with slightly different surroundings.

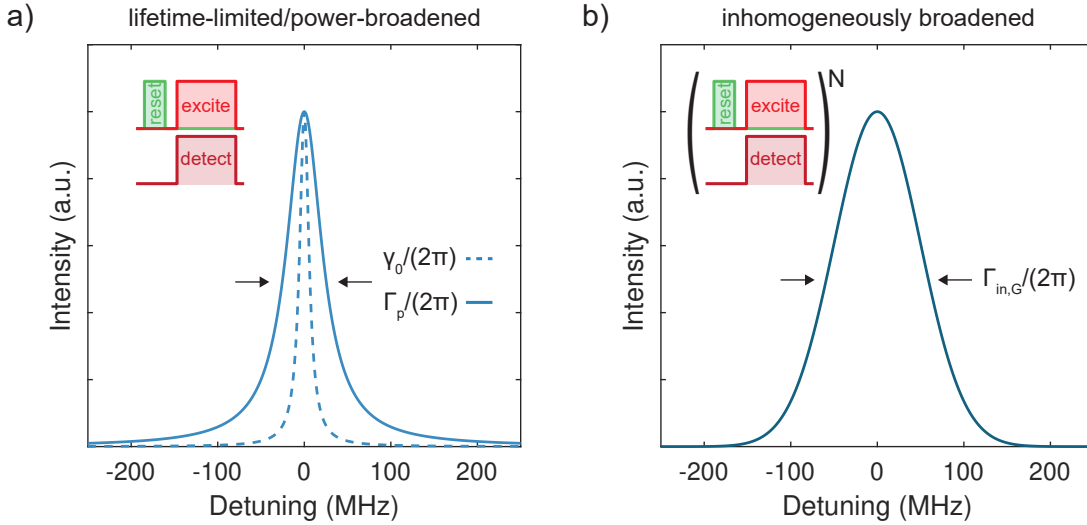


Figure 2.5.: Simulated single-scan linewidths. (a) A lifetime-limited NV linewidth with a FWHM of $\gamma_0/(2\pi) = 13$ MHz (dashed line), given solely by the NV’s radiative decay time, and a homogeneously and power-broadened linewidth of $\Gamma_p/(2\pi) = 50$ MHz (solid line), given by non-radiative transitions, interactions with phonons and the excitation power. Both are described by a Lorentzian lineshape. (b) Inhomogeneously broadened linewidth with a FWHM of $\Gamma_{in}/(2\pi) = 100$ MHz, described by a Gaussian. The insets in (a) and (b) show the measurement sequences that would yield the respective lineshapes.

where f_0 is the common central frequency of the two lineshapes. $V(f)$ is a Voigt function, which has no simple analytical expression¹¹¹. Depending on the dominating broadening mechanism, the Voigt profile can be simplified to a Lorentzian or a Gaussian.

The spectral jittering induced by green illumination is one of the main contributions to NV linewidth broadening. As green “repump” is systematically used to restore both the NV charge state and the NV spin state, it is important to quantify its effect on the linewidth. If a single green pulse is applied at the beginning of a PLE scan, only the homogeneous broadening and the power broadening is detected (Fig. 2.5a). If green pulses are applied at a high rate interleaved with the resonant excitation during a PLE measurement, the “single-scan linewidth” is broadened due to spectral jumps happening faster than the tuning of the excitation frequency across the ZPL (Fig. 2.5b). In the latter case, the resulting lineshape has a larger Gaussian contribution.

In order to properly separate these cases, average linewidths given by repeated measurements of the same NV transition will in this thesis be categorized according to Fig. 2.6 as

- Dephasing linewidths, if multiple single-scan linewidths are fitted individually and averaged. In this case, the effect of linewidth broadening due to slow drifts and spectral diffusion is excluded – only the homogeneous broadening and the power broadening is measured – and the resulting average lineshape is described by a Lorentzian.
- Extrinsically broadened linewidths, if all broadening mechanisms contribute during a measurement. The true lineshape is given by a Voigt function, but for a high level of charge noise in the vicinity of the measured NV, the spectral diffusion leads to a Gaussian-dominated lineshape.

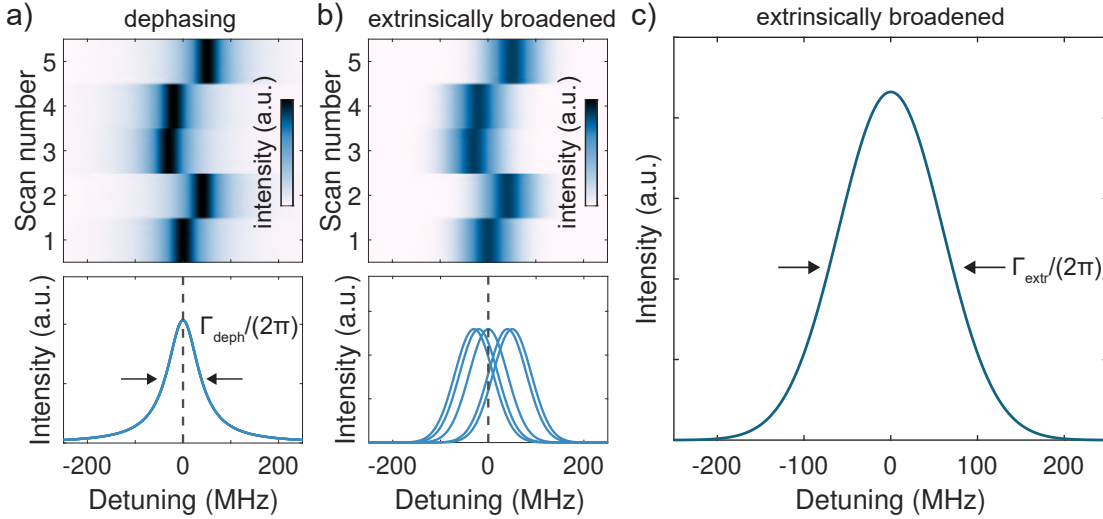


Figure 2.6.: Simulated average linewidths, given by repeated PLE scans. (a) A dephasing linewidth is given by the average of re-centered individual measurements (with a green repump applied only at the beginning of each scan) and therefore excludes repump-induced spectral shifts as well as slow drifts. The resulting average linewidth is described by a Lorentzian with a FWHM of $\Gamma_{\text{deph}}/(2\pi)$. (b) An extrinsically broadened linewidth includes the effect of all broadening mechanisms. In the illustrated example, green repump is applied at a fast rate during each scan, giving inhomogeneously broadened single-scan linewidths. (c) An extrinsically broadened linewidth, described by a Gaussian with a FWHM of $\Gamma_{\text{extr}}/(2\pi)$.

2.1.2.3 Spin coherence

The spin dynamics of NV^- are characterized by the electron spin longitudinal (spin-lattice) relaxation time T_1 , the homogeneous dephasing (spin-spin relaxation) time T_2 and the inhomogeneous dephasing (transverse relaxation) time T_2^* .

The T_1 time is given by transitions between spin sublevels, reducing their population difference. It is affected by magnetic resonances of close-lying substitutional N (resulting in energy-conserving spin flip-flops), electric and magnetic noise for near-surface NVs¹¹², and is otherwise limited by phonon-induced transitions between the spin sublevels³⁸. Such two-phonon processes lead to a temperature-dependence of the spin relaxation, given by $1/T_1 \propto \omega^3/(e^{\hbar\omega/k_B T} - 1)$ with $\hbar\omega = 63 \text{ meV}$ up to room temperature, and $1/T_1 \propto T^5$ above room temperature^{113,114}. At room temperature, the NV^- T_1 time has been measured to be up to 7.5 ms³⁶. At $\sim 4 \text{ K}$ and in natural-abundance (1.1% ^{13}C), electronic-grade diamond, $T_1 = 3600 \text{ s}$ was measured, which is the longest lifetime reported to date for a single electron spin qubit³⁷. NV^0 has shown a much shorter spin relaxation of $T_1 = 1.5 \text{ ns}$ at low temperature⁸⁹, limited by interactions with phonons due to its spin-1/2 nature.

The T_2 time is given by fluctuating interactions that dephase the spin state. Governed by spin-spin interactions between the NV and other electronic and nuclear spins, it mainly depends on the density and type of paramagnetic impurities close to the NV, but also on temperature³⁸. For nitrogen-poor diamonds of type IIa, the dominant dephasing mechanism is interactions with the ^{13}C spin bath¹¹⁵⁻¹¹⁷. Dynamical decoupling sequences can be used to mitigate the dephasing from specific nuclei, reaching a longer trans-

verse relaxation time T_2^{dec} , which is ultimately limited by $2 \cdot T_1$. The longest measured T_2^{dec} times at room temperature are 2.4 ms, measured with a Hahn-echo sequence on phosphorus-doped diamond¹¹⁸, and 3.3 ms, measured using dynamical decoupling¹¹⁹. The longest measured T_2^{dec} time at ~ 4 K is 1.6 s³⁷.

T_2^* , with $T_2^* < T_2$, is governed by the slow temporal changes of local fields at a single NV due to fluctuations of the magnetic or electric environment³⁸. The longest measured values include $T_2^* = 1.5$ ms in phosphorus-doped diamond¹¹⁸ and $T_2^* = 470$ μ s in isotopically purified diamond³⁶. Isotopic purification reduces the amount of nuclear spins that can dephase the spin, while phosphorus doping leads to n-type conductivity, stabilization of NV^- , and suppression of the formation of vacancy complexes during nitrogen implantation by vacancy charging¹¹⁸.

2.1.3 Formation

NVs can be formed either naturally during the growth of the diamond, or by a wide range of methods designed to introduce either vacancies, nitrogen, or both, into the lattice post-growth. During annealing, the created vacancies diffuse and form NVs either with the nitrogen atoms that were implanted or with nitrogen which was already present in the lattice.

2.1.3.1 Ion implantation

A widely used method for the creation of NVs is nitrogen ion implantation^{47,48} followed by high-temperature annealing^{108,120}. The method is based on an ion penetrating the diamond lattice, creating a trail of vacancies and carbon interstitials, and stopping at a certain depth within the material (Fig. 2.7a). During the subsequent thermal annealing, the created vacancies diffuse in the diamond lattice and form NVs with either native or implanted nitrogen (Fig. 2.7b).

A multi-step annealing, illustrated in the top panel in Fig. 2.7b, is motivated by the fact that the thermal annealing should not only facilitate the NV formation, but also remove residual lattice defects. Carbon interstitials anneal out at a temperature around 400°C, while vacancies become mobile (with a migration activation energy of 2.3 eV¹²¹) at a temperature of 600°C. A slightly higher temperature of 800°C is typically used to facilitate faster formation of NV^- (formation energy of 8.8 eV). NVs remain immobile up to a temperature of approximately 1700°C¹²². Without a final, above-800°C annealing step, NVs formed via implantation typically show short T_2 times, indicating the presence of residual paramagnetic defects (such as divacancies and longer vacancy chains) that reduce the spin coherence¹²⁰. The concentration of residual paramagnetic defects has been shown to be minimized after annealing to ~ 1250 °C¹²³. Other studies have supported the claim by demonstrating a positive effect on the NV T_2 time¹²⁴ and on NV optical linewidths¹⁰⁸ when additionally annealing to a temperature of 1200°C.

The method of ion implantation followed by annealing is useful for creating NVs with high depth precision (down to a few nm) and good formation yield ($\sim 10\%$, depending on the implantation energy¹²⁵), but subsequent micro- and nanofabrication has been shown

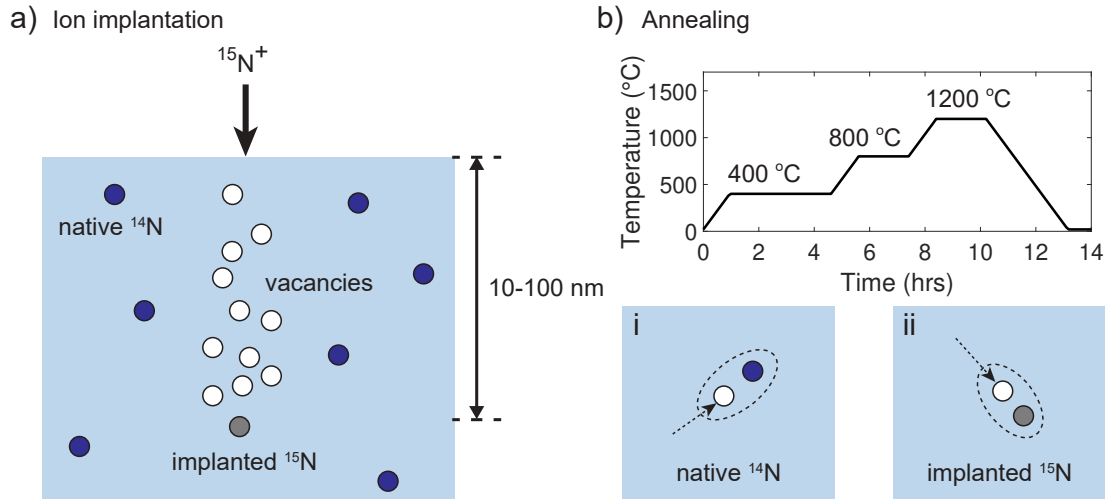


Figure 2.7.: Nitrogen implantation and annealing for NV formation. (a) Nitrogen ions are implanted into the diamond and create a trail of lattice vacancies. (b) During annealing, the vacancies diffuse and form NVs either with native (i) or implanted (ii) nitrogen. Top panel: temperature ramping during a multi-step high-temperature annealing following Ref. 108.

to severely affect the NV optical properties. In $\sim 1 \mu\text{m}$ thick diamond, the extrinsically broadened linewidths are on the order of GHz due to strong spectral diffusion⁵⁸. Only very few cases of <500 MHz extrinsically broadened linewidths have been reported on microstructures^{126–128}, and close-to lifetime-limited extrinsically broadened linewidths on NVs created with this method have only been measured in bulk¹⁰⁸.

Implantation of ^{15}N , which has a natural abundance of only 0.37%¹²⁹, allows the origin (native N or implanted N) of an NV to be determined by comparing the features seen in an ODMR measurement. A hyperfine structure corresponding to the $I = 1$ nature of ^{14}N is a signature of NVs formed from native nitrogen, while a $I = 1/2$ signature corresponding to ^{15}N indicates an NV formed from implanted nitrogen. Studies comparing the linewidths of NVs in this way have shown that NVs formed from native nitrogen tend to have narrow dephasing- and extrinsically broadened linewidths, while NVs formed from implanted nitrogen exhibit significantly larger extrinsic broadening. Some cases of narrow-linewidth NVs formed from ^{15}N can nevertheless be found, indicating that the difference in linewidth is not isotope-related^{127,130}.

Depending on the implantation depth, the diamond surface also contributes to the optical coherence of NVs. Shallow NVs tend to have orders-of-magnitude broader linewidths compared to NVs deeper in the bulk, even when implanted with parameters creating the same amount of lattice damage. This indicates that the surface is a larger source of noise compared to the lattice damage induced by the implantation¹³¹. The effects of the surface can partially be mitigated by an improved surface morphology and oxygen-termination of the surface, achieved by high-temperature annealing to 1200°C , oxygen annealing at $\sim 450^\circ\text{C}$, and wet oxidation¹³². The effect of such a surface treatment on NV linewidths has however not yet been studied.

2.1.3.2 Electron irradiation

Electron irradiation is a method for NV creation in which vacancies are created throughout the full extent of a diamond by high-energy (\sim MeV) irradiation with a stream of electrons. With this approach, narrow extrinsically broadened (\sim 190 MHz) and dephasing linewidths (\sim 90 MHz) have been measured even in microstructured, 3.8 μ m thick diamond¹²⁸. The technique nevertheless lacks the depth precision available through ion implantation, since vacancies and thus NVs are formed across the full diamond. A way to improve the depth accuracy down to a few nanometers¹³³ is to combine electron irradiation with nitrogen delta-doping, in which a few-nanometer thick nitrogen-rich layer is formed during CVD growth by injecting nitrogen gas into the growth chamber^{134–136}.

2.1.3.3 Laser writing and ablation

A method which circumvents the need to irradiate a diamond with massive particles to create vacancies, and which therefore leads to less overall- and more localized lattice damage, is laser writing. It further has the advantage, just like electron irradiation, that it forms NVs only with native nitrogen.

In laser writing, a strongly focused pulsed laser is used to deterministically create damage within the diamond lattice. After annealing and vacancy diffusion, NVs are formed. With this method, lifetime-limited single-scan linewidths, close-to lifetime-limited dephasing linewidths, and narrow mean extrinsically broadened linewidths (\sim 180 MHz) have been measured on NVs in bulk diamond⁴⁹. Density functional theory has been used to argue that laser writing results in fewer interstitial defects and therefore less stress in the vicinity of the created NVs compared to implantation¹³⁷.

Laser ablation is instead based on the laser-irradiation of the diamond-air interface. In this case, only very broad NV linewidths (\sim 200 GHz) have been reported, most probably related to the vicinity to the diamond surface¹³⁸. More details on laser writing and ablation will be introduced in Section 2.2.

2.1.3.4 Other methods for NV creation

Other methods for NV creation include helium ion implantation, a method less suitable for applications requiring NVs located at specific depths due to its worse depth resolution (hundreds of nanometers, in comparison to tens of nanometers achieved for implantation of heavier particles such as N ions)¹³⁹. The method is mainly used to create high-density NV layers for sensing purposes¹⁴⁰, with improved depth control enabled by nitrogen delta-doping¹⁴¹. Only broad optical linewidths above 25 GHz have been reported¹⁴².

Another method suitable for creating shallow layers of NVs for sensing applications is plasma ion implantation. Through the acceleration of nitrogen ions into diamond from a plasma, homogeneous NV layers can be formed within less than 4 nm from the surface. However, the method relies on nitrogen-rich diamond of type Ib, and results only in dim, low-quality NVs when used on a nitrogen-poor diamond. No PLE linewidths have been

reported with this method¹⁴³.

2.1.4 NVs as quantum network nodes

We can conclude that the NV possesses a number of key properties that make it an excellent candidate for a quantum network node. They can be summarized following Ref. 38 as:

1. A bright, photostable optical transition (here, described in Section 2.1.2.2)
2. A low-temperature fine structure that can be controlled by and used to read out electric, magnetic and strain fields (Section 2.1.1.1)
3. A ground-state electronic spin with long spin coherence and coherent coupling to neighboring electronic and nuclear spins (Section 2.1.2.3)
4. Optical spin-initialization and optical spin readout (Section 2.1.2.1)
5. Straightforward formation (Section 2.1.3)

The following sections will introduce the progress achieved so far in terms of implementing a quantum network based on NVs.

2.1.4.1 Optical and spin-state control

A spin qubit based on an NV can be initialized into $m_s = 0$ by optical spin-polarization via green repump pulses. Under the subsequent application of short resonant pulses, optical Rabi oscillations can be detected, with a coherence limited by the repump-induced spectral diffusion¹⁴⁴. Complete control of an NV at low temperature, including spin-state initialization, coherent manipulation and single-shot electron spin readout, was first demonstrated in 2011⁴³.

After initialization into $m_s = 0$ and subsequent application of MW fields, the spin can be rotated to induce Rabi oscillations between the spin sublevels in the NV ground state. The spin state can be read out optically, with an efficiency scaling with the detected photon flux³⁸. The photon collection efficiency can be increased by fabricating a solid-immersion lens (SIL) around the NV by focused-ion beam milling (FIB)^{145,146} or by incorporating the NV into a microcavity^{58,60–64,147}. The latter approach not only improves the collection efficiency, but also increases the coherent photon flux via the Purcell effect. Until now, this has however never been achieved simultaneously – a large motivation behind this work.

The nuclear spin bath felt by the NV is the largest source of its electron spin decoherence. Nevertheless, the interaction with isolated single nuclear spins is what allows using an NV and its surrounding lattice as a quantum memory by mapping quantum states between the NV's electron and a nucleus. Nuclear spins possess coherence times exceeding milliseconds even at room temperature, limited by the electron spin relaxation time T_1 and interactions with other nuclei¹⁴⁸. By decoupling the electron spin, the coherence time

can be extended to several seconds³². Strongly coupled nuclear spins, such as the intrinsic N forming the NV and near-lying ¹³C atoms¹⁴⁹, exhibit hyperfine couplings that are larger than the electron spin resonance (ESR) linewidth, set by the dephasing rate $1/T_2^*$. For such nuclei, it is possible to perform fast controlled-NOT gates, conditional either on the nuclear spin state ($C_n\text{NOT}_e$) by applying MW π -pulses at the ESR frequencies⁵⁷, or conditional on the electron spin state ($C_e\text{NOT}_n$) by applying radio-frequency π -pulses to directly drive nuclear spin transitions¹⁵⁰. After mapping the nuclear spin-state population back onto the electronic spin, readout of the nuclear spin state can be performed optically^{32,151}.

Weakly-coupled nuclear spins, with hyperfine couplings less than $1/T_2^*$, result in much slower control but can increase the number of register qubits in a quantum memory. The NV electron spin coherence can in the case of such spins be extended via dynamical decoupling. When a targeted nuclear spin is on resonance with the periodicity of the dynamical decoupling pulses, the precession of the nuclear spin accumulates, while the opposite is true for nuclear spins that are out of sync with the dynamical decoupling sequence^{32,44,152,153}. A ten-qubit register, consisting of an NV, its ¹⁴N nuclear spin, and eight neighboring ¹³C spins, was implemented using this method in 2019, protecting a single-qubit state for over 75 s and setting the record for a single solid-state qubit⁴⁵.

2.1.4.2 Spin-photon and spin-spin entanglement

Spin-photon entanglement is based on the spin-state-dependent emission of a photon. In the case of an NV, this can for example be achieved by using a Λ system, in which the NV is excited to its A_2 state by means of circularly polarized excitation. Since A_2 decays with equal probability to the $| -1 \rangle$ state through a σ_+ polarized photon and to $| +1 \rangle$ through a σ_- polarized photon, the resulting entangled state is

$$|\Psi\rangle = \frac{1}{\sqrt{2}}(|+1\rangle |\sigma_-\rangle + |-1\rangle |\sigma_+\rangle) \quad (2.10)$$

The resulting entanglement fidelity relies on a high cyclicity of the involved transitions as well as on a high ZPL photon flux and collection efficiency¹⁵⁴. Other spin-photon entanglement approaches include entangling the NV spin state with the absence or presence of a photon^{43,54} or with the time of arrival of an emitted photon¹⁵⁵.

After generating spin-photon entangled states on two separate NVs, the photons can be used to create spin-spin entanglement. For this, the photons have to be indistinguishable – achieved either by having emitters with the same transition frequency, or by tuning the frequency of one of the emitters into resonance with the other. In the case of NVs, both are possible: emitters with similar $E_{x/y}$ transitions can be found, and otherwise an electric- or strain field can be applied to frequency-tune their E_y transitions. Two-mode quantum interference using this approach was first demonstrated in 2012⁴¹. Photons with a frequency difference can also exhibit quantum interference, but with a reduced visibility that is set by the frequency separation and the amount of temporal filtering in the photon detection^{59,156,157}.

A protocol often used for spin-spin entanglement is the Barrett-Kok protocol, which was proposed in 2005 as a way to scale optical readout-based quantum computing¹⁵⁸.

In the protocol, the matter qubits are spatially separated and entangling operations are performed via the above-mentioned single-photon interference effects. It requires two long-lived, low-lying spin states $|\uparrow\rangle$ and $|\downarrow\rangle$ and one excited state $|e\rangle$; an optical π pulse should transfer the population from $|\downarrow\rangle$ to $|e\rangle$ and the transition from $|\uparrow\rangle$ to $|e\rangle$ should be forbidden. Each of the systems can be put in an optical cavity enhancing the $|\downarrow\rangle \leftrightarrow |e\rangle$ transition to increase the success probability¹⁵⁸.

The protocol is schematically illustrated in Fig. 2.8. Each NV is first prepared into a superposition of two spin states, $\frac{1}{\sqrt{2}}(|\uparrow\rangle + |\downarrow\rangle)$ (Fig. 2.8b). Here, $|\uparrow\rangle$ and $|\downarrow\rangle$ represent the two spin-qubit states, for example the spin sublevels $m_s = 0$ and $m_s = -1$. After a resonant excitation from $|\downarrow\rangle$ to the excited state $|e\rangle$ with the same spin projection, followed by spontaneous emission, the qubit state becomes entangled with the photon number and each NV is in the state $\frac{1}{\sqrt{2}}(|\uparrow\rangle |1\rangle + |\downarrow\rangle |0\rangle)$ (Fig. 2.8d, left panel). Here, 1 stands for the emission of a photon and 0 for the absence of a photon.

The photons from the two separate NVs are then overlapped on a 50-50 beamsplitter, the outputs of which are connected to two separate detectors (Fig. 2.8c). In the case of indistinguishable photons, detecting one photon on either detector would correspond to measuring the photon state $\frac{1}{\sqrt{2}}(|1_A\rangle |0_B\rangle \pm |0_A\rangle |1_B\rangle)$ and projecting the qubits onto the maximally entangled state

$$|\psi\rangle = \frac{1}{\sqrt{2}}(|\uparrow_A\rangle |\downarrow_B\rangle \pm e^{-i\phi} |\downarrow_A\rangle |\uparrow_B\rangle) \quad (2.11)$$

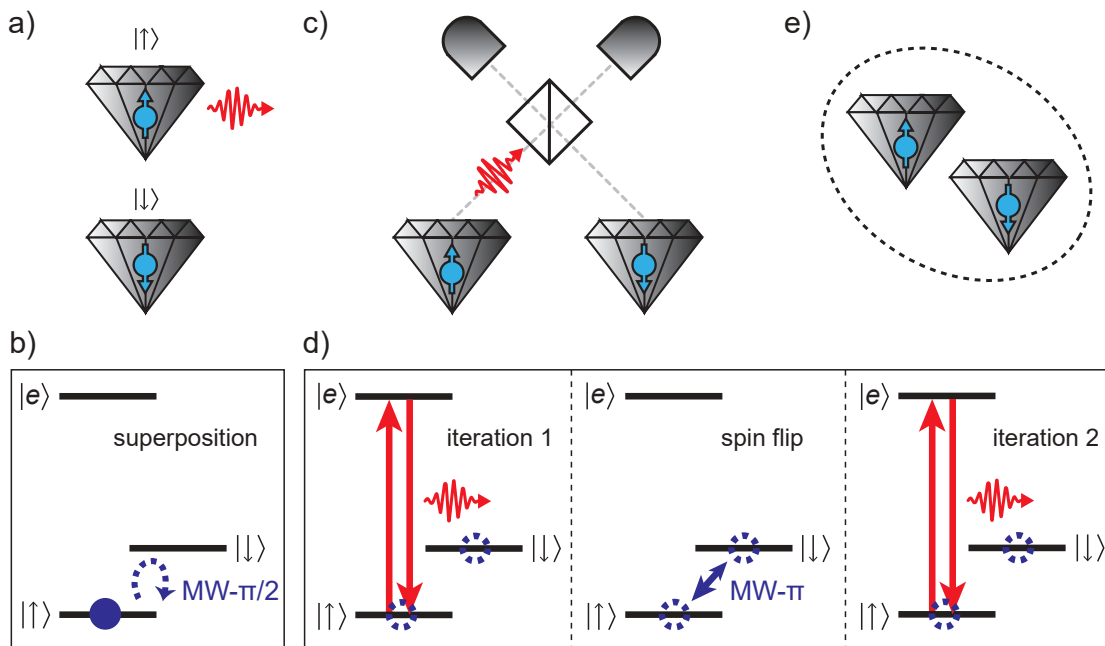


Figure 2.8: The Barrett-Kok protocol for spin-spin entanglement. (a) The emitter has two spin states, where a photon is emitted only upon optical excitation of one of them. (b) Two emitters are prepared in a spin-state superposition. (c,d) A resonant pulse is sent to each NV; only one of the spin projections results in the emission of a photon. The photons are overlapped on a beamsplitter whose outputs are connected to separate detectors. After a π pulse on each NV, flipping the spin state, the excitation is repeated. (e) If one of the detectors clicks in each round of the experiment, the two NVs are in a maximally entangled state.

with the phase ϕ depending on the optical path length.

By applying an X operation to both qubits (in the case of NVs, by using a MW π -pulse), the population is coherently flipped from $|\uparrow\rangle$ to $|\downarrow\rangle$ and from $|\downarrow\rangle$ to $|\uparrow\rangle$ (Fig. 2.8d, middle panel). After this, the protocol is repeated (Fig. 2.8d, right panel). If a photon is detected only on one of the detectors in each round of the protocol, it heralds the generation of one of the maximally entangled Bell states (Fig. 2.8e)

$$|\Psi^\pm\rangle = \frac{1}{\sqrt{2}}(|\uparrow_A\rangle|\downarrow_B\rangle \pm |\downarrow_A\rangle|\uparrow_B\rangle) \quad (2.12)$$

with the \pm sign depending on whether the same (+) or different (−) detectors clicked in the two rounds of the experiment.

The repeated measurement makes the protocol robust against photon loss and the possibility of an initial state preparation into $|\uparrow\uparrow\rangle$, in which case there would be no photon emission in the second round of the experiment. Photon loss does not reduce the entanglement fidelity, but only adds to the experimental overhead since the experiment has to be repeated. The two iterations furthermore make it possible to use non-photon-number-resolving detectors, which cannot distinguish between the states $|\uparrow\uparrow\rangle$, $|\uparrow\downarrow\rangle$ and $|\downarrow\uparrow\rangle$. The fact that the spin-spin entanglement is based on two rounds further changes ϕ into a global phase and makes the protocol independent of the optical path length difference, relaxing the need to phase-stabilize the optical circuit^{109,158}. The success probability of the protocol is given by $P_\Psi = \frac{1}{2}\eta_A\eta_B$, with η_i being the overall detection efficiency from NV i and the factor $\frac{1}{2}$ stemming from the repeated runs of the experiment¹⁰⁹. The main experimental imperfections that limit the fidelity are decoherence of the matter qubits, dark counts in the detectors and remaining distinguishability of the photons going through the beamsplitter¹⁵⁸.

The protocol was used to show spin-spin entanglement between NVs separated by three meters in 2013, relying on techniques mentioned earlier in this chapter: improved PSB collection efficiency through a FIB-SIL, native NVs with narrow extrinsically broadened linewidths, and electric-field tuning of the E_y transitions in order to create indistinguishable photons. The experiment showed a success probability of $\sim 10^{-7}$ and an entanglement event per 10 min¹⁰⁹. A later experiment, based on the same protocol, demonstrated entanglement between NVs separated by as much as 1.3 km. There, the success probability per entanglement generation attempt was $6.4 \cdot 10^{-9}$, resulting in a reduced rate of successful entanglement events of approximately once per hour. The reduction was attributed mainly to the additional photon loss in the optical fibers connecting the remote locations⁵⁴.

2.1.4.3 Extension to networks and further improvements

The spin-spin entanglement rates between two separate NVs are limited by the low NV coherent photon flux. The Barrett-Kok protocol, although extremely robust and easy to implement, is a double-click protocol: it relies on the detection of a photon in each round of the experiment, and thus scales with the square of the detected photon flux.

In more recent experiments, a protocol scaling only linearly with the photon flux has therefore been used. Only the first iteration of the Barrett-Kok protocol is performed, and

instead of repeating the protocol in order to make the result independent of the phase difference between the two optical paths, the phase is stabilized to a known value using a feedback loop. Technologically more complex, this requires a phase-stabilization scheme that works individually on each node, since they are subject to different amounts and sources of noise. This single-photon protocol was implemented in experimental demonstrations of a three-node quantum network based on NVs in 2021¹¹ and 2022¹². The highest entanglement rate achieved so far between separate NVs using this protocol is 39 Hz¹⁵⁹.

Another limitation are the losses in optical fibers. 637 nm photons experience a loss of approximately 8 dB/km, which in the case of Ref. 54 led to a 30 times lower remote entanglement rate compared to a local experiment. A way to mitigate this problem is to convert the photons to the telecommunication wavelength range, where optical losses are less than 0.2 dB/km. This has been demonstrated by quantum frequency down-conversion of NV ZPL photons to 1588 nm, with a current state-of-the-art conversion efficiency of approximately 17%¹⁶⁰. The resulting photons were shown to preserve their single-photon characteristics, however with a reduced single-photon purity due to noise produced in the quantum frequency generation process.

2.1.5 Other color centers in diamond

The limitations related to the optical properties of NVs have triggered interest in employing other color centers in diamond as quantum network nodes. Characteristics to consider when comparing emitters to the NV include the Debye-Waller factor ζ (describing the fraction of photons emitted into the ZPL), the excited-state lifetime τ_0 , the quantum efficiency (QE, describing how much of the total decay is radiative), the ZPL frequency, the spin coherence, and the sensitivity to surface noise¹⁶¹.

Group-IV defects in diamond, with an interstitial group-IV atom sitting between two adjacent vacancies (inset in Fig. 2.9a), possess an inversion symmetry. This leads to a vanishing permanent electric dipole moment in the excited state and makes the defects first-order insensitive to electric field and strain variations¹⁶². This enables microfabrication of diamond and positioning of the emitters closer to the diamond surface without the severe degradation of the optical properties that is observed for NVs. Experimentally explored group-IV defects include the silicon-vacancy center (SiV), germanium-vacancy center (GeV), tin-vacancy center (SnV) and lead-vacancy center (PbV). Apart from SiV⁰, neutrally-charged defects with heavier ions have not yet been observed, probably due to an unfavorable Fermi level for their stabilization or a low quantum efficiency¹⁶³. More recently, another so far unidentified silicon-related defect emitting at 1221 nm was identified, promising due to its emission in the telecom O-band¹⁶⁴.

Negatively charged group-IV centers possess orbital- and spin-doublet ground states, giving rise to four ZPL transitions (Fig. 2.9b). Rapid ground-state dephasing due to phonon transitions between orbital states requires operation at lower temperatures compared to NVs, with a slight improvement for the heavier group-IV ions¹⁶¹ or by increasing the ground-state splitting by the application of strain^{165,166}. The insensitivity of the ZPL frequency to electric fields leads to inefficient spectral tuning via the Stark effect, and instead requires two-photon Raman schemes or dynamical strain-environment control¹⁶¹.

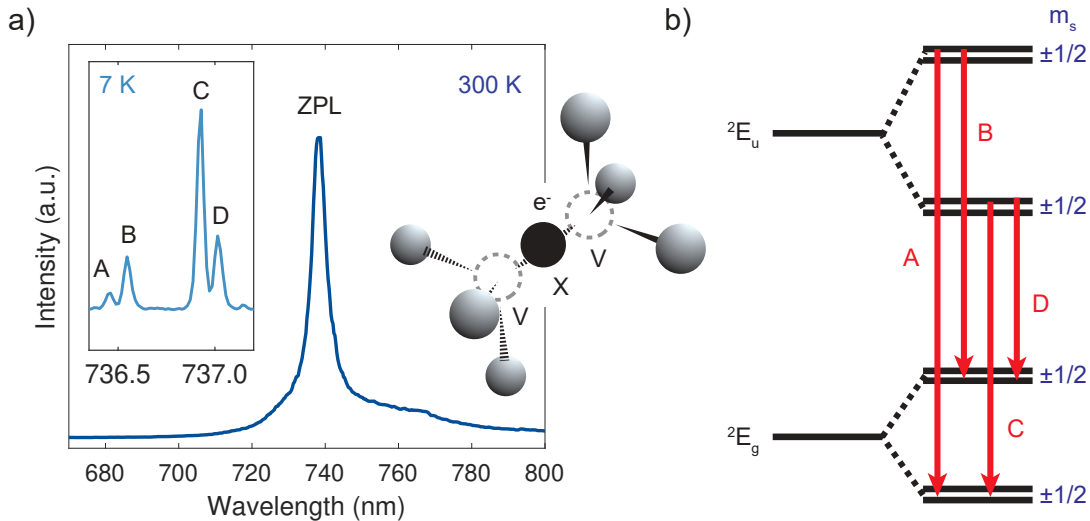


Figure 2.9.: Group-IV defects in diamond. (a) Room- and low-temperature spectra of a SiV^- . At low temperature, the ZPL splits up into four transitions. Data: courtesy of Josh Zuber. Inset: atomic structure of a group-IV defect, consisting of two substitutional vacancies (V) with a group-IV interstitial (X), oriented along the $\langle 111 \rangle$ direction in the diamond lattice. (b) Electronic level structure of group-IV defects. The four transitions A, B, C, and D visible at low temperature are indicated.

2.1.5.1 The silicon-vacancy center

The group-IV defect in diamond which has been characterized the most until now is the negatively charged silicon-vacancy center (SiV^-)^{162,167}. Its emission spectrum at room and low temperature is shown in Fig. 2.9a. SiV^- shows close-to lifetime-limited optical linewidths in bulk diamond¹⁶², in nanodiamonds^{168,169}, and in single-mode diamond waveguides¹⁷⁰. Other examples of photonic integration of SiVs include fiber-based microcavities (with nanodiamonds¹⁷¹ or diamond membranes¹⁷²), nanowires¹⁷³ and photonic integrated circuits^{174,175}.

SiV^- and SiV^0 have high Debye-Waller factors of 0.7 and 0.9, respectively, and a short radiative lifetime of 1.6-1.8 ns, making them attractive coherent photon emitters^{32,161,163}. With ZPLs at 737 nm and 946 nm, they are easily addressed by commercially available lasers.

A drawback of SiV^- is the low inferred $\text{QE} \approx 0.1$ ^{161,163} (to be compared with an NV QE above 0.7^{39,176}). For emitters with $\text{QE} \ll 1$, it is however difficult to estimate the QE with methods based on the sensitivity of the emitters to their local photonic environment, since the induced changes are small. The presence of strong phonon-mediated transitions between the two ground-state orbital branches furthermore leads to short SiV^- spin dephasing times T_2^* on the order of 100 ns at 4 K. At 100 mK and in isotopically purified samples, the spin coherence increases to $T_2^* \sim 10 \mu\text{s}$ and $T_2 \sim 10 \text{ms}$ ^{177,178}.

SiV^0 , which has only recently been stabilized due to the requirements it sets on doping and surface engineering, promises better properties compared to its negatively charged counterpart, with long spin coherence times even at elevated temperatures ($T_1 \approx 25 \text{s}$ at 15 K, $T_2 \approx 1 \text{ms}$ at 4 K)^{179,180}, coherent optical transitions, higher QE^{161,163} and spin-dependent PL^{181,182}. However, population trapping into a dark state leads to quenching

of the PL below a temperature of 70-80 K^{182,183}.

2.1.5.2 Heavier group-IV centers

GeVs and SnVs have a Debye-Waller factor of 0.6 and radiative lifetimes of 5-6 ns. The Debye-Waller factor for PbV, with a radiative lifetime above 3 ns, is currently unknown. Photon count rates in experiments involving SnVs and GeVs indicate high QEs^{161,163,184}. All of the heavier group-IV color centers suffer from poor laser availability due to their ZPL at 602 nm (GeV), 619 nm (SnV), and 520-552 nm (PbV)^{161,163}.

For GeVs, optical- as well as MW spin control has been demonstrated, with a spin dephasing time of $T_2^* = 19$ ns at 2 K¹⁸⁵. The defect has been integrated into microdisk resonators¹⁸⁶, diamond waveguides¹⁸⁴ and photonic integrated circuits^{174,175}. Cavity-enhanced single-photon emission¹⁸⁷ as well as two-mode interference of resonance fluorescence^{188,189} has been demonstrated.

Transform-limited photons from individual SnVs¹⁹⁰ as well as single-shot spin readout and a spin-dephasing time of $T_2^* = 5$ μ s at 2 K has been measured¹⁹¹. SnVs have been integrated into photonic crystal resonators¹⁹², waveguides¹⁹³ and nanopillars¹⁹⁴. So far, the only known photonic integration of PbVs is into nanopillars¹⁹⁵.

2.1.6 Optically active defects in other materials

Diamond is not the only material that acts as a host for impurity spins with coherent properties. Defects in silicon and silicon carbide as well as rare-earth ions in solids all present certain advantages compared to color centers in diamond.

2.1.6.1 Defects in silicon and silicon carbide

Silicon (Si) is a material that has long dominated the world of electronics, with a wide applicability, well-established nanofabrication methods and possibility for extreme device miniaturization. The defect in Si that has demonstrated the largest progress in spin- and photonic applications is the single phosphorous donor, ³¹P, whose electron and nuclear spins show coherence times exceeding 0.5 s at 100 mK. Challenges still remain in coupling multiple donor spins^{32,196}.

Silicon carbide (SiC) is another wide-bandgap semiconductor that is host to a broad range of optically active defects. It is an attractive candidate for scalable and integrated quantum photonics owing to its compatibility with existing Si large-scale nanofabrication. Different stacking sequences of the Si-carbon bilayer unit result in over 250 polytypes of SiC¹⁹⁷, allowing for material optimization depending on the wanted properties.

Two color centers in SiC have so far shown long spin coherence, optical addressability of the electron and nuclear spin, and single-defect isolation, making them attractive candidates for quantum applications: the neutral divacancy (V_C-V_{Si} , a missing C atom next to a missing Si atom) and the negatively charged vacancy (V_{Si} , a single missing Si

atom)^{198–201}. V_{Si} in 4H-SiC has a $T_2^{dec.}$ coherence time on the order of milliseconds under dynamical decoupling and emits 40% of its photons into the ZPL at 4 K^{202,203}.

The neutral divacancy has the same symmetry as the NV, giving it similar spin and optical properties²⁰⁴, but has the advantage of emitting at near-infrared wavelengths close to 1100 nm (resulting in an 8-fold reduction in optical fiber losses³²). It has an electron spin coherence time of $T_2 > 1$ ms¹⁹⁸, which is high considering the fact that the material contains a higher fraction of nuclear spins than diamond^{205,206}. High-fidelity resonant spin readout²⁰¹ as well as Stark tuning of the optical transition²⁰⁷ have been demonstrated. However, only 5–7% of the emission is directed into the ZPL²⁰¹, leading to similar issues as for the NV. The problem can be circumvented by using another polytype, 3C-SiC, which can be epitaxially grown on Si and offers a platform for fabricating photonic structures^{208,209}.

2.1.6.2 Rare-earth ions in solids

Rare-earth ions in solid-state crystals have states with narrow optical linewidths and high spectral stability, all owing to the isolation from environmental noise provided by filled outer electronic shells³². Extraordinary nuclear spin relaxation times on the order of days²¹⁰ and $T_2^{dec.}$ coherence times on the order of hours²¹¹ have been demonstrated, motivating their use for quantum repeaters and transducers. Single rare-earth ions, however, possess a very small optical dipole moment and show only weak emission and high background fluorescence in low-purity samples.

Just like for defects in SiC, the robustness of rare-earth ions against surface noise enables extensive micro- and nanofabrication of photonic structures in order to increase their coherent photon flux. There are two main approaches: focused-ion-beam fabrication of cavities directly into glassy rare-earth ion host materials^{212,213}, or fabrication of cavities in a different material such as Si, with a subsequent transfer onto the rare-earth ion host for evanescent coupling²¹⁴. An example is the integration of Er^{3+} ions into $CaWO_4$, showing narrow optical linewidths, indistinguishable single-photon emission and a cavity Purcell-factor of 250²¹⁵.

2.2 Laser writing of defects in diamond

An important requirement for realizing scalable quantum networks is the capability to create the network nodes deterministically – a potential offered by femtosecond laser writing. Until now, femtosecond laser machining has demonstrated its use in applications such as nanosurgery and microfluidics, and has been employed to write components ranging from waveguides and amplifiers to filters and resonators²¹⁶. The method was only recently utilized as a technique for creating defects in diamond.

2.2.1 Interaction of ultrashort pulses with dielectrics

In order to produce permanent damage to a transparent material by means of an optical pulse, enough energy has to be deposited into the material. In a transparent material, the cross-section of linear absorption of the laser light is extremely small, which means that the energy has to be transferred through a nonlinear absorption mechanism²¹⁷. There are two nonlinear processes that promote electrons in a transparent material from the valence- to the conduction band: nonlinear photoionization and avalanche ionization²¹⁸.

Nonlinear photoionization, in turn, has two regimes – multi-photon ionization (MPI) and tunneling, schematically illustrated in Fig. 2.10a. For strong laser fields and small laser frequencies (long wavelengths), tunneling dominates, while higher laser frequencies and shorter wavelengths predominantly lead to MPI. Depending on the used parameters, the two regimes overlap; the dominating mechanism can be described by the Keldysh parameter²¹⁹:

$$\gamma = \frac{\omega}{e} \left[\frac{mcn\epsilon_0 E_g}{I} \right]^{1/2} \quad (2.13)$$

where ω is the laser angular frequency, e the charge of the electron, m its reduced mass, c the speed of light, n the refractive index of the transparent material, ϵ_0 the permittivity of free space, E_g the bandgap of the transparent material, and I the laser intensity at the focus. Tunneling is the dominant process when $\gamma < 1.5$, while MPI dominates for $\gamma > 1.5$. In the intermediate regime around $\gamma \sim 1.5$, both processes occurⁱⁱ.

Tunneling ionization takes place for strong laser fields and short pulses, where the superposition of the nucleus Coulomb field and the laser electric field results in an oscillating finite potential barrier through which a valence electron can tunnel^{217,218}. For this to occur, the field strength must be on the order of 10^9 V/m, corresponding to a power density of $5 \cdot 10^{20}$ W/m² and given for example by a focus size of $200 \mu\text{m}^2$, a pulse of energy $1 \mu\text{J}$ and pulse length of 100fs ²¹⁶. MPI instead relies on the simultaneous absorption of multiple photons, promoting a valence electron to the conduction band. The two processes scale differently with the laser intensity: in the case of tunneling, the photoionization rate scales only weakly with the laser intensity, while in MPI, the photoionization rate scales as $\propto \sigma_k I^k$, with σ_k being the multi-photon absorption coefficient for the absorption of k photons, and the minimum number of photons given by the k that satisfies $k\hbar\omega > E_g$ ²¹⁸.

The second type of nonlinear process, avalanche ionization, is illustrated in Fig. 2.10b-c. First, free carrier absorption occurs, in the course of which an electron in the conduction band sequentially absorbs several laser photons that promote it higher into the conduction band. Once a minimum of n photons, with n satisfying $n\hbar\omega > E_g$, has been absorbed, impact ionization takes place. Subsequently, an excited electron can ionize another electron from the valence band, resulting in two electrons near the conduction band minimum. Subsequent photoionization of both of these electrons will ionize more valence band electrons, leading to avalanche ionization as long as the electromagnetic field from the laser is present and strong enough²¹⁷. The needed initial free carriers (or

ⁱⁱRef. 218 uses 1.5 as the separator between the two regimes; the dividing value used by Ref. 217 is 1.

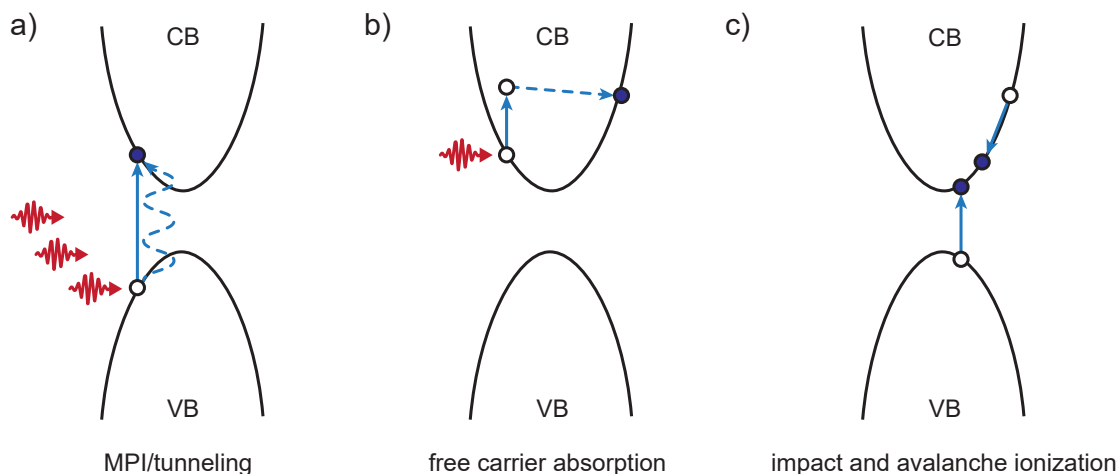


Figure 2.10.: Interaction of an ultrashort pulse with a dielectric material. (a) A short energetic pulse promotes an electron from the valence band (VB) to the conduction band (CB) via MPI or tunneling. (b) Further absorption of photons promotes the electron higher into the CB. (c) Impact ionization of the electron promotes another electron from the VB into the CB, and the process in (b) can be repeated under continued excitation, creating an avalanche process. Adapted from Ref. 217.

seed electrons) in the conduction band are provided either by tunneling, MPI, thermal excitation, or ionized impurity or defect states²¹⁸. The avalanche ionization rate has been described as either linearly proportional²²⁰ or proportional to the square root²²¹ of the laser intensity.

Once sufficient energy has been transferred from a laser pulse to a transparent material, permanent damage can be produced. The exact mechanism for the creation of damage depends strongly on the duration of the laser pulse. For pulses longer than tens of picoseconds, the energy transfer to the lattice occurs on a timescale corresponding to the pulse duration; thermal diffusion transfers energy from the focus and damage occurs when the temperature is above the melting or fracturing point of the material. Since a large pulse duration allows for a longer accumulation of electrons in the conduction band, avalanche ionization is efficient. This also leads to difficulties in determining an exact threshold for optically induced lattice damage, since the seed electron density is heavily affected by impurities in the material²¹⁸. For pulse durations of 10 ps or longer, the threshold laser fluence for material damage depends on the square root of the pulse length²¹⁷.

For sub-picosecond pulses, the absorption of energy from the laser pulse instead occurs on a timescale much shorter than the transfer of heat to the lattice. The rapid accumulation of electrons during avalanche ionization leads to the formation of a plasma, rapidly transferring energy to the lattice and resulting in permanent structural changes. The energy required for this damage is smaller than that for longer pulses. Furthermore, the heat diffusion outside the focal area is minimized, leading to more precise changes to the material. Since sufficient seed electrons are created during the first tens of femtoseconds of the pulse, the process for femtosecond laser pulses is deterministic and gives more reproducible shot-to-shot damage compared to longer pulses. Even though the absorption of light, avalanche ionization and carrier-carrier scattering occurs on the timescale of the pulse, structural changes in the material can take place up to microseconds later²¹⁶⁻²¹⁸.

2.2.2 Creation of NVs via laser writing

Turning to the specific case of ultrafast laser processing of diamond, there are two regimes: a high-energy regime, where non-thermal melting, short-timescale Coulomb explosions and re-solidification of the material lead to ablation and graphitization of the surface¹³⁸, and a lower-energy regime, in which the nonlinear processes described in Section 2.2.1 promote non-equilibrium charge carriers and create localized damage in the bulk²²². Each of these regimes can lead to the creation of NVs in diamond; in order to distinguish between the two, the former will be referred to as laser nanoablation, and the latter as laser writing.

Laser writing of NV centers in diamond can be described with two steps: the “writing” (step 1 in Fig. 2.11a), in which an ultrashort laser pulse transfers energy to the lattice via nonlinear processes and creates permanent damage in the form of lattice vacancies, and the annealing (step 2 in Fig. 2.11a), in which the created vacancies diffuse and form NVs with native nitrogen in the lattice.

Neutral vacancies in diamond, also known as GR1 radiation damage centers, are defects with tetrahedral symmetry that can be produced in all types and purities of diamond. Under green illumination, the PL is characterized by a peak close to 740 nm (ZPLs at 744.6 nm and 741.1 nm), with an intensity increasing with the number of vacancies and decreasing with temperature²²³. The defect is stable up to 850°C. The GR1 spectral signature is shown in Fig. 2.11b; the peak broadens as the lattice becomes less periodic, eventually turning into broadband fluorescence indicating diamond graphitization and the creation of more severe dislocations^{49,222}.

The creation of a vacancy in diamond inherently leads to the formation of a vacancy-interstitial pair, a Frenkel defect. The threshold energy for an atomic displacement in

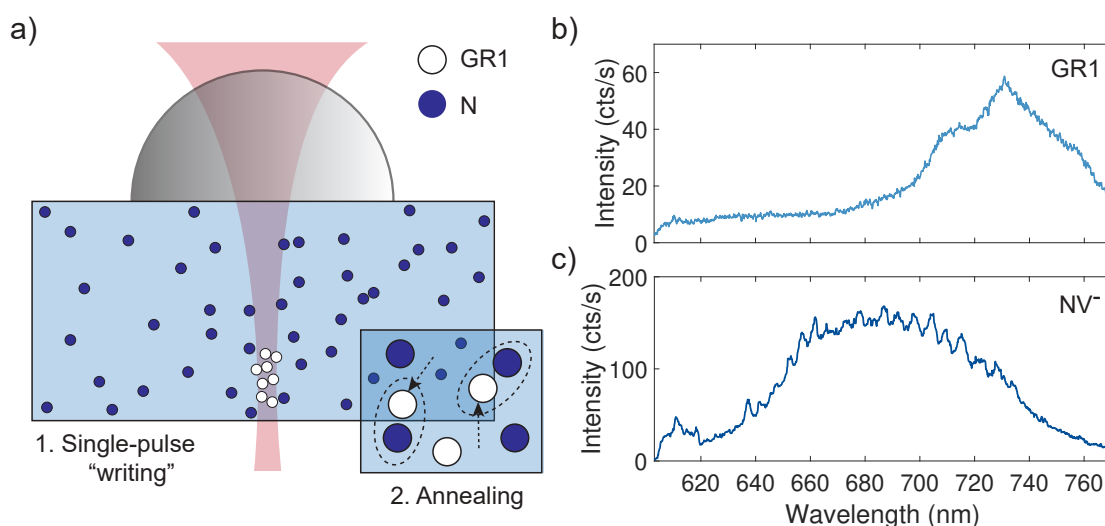


Figure 2.11.: Creation of NVs via laser writing. (a) Single ultrashort pulses are focused inside diamond to create vacancy clusters (1). A subsequent annealing step causes the created vacancies to diffuse and form NVs with diamond-native nitrogen (2). (b) Spectral signature of GR1, measured before annealing the diamond. (c) Spectral signature of NV⁻, measured after annealing the diamond.

diamond has been measured to be $35 \pm 5 \text{ eV}$ ²²⁴. A more recent study suggests that the threshold energy for Frenkel defect formation, described by the recombination of a bound biexciton as the laser-induced electron plasma cools down, is about 8 eV ^{122,222,225}. After annealing a laser-irradiated sample to $1000\text{--}1100^\circ$, NVs are formed owing to the laser-induced vacancies diffusing in the lattice (see Section 2.1.3.1) and forming NVs with native nitrogen (Fig. 2.11c).

The first case of laser writing of NVs inside bulk diamond was demonstrated in 2016, where the enhancement of NV^0 and NV^- PL in an optical-grade diamond from a train of picosecond laser pulses was shown. The exposures were carried out using 532 nm , 10 or 46 ps pulses at a repetition rate of 50 kHz and energy of $0.2\text{--}5 \mu\text{J}$. No separate annealing step was required since high enough temperatures to induce vacancy diffusion were reached during the multi-pulse exposures²²⁶.

In 2017, deterministic single-pulse creation of NVs was shown for the first time. Single 300 fs pulses with a wavelength of 790 nm and energy of approximately $14\text{--}25.5 \text{ nJ}$ (measured at the output of the focusing objective) induced GR1 photoluminescence at a depth of $50 \mu\text{m}$ in electronic-grade diamond. Negatively charged NVs were formed after annealing the diamond to 1000°C . A lateral NV positioning precision of 200 nm could be demonstrated, limited by the vacancy diffusion during the annealing. Above a pulse energy of 25.5 nJ , the writing sites showed broadband fluorescence, indicating graphitization. In the study, adaptive optics (a liquid crystal spatial light modulator) was used together with a oil-immersion objective, giving a combined NA of 1.4 . The writing was performed in the MPI regime, where an average of nine photons were needed to excite an electron from the valence to the conduction band⁴⁹.

The same authors later achieved laser writing with a higher positioning accuracy (33 nm) and yield (96%), by using the writing laser at a higher repetition rate (1 kHz) after a single-pulse exposure to locally induce vacancy diffusion and form NVs without requiring a separate annealing step. The study, however, relied on a high pre-existing nitrogen content of 1.8 ppm . Real-time fluorescence monitoring enabled the annealing process to be halted as soon as the wanted fluorescence intensity was reached, enabling preselection of the number of NVs formed as well as of the NV orientation²²⁷.

Since then, it has been shown that shortening the laser writing pulse length widens the range of useful pulse energies, and that it increases the pulse energy that can be used without inducing diamond graphitization²²⁸. It has further been seen that shorter pulses require higher pulse energies, and that the defect generation threshold decreases with an increase in NA (up to an NA of 1.25 , above which additional aberrations are introduced)²²².

2.2.3 Creation of NVs via laser ablation

Laser ablation, or nanoablation, is a method for creating NVs close to the surface without inducing bulk damage. So far, it has only been demonstrated on optical-grade diamond^{138,229,230}, and, as mentioned in Section 2.1.3.3, only resulted in NVs with extremely broad ($\sim 200 \text{ GHz}$) ZPL linewidths. The nanoablation regime can be reached with a lower laser fluence compared to what is needed for bulk damage, while operating at the diamond-air interface. In this regime, the required high density of free carriers

is produced without inducing surface graphitization. Instead, the increase in NV PL is accompanied by the appearance of a shallow crater in the material. In contrast to laser writing in bulk, an annealing step after the ablation does not increase the PL intensity further.

By increasing the laser fluence, the regime of conventional ablation can be reached, in which the field penetration depth is much larger than the diffusion length of the induced carriers. In the case of nanoablation, the energy transfer is more localized, such that diffusion dominates the energy transfer within the lattice²³¹.

Nanoablation under 266 and 400 nm irradiation has been shown to controllably create NVs, with a concentration increasing logarithmically with the number of pulses and a formation rate scaling with the sixth power of the fluence^{138,230}. It has not been achieved with longer wavelengths, a possible reason being that nanoablation requires excitation of oxygen-containing sites at the surface in addition to exciting the diamond lattice itself – a process happening less efficiently at longer wavelengths²³⁰.

2.2.4 Laser writing of other defects

In diamond, not only NVs have been created via laser writing: by focusing a femtosecond laser through a layer of Si nanoballs on a diamond surface, shallow SiVs have been created, however requiring high pulse energies on the order of $10 \mu\text{J}$ ^{232,233}. Laser writing of defects in other wide-bandgap materials such as GaN²³⁴, cubic boron nitride²³⁵ and SiC^{236–239} has also been demonstrated.

Defects in a range of alkali metal halides (LiF, NaF, MgF₂, NaCl, KCl, KBr, KI and CaF₂) have also been created via laser writing^{239–241}. Many of the alkali metal halides are attractive for novel photonic applications owing to their large bandgap, wide transparency window and solubility. Laser writing has further been used to create clusters of color centers in nonlinear crystals such as YLF^{242,243} and YAG²⁴⁴ and in oxide crystals such as titanium dioxide and quartz^{245,246}. Finally, laser writing of color centers has not only been performed in bulk and crystalline materials, but also in low-dimensional materials such as single-walled carbon nanotubes (SWCNT)²⁴⁷ and hexagonal boron nitride (hBN)^{239,248,249}.

2.2.5 Minimizing spherical aberrations

Laser writing of NVs is based on focusing a laser within the bulk of diamond. In order to create as concentrated lattice damage as possible (minimizing the charge noise in the vicinity of the eventually created emitters), and in order to minimize the probability of graphitizing the diamond surface, it is crucial to maintain a tight laser focus within the material. The size of the focus and the imaging resolution is ultimately determined by the spherical aberrations introduced at the interface between the diamond and the imaging medium. The difference in refractive index between the air and diamond severely affects the focus quality, reduces the probability that the highest-angle rays contribute to the focus, and worsens the transverse and axial resolution compared to the diffraction limit.

2.2.5.1 Diffraction limits

In the case of no aberrations, the lateral and axial spatial resolution of any optical microscope are given by the diffraction limit. A way to derive this limit is by looking at the three-dimensional light distribution around the focal plane of a lens, given by an Airy pattern described by

$$I(0, v) = \left[\frac{2J_1(v)}{v} \right]^2 I_0 \quad (2.14)$$

across the optical axis and

$$I(u, 0) = \left[\frac{\sin(u/4)}{u/4} \right]^2 I_0 \quad (2.15)$$

along the optical axis in the case of a plane wave impinging on the lens²⁵⁰. Here, I_0 is the intensity at the center of the pattern and v, u are given by

$$v = \frac{2\pi}{\lambda} NA \cdot r \quad (2.16)$$

$$u = \frac{2\pi}{\lambda} NA^2 \cdot z \quad (2.17)$$

with the numerical aperture defined as $NA = \sin(\theta)$, θ being the half-angle of the maximum cone of light that can enter or exit the lens. r and z denote the distance from the center of the lateral focus and the distance from the focal plane, respectively. By defining the full extent of the focus as the distance between the first intensity minima surrounding the central maximum of the intensity distribution (at these minima, the field intensity is zero), the diffraction limit across the optical axis (lateral resolution) can be derived as

$$\Delta x = \frac{1.22\lambda}{NA} \quad (2.18)$$

and the diffraction limit along the optical axis (axial resolution) as

$$\Delta z = \frac{4\lambda}{NA^2} \quad (2.19)$$

where λ is the free-space wavelength of the light. Inside a medium, the wavelength λ reduces to λ/n ²⁵⁰. The FWHM is given by

$$\Delta x_{FWHM} = \frac{0.52\lambda}{NA} \quad (2.20)$$

$$\Delta z_{FWHM} = \frac{1.77\lambda}{NA^2} \quad (2.21)$$

From these expressions, it is apparent that the spatial resolution can be improved by increasing θ or by reducing λ . The latter can be done either by using light with a shorter wavelength, or by increasing the refractive index of the medium surrounding the focal plane, for example by liquid immersion techniques, where oils with high refractive indices are introduced into the optical system²⁵¹.

2.2.5.2 Adaptive optics and solid-immersion-lens microscopy

A way to optimize the temporal and spatial profile of the laser focus and reduce the aberrations is to use adaptive optics, which can dynamically modify the phase, amplitude and polarization of a laser beam before it enters a material. Examples include spatial light modulators, digital mirror devices, and deformable mirrors. Adaptive optics have the advantage over passive elements in that the threshold pulse energy can be made invariant of the depth within the material. Aberrations typically depend on the focusing depth and can therefore be compensated equally. Adaptive optics furthermore allow for temporal and more distinguished shaping of the incoming beam, which is not possible with a passive element²⁵².

Nevertheless, a passive element such as a solid-immersion lens (SIL) presents advantages in its low cost and ease of operation. It is a simple optical component that offers an improvement in both spatial resolution, collection efficiency, and magnification, all owing to the increase in numerical aperture provided by it²⁵¹. For particular SIL focusing conditions, spherical aberration can be completely eliminated²⁵³.

Solid immersion microscopy was invented in 1990²⁵⁴. It is based on liquid immersion microscopy, but has the advantage of including also the light beyond the critical angle in the system. This increases both the spatial resolution and the collection efficiency. Especially since there are no immersion oils matching the refractive index of many common semiconductors, and because it is not possible to physically immerse the objective lens into solid samples, SILs are attractive for the fabrication and characterization of photonic nanostructure devices²⁵¹. As will be shown in this thesis, SILs are also extremely useful for the creation of NVs in diamond.

There are two main categories of SILs, hemispherical SILs (h-SILs, Fig. 2.12) and super-SILs (s-SILs, or Weierstrass Optic, Fig. 2.13). When focusing through a high-index sphere, light is focused without spherical aberrations at two so-called aplanatic points. h-SILs use the first aplanatic point, located at the center of the sphere, as their focal point. Such SILs are well-suited for focusing close to or right below the SIL. s-SILs instead use the second aplanatic focusing point, located at a distance $z_0 = (n_1/n_2)/R$ from the center of the sphere, with R being the radius of the sphere, n_0 the refractive index of the s-SIL and n_1

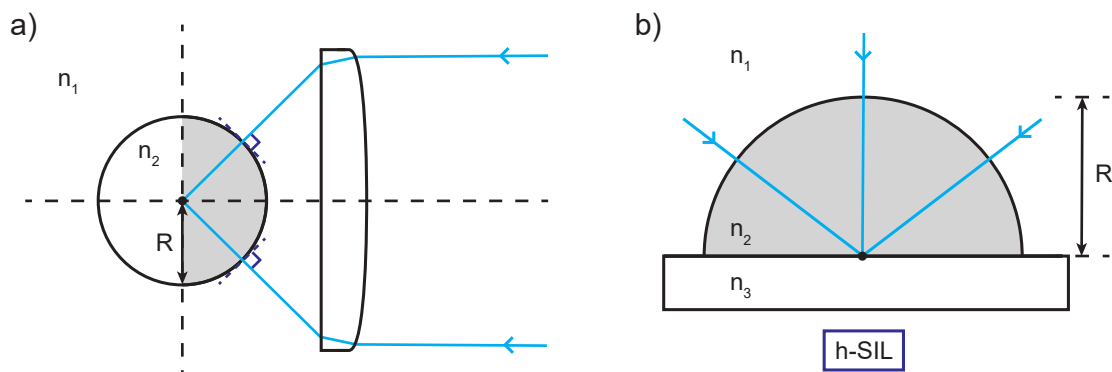


Figure 2.12.: Design of an h-SIL. (a) Focusing light through an objective lens into the first aplanatic point of a sphere with $n_2 > n_1$. (b) An h-SIL, exploiting the first aplanatic point as the focus.

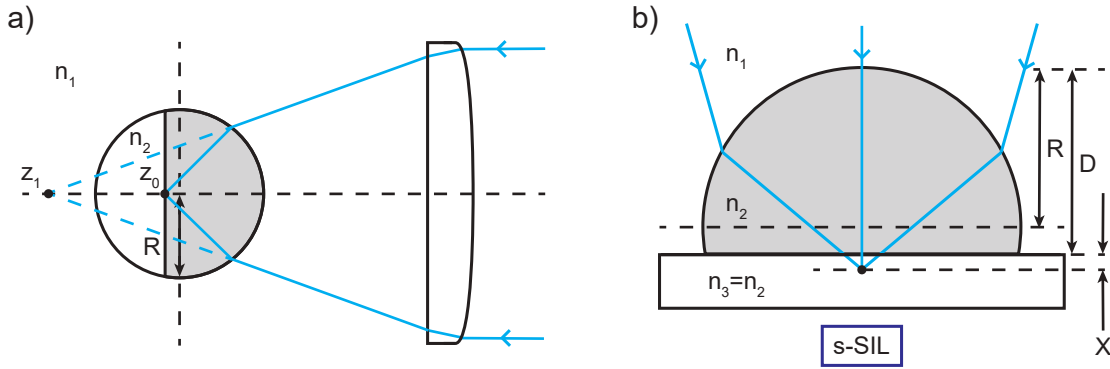


Figure 2.13.: Design of an s-SIL. (a) Focusing light through an objective lens into the second aplanatic point of a sphere, with $n_2 > n_1$. (b) An s-SIL, exploiting the second aplanatic point z_0 as the focus.

the refractive index of the surrounding medium. A second, virtual, s-SIL focus is located at a distance $z_1 = (n_2/n_1)/R$ from the center of the sphere²⁵¹.

Either type of SIL can be used for sub-surface imaging or writing. The s-SIL has the advantage of not being limited by the NA of the focusing optics and provides a higher magnification ($\sim n^2$, giving a resolution gain of $1/n^2$) compared to the h-SIL (magnification scaling n and a resolution gain of $1/n$). However, if an s-SIL is made to maximize the NA, its focal position (located at a depth X below its planar interface) is related to its physical height D via

$$D = R \left(1 + \frac{1}{n} \right) - X \quad (2.22)$$

which means that the focal position is wavelength-dependent²⁵¹. In order to eliminate chromatic aberrations, which is important for focusing temporally short (spectrally wide) laser pulses, an h-SIL is therefore advantageous.

In this work, a truncated hemispherical SIL (t-SIL) is used, in which a part is removed from the flat facet of a h-SIL, reducing the physical height of the lens (Fig. 2.14). For focusing light into a material with a refractive index matching the one of the SIL, this leads to an aberration-free focus at a depth within the material exactly corresponding to the truncation depth.

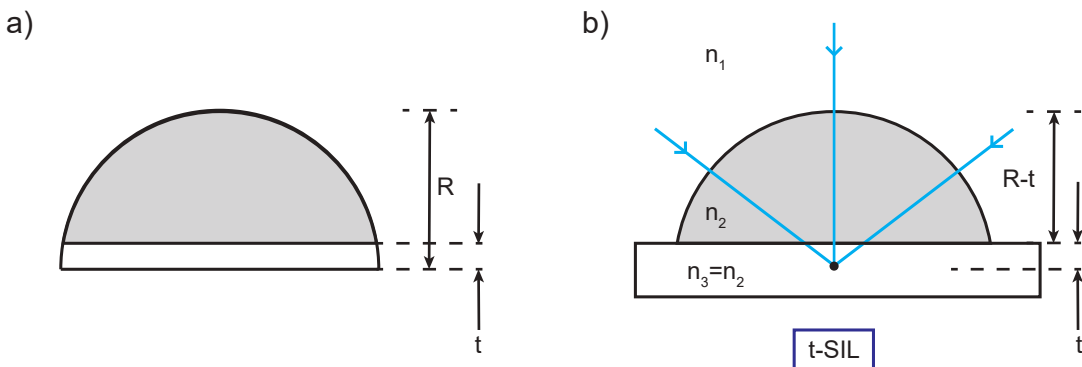


Figure 2.14.: Design of a t-SIL. (a) A t-SIL is created by truncating a h-SIL by removing a thickness t from its planar facet. (b) A t-SIL, giving a spherical-aberration-free focus at a depth corresponding to the truncation if the material has the same refractive index as the t-SIL itself.

2.3 Cavity quantum electrodynamics

Cavity quantum electrodynamics (cavity QED) describes the coherent coupling between a quantum emitter and a cavity. The emitter can absorb photons from the cavity mode, but also emit photons into it. Depending on the characteristics of this exchange, the flux of indistinguishable photons from the emitter and out of the cavity can be increased – a desired interplay for an NV.

2.3.1 The Jaynes-Cummings model

The interaction of a two-level emitter and an electromagnetic field can be modeled through perturbation theory, either for a classical driving field or a quantum mechanical field. In order to explain the existence of spontaneous emission, the latter – a fully quantum mechanical treatment – is necessary, which is described by the Jaynes-Cummings model^{255,256}.

In a small optical cavity, only one or a few widely spaced modes are supported, compared to the infinite number of modes in free space. This makes it possible to implement an ideal emitter-single-mode interaction, if a single optical cavity mode is close in frequency to the emitter frequency. The single-mode cavity field that the NV interacts with is given by the quantized electric field operator $\hat{\mathbf{E}}$. The atom-field interaction Hamiltonian is derived from the dipole moment operator $\hat{\mathbf{d}}$ via

$$\hat{H}^{(I)} = -\hat{\mathbf{d}} \cdot \hat{\mathbf{E}} = \hbar g_0 (\hat{\sigma}_+ + \hat{\sigma}_-) (\hat{a} + \hat{a}^\dagger) \quad (2.23)$$

with \hat{a} and \hat{a}^\dagger describing the creation and annihilation of a cavity photon and the atomic transition operators being $\hat{\sigma}_+ = |e\rangle \langle g|$ and $\hat{\sigma}_- = |g\rangle \langle e|$. Here, an atom-cavity coupling constant g_0 has been defined as

$$g_0 = \frac{\mu_{eg}}{\hbar} |\mathbf{E}_{\text{vac}}| \quad (2.24)$$

with the electric dipole moment of the transition μ_{eg} given by

$$\mu_{eg} = e \langle g | \hat{\mathbf{d}} | e \rangle \quad (2.25)$$

and the absolute value of the vacuum electric field \mathbf{E}_{vac} by

$$E_{\text{vac}} = \left(\frac{\hbar \omega}{2 \epsilon_0 V} \right)^{1/2}. \quad (2.26)$$

ω is the angular frequency of the field and V the volume to which the field is confined.

The total Hamiltonian describing the atom, the field, and their interaction, is given by the sum of the respective Hamiltonians as

$$\hat{H} = \hat{H}_A + \hat{H}_F + \hat{H}^{(I)} \quad (2.27)$$

where the free atomic- and free field Hamiltonian (after dropping the zero-point energy term) are given by

$$\hat{H}_A = \frac{1}{2}(E_e - E_g)\hat{\sigma}_3 = \frac{1}{2}\hbar\omega_0\hat{\sigma}_3 \quad (2.28)$$

and

$$\hat{H}_F = \hbar\omega\hat{a}^\dagger\hat{a}. \quad (2.29)$$

Here, the transition angular frequency between $|g\rangle$ and $|e\rangle$ is ω_0 and the inversion operator is defined as $\hat{\sigma}_3 = |e\rangle\langle e| - |g\rangle\langle g|$. The energy level $E = 0$ is set to be halfway between the ground- and excited level.

The creation, annihilation and transition operators evolve as

$$\begin{aligned} \hat{a}(t) &= \hat{a}(0)e^{-i\omega t} \\ \hat{a}^\dagger(t) &= \hat{a}^\dagger(0)e^{i\omega t} \\ \hat{\sigma}_+(t) &= \hat{\sigma}_+(0)e^{i\omega_0 t} \\ \hat{\sigma}_-(t) &= \hat{\sigma}_-(0)e^{-i\omega_0 t} \end{aligned} \quad (2.30)$$

which leads to the product terms in Eq. (2.23) having a time-dependence of either $\sim (\omega_0 - \omega)$ or $\sim (\omega_0 + \omega)$. The term $\hat{\sigma}_-\hat{a}^\dagger$ corresponds to the emission of a photon as the atom deexcites from $|e\rangle$ to $|g\rangle$, and the term $\hat{\sigma}_+\hat{a}$ corresponds to the absorption of a photon as the atom is excited from $|g\rangle$ to $|e\rangle$, both conserving the number of energy quanta. On the other hand, the terms $\hat{\sigma}_+\hat{a}^\dagger$ and $\hat{\sigma}_-\hat{a}$, corresponding to the emission of a photon during excitation of the atom and the absorption of a photon during deexcitation of the atom, do not conserve the number of quanta. After performing the so-called rotating wave approximation, in which the rapidly changing (and non-energy-conserving) terms $\sim (\omega_0 + \omega)$ are dropped due to the terms $\sim (\omega_0 - \omega)$ dominating close to resonance ($\omega_0 \approx \omega$), the total Hamiltonian, known as the Jaynes-Cummings Hamiltonian, is obtained:

$$\hat{H} = \frac{1}{2}\hbar\omega_0\hat{\sigma}_3 + \hbar\omega\hat{a}^\dagger\hat{a} + \hbar g_0(\hat{\sigma}_+\hat{a} + \hat{\sigma}_-\hat{a}^\dagger). \quad (2.31)$$

A state vector can be written as

$$|\psi(t)\rangle = C_i(t)|i\rangle + C_f(t)|f\rangle \quad (2.32)$$

with $|n\rangle$ being the number state of the field and the initial and final state of the atom-field system defined as $|i\rangle = |e\rangle|n\rangle$ and $|f\rangle = |g\rangle|n+1\rangle$, respectively. With $C_i(0) = 1$ and $C_f(0) = 0$, the probability of the system making a transition from $|i\rangle$ to $|f\rangle$ is given by

$$P_f(t) = |C_f(t)|^2 = \sin^2(g_0 t \sqrt{n+1}). \quad (2.33)$$

This is a sinusoidal oscillation, with a frequency given by the photon number and coupling strength between the two-level system and field. The frequency of this oscillation, the Rabi frequency, is

$$\Omega(n) = 2g_0\sqrt{n+1}. \quad (2.34)$$

This means that Rabi oscillations arise also for $|n\rangle = 0$ (for the atom in $|e\rangle$), i.e. when there is no field present initially. Such vacuum Rabi oscillations have no classical counterpart and correspond to the cyclic case where the atom deexcites via spontaneous emission,

subsequently reabsorbs the emitted photon, and is excited again²⁵⁷.

2.3.2 Light-matter interaction including system losses

Until now, the interaction between the two-level emitter and the cavity field has been postulated to be lossless, i.e., it has been assumed that no excitations are lost from the system. In reality, the photon loss rate out of the cavity κ and the photon loss rate γ via decay into modes that are not resonant with the cavity have to be taken into account. κ is given by scattering, absorption and transmission through the cavity mirrors and corresponds to the spectral linewidth of a cavity resonance. It can be expressed for a resonance angular frequency ω_c via the cavity quality factor (Q-factor) as

$$\kappa = \frac{\omega_c}{Q}. \quad (2.35)$$

Together with γ and the atom-cavity constant g_0 , given by Eq. (2.24), κ characterizes the light-matter interaction. This is schematically illustrated in Fig. 2.15.

The cooperativity C is defined as

$$C = \frac{4g_0^2}{\kappa\gamma} \quad (2.36)$$

or, in the presence of dephasing with a rate γ^* , as $C = 4g_0^2/(\kappa(\gamma + \gamma^*))$. With this definition, the cooperativity directly compares the coherent emitter-cavity coupling and rate of radiation via the cavity to all emitter dephasing mechanisms¹⁶¹. In the case of NVs, where the contribution of dephasing to the optical linewidth (homogeneous broadening) is typically comparable to the lifetime-limited linewidth, Eq. (2.36) is a reasonable approximation. Depending on the relative values of κ , γ and g_0 , a light-matter interaction can be categorized as either weak or strong.

The strong coupling regime of cavity QED occurs when $g_0 \gg \kappa, \gamma$. The vacuum Rabi oscillations described by Eq. (2.34) for $|n\rangle = 0$ is an effect seen in this regime. In the

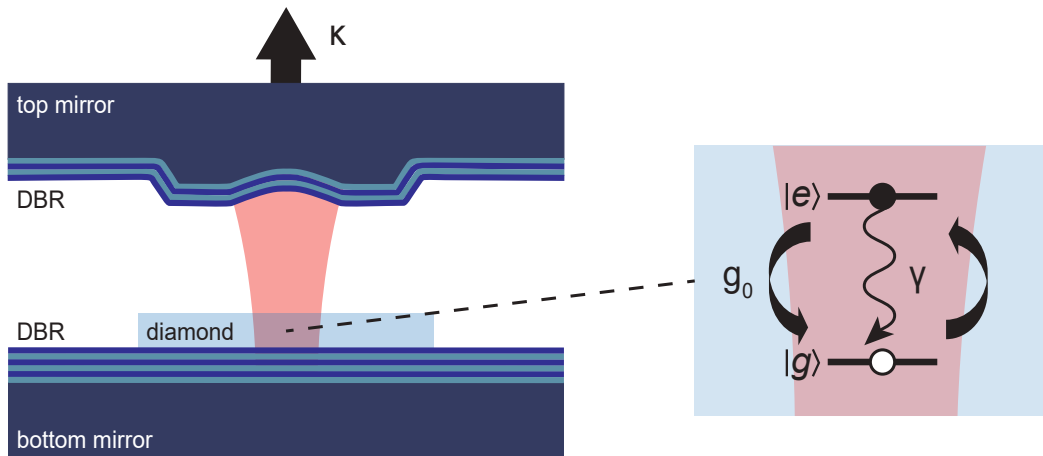


Figure 2.15.: Light-matter interaction in a tunable open microcavity. A two-level system with a decay rate γ , in this case an NV in diamond, interacts with the intracavity field with a coupling strength g_0 . The leakage rate of the intracavity field out of the cavity is given by κ .

strong coupling regime, the bare product states (e.g. $|e\rangle |n\rangle$ and $|g\rangle |n+1\rangle$, given by the unperturbed atom and field), are mixed by the electric-dipole interaction between the atom and the cavity photon and form dressed states. The dressed states consist of pairs of states split by $\Delta E_n = 2\sqrt{n}\hbar g_0$ in a system known as the Jaynes-Cummings ladder^{257,258}.

The weak coupling regime can instead be expressed as the regime where $\kappa > g_0 \gg \gamma$. In this regime, there is an irreversible emission of light, where photons are lost from the atom-cavity system faster than the time it takes for the emitter to reabsorb a photon. The cavity either enhances or suppresses the photon density of states compared to free space, depending on whether it is on resonance with the emitter's transition or not^{257,258}. The small Debye-Waller factor of NVs gives a low effective optical dipole moment μ_{eg}^{eff} and therefore a low value of g_0 compared to realistic values of $\kappa/(2\pi) \sim \text{GHz}$ achieved with open microcavities^{58,64,259} and $\gamma/(2\pi) \sim 13 \text{ MHz}$. This places NV-cavity interactions in the weak-coupling regime of cavity QED.

2.3.3 Purcell-enhancement

When a two-level emitter is coupled to a single (or spectrally isolated) mode of a cavity in the weak coupling regime, the spontaneous emission rate of the emitter is increased due to the Purcell effect²⁶⁰. In the case of an NV, only the ZPL transition is an effective two-level system. A ZPL photon can be emitted either into free space, with a free-space spontaneous emission rate of γ^{ZPL} , or into the cavity mode, with an increased spontaneous emission rate of $\gamma_{Purcell}^{ZPL}$. The ZPL Purcell-factor F_P^{ZPL} quantifies the relative magnitude of these rates. Here, we use the definition

$$F_P^{ZPL} = \frac{\gamma_{Purcell}^{ZPL} + \gamma^{ZPL}}{\gamma^{ZPL}} = \frac{\gamma_{Purcell}^{ZPL}}{\gamma^{ZPL}} + 1. \quad (2.37)$$

The rate of spontaneous emission for a two-level emitter can be described using Fermi's golden rule:

$$\gamma_{eg} = \frac{2\pi}{\hbar^2} |M_{eg}|^2 D(\omega). \quad (2.38)$$

Here, $D(\omega)$ is the photon density of states and M_{eg} a transition matrix element describing the overlap between the emitter dipole and the vacuum electric field. We can write M_{eg} as

$$M_{eg}^2 = \zeta^2 \mu_{eg}^2 E_{vac}^2 \quad (2.39)$$

where ζ is a normalized dipole orientation factor defined as

$$\zeta = \frac{|\mathbf{d} \cdot \mathbf{E}_{vac}|}{|\mathbf{d}| |\mathbf{E}_{vac}|}. \quad (2.40)$$

$\zeta^2 = 1/3$ in the case of free-space emission, averaging over all possible relative orientations of the emitter dipole and the field²⁵⁸.

In free-space, the photon density of states is given by

$$D(\omega) = \frac{\omega^2 V}{\pi^2 c^3}, \quad (2.41)$$

with a quadratic dependence on the angular frequency. In a cavity, the density of states is instead described by the Lorentzian lineshape of the cavity resonance, with a linewidth κ :

$$D(\omega) = \frac{2}{\pi\kappa} \frac{\kappa^2}{4(\omega - \omega_c)^2 + \kappa^2} \quad (2.42)$$

Using Eqs. (2.26), (2.39), (2.41) and (2.42) for Eq. (2.38) and evaluating the expressions at the ZPL angular frequency ω_0 gives the free-space and cavity-enhanced spontaneous emission rate:

$$\gamma^{ZPL} = \frac{\mu_{eg}^2 \omega^3}{3\pi\epsilon_0 \hbar c^3} \quad (2.43)$$

$$\gamma_{Purcell}^{ZPL} = \zeta^2 \frac{2\mu_{eg}^2 Q}{\hbar\epsilon_0 V} \frac{\kappa^2}{4(\omega_0 - \omega_c)^2 + \kappa^2} \quad (2.44)$$

Inserting Eq. (2.43) and Eq. (2.44) into Eq. (2.37) finally gives the ZPL Purcell-factor:

$$F_P^{ZPL} = 1 + \frac{6\pi c^3 Q}{\omega^3 V} \left(\frac{|\mathbf{d} \cdot \mathbf{E}_{vac}|}{|\mathbf{d}| |\mathbf{E}_{vac}|} \right)^2 \frac{\kappa^2}{4(\omega_0 - \omega_c)^2 + \kappa^2} \quad (2.45)$$

The expression can be simplified when the NV dipole is oriented along the field ($\mathbf{d} \parallel \mathbf{E}_{vac}$) and the cavity is tuned to resonance with the ZPL ($\omega_0 = \omega_c$):

$$F_P^{ZPL} = 1 + \frac{3}{4\pi^2} \frac{Q}{V} \left(\frac{\lambda}{n} \right)^3 \quad (2.46)$$

where c/ω has been replaced by $\lambda/2\pi n$, with λ the free-space wavelength of light and n the refractive index of the cavity mode²⁵⁸. The higher the Q-factor and the smaller the mode volume of the cavity, the higher the Purcell-enhancement. This is, however, a simplification: the full expression for the Purcell-factor in Eq. (2.45) illustrates that a high Purcell-enhancement relies on good relative alignment between the NV dipole and the field, as well as close-to-resonance conditions between the cavity and the NV²⁵⁸.

In an experiment, the total NV decay rate is measured. The total decay rate γ_0 in free space can be described by the sum of the decay rate into the ZPL, γ^{ZPL} , and the decay rate into the PSB, γ^{PSB} , scaled by the NV branching ratio given by the Debye-Waller factor ζ :

$$\gamma_0 = \gamma^{ZPL} + \gamma^{PSB} = \zeta\gamma_0 + (1 - \zeta)\gamma_0. \quad (2.47)$$

Note that $\gamma^{ZPL} \ll \gamma^{PSB}$. Here, we assume a QE of 1. The total Purcell-enhanced decay rate $\gamma_{Purcell}$ in a cavity can be written as

$$\gamma_{Purcell} = \gamma_{Purcell}^{ZPL} + \gamma^{PSB} = F_P^{ZPL} \gamma^{ZPL} + \gamma^{PSB} \quad (2.48)$$

with F_P^{ZPL} given by Eq. (2.45). Owing to the broadband nature of the PSB decay, leading only to minor changes in the PSB decay rate with changes in the cavity resonance frequency, the Purcell-enhancement of γ^{PSB} is assumed to be negligible. Rewriting Eq. (2.48) using Eq. (2.47) gives

$$F_P^{ZPL} = \frac{\gamma_{Purcell} - (1 - \zeta)\gamma_0}{\zeta\gamma_0} = \frac{\gamma_{Purcell} - \gamma_0}{\zeta\gamma_0} + 1. \quad (2.49)$$

which expresses the ZPL Purcell-enhancement in terms of the measured decay rates.

The overall Purcell-factor F_P is instead given by

$$F_P = \frac{\gamma_{Purcell}}{\gamma_0}, \quad (2.50)$$

which is typically much smaller than F_P^{ZPL} since the cavity couples almost exclusively to the transition represented by the ZPL, influencing only a fraction of the possible NV decay paths.

F_P can furthermore be expressed in terms of the cooperativity as

$$F_P = 1 + C \quad (2.51)$$

in the case when the cooperativity is expressed using γ . With the unfavorable branching ratio of an NV, realistic values for F_P limit the experimentally achievable cooperativities. This emphasizes why NV-cavity coupling experiments typically operate in the weak-coupling regime of cavity QED.

The spontaneous emission coupling factor β , describing the fraction of photons emitted into the cavity mode, needs to take both the coherent (ZPL) and incoherent (PSB) parts of the NV emission into account. Hence, β is given by the overall Purcell-enhancement:

$$\beta = \frac{F_P - 1}{F_P}. \quad (2.52)$$

The expression can be understood using Eqs. (2.36) and (2.51). For free-space emission, or when the cavity is detuned far off-resonance with the NV ZPL, the NV-cavity coupling strength g_0 goes to 0 and the NV decay rate is unaffected by the cavity. This corresponds to $F_P = 1$ and $\beta = 0$, meaning that none of the NV photons are emitted into the cavity mode. When the cavity is tuned close to resonance with the NV ZPL, $g_0 > 0$, $F_P > 1$ and $\beta > 0$, leading to an increased decay rate and some fraction of the photons being emitted into the cavity mode.

2.3.4 A plano-concave open microcavity

In this work, Purcell-enhancement of NVs is realized by placing an NV-containing diamond membrane into a plano-concave optical microcavity.

2.3.4.1 Cavity characteristics

Two important characteristics of a cavity are its finesse and Q-factor. The finesse can be seen as the "resolving power" of the cavity and conveys information about the losses in the system. It is defined as the fraction between the free spectral range (FSR), given by the difference in frequency or cavity length between consecutive resonances, and the width of each resonance. The lossless finesse, when assuming no absorption and scattering losses, can be derived solely from the reflectivities \mathcal{R}_1 and \mathcal{R}_2 of the mirrors forming the

cavity:²⁵⁸

$$\mathcal{F} = \frac{\pi(\mathcal{R}_1\mathcal{R}_2)^{1/4}}{1 - \sqrt{\mathcal{R}_1\mathcal{R}_2}}. \quad (2.53)$$

Taking losses into account, the finesse is instead expressed by

$$\mathcal{F} = \frac{2\pi}{\mathcal{L}_{tot}}. \quad (2.54)$$

Here, the round-trip loss is defined as $\mathcal{L}_{tot} = \mathcal{T}_1 + \mathcal{T}_2 + \mathcal{L}_1 + \mathcal{L}_2$, with $\mathcal{T}_{1/2}$ the transmission of mirror 1 and 2, respectively, and $\mathcal{L}_{1/2}$ the absorption- and scatter losses of mirror 1 and 2, respectively.

The Q-factor of the cavity, introduced in Eq. (2.35) and describing the relative energy loss rate of a resonator compared to its stored energy, is for a bare cavity related to the finesse via

$$Q = \frac{\mathcal{F}L}{(\lambda/2)} \quad (2.55)$$

and to the Purcell-enhancement via Eqs. (2.45) and (2.46). The advantage of the finesse over the Q-factor as a figure of merit is that it is independent of the cavity length²⁶¹.

2.3.4.2 A coupled diamond-cavity system

In a bare cavity, schematically illustrated in Fig. 2.16a, two highly reflective mirrors are separated by an air gap of length L_{air} . In reality, the optical distance L between the mirrors is slightly larger than L_{air} and takes into account also the penetration of the optical field into the mirrors. The optical cavity length at resonance is given by $L = m\frac{\lambda_r}{2}$, with λ_r being the resonance wavelength and m an integer. The bare-cavity mode structure, derived in Section B.1 under the one-dimensional simplification of an ideal cavity, is illustrated in Fig. 2.16d.

Inserting a diamond slab of thickness t_d into the system leads to two coupled cavities, one defined by the air gap and one by the diamond itself. In this coupled system, some of the field is confined within the air gap and some within the diamond (Fig. 2.16b-c). The mode structure of the coupled system, derived in Section B.2, is illustrated in Fig. 2.16e-f.

Each mode of the coupled system has features with a steep slope (purple), given by the resonances within the air gap and resembling the bare cavity resonances, as well as features with a shallow slope (orange), given by the resonances within the diamond and constant with respect to the cavity length. Depending on what feature dominates at the emission frequency of an NV, the coupled NV-cavity system is said to be in a diamond- or an air-confined mode.

For perfect mirrors, assuming vanishing field penetration into the mirrors, L is given purely by L_{air} and t_d . The cavity resonances occur for values of L_{air} and t_d that fulfill the condition

$$L_{air} + t_d n_d = j\frac{\lambda}{2} \quad (2.56)$$

with n_d being the refractive index of diamond and j an integer.

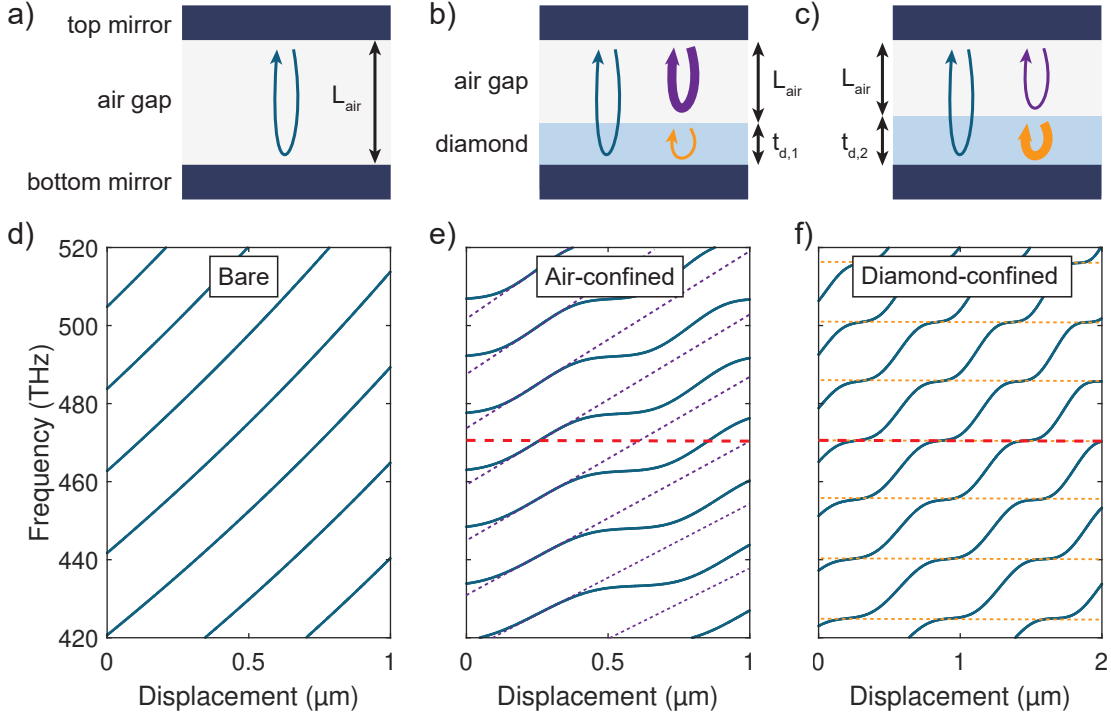


Figure 2.16.: Simulated cavity mode structure. (a) A bare cavity, formed by two reflective mirrors separated by L_{air} . (b) A cavity with diamond, forming two coupled cavities: one of length t_d , given by the diamond thickness, and one of length L_{air} , given by the air gap. The thickness $t_{d,1}$ of the diamond yields an air-confined mode. (c) A cavity with diamond, where the diamond thickness $t_{d,2}$ yields a diamond-confined mode. (d) Mode structure of a bare cavity. (e) Mode structure of a cavity with diamond in an air-confined mode. The diamond thickness is $t_{d,1} = 2.11 \mu\text{m}$. (f) Mode structure of a cavity with diamond in a diamond-confined mode. The diamond thickness is $t_{d,2} = 2.05 \mu\text{m}$. The red dashed lines indicate the ZPL frequency of NV^- .

2.3.4.3 Cavity design

We now turn to the design of the cavity. Possible stable cavity geometries are given by the condition

$$0 \leq \left(1 - \frac{L}{R_1}\right) \left(1 - \frac{L}{R_2}\right) \leq 1, \quad (2.57)$$

denoting the radius of curvature (ROC) of the top and bottom mirror as R_1 and R_2 , respectively. The condition is derived using Gaussian optics under the paraxial approximation and assuming perfect mirrors²⁶². For a plano-concave cavity with $R_2 \rightarrow \infty$, this translates into the condition $L \leq R_1$.

In order to optimize the cavity-emitter coupling, a small cavity waist is required. In the case of a short plano-concave cavity, the cavity mode waist can be approximated by

$$\omega_0 \approx \frac{\lambda}{\pi} (LR_1)^{1/4}. \quad (2.58)$$

The corresponding mode volume is given by²⁶¹

$$V = \frac{\pi}{4} \omega_0^2 L. \quad (2.59)$$

Cavity mirrors can be made by coating a substrate with a distributed Bragg reflector (DBR, also known as a quarter-wave stack). A DBR consists of dielectric layers with alternating high and low refractive index. Making the layers $\lambda/4$ thick leads to constructive interference of the reflected light for a wavelength of λ , with the reflectivity increasing with the number of layer pairs and the refractive index contrast between the layers. The transmission of light through a DBR can analytically be described using a one-dimensional transfer matrix model, in which each layer and interface is described by a matrix and the transmitted and reflected fields are obtained from the total transfer matrix of the system²⁶³.

The result of such a simulation (Essential Macleod, Thin Film Center Inc.) for a DBR stack designed for maximal reflection at 637 nm is illustrated in Fig. 2.17. The resulting "window" of low transmission centered around the design wavelength is referred to as the stopband of the mirror. The high-refractive-index material is set to be Ta₂O₅ (with $n_H = 2.12$ for $\lambda = 637$ nm) and the low-refractive-index material is set to be SiO₂ (with $n_L = 1.46$ for $\lambda = 637$ nm).

In Fig. 2.17a, a bare DBR without diamond is simulated. The transmission is calculated for three cases: a high-index-terminated (H-terminated) DBR consisting of 15 layer pairs, a low-index-terminated (L-terminated) DBR with 15 layer pairs, and an H-terminated DBR consisting of 11 layer pairs. The latter is used to show that a reduction in the number of layer pairs leads to an increase in the transmission of the mirror. This can be exploited to create an asymmetric cavity which preferentially leaks photons through one of its mirrors. H-termination results in a slightly higher reflectivity compared to L-termination, as it results in a higher refractive index contrast between the top DBR layer and the air.

In Fig. 2.17b, a DBR with a diamond layer on top is simulated. For a cavity with H-terminated mirrors, a mode is air-confined if the thickness of the diamond fulfills

$$t_d = q \frac{\lambda}{2n_d}, \quad (2.60)$$

with q an integer. A mode is diamond-confined if the diamond thickness fulfills

$$t_d = (2q + 1) \frac{\lambda}{4n_d}, \quad (2.61)$$

For a cavity with an L-terminated bottom mirror and an H-terminated top mirror, an air-confined mode is obtained if the diamond thickness fulfills Eq. (2.61) and a diamond-confined if the diamond thickness fulfills Eq. (2.60). Since the addition of a diamond layer changes the refractive index contrast with respect to the top layer of the DBR, the DBR transmission depends strongly on the mirror termination. The highest mirror reflectivity is achieved for an L-terminated DBR with a diamond on top with a thickness matching the condition for an air-confined mode.

The transfer matrix method can be further extended to the case of a full cavity. The result of such a simulation, used to calculate the vacuum electric field E_{vac} within the cavity, is shown in Fig. 2.18. Three different cases have been simulated, all using H-terminated mirrors: a bare cavity without diamond, a cavity in an air-confined mode, and a cavity in a diamond-confined mode, with parameters chosen such that the total cavity length including the mirrors is similar. The diamond is positioned on the bottom

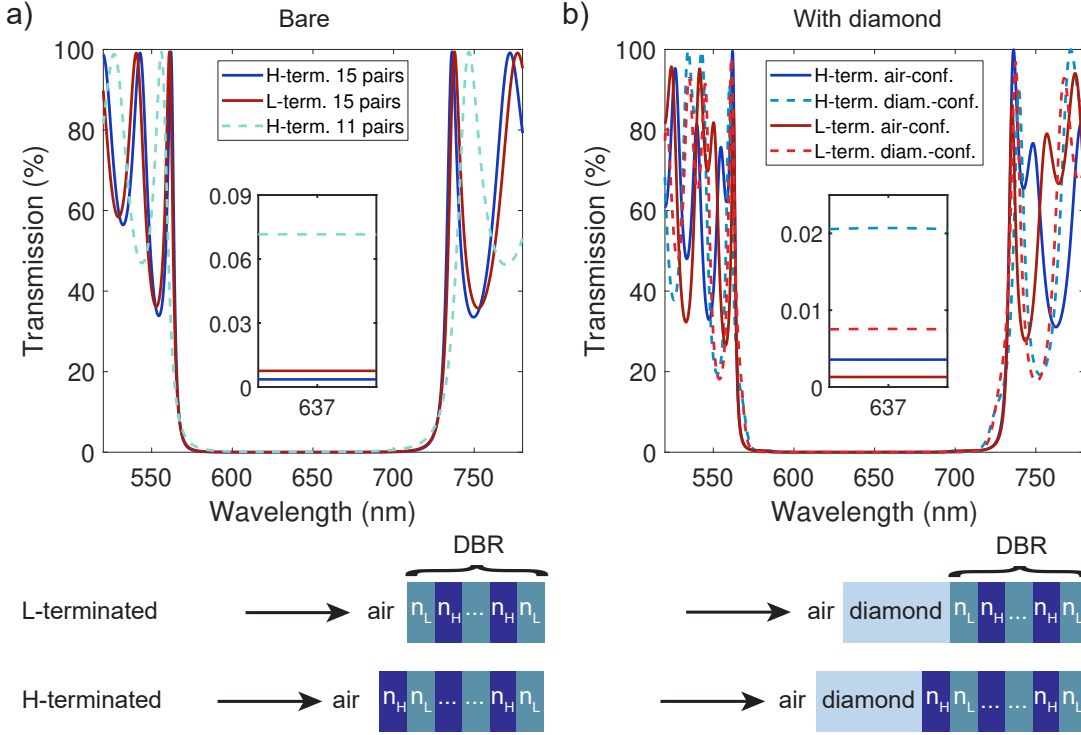


Figure 2.17.: Simulated DBR transmission. A layer pair consists of a $\lambda/4$ -thick layer of SiO_2 (n_L) and a $\lambda/4$ -thick layer of Ta_2O_5 (n_H). (a) Transmission of a bare DBR, for an H-terminated stack of 15 layer pairs, an L-terminated stack of 15 layer pairs, and an H-terminated stack of 11 layer pairs. (b) Transmission of a DBR with diamond on top, for an H-terminated stack of 15 layer pairs with a diamond thickness ($1.98 \mu\text{m}$) giving an air-confined mode, the same DBR but with a diamond thickness ($1.92 \mu\text{m}$) giving a diamond-confined mode, as well as for the same two cases but with L-terminated stacks (with a diamond thickness of 1.92 and $1.98 \mu\text{m}$ for the air-confined and diamond-confined mode, respectively).

DBR.

The simulation illustrates some important differences in the electric field distribution between air- and diamond-confined modes. In an air-confined mode (Fig. 2.18b), the field has a node at the diamond-air interface, which makes such a configuration less sensitive to scattering losses at the diamond-air interface. A diamond-confined mode (Fig. 2.18c), on the other hand, has a field antinode at the diamond-air interface. The location of the field antinodes also affects the optimal placement of the emitter. For maximal NV-cavity coupling strengths, an NV needs to be located at a distance corresponding to $\lambda/4$ ($\lambda/2$) from the bottom DBR in the case of H-terminated (L-terminated) mirrors²⁶⁴.

The transfer matrix method can be used to extract the location and width of the cavity resonances, giving the Q-factor and photon loss rate according to Eq. (2.35). The photon loss rate κ_{top} through the top mirror can then be extracted through

$$\kappa_{top} = \kappa \cdot \frac{\mathcal{T}_{top}}{\mathcal{T}_{top} + \mathcal{T}_{bottom} + \mathcal{L}} \quad (2.62)$$

where $\mathcal{T}_{top/bottom}$ is the transmission of the top and bottom mirror, respectively, and \mathcal{L} represents the losses in the cavity not related to the transmission of photons through either of its mirrors. Such losses mainly stem from scattering and absorption losses related

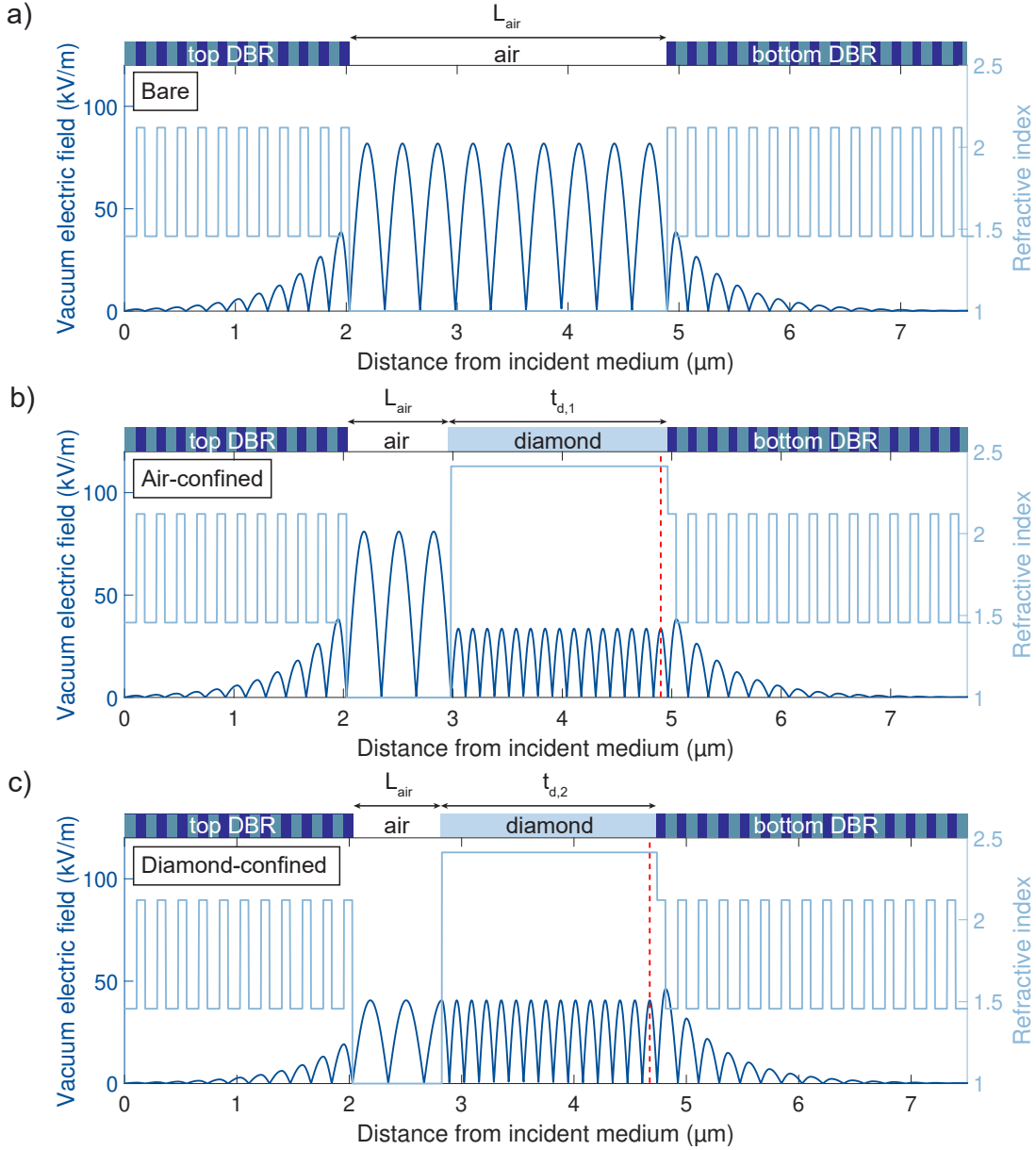


Figure 2.18.: Example vacuum electric field distribution for a cavity with H-terminated mirrors. (a) Field distribution in a bare cavity. (b) Field distribution in an air-confined mode, with a diamond thickness of $1.98 \mu\text{m}$. The maximum field strength is found within the airgap and there is a field node at the air-diamond interface. (c) Field distribution in a diamond-confined mode, with a diamond thickness of $1.92 \mu\text{m}$. There is a field antinode at the air-diamond interface. The red dashed lines indicates the optimal location of an NV for achieving the maximal coupling strength.

to the diamond, but can also arise due to coupling of fundamental cavity modes with higher-order transverse modes^{147,265}.

From κ_{top} , the outcoupling efficiency through the top mirror can be derived:

$$\eta_{\text{out}} = \frac{\kappa_{\text{top}}}{\kappa + \gamma}, \quad (2.63)$$

as well as the total efficiency of the system, which is given by the fraction of photons emitted into the cavity mode and the efficiency with which photons are coupled out of

the cavity:²⁶⁶

$$\eta_{tot} = \beta \cdot \eta_{out}. \quad (2.64)$$

Using the definition in Eq. (2.52), this can be expanded as

$$\eta_{tot} = \frac{4g_0^2/(\kappa\gamma)}{4g_0^2/(\kappa\gamma) + 1} \cdot \frac{\kappa_{top}}{\kappa + \gamma'}, \quad (2.65)$$

which for $\kappa_{top} \approx \kappa$ and $\kappa \gg \gamma$ can be approximated as

$$\eta_{tot} \approx \frac{C}{1 + C}. \quad (2.66)$$

This means that the total efficiency of the system converges to 1 for high cooperativities.

3

LASER WRITING OF NVs IN DIAMOND USING A SOLID-IMMERSION LENS

The content of this chapter is partially adapted from:

V. Yurgens, J. A. Zuber, S. Flågan, M. De Luca, B. J. Shields, I. Zardo, P. Maletinsky, R. J. Warburton, and T. Jakubczyk. **Low-charge-noise nitrogen-vacancy centers in diamond created using laser writing with a solid-immersion lens.** *ACS Photonics* **8**, 1726–1734 (2021).

3.1 Summary

Laser writing of NVs in diamond has recently emerged as a reliable method to create emitters with long charge-state stability at desired locations within the material. We report on pulsed-laser induced generation of NVs in diamond facilitated by a SIL. The SIL enables laser writing at energies as low as 5.8 nJ per pulse and allows vacancies to be formed close to a diamond surface without inducing surface graphitization. We operate in the previously unexplored regime where lattice vacancies are created following tunneling breakdown rather than multi-photon ionization. We present three samples in which NV-center arrays were laser-written at distances between $\sim 1 \mu\text{m}$ and $40 \mu\text{m}$ from a diamond surface, all presenting narrow distributions of optical linewidths with medians between 51.2 MHz and 58.3 MHz. The linewidths include the effect of long-term spectral diffusion induced by a 532 nm repump laser for charge-state stabilization, thereby emphasizing the particularly low charge-noise environment of the created color centers. We propose a model for disentangling power broadening from inhomogeneous broadening in the NV optical linewidth. We furthermore demonstrate that the laser-written NVs exhibit low transverse strain levels and low spin-flip rates at zero magnetic field, and measure narrow extrinsically broadened NV linewidths even in an etched $6 \mu\text{m}$ thick diamond membrane. Such high-quality NVs are excellent candidates for practical applications employing two-mode quantum interference with separate NVs.

3.2 Introduction

The negatively charged NV in diamond is among the most promising solid-state implementations of a quantum bit^{150,267}. However, long-distance quantum communication links based on NVs^{11,12,54} all suffer from the low generation rate of indistinguishable photons from each emitter. A way to radically enhance this rate is to use an open Fabry-Perot microcavity^{60–64}, which requires only minimally invasive fabrication of the diamond, thinning it down to a few-micron thick membrane^{58,147,268–270}. However, even such minimal processing has so far resulted in degradation of the NVs' optical quality, manifested in a large spectral diffusion due to charge noise^{58,128}. Methods of NV creation that do not result in the formation of parasitic defects and impurities are therefore desired.

The creation of an NV typically involves displacing a carbon atom from its lattice site to create a vacancy. While proximity to the surface is required for photonic applications, it is at the same time desirable to form the NVs at a depth of at least tens of nanometers in order to minimize the impact of the surface charge- and magnetic-noise on the NVs' spin- and optical coherence. The challenge is therefore to provide the required energy inside the crystal lattice. Electrons or ions with kinetic energies far above keVs readily provide this energy²⁷¹, but most of it is released via collisions on the particles' trajectory, leaving extended damage and presumably hard-to-anneal vacancy complexes. Nitrogen-ion implantation followed by high-temperature annealing¹⁰⁸ has been shown to create NV populations where approximately half of the NVs show spectral diffusion above a few GHz^{127,130}. In addition, NVs formed from implanted nitrogen have on average poorer optical quality than their counterparts formed from the native nitrogen, suggesting that vicinity to the fabrication-related damage plays a crucial role for the spectral diffusion.

Laser writing has emerged as a promising technique for creating deterministically positioned NVs in diamond. By irradiating a diamond sample with single high-energy femtosecond pulses and subsequently performing a thermal annealing step, NVs can be formed from the laser-induced lattice vacancies and diamond-native nitrogen. NVs created through laser writing in ultrapure diamond are characterized by long spin coherence times, low spectral noise and high charge stability⁴⁹. Crucially, their fabrication induces minimum damage to the diamond lattice, potentially reducing the charge noise in thin diamond membranes. Initial studies demonstrated laser writing of NVs using an oil-immersion lens in combination with wavefront correction^{49,227}.

3.3 Experimental setup

Here, we report a different approach employing a standard air objective together with a SIL, giving a high NA together with minimized aberrations and a diffraction-limited laser focal volume inside diamond. This technique not only enables creation of NVs with low pulse energies, but also makes it possible to laser-write in close proximity to the diamond surface, owing to the decreased laser intensity at the diamond-air interface.

3.3.1 Solid immersion lens

We use a truncated hemispherical cubic zirconia SIL (t-SIL) with a refractive index of $n = 2.14$. Figure 3.1 shows the spherical aberrations introduced at an air-diamond interface with and without such a SIL. A SIL results in a higher total focusing NA, but depending on the wanted depth of writing, the refractive index of the material and the wavelength of the focused light, it does not always provide an advantage over focusing the light directly into the material.

By using geometrical optics (ray tracing), the distortion of the focus due to spherical aberrations can be simulated. Figure 3.2 compares the dimensions of the focus when using a cubic zirconia t-SIL to using no SIL. A t-SIL truncation of $30\ \mu\text{m}$, laser wavelength of $800\ \text{nm}$ and external focusing NA of 0.9 has been assumed. Details of the derivation can be found in Section A. It is clear that the t-SIL provides an advantage in terms of the focal spread along the optical axis (Δz), while focusing without a SIL actually leads to a tighter lateral focus (Δx) for laser writing depths above a few μm . For this NA, and for writing deeper than $35\ \mu\text{m}$, the t-SIL results in a larger focal volume (V) compared to using no SIL, while performing similarly for shallower writing depths.

The situation looks quite different for a focusing NA of 0.6 , as seen in Fig. 3.3. There, the focal spread both along and across the optical axis is reduced with a t-SIL, for focusing deeper than a few μm . In the case of shallow writing, a large enough Δz_{FWHM} could lead to surface graphitization before vacancy creation within the diamond. In the limit that the t-SIL is made of diamond, spherical-aberration-free imaging is achieved at a depth d which matches the truncation t . Furthermore, the diffraction limit reduces simply because the relevant wavelength is the wavelength in the diamond, λ/n . For $\text{NA} = 0.6$, Δz_{FWHM} reduces to $1.6\ \mu\text{m}$ (Eq. (2.21)). These considerations suggest that vacancy creation is possible at depths starting at about $2\ \mu\text{m}$ from the diamond surface. In practice,

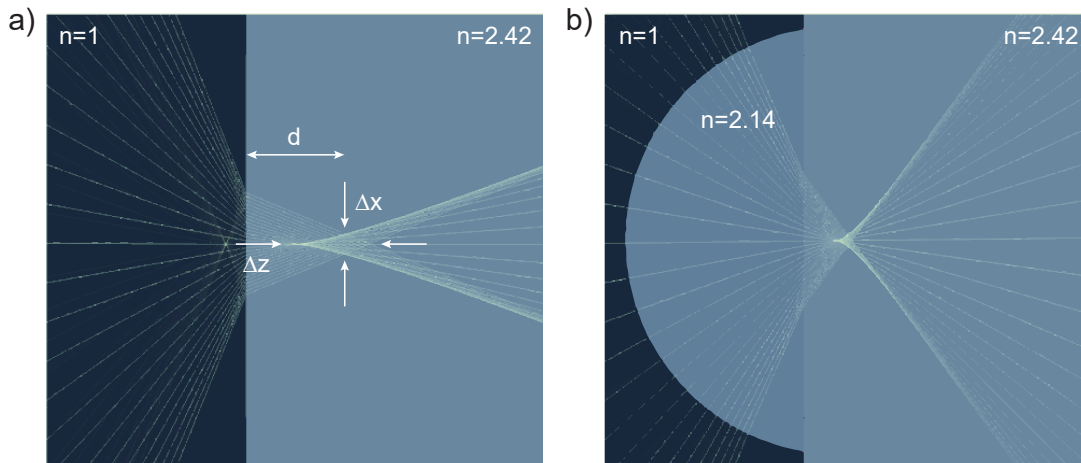


Figure 3.1.: Geometrical optics simulation of focusing light from air into diamond²⁷². (a) Spherical aberration for rays passing from air (left) to diamond (right) without corrective optics. Δx is the in-plane focal spread and Δz is the focal spread along the optical axis; d is the distance from the point of minimum Δx to the diamond surface. (b) Spherical aberration for rays passing from air to diamond through a truncated hemispherical solid-immersion lens (t-SIL).

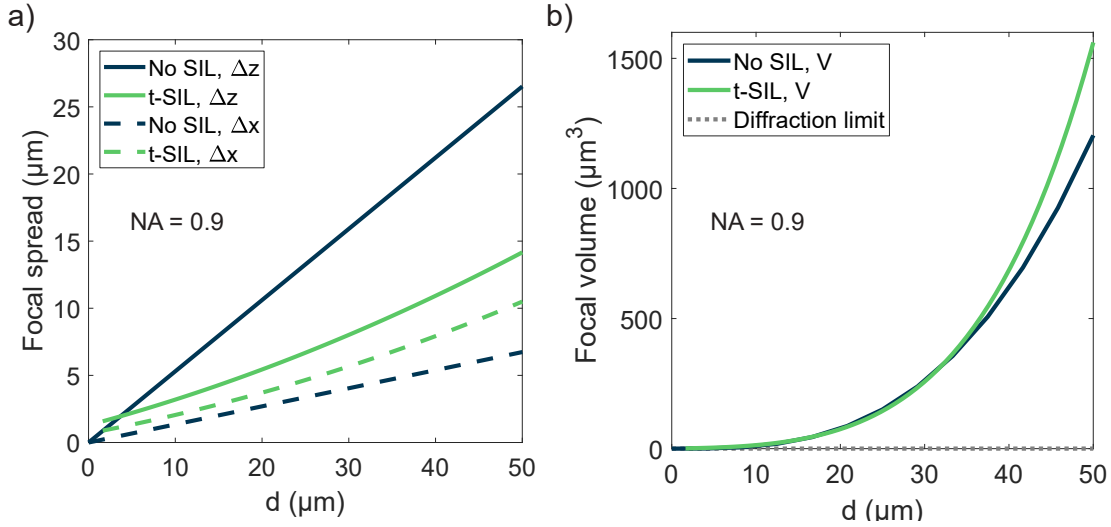


Figure 3.2.: Simulated focal spread and focal volume inside diamond for a focusing NA of 0.9 and wavelength of 800 nm. (a) Calculated focal spread in-plane (dashed lines, Δx) and along the optical axis (solid lines, Δz) with and without a t-SIL on passing through an air-diamond interface, as a function of the focusing depth d . The t-SIL provides an advantage in terms of the extent of the focus along the optical axis. (b) Focal volume, calculated as $(\Delta x)^2 \Delta z / 2$ following Eq. (A.10), versus d with and without a t-SIL. The t-SIL provides no clear advantage over focusing directly into the diamond. The diffraction limit, calculated using Eqs. (2.18) and (2.19), is indicated by a gray dashed line and corresponds to $0.2 \mu\text{m}^3$ for the given experimental conditions.

the t-SIL has a slightly lower refractive index than diamond and it is impractical to use a different t-SIL for each depth. Our simulations nevertheless show that a t-SIL gives good

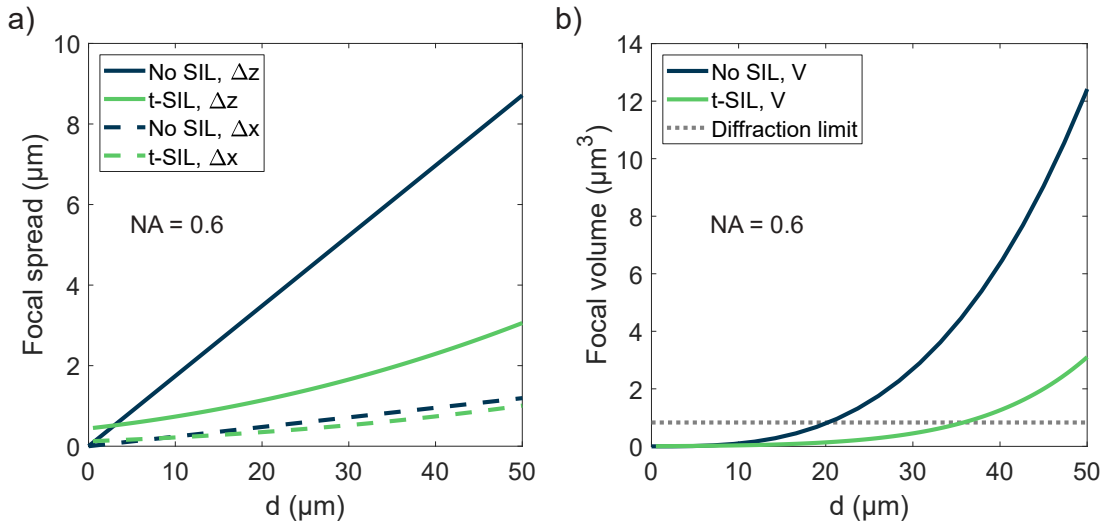


Figure 3.3.: Simulated focal spread and focal volume inside diamond for a focusing NA of 0.6 and wavelength of 800 nm. (a) Calculated focal spread in-plane (dashed lines, Δx) and along the optical axis (solid lines, Δz) with and without a t-SIL on passing through an air-diamond interface, as a function of the focusing depth d . The t-SIL provides an advantage in terms of the extent of the focus both along and across the optical axis. (b) Focal volume, calculated as $(\Delta x)^2 \Delta z / 2$ following Eq. (A.10), versus d with and without a t-SIL. The t-SIL provides a clear advantage over focusing directly into the diamond. The diffraction limit, calculated using Eqs. (2.18) and (2.19), is indicated by a gray dashed line and corresponds to $0.8 \mu\text{m}^3$ for the given experimental conditions.

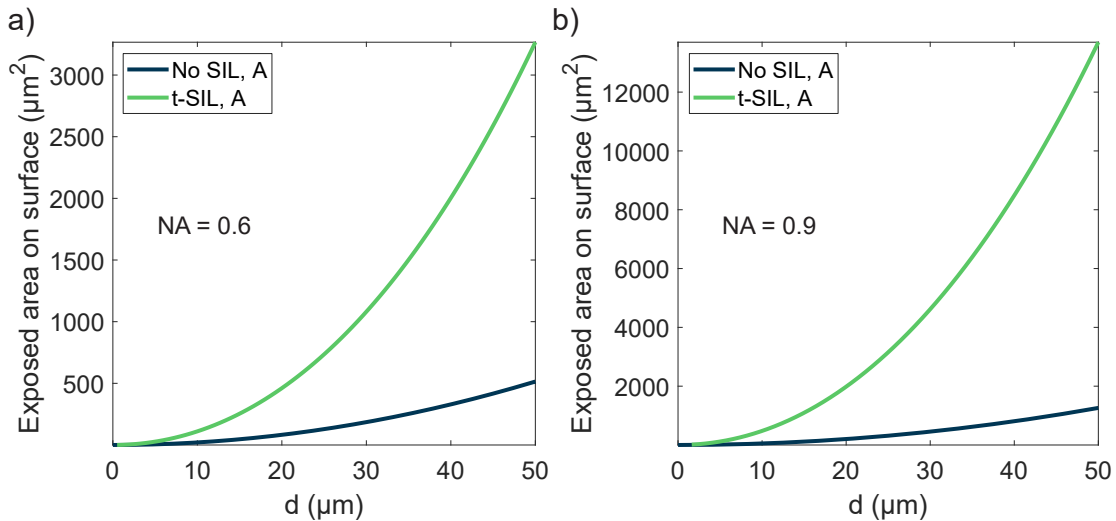


Figure 3.4.: Exposed area on the diamond surface for different focusing NAs. (a) Exposed area on the diamond surface for a focusing NA of 0.6. (b) Exposed area on the diamond surface for a focusing NA of 0.9. In both (a) and (b), there is a clear advantage of using a SIL to protect the diamond surface from graphitization.

imaging out to a depth up to 50 μm.

A crucial factor to consider is that the energy of the laser pulses required to create vacancies in bulk diamond typically exceeds the threshold at which the diamond surface is degraded^{49,138,273}. Creating vacancies in bulk diamond with laser writing is therefore only possible if the laser focus is spread over a significant area at the surface. Fig. 3.4 compares the exposed area on the surface for focusing 800 nm light with and without a t-SIL with a truncation of 30 μm. In Fig. 3.4a, the NA is 0.6; in Fig. 3.4b, the NA is 0.9. It is clear that the t-SIL presents an advantage in both cases, leading to a reduced intensity on the surface.

We can conclude that for an NA of ~ 0.6 and the mentioned writing specifications, a t-SIL both improves the quality of the focus and reduces the intensity at the surface. A way to gain the advantages provided by an NA of 0.6 using a NA=0.9 objective is to reduce the contribution of high-angle rays by underfilling the back aperture of the objective.

A further advantage of the t-SIL is that it improves the photon collection efficiency and thereby the sensitivity to the weak signals emitted by the created vacancies. It does so by reducing the number of photons lost due to total internal reflection at the diamond-air interface^{251,253,274}. Moreover, the implementation of a t-SIL is both cost-effective and easily implemented. A limitation is perhaps the writing area – excellent imaging is achieved only close to the center of the t-SIL. However, a writing area of approximately 25-by-25 μm² is available for a t-SIL with a diameter of 1 mm, sufficiently large for our purposes.

Figure 3.5 shows one of the cubic zirconia t-SILs used in this work (radius 500 μm, truncation between 0 and 50 μm). In Fig. 3.5a and Fig. 3.5b, scratches on the planar interface of the SIL are visible; for optimal writing performance, these are removed by using a polishing suspension containing 50 nm-sized alumina particles. Movements of the SIL on the diamond between exposures is done by means of a thin glass capillary (Fig. 3.5c). In order to reduce aberrations resulting from imperfections at the diamond-SIL interface, the t-SILs are placed on the diamond samples together with an index-matching gel

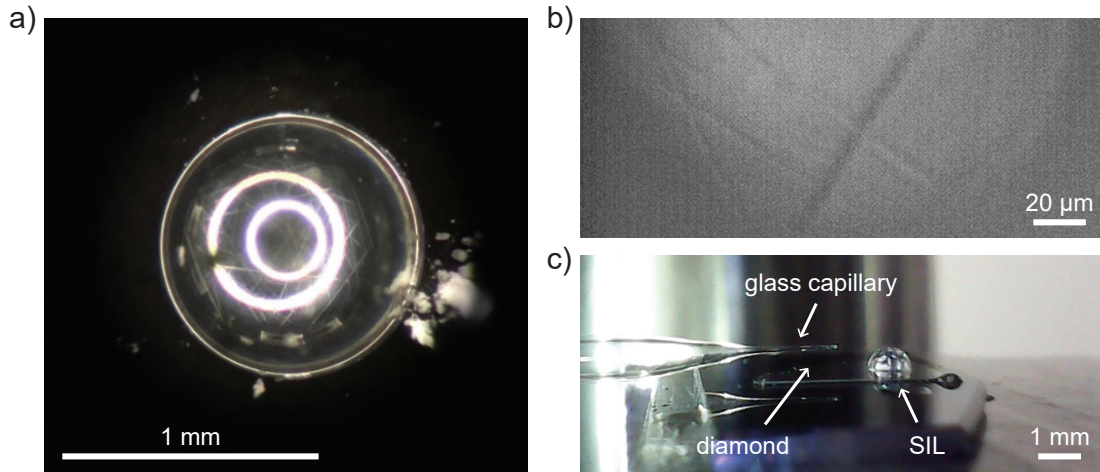


Figure 3.5.: The solid immersion lens. (a) A cubic zirconia t-SIL. (b) Optical image illustrating scratches on the flat surface of the t-SIL. (c) Moving a t-SIL on a diamond sample by means of a thin glass capillary.

(Thorlabs, G608N3).

3.3.2 Laser-writing setup

We perform laser writing in a room temperature home-built confocal microscope with a separate injection path for the femtosecond pulsed laser (Fig. 3.6). A 532 nm Nd:YAG laser is used for non-resonant (532 nm) excitation of the vacancies and NVs. Photoluminescence (PL) is filtered by a longpass filter (Semrock, 594 nm RazorEdge) and collected either by an avalanche photodiode (APD, Excelitas, SPCM-AQRH-15-FC) or a liquid nitrogen-cooled CCD camera coupled to a grating spectrometer (Princeton Instruments). The setup further allows for white-light illumination and CCD-imaging of the sample.

We use a Spectra Physics Spirit 1030-70 femtosecond ytterbium-doped fiber laser together with a Spirit-NOPA-2H non-collinear optical parametric amplifier, which together create pulses at a wavelength of 800 nm with a duration of approximately 35 fs. A half-wave plate and a Brewster-angle polarizer (BAP) is used for tuning the pulse energies. We focus the laser with a standard air objective (Olympus, MPLFLN100x, NA=0.9 or Olympus, LCPLFLN100xLCD, NA=0.85) through a t-SIL. The resulting NA including the effect of the t-SIL is about 1.8, slightly higher than what was used by Ref. 49. We note however that the full-width-at-half-maximum (FWHM) of the beam is about the same as the input aperture of the objective, reducing the contribution of the rays at the highest angle and giving us the advantages mentioned in Section 3.3.1.

We determine the performance of the optical setup including the t-SIL by confocal imaging of the emission from single, preexisting, shallow NVs, obtaining a lateral FWHM of a single bright spot of 125 ± 3 nm. This value is just above the theoretical minimum of 121.1 nm, as given by $\frac{0.52}{NA} \frac{\lambda_1 \lambda_2}{\sqrt{\lambda_1^2 + \lambda_2^2}}$ for the confocal configuration (using $\lambda_1 = 532$ nm and $\lambda_2 = 700$ nm for the excitation and main NV phonon-sideband (PSB) emission wavelength, respectively, and taking $NA = 0.85 \cdot 2.14$). This close agreement between the measured spot size and the diffraction limit demonstrates that the optical components,

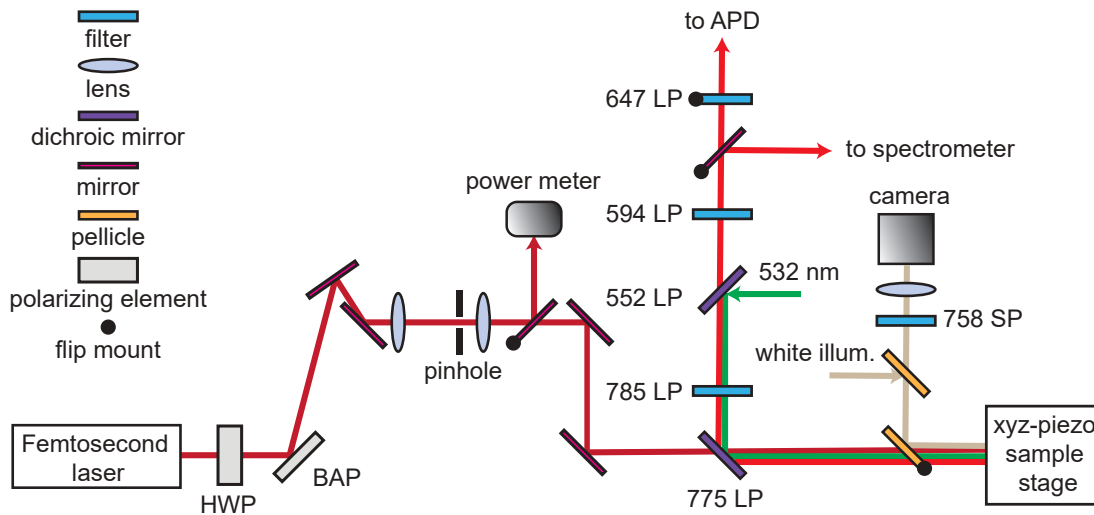


Figure 3.6.: The laser writing setup. Single pulses of a femtosecond laser are guided through a polarization-attenuation stage consisting of a rotatable half-wave plate (HWP) and a Brewster-angle polarizer (BAP), through a pinhole and onto a sample. The setup enables off-resonant (532 nm) excitation, white light illumination, and PL detection on an APD and spectrometer.

notably the objective and the t-SIL, do not introduce unwanted aberrations.

3.4 Laser writing of NVs

Photo-induced damage in a transparent wide-bandgap material such as diamond requires transfer of energy to the lattice via nonlinear mechanisms. The lattice damage can result from tunneling or multi-photon absorption followed by avalanche ionization in the volume of a tightly focused laser beam, as described in Section 2.2.1.

3.4.1 Creation of vacancies

We follow the experimental procedure described in Ref. 49 to create arrays of vacancies in bulk electronic-grade diamond samples (40 μm thick, $\langle 100 \rangle$ crystal orientation, $[\text{N}] < 5$ ppb, Element Six) by focusing 800 nm, 35 fs single pulses into diamond. Figure 3.7a shows the integrated PL intensity after such an exposure at a depth of 6.4 μm . Each bright spot corresponds to a cluster of vacancies, identified by the spectral signatures seen in Fig. 3.7b. The GR1 peak around 740 nm appears at a pulse energy of 5.2 nJ. No clear trend relating the intensity of the peak with the pulse energy can be deduced, possibly due to slight misalignment of the detection with respect to the center of the laser-induced damage.

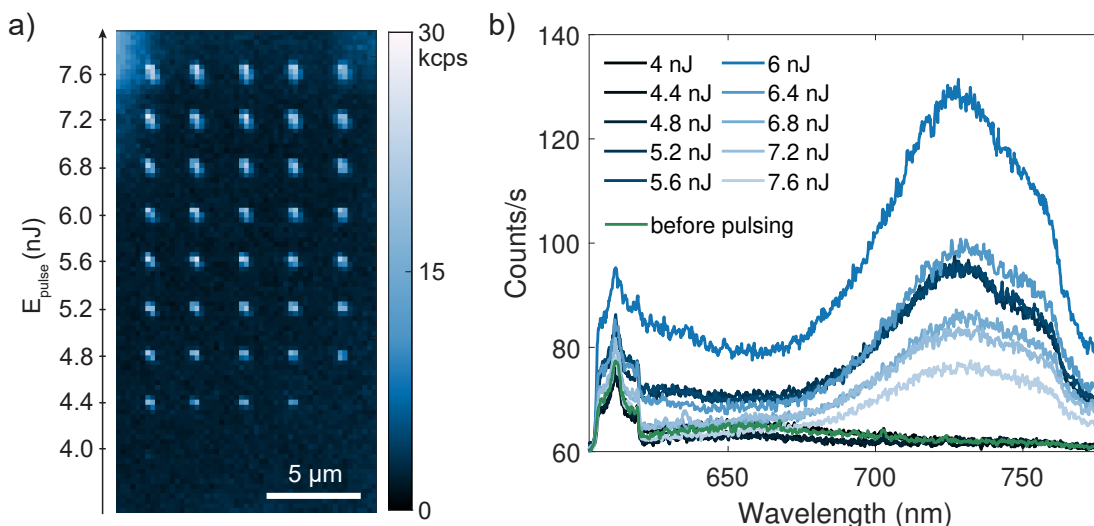


Figure 3.7.: GR1 as a function of pulse energy. (a) Integrated PL from a GR1 array, with increasing pulse energy along the y-axis. (b) GR1 spectrum as a function of pulse energy. No clear trend relating the intensity of the peak with the pulse energy can be deduced.

3.4.2 Annealing recipe optimization

Once vacancies have been created, the diamond sample is annealed in order to let the vacancies diffuse and form NVs with native nitrogen. Figure 3.8 shows the optimization of the annealing process. An array, laser-written at a depth of 7.2 μm (Fig. 3.8a), is first annealed in vacuum for three hours at 900°C after ramping up from room temperature during two and a half hours (Fig. 3.8b, left panel). Only very weak NV PL is observed, indicating the presence of residual lattice damage. After annealing for three hours at 1000°C with the same total ramping time (Fig. 3.8b, middle panel), a slight improvement

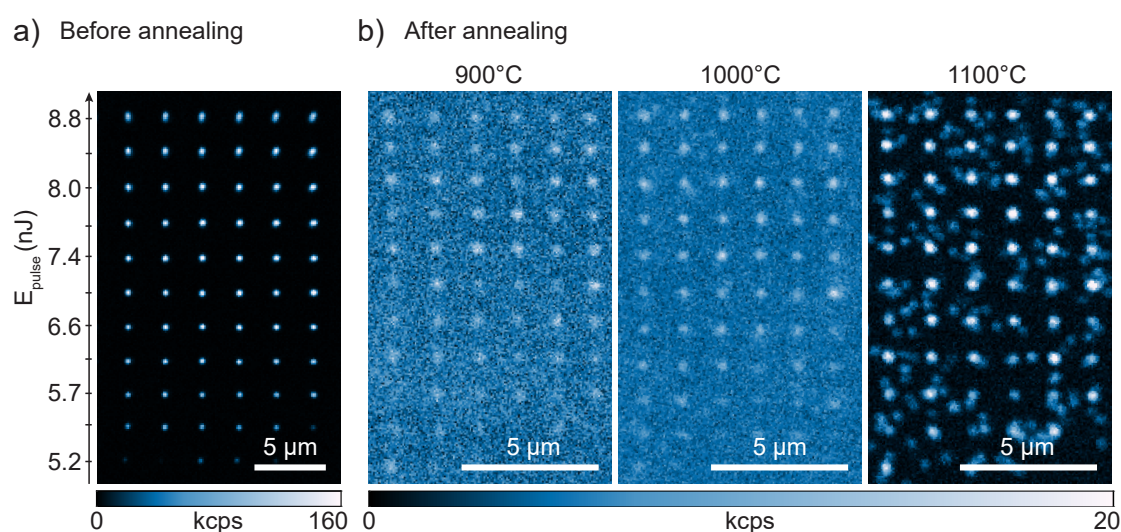


Figure 3.8.: Optimization of the annealing procedure. (a) Integrated PL from a GR1 array before annealing, with increasing pulse energy along the y-axis. (b) The same array after annealing to 900°C (left), 1000°C (middle), and 1100°C (right).

in the count rate is seen. More importantly, NVs seem to have formed also outside of the main array points, indicating that some vacancy diffusion has taken place. Annealing for three hours at 1100°C with the same total ramping time (Fig. 3.8b, right panel) results in a drastically increased PL, with clear NV PL also outside of the main writing sites. The sample was kept for another five hours at 800°C before ramping down to room temperature, a step omitted in subsequent sample annealing processes as it was assumed not to contribute significantly to the NV formation after the 1100°C-annealing step.

3.4.3 Formation of NVs in bulk diamond

Once optimal parameters for successful SIL-assisted laser writing have been found, we use single pulses at increasing pulse energies (3.8-35.8 nJ) to create NVs at different depths in multiple samples. Surface markers for locating the laser-written arrays after annealing are made through graphitization of the diamond surface by increasing the pulsing frequency of the femtosecond laser to 100 kHz, removing the t-SIL, and increasing the energy to a value above the graphitization threshold of the surface (typically around 5 nJ). Examples of such markings are shown in Fig. 3.9.

Two laser-written arrays are shown in Fig. 3.10, with arrays of vacancies (Fig. 3.10a-b) and NVs (Fig. 3.10c-d), respectively, created with increasing pulse energies from the bottom of the arrays. The scans were recorded at room temperature. The arrays were made at a depth of 2.0 μm and 7.0 μm below the diamond surface, respectively, where we note that the former demonstrates that our method can be used to create NVs in close proximity to the diamond surface without inducing graphitization. For sample A, pulse energies between 4.8 nJ and 7.6 nJ were used, with visible GR1 PL (inset Fig. 3.10b), 100 s integration time) appearing for 5.8 nJ per pulse; for sample B, pulse energies between 3.8 nJ and 8.4 nJ were used, with visible GR1 PL appearing for 6.1 nJ per pulse. All pulse energies refer to values at the output of the microscope objective. Both samples were annealed in vacuum for three hours at 1100°C, after which the spectral signatures of

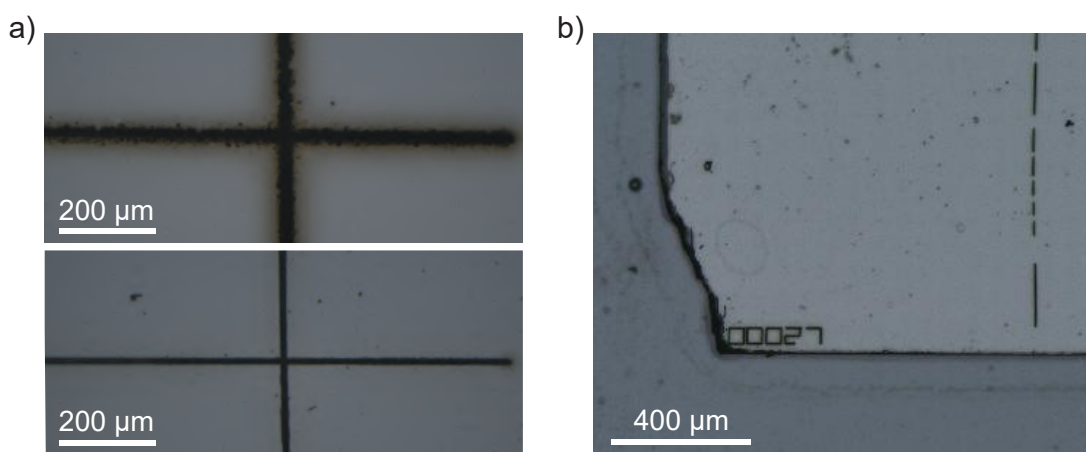


Figure 3.9.: Graphitization as a means of diamond marking. (a) Graphitized lines made on the diamond surface (top) and the same lines after a solvent cleaning process (bottom). (b) A marker indicating the sample name, made by graphitization.

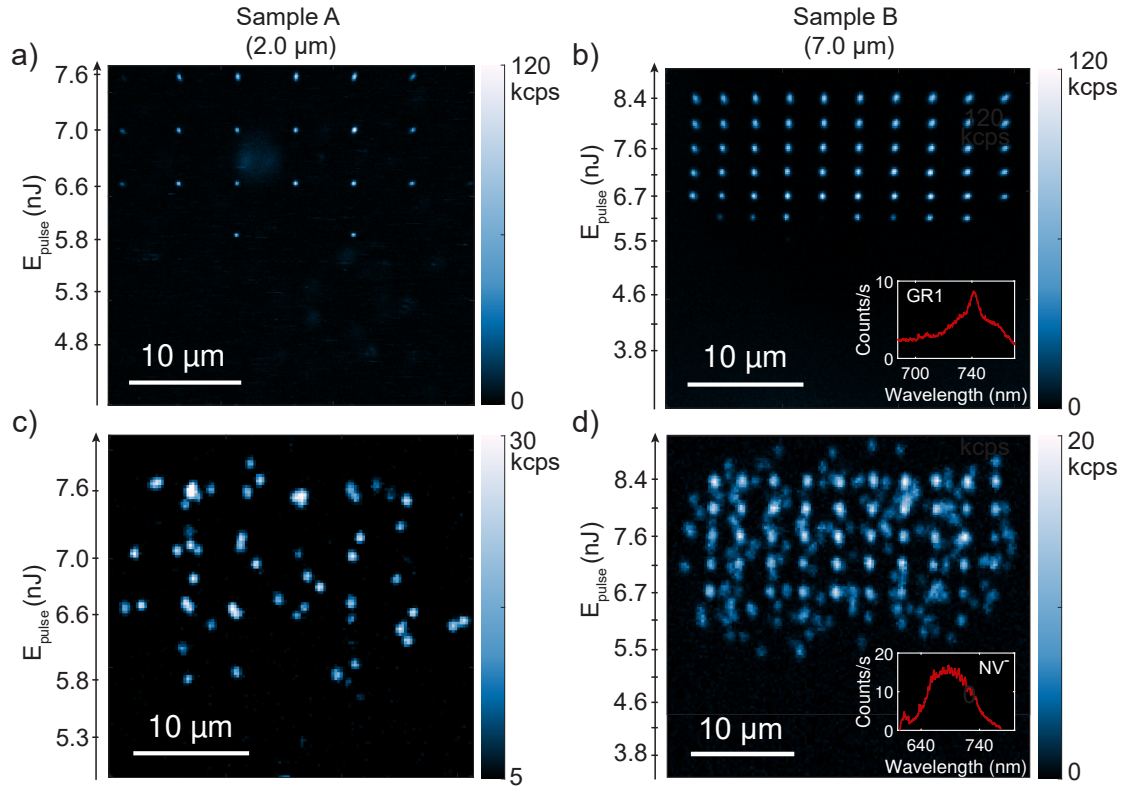


Figure 3.10.: Laser-written arrays before and after annealing. (a,b) Confocal scans of samples A and B, showing GR1 PL (inset in b) at room temperature before annealing. The scans were performed through a t-SIL. (c,d) Confocal scans of samples A and B, showing NV^- PL (inset in d) at room temperature after annealing to 1100°C .

negatively charged NVs (inset Fig. 3.10d, 100 s integration time) were observed.

Calculation of the Keldysh parameter γ for these vacancy-creation threshold energies, with the specified pulse duration and focal area, gives $\gamma \ll 1$, meaning that we operate in a regime where tunneling breakdown is dominant over multi-photon ionization, in contrast to previous work⁴⁹. Tuning of the vacancy creation regime could be carried out by changing the laser writing wavelength and increasing the pulse length, but with the latter shrinking the window for NV creation due to a decrease of the graphitization threshold²²⁸.

Sample B shows a clear array-like NV pattern after annealing, where the main array points contain multiple NVs, as demonstrated by the photon count in the confocal scans and by the existence of multiple, uncorrelated emission lines in subsequent photoluminescence excitation (PLE) measurements. The diffusion of vacancies during annealing is also clearly visible – single NVs form up to several hundreds of nanometers from the array spots, similar to the results of previous experiments^{49,275,276}. Lower pulse energies and a larger spatial separation between the focal spots were therefore used for sample A in order to obtain predominantly spots with single rather than multiple NVs.

Vacancy PL after laser writing was observed both with the t-SIL and after displacing the t-SIL from the laser-processed area. If no t-SIL was used during the laser-writing process, neither graphitization nor GR1 PL could be detected in the bulk of the sample up to a pulse energy of 52 nJ (highest available in our experimental configuration) and a continuous exposure with a pulse repetition rate of 1 MHz with durations up to tens

of seconds. Similar observations were made after exposures performed with a t-SIL but without using the index-matching gel. Also after annealing, there was no NV PL in areas exposed without a t-SIL. These observations indicate that the use of a t-SIL dramatically reduces the input power threshold for vacancy generation and can act as the key element enabling laser-induced NV formation using femtosecond laser sources.

3.4.4 Laser writing close to a surface

The increased energy density on the diamond surface upon focusing the laser close to the top surface typically resulted in graphitization of the diamond surface or damage of the t-SIL. For such shallow writing, "donut"-like features could in some cases be seen within the diamond. This is illustrated in Fig. 3.11a, where pulse energies between 10.8 and 14.8 nJ were used to create arrays at different depths close to the top surface. Arrays written deeper than $2.4\ \mu\text{m}$ from the surface contain point-like features, and show the expected GR1 spectral signature. In shallower arrays, the created features are donut-

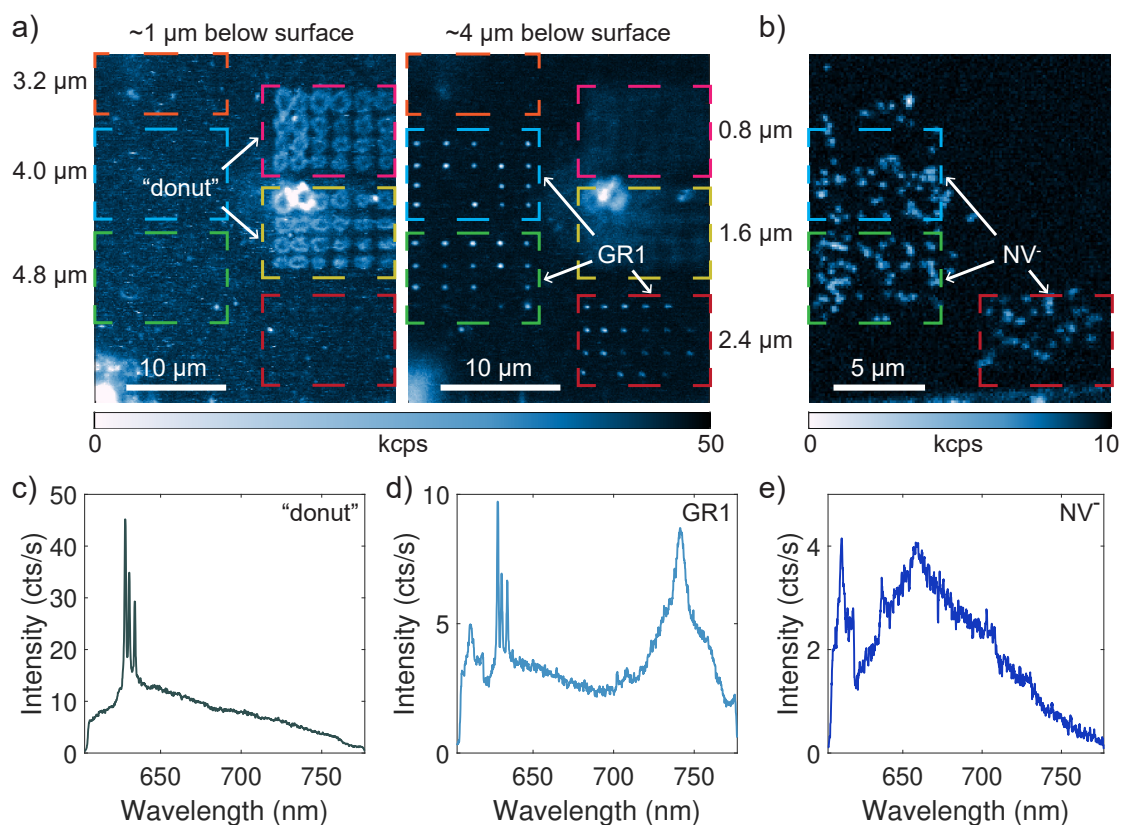


Figure 3.11. Laser writing close to the top surface. (a) Arrays before annealing, written at different depths under the top surface and imaged either $\sim 1\ \mu\text{m}$ or $\sim 4\ \mu\text{m}$ below the surface. In arrays written deeper than $2.4\ \mu\text{m}$ from the surface, the write sites exhibit point-like features and an associated GR1 spectral signature. In arrays written less than $2.4\ \mu\text{m}$ below the surface, donut-like features can be seen. The array made at $3.2\ \mu\text{m}$ depth was too far from the center of the SIL to successfully create vacancies. (b) Arrays after annealing. NVs formed only where a GR1 signature and point-like features were detected before the annealing. (c) Spectrum measured on a donut-like feature before annealing. (d) GR1 spectrum, measured at a point-like feature before annealing. (e) NV⁻ spectrum, measured on a spot with visible PL after annealing.

instead of point-like, show no sign of GR1 in emission (Fig. 3.11c), and do not result in NVs after annealing. Only write sites showing GR1 PL before annealing result in NVs after annealing (Fig. 3.11b). The fact that successful laser writing with our configuration works at a depth $> 2 \mu\text{m}$ aligns well with the analysis of the dimensions of the focal spot in Section 3.3.1.

In order to be able to create NVs close to a surface, we employ an inverse geometry in which laser pulses are applied through the t-SiL and diamond, but focused close to the diamond back surface. We use an objective lens with $\text{NA}=0.85$ and correction ring to further minimize the spherical aberration, with the correction ring set to maximize the laser focus intensity at the bottom surface of the sample. We pattern several NV arrays in a sample referred to as sample C in this configuration. In order to test NV writing at various depths and in order to find a possible distance limit from the surface for NV creation, each array additionally includes a smaller depth variation of $0.4 \mu\text{m}$ between each laser writing spot within a row. This results in NVs covering distances from $\sim 1 \mu\text{m}$ up to $15 \mu\text{m}$ from the bottom diamond surface, corresponding to laser writing depths of between $25 \mu\text{m}$ and $40 \mu\text{m}$ from the top surface. PL images of the resulting NV arrays are shown in Fig. 3.12a.

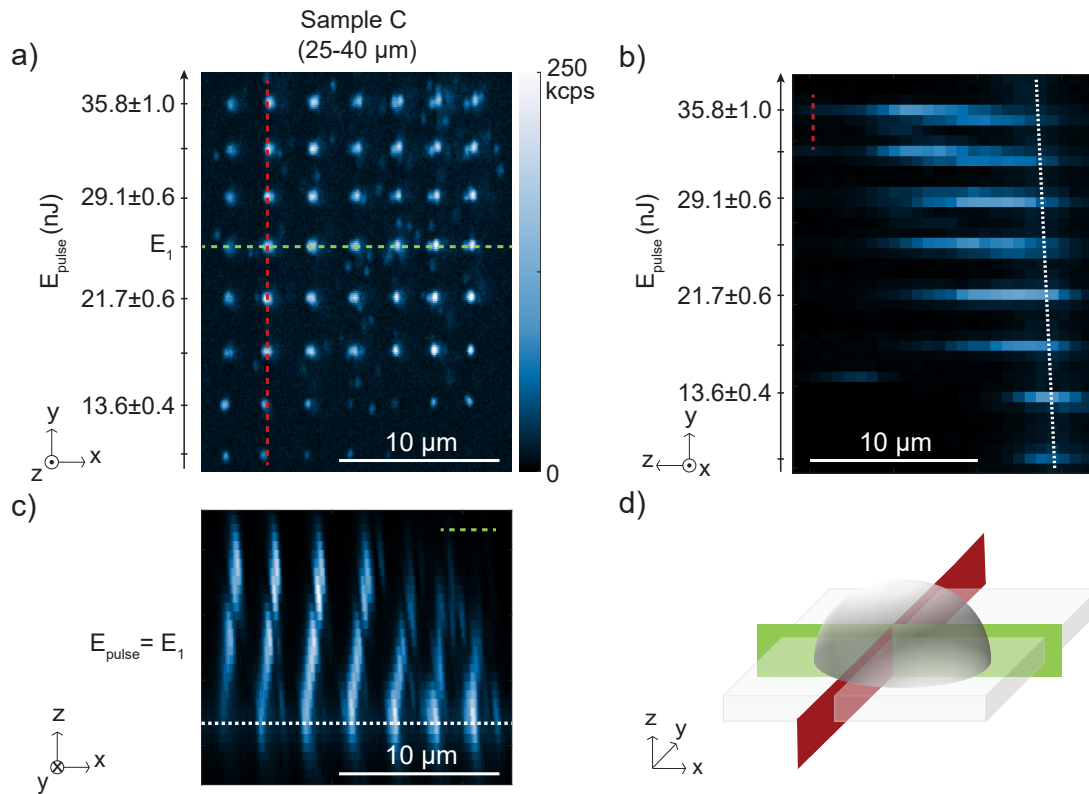


Figure 3.12.: Laser writing close to the bottom surface. (a) Confocal scan of NVs in sample C, laser-written in an inverse geometry where laser pulses were focused close to the bottom surface of the diamond. The colorbar applies to a-c. (b) Cross-section in the plane indicated by the red dashed line in (a). The white dashed line indicates the bottom diamond surface, determined by the position at maximum intensity of the reflected excitation laser. (c) Cross-section in the plane indicated by the green dashed-line in (a), for a pulse energy $E_1 = 25.7 \pm 0.5 \text{ nJ}$. The white dashed line indicates the bottom diamond surface. (d) Schematic of the t-SiL and two cross-sections through the diamond.

Fig. 3.12b-c show cross-sections through the sample to illustrate the slightly tilted layers of NVs within the diamond. In Fig. 3.12b it is apparent that a lower pulse energy was needed to create the NVs closest to the surface, as compared to writing NVs further inside the bulk. The reason for this is presently unknown. Fig. 3.12d illustrates the cross-sections and the t-SIL-on-diamond geometry. NVs were created over the full range of pulse energy in Fig. 3.12a, from 7.6 ± 0.4 nJ to 35.8 ± 1.0 nJ. Even at the highest pulse energies there were no signs of graphitization. This energy window is remarkably wide compared to previous studies^{49,227}. We propose that this is a key consequence and advantage of NV laser writing in the tunneling regime instead of the multi-photon ionization regime.

3.5 Linewidth characterization

In order to characterize the optical linewidths of the NVs created via laser writing, we perform PLE measurements at low temperature. The samples are positioned on a stack of cryogenic piezo-driven nanopositioners (attocube, ANPx101, ANPz101 and ANSxyz100), enabling scanning and long-range positioning with respect to the excitation and detection axis. The stack is placed into a home-built titanium cage; light is in- and out-coupled through an objective (Partec 50x, 0.82 NA) mounted at the top of this cage. The cage is suspended at the end of a non-magnetic "skeleton" inside a steel tube, which is evacuated and subsequently filled with 25 mbar He exchange gas to ensure good thermalization of the sample. The tube is immersed in liquid helium in a bath cryostat, with optical access possible through a laser window (Thorlabs, WL11050-C13).

3.5.1 Photoluminescence excitation

We use a microscope "head", schematically illustrated in Fig. 3.13, for the PLE measurements. Light is in- and out-coupled from optical fibers and filtered depending on the wavelength (532 nm excitation: Semrock, HC Laser Clean-up MaxLine 532/2 and 561 SP Edge Basic; 637 nm excitation: Semrock, 650 SP BrightLine HC and 637/7 BrightLine HC; detection: Semrock, 532 LP RazorEdge, 594 LP Edge Basic and 635 LP Edge Basic). The two excitation laser beams are combined using a dichroic mirror (DM, Semrock, HC 560 Beamsplitter) and non-polarizing 90:10 beamsplitters (BS, Thorlabs, BS025) separate the signal from the resonant excitation. Broadband illumination is provided by an LED ($\lambda \sim 660$ nm, Osa-Opto, OCL-440-MURSTAR) and a CMOS camera (Allied Vision, Guppy Pro F-503 1/2.5") is used for imaging. Adjustable mirrors allow for angular and lateral positioning of all beams and optimal alignment with respect to the objective located at low temperature. The full microscope head is 30 mm-cage compatible and positioned on top of the cryostat.

NVs are resonantly excited using a tunable narrow-linewidth external cavity diode laser (New Focus Velocity TLB-6704) locked to a high-precision wavemeter (HighFinesse, Ångstrom WS/U-30U) using powers between 15 nW and 450 nW. The linewidths are determined by sweeping the excitation frequency over the ZPL resonance while recording

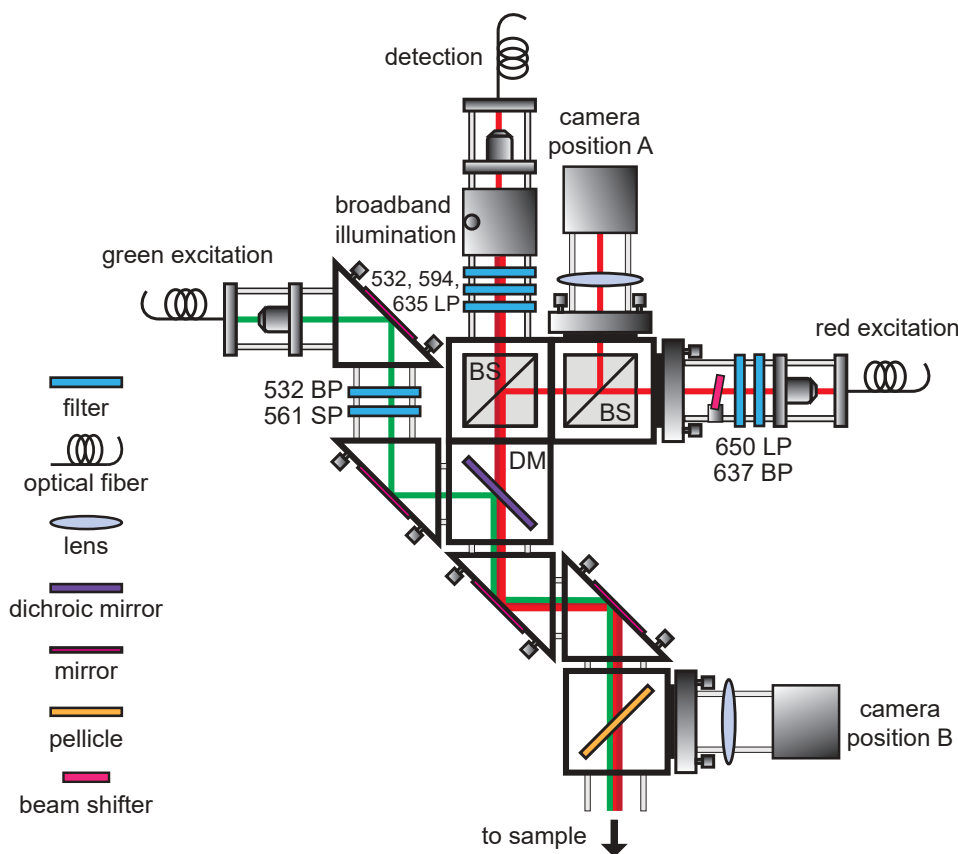


Figure 3.13.: Microscope head for linewidth measurements, enabling off-resonant green excitation as well as resonant red excitation and broadband illumination of the sample.

the photons emitted into the PSB on an APD (Excelitas, SPCM-AQRH-15-FC). We use an integration time of 10 ms for each laser detuning. We minimize power broadening in the resulting PLE spectra by measuring at the lowest possible resonant laser power that still gives an adequate signal-to-noise ratio. Between the periods of excitation and readout, a negative charge-state repump is carried out with a 532 nm Nd:YAG-laser (Laser Century, GL532N6-2500) with an average power of 0.6 mW. The full cycle of repump followed by resonant excitation and readout is repeated at a frequency of 100 kHz, with a 21-to-68 green-to-red laser duty cycle (2.1 μ s green exposure, 550 ns wait time, 6.8 μ s red exposure, 550 ns wait time). The interleaved red and green exposure is created by acousto-optic modulators (AOM, Crystal Technology, 200-146), with waveforms provided by an arbitrary waveform generator (Agilent).

Two PLE scans are presented in Fig. 3.14, showing ZPL resonances with Lorentzian lineshapes with FWHM linewidths of 34.5 ± 1.8 MHz, 32.6 ± 2.3 MHz and 35.9 ± 0.9 MHz, close to the lifetime-limited linewidth of 13 MHz measured for a native NV in a bulk natural diamond sample⁴⁰. We note that Ref. 40 measured linewidths between the repump pulses and thereby excluded a major source of inhomogeneous broadening – charge reconfiguration of the environment on resetting the NV charge. In our case, we integrate over many repump cycles, thereby including all the linewidth broadening contributions and measuring the extrinsically broadened linewidths.

Fitting the lines measured at low power (where extrinsic broadening dominates) with Gaussian functions rather than Lorentzians (average mean-standard-errors 0.014 and

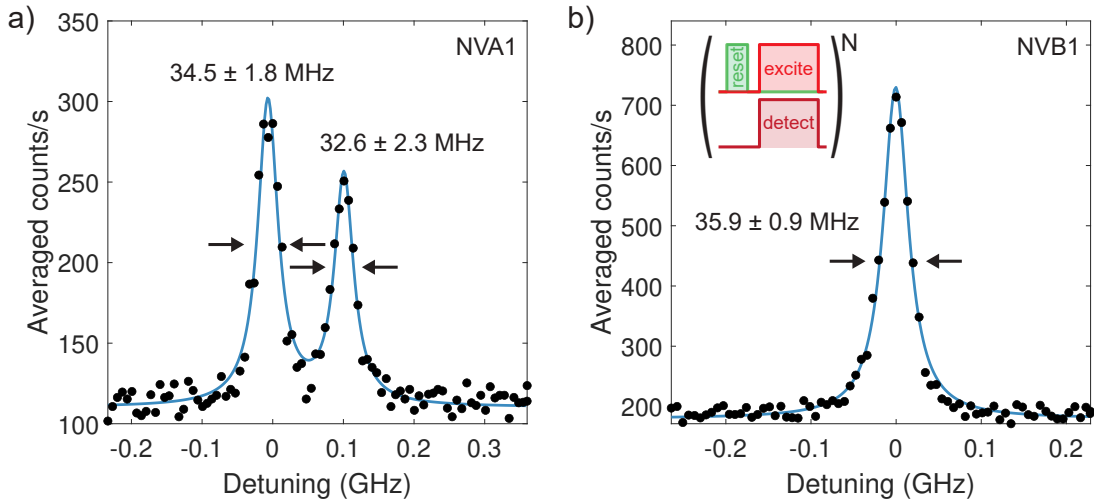


Figure 3.14.: ZPL linewidths. (a) Optical linewidth measured on an NV in sample A. Zero detuning corresponds to a ZPL frequency of 470.509 THz. The inset shows the measurement sequence for the PLE measurement. (b) Linewidth measured on an NV in sample B. Zero detuning corresponds to a ZPL frequency of 470.494 THz.

0.017, respectively) yielded an average difference in FWHMs of only 1.5% for the three samples, justifying the use of a Lorentzian function to describe the extrinsic broadening in our case.

Fig. 3.14a shows a splitting between the resonances of just 109 MHz, which indicates a low strain level in the surroundings of the specific NV. (Here, we make the reasonable assumption that the peaks correspond to the E_x and E_y transitions of the same color center.) In general, the three laser-written samples demonstrate several doublets with exceptionally low peak splittings down to 81 MHz, but a more systematic study is required in order to obtain a definite conclusion on the strain levels of laser-written NVs and to exclude the possibility that the two lines originate from separate NVs. (Such coincidence in spatial location, linewidth and ZPL energy between different NVs is highly unlikely.) The absolute ZPL frequency has a distribution centered at 470.49 THz with a standard deviation of 14 GHz, similar to the distribution in Ref. 130.

Fig. 3.15a shows the dependence of the linewidths on the femtosecond laser pulse energy, where the dotted line is a linear fit to the data. A Pearson's $\rho = 0.05$ for the fit indicates no significant correlation between ZPL linewidth and pulse energy, in contrast to Ref. 49.

3.5.2 Power dependence

To disentangle inhomogeneous broadening of the linewidths due to spectral jittering (Γ_{in}) from power broadening characterized by the Rabi coupling Ω , we perform a systematic study of the linewidth as a function of resonant power. Following the results presented in Section 3.5.1, we take a Lorentzian spectral diffusion shape characterized by FWHM Γ_{in} : the probability of the emitter frequency being equal to $f^* \in [f^* + df^*]$ is given by the (normalized) Lorentzian function $L(f^* - f_0, \Gamma_{\text{in}}) \cdot df^*$ where f_0 is the average emitter frequency. The occupation of the excited level of a driven two-level system with radiative

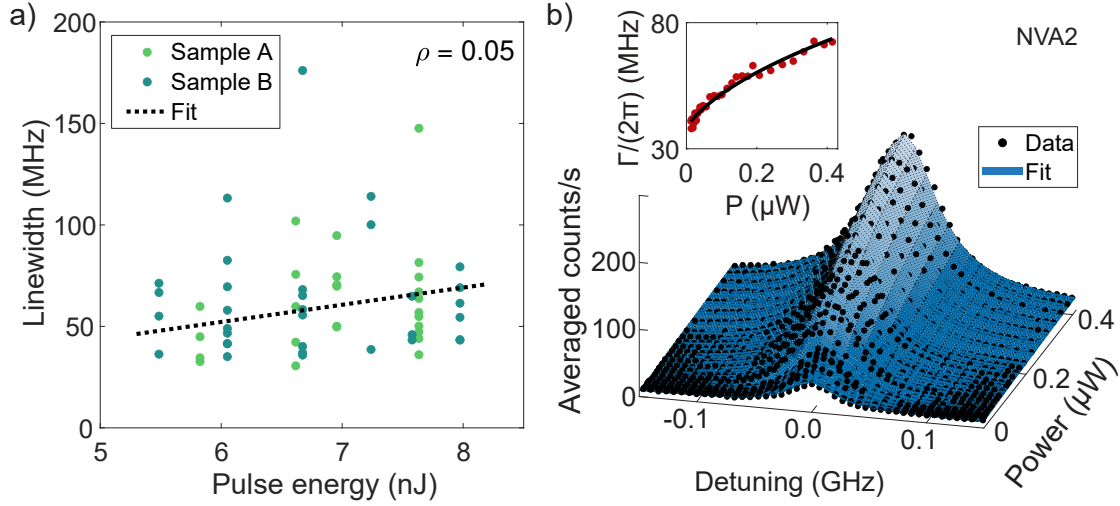


Figure 3.15.: Linewidth dependence on pulse energy and excitation power. (a) Dependence of the linewidths on the laser writing pulse energy. Each data point corresponds to a separate NV, except for a few cases where two lines were measured for one NV. The dotted line is a linear fit with a Pearson's $\rho = 0.05$ indicating little or no correlation between linewidth and pulse energy. (b) Resonant-power dependence of the ZPL of an NV in sample A, fitted according to Eq. (3.2). The inset shows the dependence of the extracted FWHM linewidth on power, fitted following Eq. (3.3) and demonstrating clear power broadening.

decay rate γ is given by¹¹¹

$$\rho_{22} = \frac{\left(\frac{1}{2}\Omega\right)^2}{4\pi^2(f - f^*)^2 + \left(\frac{1}{2}\gamma\right)^2 + \frac{1}{2}\Omega^2} \quad (3.1)$$

where $\Omega = \sqrt{c \cdot P}$, with P the excitation power and c an effective coupling strength which depends on the laser's focal volume, laser incoupling efficiency and the NV's dipole moment and orientation. The experimentally measured line shapes can be described by a convolution of L with ρ_{22} , yielding an expression for the counts as a function of frequency in a PLE measurement:

$$C(f) = \frac{A}{4\pi} \frac{\Omega^2}{\sqrt{\gamma^2 + 2\Omega^2}} \frac{\frac{1}{2}\Gamma}{(f - f_0)^2 + \left(\frac{1}{2}\Gamma\right)^2} \quad (3.2)$$

where A depends on the setup's collection efficiency and the average NV photon emission rate, the "dead" time during the repump pulse and the time spent in the NV^0 charge state, as well as the time spent in spin states that are not cycled with the resonant laser²⁷⁷. The FWHM linewidth is

$$\Gamma = \Gamma_{\text{in}} + \frac{\sqrt{\gamma^2 + 2\Omega^2}}{2\pi} \quad (3.3)$$

where we use $\gamma = 2\pi \cdot 13$ MHz.

Fig. 3.15b shows a PLE measurement as a function of the resonant excitation power. The data is well-fitted with Eq. (3.2). The inset shows the extracted FWHM linewidth as a function of power, fitted with the linewidth described by Eq. (3.3). Power broadening is clearly visible. The full model gives a value of $c = (1.0 \pm 0.1) \cdot 10^5$ $\text{MHz}^2/\mu\text{W}$ for the effective coupling strength and a value of only $\Gamma_{\text{in}} = 25.5 \pm 1.2$ MHz for the inhomoge-

neous broadening.

3.5.3 Linewidth statistics

Fig. 3.16 summarizes the linewidth measurements on samples A, B and C, demonstrating narrow distributions of linewidths. Of the 15, 20, and 14 NVs measured in sample A, B, and C, respectively, 87%, 75%, and 93% showed clear PLE signals. We measure linewidths as narrow as 27.6 MHz, only two times higher than the lifetime limit^{56,57}. The median (mean) linewidths are 58.3 (62.1) MHz, 55.6 (62.1) MHz and 51.2 (74.5) MHz, respectively. The standard deviations (standard errors of the mean) are 23.8 (4.7) MHz, 24.6 (4.3) MHz and 50.3 (8.3) MHz, respectively, when fitting to log-normal distributions¹²⁷. We argue that the median is a better figure-of-merit than the mean, as the linewidth distributions are asymmetric: a few broad-linewidth NVs in the tail of the distribution will increase the mean, but barely affect the amount of preselection needed in any application requiring narrow-linewidth NVs. In this case, the median is more informative, providing the linewidth value for which half of the population is equal or narrower. Combining the data from the three samples yields a median linewidth of 54.9 MHz.

In order to provide a quantitative threshold under which NV linewidths can be described as narrow, we base ourselves on the projected indistinguishability between two ZPL photons – a cornerstone for remote entanglement generation¹⁰⁹. Two-photon interference with high (0.9) visibility can still be obtained despite broadening at the cost of

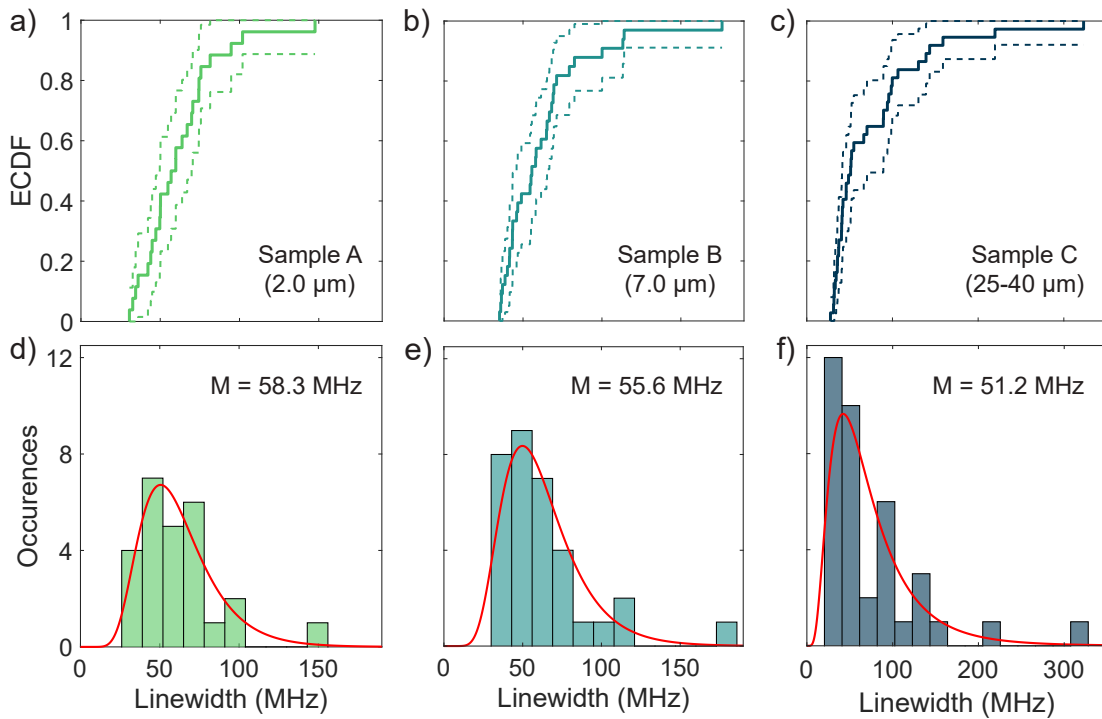


Figure 3.16.: Linewidth statistics. (a)-(c) Empirical cumulative distribution functions (ECDF) over the measured linewidths in sample A, B and C, respectively, with 95% confidence intervals. (d)-(f) Linewidth histograms with log-normal fits for sample A, B, and C. The median is specified for each distribution.

temporal filtering, down to the typical ~ 300 ps timing resolution of silicon single photon counting diodes^{59,156,157}. In our case, we cannot discriminate between broadening due to spectral jumps and broadening due to pure dephasing. Considering the latter as the sole contribution leads to the worst-case scenario, in which temporal selection is technically possible for measured linewidths $\lesssim 150$ MHz.

The empirical cumulative distribution functions (ECDF) in Fig. 3.16a-c show that from the measured distributions, there is a probability above 90% of measuring a linewidth below 150 MHz for each of the three samples. Combining all the data, there is a 96% chance of measuring a linewidth below 150 MHz. This emphasizes the excellent optical quality and low charge-noise environment of the created NVs. Similar probability values are obtained by using a Bayesian approach for analyzing linewidth distributions¹²⁷; with this approach, we determine the probability that the next measured line has a linewidth below 150 MHz of 99.2%, 99.1%, and 92.2% for sample A, B, and C, respectively. With the same approach we also calculate the probability that the median of the distributions is below this threshold, giving a probability of above 99.9% for each of the three samples. The higher mean linewidth of the NVs in sample C could be related to the fact that in this case, the writing was performed deeper inside the diamond where it is particularly difficult to avoid spherical aberrations (even with the corrective capability of the objective lens), such that more lattice damage and therefore sources of charge noise are created compared to the other two samples.

3.6 Further characterization of laser-written NVs

We further characterize the laser-written NVs by studying the time-dependence of the excited-state PLE as a function of the resonant excitation power, and correlate the results with a measurement of the transverse strain experienced by the NVs.

3.6.1 Time-dependent PLE

Early studies demonstrated the long charge-state stability of laser-written NVs⁴⁹. We quantify the charge- and spin-state stability of NVs in sample B by measuring the peak counts in a PLE measurement as a function of the readout time, keeping the charge- and spin-state resetting pulse length constant. We first quantify the power broadening experienced by an NV in sample B by recording the PLE linewidth as a function of power, shown in Fig. 3.17a. The peak PLE counts as a function of time for a resonant excitation power of 360 nW are shown in Fig. 3.17b. We fit the decay of the counts $C(t)$ with

$$C(t) = A \cdot \frac{1 - e^{-\gamma^d(t-t_0)}}{t - t_0} + B \quad (3.4)$$

where γ^d is the decay rate and A and B are fitting constants. The fit gives a decay rate of $\gamma^d = 46$ kHz; the same is done for a number of other powers, shown in the inset.

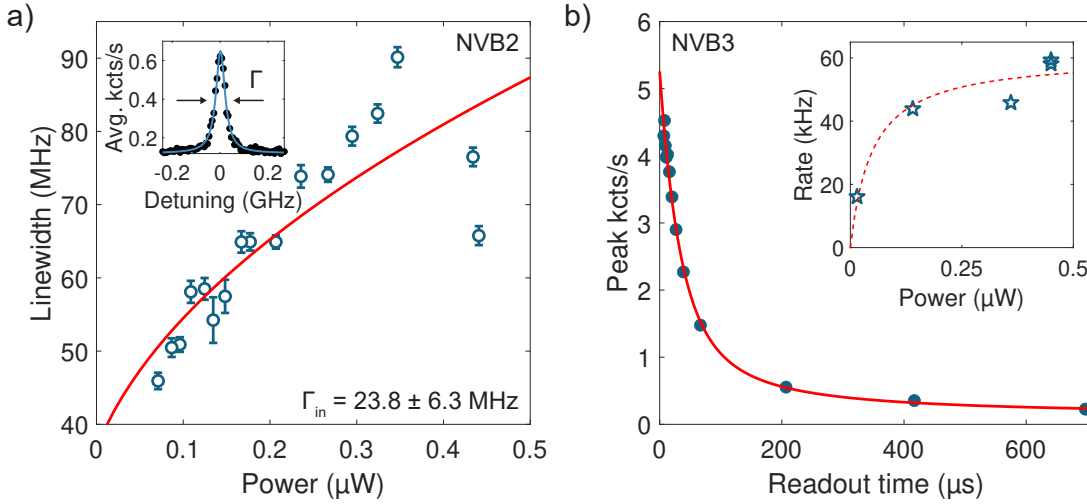


Figure 3.17.: Power dependence and shelving rate study. (a) Power dependence of the linewidth of NVB2. The fit yields an inhomogeneous linewidth of 23.8 ± 6.3 MHz. The inset shows a PLE measurement at the lowest power, giving a linewidth of 45.9 ± 1.1 MHz. (b) Dependence of the peak PLE counts on the readout time for NVB3, for a power of 360 nW. The inset shows the extracted shelving rate for different powers.

We fit the decay rate as a function of power according to

$$\gamma^d(P) = \gamma_{sat}^d \cdot \frac{P}{P + P_{sat}} \quad (3.5)$$

where P_{sat} is the saturation power and γ_{sat}^d the saturation decay rate. Here, we use a toy model that accounts for incoherent excitation of the NV's excited state followed by spin-shelving at a rate of $\gamma_{sat}^d/2$. The obtained rates of 16-59 kHz indicate a decay process happening faster and at lower power density than what is usually observed for ionization^{144,278}. This observation motivates the attribution of the decay to weakly allowed spin-flipping transitions and subsequent shelving into the ground state spin sub-levels with $m_s = \pm 1$.

We compare the obtained rates with Ref. 144, where spin-flip rates (at saturation) of approximately 150 kHz for a low-strain NV and approximately 400 kHz for a moderately strained NV were demonstrated. From this, we can conclude that our spin-flip rates point towards low transverse strain values. A further indication is that the measured NV shows two peaks with similar linewidth in the PLE measurement (41.6 MHz and 41.4 MHz), split only by 1.4 GHz; attributing the lines to the E_x and E_y transitions of the same NV would indicate that the NV in question experiences little transverse strain⁸².

3.6.2 Transverse strain

In order to characterize the transverse strain experienced by laser-written NVs, we follow the procedure described in Ref. 86. NVs are excited off-resonantly with 532 nm continuous-wave illumination close to saturation and the emitted PSB photons are recorded on an APD as a function of an external magnetic field. The magnetic field is aligned to the NV-axis using a three-axis vector magnet and the experiment is performed

in a closed-cycle cryostat at a temperature close to 4 K. As a function of the magnetic field in such a measurement, NV PL shows reductions in intensity at values corresponding to the ground-state anticrossing (GSLAC, at around 100 mT) as well as one or several excited-state anticrossings (ESLACs). The reduced PL intensity stems from the fact that the GSLAC and the ESLACs result in spin mixing, leading to a higher probability for population shelving into the NV's dark singlet state. The magnetic fields at which the ESLACs occur depend on the exact transverse strain and electric field that an NV experiences (here, the combination of the electric field and stress is treated as one effective field), giving a direct way to measure the transverse strain level experienced by an NV.

The results of such a measurement on two laser-written NVs, referred to as NVB4 and NVB5, is shown in Fig. 3.18. We use a rate-equation model¹⁸⁶ to fit the data, applying the transition rates presented in Ref. 92 and assuming a field dependence given by the excited-state Hamiltonian in Ref. 38 (introduced in Section 2.1.1.1). We leave the transverse strain δ_{\perp} (given by the two orthogonal strain components via $\delta_{\perp} = \sqrt{\delta_x^2 + \delta_y^2}$) and a small misalignment angle θ_B of the magnetic field to the NV quantization axis as free parameters. Additionally, the relative excitation efficiency into the E_x and E_y orbitals and a scaling constant for the measured background counts is included. The fit gives a low transverse strain of 4.7 GHz for NVB4 and a similarly low strain of 4.8 GHz for NVB5. (NVB4 was also measured in PLE, resulting in a ZPL linewidth of 176 MHz.)

We use the model to attribute PL dips to specific ESLACs. As illustrated in Fig. 2.2a, transverse strain and an electric field split the NV's excited state 3E into six sublevels, grouped into the E_x and the E_y orbital branch. Each transition in the branch can further be labeled according to its spin nature, meaning that E_y^0 corresponds to the orbital E_y branch and the $m_s = 0$ spin sublevel.

The leftmost dip in both Fig. 3.18a and Fig. 3.18b can be attributed to the $E_y^0 \leftrightarrow E_y^{+1}$

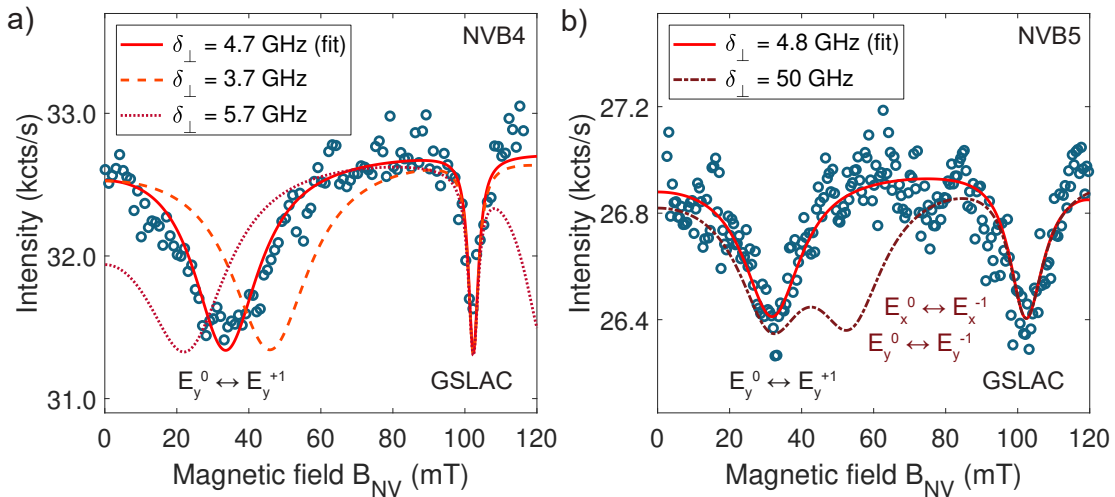


Figure 3.18.: Measuring the transverse strain of laser-written NVs. (a) PL as a function of magnetic field for NVB3. A fit yields a transverse strain value of 4.7 GHz; fitting the data with a lower strain value of 3.7 GHz or a higher strain value of 5.7 GHz while keeping the other fitting parameters constant illustrates how the $E_y^0 \leftrightarrow E_y^{+1}$ ESLAC is sensitive to the exact transverse strain experienced by the NV. (b) PL as a function of magnetic field for NVB4. A fit yields a transverse strain value of 4.8 GHz; fitting the data with a high strain value of 50 GHz while keeping the other fitting parameters constant does not reproduce the number of PL dips in the dataset.

ESLAC. This ESLAC is highly sensitive to the exact strain experienced by the NV, as demonstrated by the two dashed lines in Fig. 3.18a. This applies under the assumption that the strain experienced by the NV is lower than approximately 15 GHz: at higher transverse strain values, both the $E_y^0 \leftrightarrow E_y^{-1}$ and the $E_x^0 \leftrightarrow E_y^{-1}$ ESLAC occur at magnetic fields lower than the GSLAC. As demonstrated by the dashed line in Fig. 3.18b, this yields a splitting in the leftmost PL dip and does not reproduce the measured data. This demonstrates that the transverse strain must be below 15 GHz for both of the NVs and constitutes a strong indication that laser writing results in low stress in the vicinity of the created NVs.

3.7 Towards laser-written NVs in thin structures

In Section 3.5.3, we demonstrated that laser-written NVs experience low charge noise in bulk. For most photonic applications, however, the low charge noise needs to be maintained also in microstructures, requiring a certain degree of etching which is known to degrade the optical quality of NVs⁵⁸. A possible way to circumvent this problem is to perform laser writing directly into a thinned-down diamond membrane. Here, we explore both options: we measure linewidths after etching a bulk laser-written sample to a thin membrane, and attempt laser writing directly into such a thin membrane.

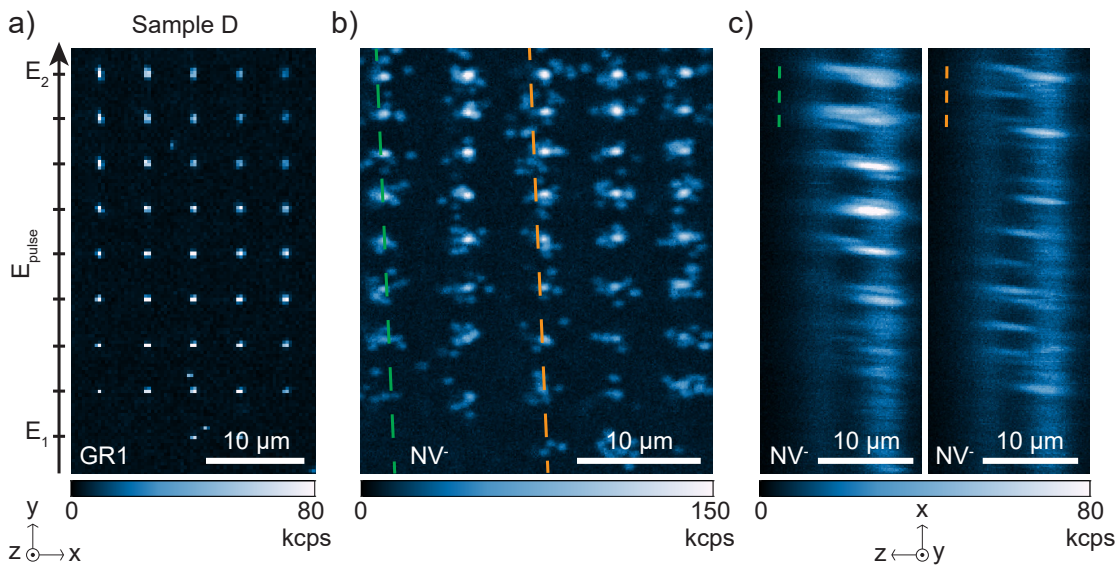


Figure 3.19.: A thinned-down laser-written sample. (a) GR1 array before annealing. Pulse energies between $E_1 = 14.5 \text{ nJ}$ and $E_2 = 23.6 \text{ nJ}$ were used to create the vacancies. (b) NV array after annealing and subsequent etching to a $6 \mu\text{m}$ thick membrane. (c) Cross-sections of the array in (b), showing the distribution of NVs across the membrane.

3.7.1 Linewidths after etching

We investigate the first approach, etching after laser writing, by first creating vacancies (Fig. 3.19a) and subsequently NVs in a bulk sample, referred to as sample D, and then etching it to a 6 μm thick membrane (Fig. 3.19b-c). We etch using inductively-coupled reactive ion etching (ICP-RIE, Sentech ICP 500) with a combination of O_2 and Ar/Cl_2 plasmas. We use an O_2 plasma with 60 sccm, 1.3 Pa O_2 under 700 (50) W source (RF) power and an Ar/Cl_2 plasma with 40/25 sccm, 1.0 Pa Ar/Cl_2 under 400 (100) W source (RF) power. In the membrane, we measure PLE as described in Section 3.5.1; the results are shown in Fig. 3.20.

We measure a FWHM Lorentzian median (mean) linewidth of 122 (187) MHz. The resulting mean is higher than previously reported values for bulk laser-written NVs in Ref. 49 and approximately two times higher than the data presented in Section 3.5.3. Nevertheless, the median linewidth is still below the figure of merit of 150 MHz for achieving two-photon interference with high visibility (see Section 3.5.3), and we can extract a probability of 57.7% that the next measured line has a linewidth below 150 MHz¹²⁷. We can conclude that the low charge noise levels of laser-written NVs reported in bulk diamond are reasonably maintained also in 6 μm thick structures.

Further etching of the same sample to $\sim 3 \mu\text{m}$ thickness resulted in an absence of NV PL due to issues during the particular etching process. A repeated study of the linewidths after etching to a thickness below 6 μm is therefore needed in order to conclude on the charge-noise levels in even thinner diamond.

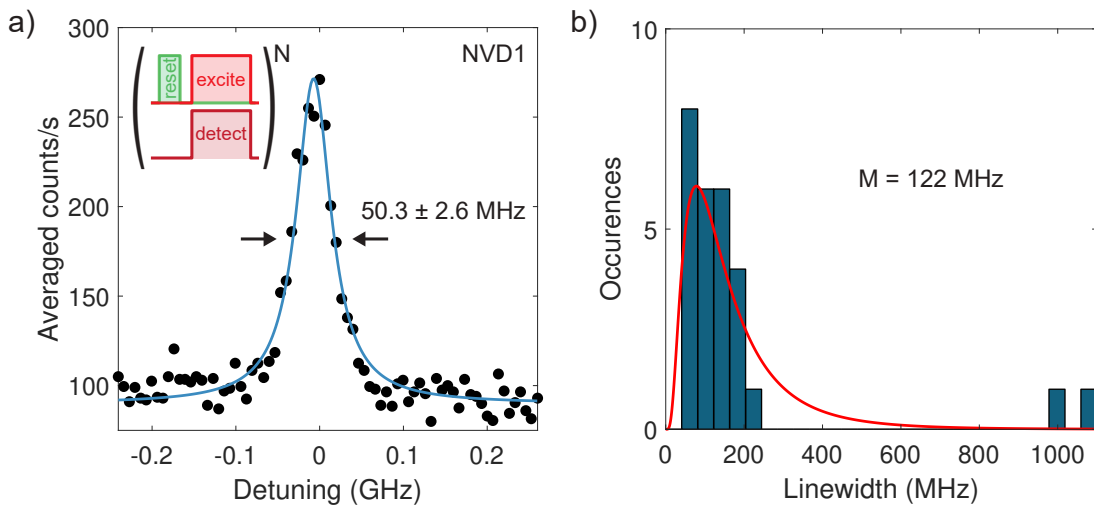


Figure 3.20.: Linewidth statistics after etching. (a) Example PLE measurement on an NV in sample D, with an extrinsically broadened linewidth of $50.3 \pm 2.6 \text{ MHz}$, fitted to a Lorentzian. The inset shows the measurement sequence, which is the same that was used for the data presented in Section 3.5.1. (b) Histogram over the measured linewidths in a 6 μm thick membrane together with a log-normal fit. The distribution has a median of 122 MHz.

3.7.2 Laser writing into thin structures

Creating low-charge-noise NVs via laser writing directly into a thin membrane would avoid the deleterious effects that etching has on existing NVs. However, as motivated in Section 3.3.1 and experimentally shown in Section 3.4.4, the intensities at the surface increase as one focuses closer to a diamond-air interface. This either leads to graphitization of the diamond surface, or gives donut-shaped features in PL intensity that do not result in NVs after annealing. The case is improved in an inverse geometry, as demonstrated in Fig. 3.12, but relies on writing into a bulk sample. Laser writing close to the top surface is limited to a minimal distance of approximately $2\ \mu\text{m}$.

We explore the possibility of laser writing directly into thinner diamond by fabricating a microstructure thick enough to allow for laser writing without damaging the bottom or top diamond surface. We locally etch a $30\ \mu\text{m}$ thick bulk sample, referred to as sample E, through the aperture of a quartz mask to a membrane thickness of $4\text{--}6\ \mu\text{m}$ using the etching process described in Section 3.7.1. The mask geometry and position results in a thickness gradient – the membrane is thinner in the center compared to at the edges. We laser-write an array at the interface between the bulk- and membrane region (Fig. 3.21a). GR1 PL is detected at the exposure sites. After annealing to 1100°C , however, no NV PL is detected (Fig. 3.21b). Only after a repeated annealing process, this time reaching a temperature of 1200°C , an array can be resolved (Fig. 3.21c). We detect spectral signatures of NV^- (Fig. 3.21g), representing the first time that laser writing of NVs has successfully been performed directly into a diamond microstructure.

Figure 3.21d demonstrates an array laser-written completely inside the membrane. Again, annealing to 1100°C results in no NV^- emission (Fig. 3.21e), and annealing to 1200°C gives a higher PL intensity on the exposure sites (Fig. 3.21f). However, spectra taken at bright spots (Fig. 3.21h) are ambiguous, lacking the features expected for NV^- . A probable reason is that the membrane location is thinner than the location shown in Fig. 3.21a at which laser writing was successful. By fitting the amplitude modulation seen in the spectrum in Fig. 3.21h, we extract a diamond thickness of $4.6\ \mu\text{m}$, which is less than the maximal thickness of approximately $6\ \mu\text{m}$ measured along the edges of the membrane. Further studies are needed to determine the exact minimum thickness that allows for laser writing directly into microstructured diamond under the specified conditions.

3.8 Conclusions and outlook

In conclusion, we have demonstrated that a t-SIL significantly lowers the threshold pulse energy for vacancy generation in bulk diamond, and enables laser-induced vacancy creation with pulse energies as low as $5.8\ \text{nJ}$. This result points to the feasibility of using a standard Ti:sapphire ultrafast laser without the need for a regenerative amplifier for vacancy creation in diamond. There is a large window in pulse energies before the pulse creates irreversible damage. We interpret this wide range of useful pulse energies as a consequence of working in the tunneling breakdown regime for vacancy creation. The

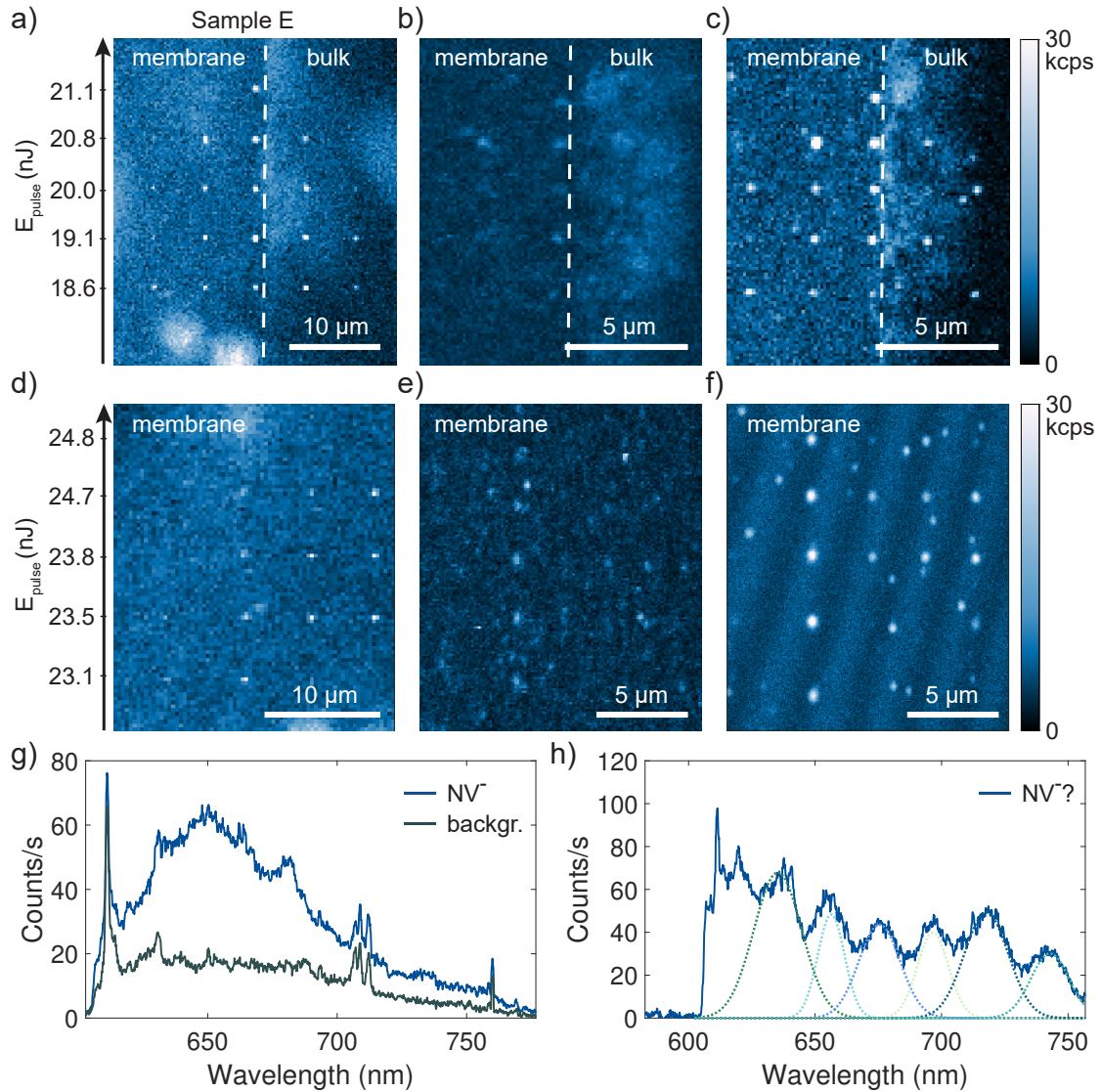


Figure 3.21.: Laser writing into a diamond membrane. (a) GR1 array written across the interface between a 6 μm thick membrane and a 30 μm thick bulk region. (b) The array in (a) after annealing at 1100°C. (c) The array in (a) after annealing to 1200°C. (d) GR1 array written in a 6 μm thick membrane. (e) The array in (d) after annealing to 1100°C. (f) The array in (d) after annealing to 1200°C. (g) Spectrum from a bright spot in (c). A background spectrum is inserted for reference. (h) Spectrum taken on a bright spot in (f). The modulation of the intensity comes from interference of light within the diamond microstructure. A fit of the amplitude modulation (dotted lines) yields a membrane thickness of 4.6 μm .

vacancies can be created across the full depth of 40 μm bulk diamond samples.

We measure a median NV optical linewidth as low as 54.9 MHz. An estimated 96% of the NVs have an extrinsically broadened linewidth below 150 MHz, illustrating that laser writing yields an exceptionally high probability of generating narrow-linewidth NVs as compared to standard implantation and annealing^{108,127,130}. This metric is crucial for applications based on spin-photon entanglement as it is greatly beneficial to perform experiments with minimal pre-selection of NVs. The narrow linewidths, with the narrowest being only two times higher than the lifetime-limit, suggest reduced damage in the vicinity of the NVs compared to other NV creation methods. To the best of our knowledge, this

is the lowest charge noise measured to date including the full effects of the off-resonant charge-state repump^{49,108,128}.

We show that the low charge noise is maintained also after etching a laser-written sample to 6 μm thickness, with an increase in the median to only 122 MHz. This is a key step toward implementing laser-written NVs into photonic structures to increase their coherent photon flux. Finally, we demonstrate that laser-written NVs exhibit low transverse strain levels and low spin-flip rates, crucial for implementing high-fidelity single-shot spin readout. In a broader context, the high-optical-quality NVs created through laser writing present attractive candidates for any application requiring low charge-noise, spectrally stable NVs.

The NV positioning accuracy is currently limited by the diffusion of vacancies during annealing, with the high annealing temperatures required to anneal out residual defects in the lattice. Better positioning accuracy in depth could be achieved by incorporating delta-doped nitrogen-rich layers in the diamond¹³⁴. In addition, it has recently been shown that three-dimensional regular arrays of spin-coherent qubits based on NVs can be created via laser writing²⁷⁹. With the demonstrated possibility of graphitization of diamond using the same femtosecond laser^{280,281}, carbon-based electrodes are within reach, as are laser-written waveguides^{282,283} and integrated photonic circuits²⁸⁴. Another promising route of investigation is laser writing into more dedicated structures, such as diamond platelets^{269,270,285} for implementation into open microcavities^{58,60–62,64}, waveguiding structures such as pillars^{96,97} for NV-based sensing⁹⁵, or SILs^{145,146} for increased collection efficiencies.

4

LOW-NOISE NVs IN DIAMOND FORMED BY CARBON IMPLANTATION

The content of this chapter is partially adapted from:

V. Yurgens, A. Corazza, J. A. Zuber, M. Gruet, M. Kasperczyk, B. J. Shields, R. J. Warburton, Y. Fontana, and P. Maletinsky. **Spectrally stable nitrogen-vacancy centers in diamond formed by carbon implantation into thin microstructures.** *Applied Physics Letters* **121**, 234001 (2022).

4.1 Summary

The NV in diamond, with its exceptional spin coherence and convenience in optical spin initialization and readout, is increasingly used both as a quantum sensor and as a building block for quantum networks. However, the high refractive index of diamond together with the long radiative lifetime and low Debye-Waller factor of the NV leads to a low flux of useful photons in these applications. Employing photonic structures for maximizing the photon collection efficiency typically leads to broadened optical linewidths for the emitters, which are commonly created via nitrogen ion implantation. With studies showing that only nitrogen atoms native to the diamond lattice contribute to optically coherent NVs, a natural conclusion is to either avoid implantation completely, or to substitute nitrogen implantation by an alternative approach to vacancy creation. Here, we demonstrate that implantation of carbon ions yields a comparable density of NVs as implantation of nitrogen ions, and that it results in NV populations with narrow optical linewidths and low charge-noise levels even in thin diamond microstructures. We measure a median NV linewidth of 150 MHz for structures thinner than 5 μm , with no trend of increasing linewidths down to the thinnest measured structure of 1.9 μm . We propose a modified NV creation procedure in which the implantation is carried out after instead of before the diamond fabrication processes, and confirm our results in multiple samples implanted with different ion energies and fluences.

4.2 Introduction

Applications in quantum communication³² and quantum sensing²⁸⁶ involving NVs rely on optical initialization and interrogation of the spin state, meaning that an efficient optical interface is critical. For NVs deep in the bulk, the solution has so far been to employ solid immersion lenses^{145,146}, which improve the collection efficiency by up to a factor of 10 over unstructured diamond but do not increase the small NV ZPL fraction. Approaches based on optical resonators such as open microcavities^{58,60–64,147,268} shorten the radiative lifetime, increase the fraction of photons emitted into the ZPL, and improve the collection efficiency, but require more extensive diamond microfabrication. For quantum sensing, the common approach to increase the collection efficiency is to use waveguiding photonic structures as scanning probes^{96,97}, an approach which also requires considerable diamond microstructuring.

On account of its permanent electric dipole moment, the NV's excited state is sensitive to charge noise and thus prone to optical linewidth broadening. In micro- and nano-fabricated diamond, remaining lattice damage from implantation as well as surface and subsurface charge traps introduced during etching conspire such that extrinsically broadened linewidths reaching up to several GHz are observed^{58,287–290}. Furthermore, studies have shown that NVs created from implanted nitrogen exhibit worse optical properties compared to NVs created from diamond-native nitrogen and irradiation-induced vacancies, in that they form a separate, broad-linewidth distribution^{127,130}. This has led to a number of studies exploring different NV creation methods where nitrogen ion implantation is avoided, including laser writing⁴⁹ (see Section 2.2.2 and Chapter 3) and electron irradiation¹²⁸. Such approaches have resulted in improved NV optical coherence in bulk and few-micron-thick diamond, but at the cost of loss of depth control (electron irradiation) and the need for specialized setups (laser writing). In general, NV linewidths have been shown to increase drastically for structure thicknesses less than $3.8\ \mu\text{m}$ ¹²⁸, with only a few cases of narrow lines reported in thinner structures^{127,291}.

In this study, we explore a refined method of NV creation, in which we avoid implantation of nitrogen ions and instead use $^{12}\text{C}^+$ implantation to generate vacancies²⁹². The NVs are formed by recombination of the created vacancies with native nitrogen in the diamond lattice. Using carbon as a substitute for nitrogen retains the ability to form NVs with nanoscale depth resolution (unlike electron irradiation or laser writing), without producing a broad-linewidth population (unlike nitrogen implantation). Using $^{12}\text{C}^+$, which has a mass comparable to $^{15}\text{N}^+$, for the implantation further ensures that the depth distribution of vacancies is very similar to the one created by implantation of nitrogen. Since the lattice consists mainly of ^{12}C , this further ensures that no heteroatoms are introduced into the lattice. In contrast to prior work, we opt for implantation post-fabrication (IPF), implanting the ions *after* fabrication of the microstructures, following the approach used by Ref. 127. The rationale behind this reversal is to avoid exposing already formed NVs to the potentially deleterious effects of fabrication, in particular the aggressive dry etching steps and electron beam lithography^{293,294}.

4.3 Sample preparation

We fabricate our samples from electronic-grade $\langle 100 \rangle$ single-crystal diamond ([N] < 5 ppb, [B] < 1 ppb, Element Six), and follow a previously developed fabrication procedure^{58,285,295}. 500 μm thick diamond is laser-cut and polished (Almax Easy Lab, Belgium) to yield $\sim 50 \mu\text{m}$ samples. Polishing-induced sub-surface damage is removed by etching away $\sim 5 \mu\text{m}$ of the surface by an interleaved Ar/Cl₂ and O₂ plasma, resulting in diamond samples with a smooth surface that are used as starting material. The ensuing main steps of the process flow are illustrated in Fig. 4.1.

4.3.1 Diamond microfabrication

First, a lithographic mask is deposited onto the top surface of the diamond by spin coating a negative photoresist (FOx-16, Dow Corning) as well as a conductive protective coating (Electra 92). Electron beam lithography (30 keV) followed by development in TMAH creates a microstructure pattern in the resist. A subsequent ICP-RIE process with an O₂ plasma transfers the pattern approximately 2.5 μm into the diamond. The mask is stripped by a dip in hydrofluoric acid (HF). A 10 nm/50 nm Cr/Au layer is then evaporated onto the top surface in order to protect it during the ensuing deep ICP-RIE etching of the back surface with interleaved Ar/Cl₂ and O₂ plasmas. We use the same ICP-RIE parameters as in Section 3.7.1. The deep etching is carried out through the aperture (typically 1-by-1 mm², not illustrated) of a quartz mask until the structures within the aperture become free-standing. A combination of the etching process, mask geometry and mask position results in a thickness gradient: the structures in the center of the aperture are up to several microns thinner compared to the structures at its edges. The thickness gradient varies in its extent from sample to sample.

Once the microstructures have been created and the protective layer stripped, a thinner Cr/Au layer (5 nm/10 nm) is evaporated at a slight angle onto the back surface to reduce charging during implantation. Finally, ¹²C⁺ is implanted into the microstructures from the front side at an angle of 7° (InnovIon Corp.). NVs are created after stripping the metal layer and performing a multi-step annealing process similar to the one described in Ref. 295 (4 hours at 400°C, 10 hours at 800°C, 2 hours at 1200°C, with one hour of ramping between each step) in a home-built high-vacuum oven (starting pressure $< 10^{-6}$ mbar). As a last step (not illustrated), the diamond is cleaned in a boiling 1:1:1 solution of sulfuric, perchloric and nitric acid for two hours in order to remove graphitic residues and oxygen-terminate the surface.

Following this procedure, we fabricate three samples, denoted sample A, B, and C. Samples A and B have square, 20-by-20 μm^2 microstructures and sample C has rectangular, 5-10 μm wide and 50-100 μm long microstructures.

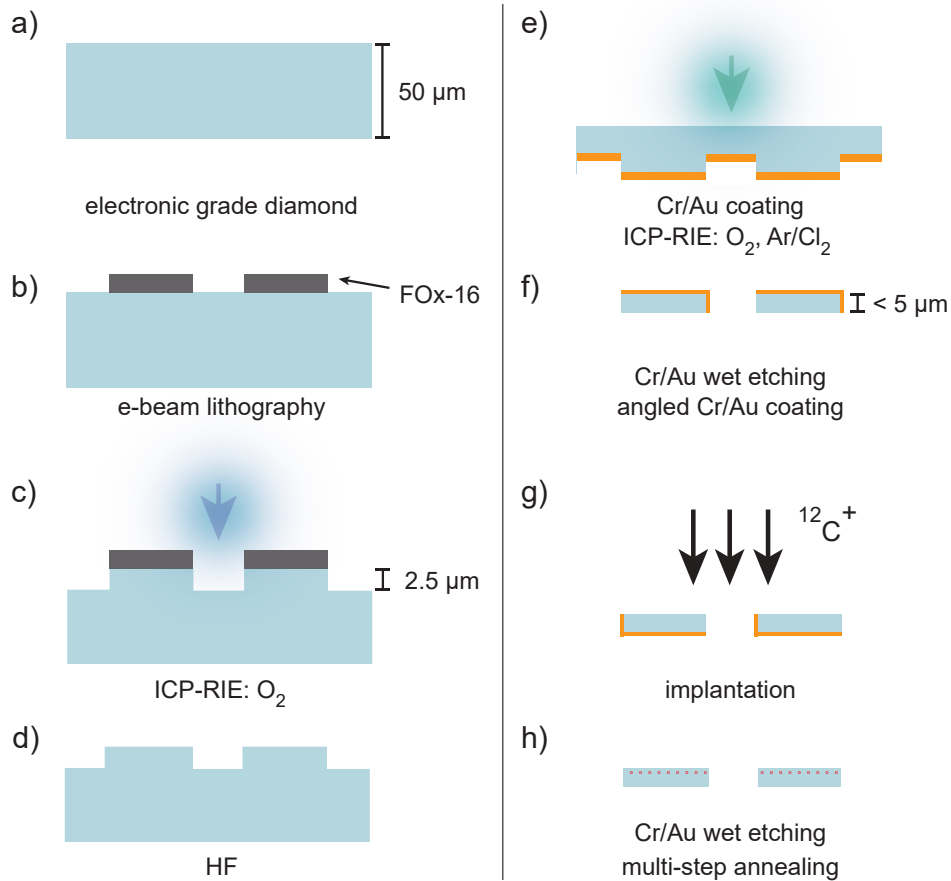


Figure 4.1.: Diamond microfabrication process. (a) The starting material is a $\sim 50\ \mu\text{m}$ thick electronic-grade diamond. (b) Electron beam lithography transfers the pattern into the diamond after (c) ICP-RIE etching with an O_2 plasma. (d) Hydrofluoric acid strips the resist. (e) Protected by an evaporated metal layer, the diamond is subsequently thinned down by ICP-RIE with interleaved Ar/Cl_2 and O_2 plasmas. (f) The protective metal layer is stripped and another layer is evaporated under an angle onto the opposite side to reduce charging during implantation. (g) $^{12}\text{C}^+$ is implanted into the structures. (h) NVs are created after stripping of the metal layer and a multi-step annealing.

4.3.2 Ion implantation

We use Stopping and Range of Ions in Matter (SRIM) methods to simulate the distribution of ions and vacancies inside the diamond and to compare the implantation of $^{15}\text{N}^+$ to implantation of $^{12}\text{C}^+$ for different implantation energies. As can be seen in Fig. 4.2, SRIM simulations show that the ion and vacancy distributions after implantation of $^{12}\text{C}^+$ differ only very marginally from those following implantation with $^{15}\text{N}^+$. For both 12 keV and 50 keV implantation energy, the difference in implantation depth of ions (vacancies) inside the diamond, defined as $\Delta_{15\text{N}} = |d_{15\text{N}} - d_{12\text{C}}|$ with d the depth corresponding to the maximum of the distributions, results in a relative depth difference $\Delta_{15\text{N}}/d_{15\text{N}}$ below 20% (15%).

We choose the implantation energies 12 keV and 50 keV for two different purposes: the former to create shallow NVs suitable for optomechanics experiments requiring coherent, near-surface NVs in cantilevers²⁹⁶, and the latter to create deeper NVs located

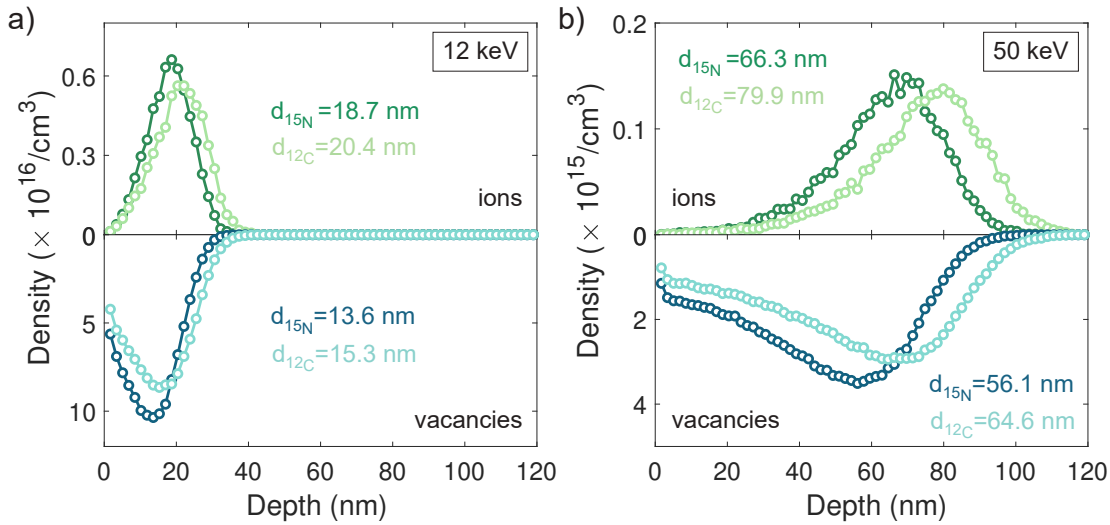


Figure 4.2.: SRIM simulations for implantation of $^{15}\text{N}^+$ and $^{12}\text{C}^+$. (a) SRIM-simulated density of implanted ions (top) and resulting vacancies (bottom) for an implantation energy of 12 keV, as a function of the depth in diamond. A fluence of $1 \cdot 10^{10}$ ions/cm² was used for the simulations. The depths corresponding to distribution maxima are stated for the two different ion species. (b) Same data as in (a), but for an implantation energy of 50 keV. Note the difference of approximately one order of magnitude in density.

at a vacuum electric field antinode in an open microcavity⁵⁸. As seen from the figure, we expect the majority of the resulting NVs created via implantation of $^{12}\text{C}^+$ to be distributed between 15.3 nm and 20.4 nm for an energy of 12 keV, and between 64.6 nm and 79.9 nm for an energy of 50 keV. According to our simulations, the expected vacancy yield per implanted ion is virtually the same for carbon and nitrogen when implanting with 12 (50) keV: 74 (175) vacancies/ion for $^{15}\text{N}^+$ and 68 (151) vacancies/ion for $^{12}\text{C}^+$.

Sample A and B are both $^{12}\text{C}^+$ -implanted with an energy of 50 keV and a fluence of $5 \cdot 10^8$ ions/cm², while sample C is implanted with an energy of 12 keV and a fluence of $1 \cdot 10^{10}$ ions/cm².

4.4 NV characterization

We image the created emitters using a home-built confocal microscope, where we use a 532 nm diode-pumped solid-state laser for samples A and B and a 515 nm diode laser module for sample C for off-resonant excitation while detecting the resulting photoluminescence (PL) after filtering by a long-pass filter (Semrock, 594 nm RazorEdge) on an APD (Excelitas). Figure 4.3 shows brightfield images as well as confocal scans of representative regions on the three samples. We identify emitters located in different regions on the three samples, characterize the structure thickness in each region, and determine the NV linewidth by photoluminescence excitation (PLE).

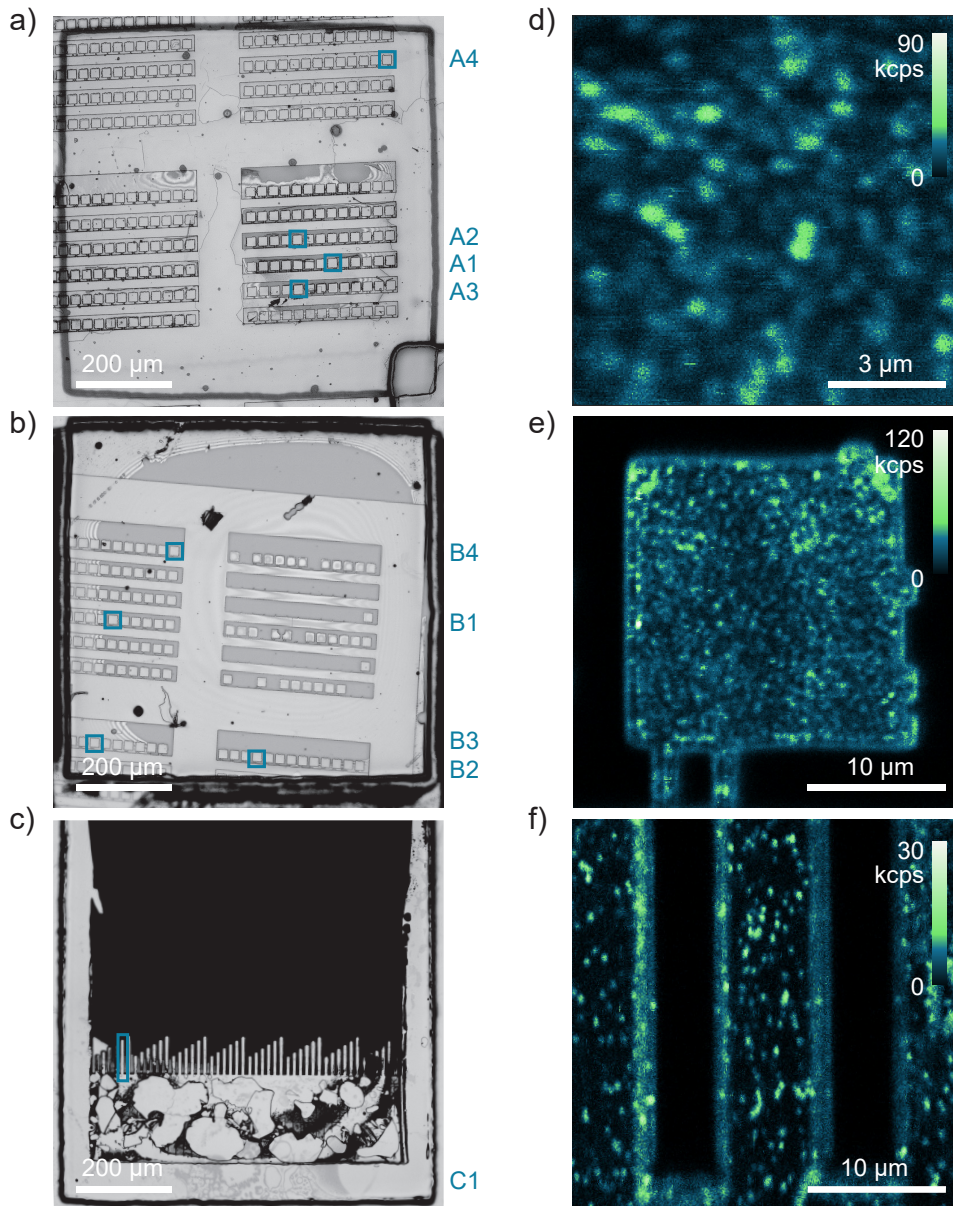


Figure 4.3.: Sample overview. (a)-(c) Brightfield microscope images of samples A-C, respectively, with labels indicating the regions which were sampled for linewidth measurements. The areas shown in the images correspond to the apertures in the quartz masks used in the etching process. (d-f) Representative confocal fluorescence image of NVs in region A2, B1 and C1, respectively.

4.4.1 Structure thickness determination

We record NV PL spectra on a cryogenically cooled CCD camera coupled to a grating spectrometer (Princeton Instruments). An example spectrum is shown in Fig. 4.4a. The thickness of the measured microstructures is determined either from the spectra by fitting the amplitude modulation of the NV's PSB arising from interference in the diamond, or by direct measurement with a commercial laser confocal microscope (Keyence VK-X1100). We choose measurement sites on the three samples covering a range of different thicknesses. The chosen regions are indicated in Fig. 4.3a-c: in sample A, thicknesses

span 1.9-4.6 μm , and in sample B 1.9-4.9 μm . The free-standing microstructures in sample C are 2.5 μm thick and we also measure in a neighboring bulk region with a thickness of approximately 50 μm (not indicated).

4.4.2 Photoluminescence excitation

We characterize the NV ZPL optical linewidths through PLE measurements in either a liquid helium bath (CryoVac) or a closed-loop cold-finger (attocube attoDRY800) cryostat, following the procedure described in Section 3.5.1. Typical resonant laser powers are on the order of 100 nW, which leads to a power broadening of up to three times the homogeneous linewidth yet remains marginal, approximately 30 MHz, compared to our measured linewidths (see Section 3.5.2).

An example PLE measurement from the average of 100 scans is shown in Fig. 4.4b. The residual PLE background arises via leakage of photons generated during the green repump pulse into the counting window. We note that by systematically using an off-resonant green initialization pulse, our experiment yields a measurement of the extrinsically broadened linewidths, i.e., linewidths including spectral jumps caused by the repump pulses. We assume that NVs created via implantation in microstructured diamond experience more spectral diffusion compared to NVs created from native nitrogen and therefore fit the PLE data with Gaussian lineshapes.

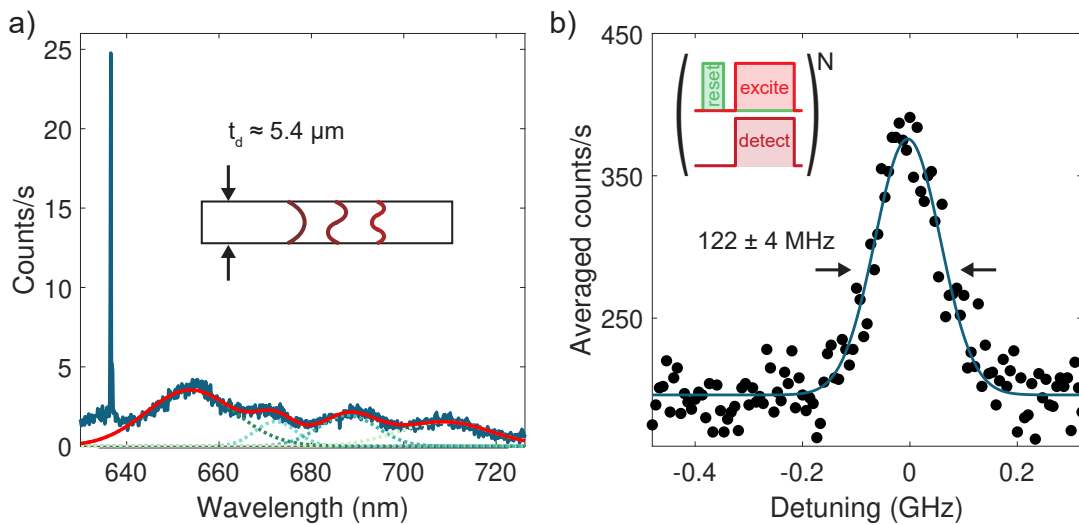


Figure 4.4.: Linewidth determination. (a) PL of an NV in sample A. The PSB has been fitted to extract the wavelengths that give constructive interference within the microstructure (dotted lines), in turn providing the structure thickness (5.4 μm). The inset illustrates the etaloning effect allowing for thickness determination. (b) PLE of the NV in (a). The inset shows the measurement sequence, which is the same that was used for the data presented in Section 3.5.1. A fit of the data with a Gaussian lineshape yields a FWHM linewidth of 122 ± 4 MHz.

4.4.3 Linewidth statistics

Figure 4.5 summarizes the measured PLE linewidths in samples A, B, and C. We measure a median (mean) Gaussian-fitted full width at half maximum (FWHM) linewidth of 143 (227) MHz, 138 (181) MHz and 304 (691) MHz for the three samples, respectively. The data are well-described by log-normal distributions¹²⁷.

We define NV linewidths as narrow if they are $\lesssim 150$ MHz, following the argumentation in Section 3.5.3: with a linewidth equal to or smaller than 150 MHz, two-photon interference with a high (0.9) visibility can still be achieved with silicon APDs when using temporal filtering^{59,156,157}.

In samples A and B, which we group as the two samples with the same implantation parameters, 54% of the measured linewidths are below 150 MHz. In sample C, only 26% of the linewidths are below 150 MHz, and the median linewidth is about two times higher compared to the other samples. This difference can be explained by the shallower implantation depth of sample C and a correspondingly larger contribution of surface-related charge noise to the linewidth broadening²⁸⁹. For the three samples combined, including bulk, we measure 48% of linewidths below 150 MHz.

Comparing the measured linewidths to the ones presented in Section 3.5.3, we can conclude that the linewidth distributions from NVs created via carbon IPF exhibit a higher median compared to laser-written NVs. Nevertheless, the linewidths presented

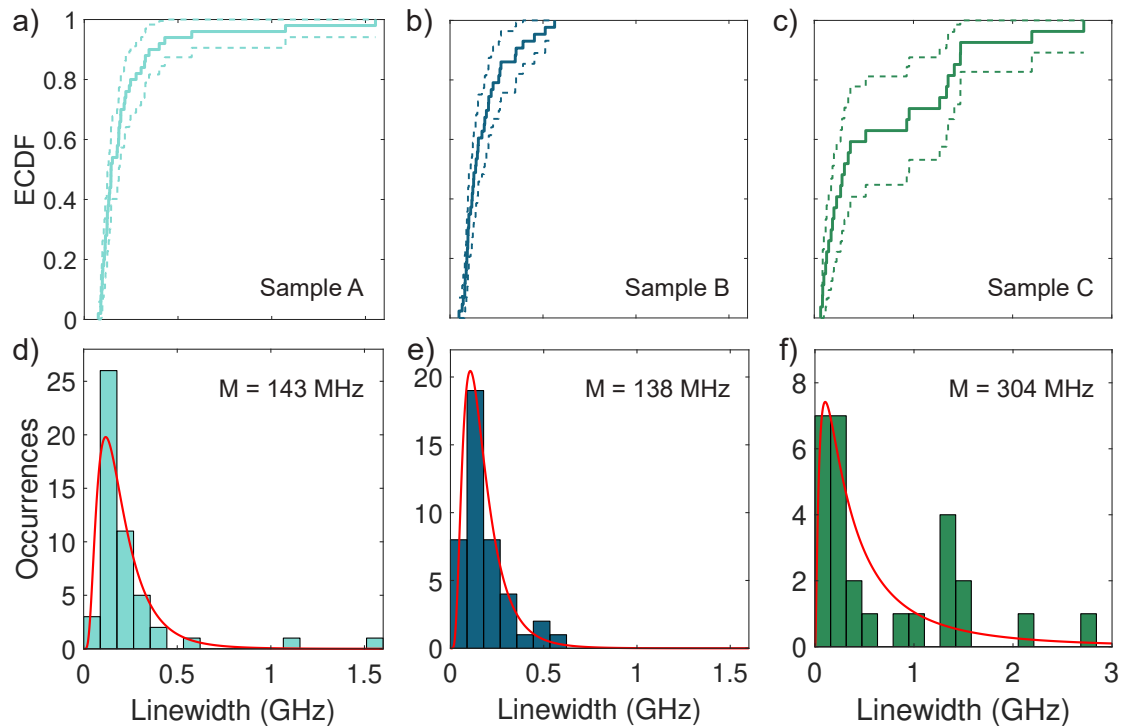


Figure 4.5.: Linewidth statistics. (a)-(c) Empirical cumulative distribution functions (ECDF) over the measured linewidths in sample A, B, and C, respectively, indicating the fraction of measured linewidths below or equal to a certain value. The dashed lines represent a 95% confidence interval. (d)-(f) Linewidth histograms with log-normal fits for sample A, B, and C. A bin width of 89 MHz (158 MHz) has been used for sample A/B (C). Solid red lines represent log-normal fits and the median M is stated for each distribution.

here have been measured on structures considerably thinner than those created after laser writing. The results thus still present an important step toward optically coherent, narrow-linewidth NVs in microstructured diamond.

4.4.4 Linewidth as a function of structure thickness

Figure 4.6 shows the measured linewidth data sorted according to sample and region. The data is summarized in Fig. 4.7, demonstrating the statistical changes in linewidths as a function of the thickness of the measured structure. There is no general trend of

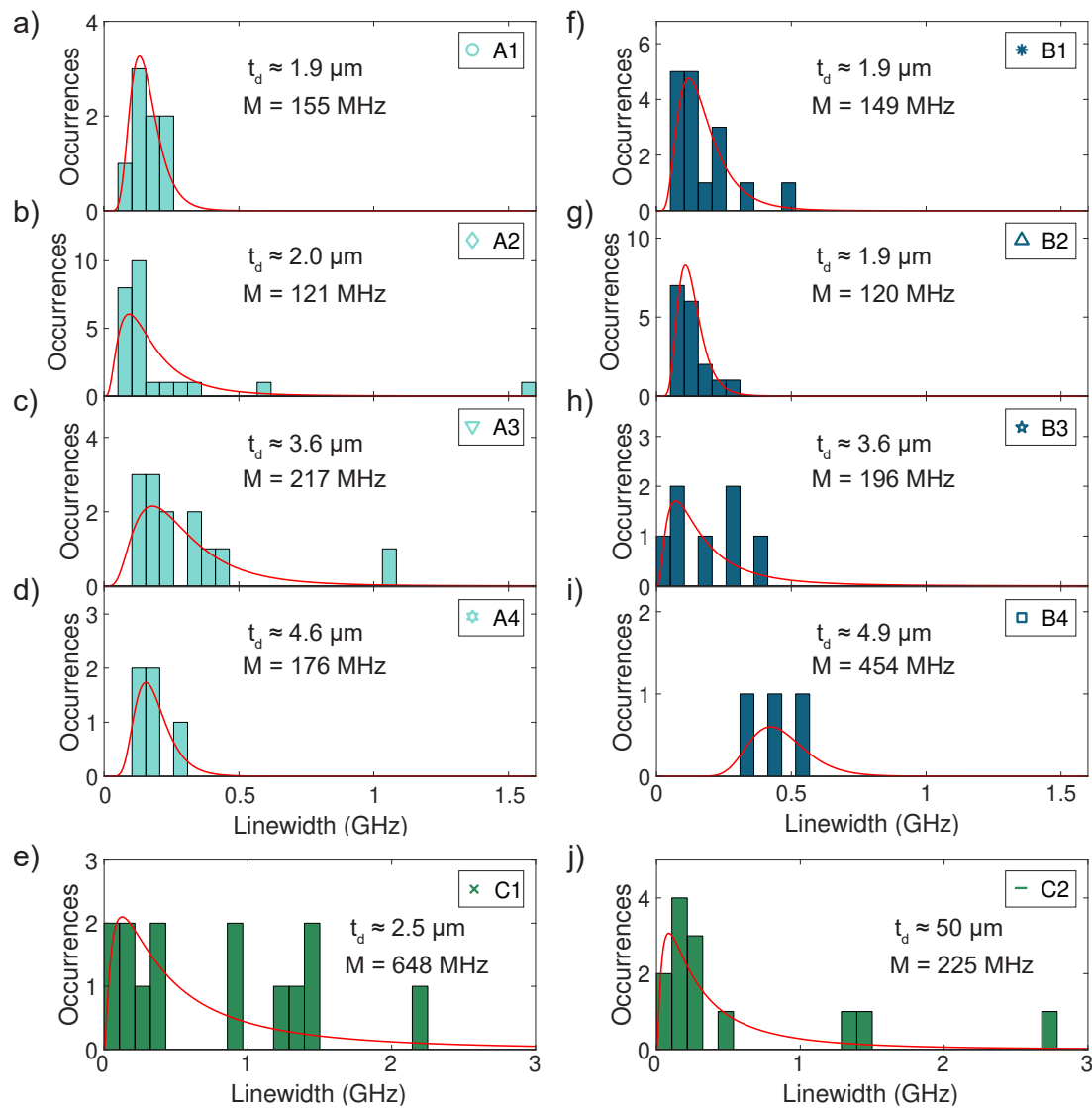


Figure 4.6.: Linewidth statistics for each sample region. (a)-(d) Histograms over the measured linewidths for sample A in region A1, A2, A3, and A4, respectively. The bin width is 52 MHz. (f)-(i) Histograms over the measured linewidths for sample B in region B1, B2, B3, and B4, respectively. The bin width is 52 MHz. (e),(j) Histograms over the measured linewidths for sample C in region C1 and C2. The bin width is 107 MHz. Solid red lines represent log-normal fits. The diamond structure thickness t_d is stated for each sample region, together with the median M of the linewidth distribution.

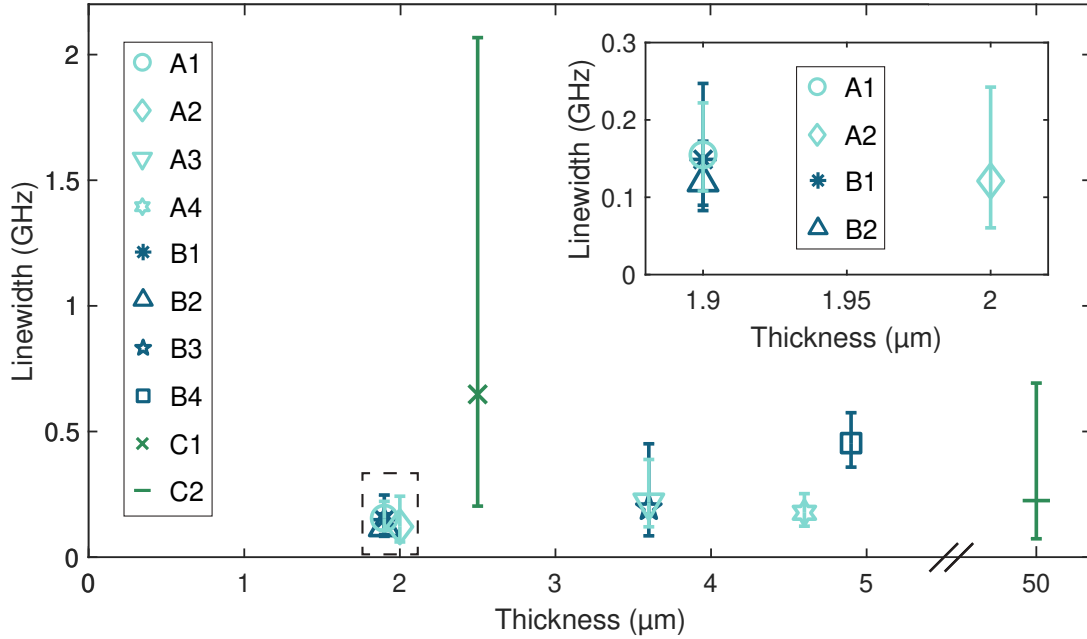


Figure 4.7.: Median linewidth as a function of diamond thickness. The error bars correspond to the geometrical standard deviation of a log-normal fit to each distribution. The data points are labelled according to the sample and corresponding microstructure, in order of increasing thickness within each sample. The inset shows a close-up of the median linewidths of the four thinnest microstructures.

increasing mean (not shown) or median linewidth with decreasing structure thickness, in contrast to previous studies^{58,128}. Sample C shows broader lines than the other two samples regardless of the sampled thickness, which we attribute to the shallower NV depth in this sample.

Considering all the sampled microstructures, spanning 1.9-4.9 μm in thickness, 52% of the NVs have a linewidth below 150 MHz. No thinner regions were created on samples A and C. On sample B, the fraction of NVs exhibiting optically addressable ZPLs dropped significantly for structures less than 1.9 μm thick, which precluded further studies. We note that extrinsically broadened linewidths below 250 MHz have previously not been measured consistently in diamond microstructures thinner than 3.8 μm ^{127,128,291}. IPF with nitrogen as employed by Ref. 127 described a few cases of narrow linewidths in thin structures; as we show here, going one step further and substituting nitrogen for carbon avoids the formation of broader-linewidth NVs from implanted nitrogen and therefore results in only the native-nitrogen, narrow-linewidth NV distribution.

We speculate that a possible explanation for the positive effect of IPF on NV optical linewidths is that the dynamics of NV formation are affected by preexisting lattice damage. Performing etching and electron beam lithography on structures with existing emitters imposes lattice damage on the complete structure, while implantation after the microfabrication might preferentially create emitters on sites with less lattice disorder. Dedicated studies are however required to single out the effect of IPF from carbon substitution alone.

4.5 Conclusions and outlook

In conclusion, we demonstrate that carbon IPF creates NVs with on average lower charge-noise and reduced spectral diffusion compared to other NV creation approaches. We show that substituting nitrogen with carbon during implantation results in similar NV densities for moderate implantation fluences that allow optical isolation of single emitters. We measure narrow linewidths with high probability: 48% of the measured NVs have an extrinsically broadened linewidth below 150 MHz, and this applies across the full measured range of diamond microstructure thicknesses down to 1.9 μm . We show that by implanting an ion species other than nitrogen, the creation of NVs displaying extreme linewidth broadening is avoided, confirming earlier conjectures^{127,130}. Moreover, we demonstrate that our method is easy to implement, is reproducible and provides an advantage over conventional fabrication methods for different samples and implantation parameters.

Our method should prove useful for any application relying on optically coherent NVs, both in bulk and in microstructured diamond. As an example, coupling the emission of such NVs (~ 150 MHz linewidth, ~ 2 μm thick microstructure) to an open microcavity with a finesse of a few thousand would increase the fraction of photons emitted into the ZPL by more than an order of magnitude⁵⁸ (see Chapter 5). This would dramatically improve the generation rate of entangled qubit pairs and remove an important roadblock toward quantum networks beyond few-node prototypes.

5

PURCELL-ENHANCEMENT OF A LOW-NOISE EMITTER IN DIAMOND

5.1 Summary

The NV in diamond is an extremely attractive qubit due to its spin properties, but possesses sub-optimal optical properties hindering quantum communication. Only a small fraction of all the emitted photons are emitted into the ZPL, the radiative lifetime is long and the extraction of photons out of diamond is hampered by its high refractive index. Here, we demonstrate an efficient photonic interface with an NV inside an open optical microcavity, mitigating these problems. We use a 1.6 μm thick diamond membrane with NVs created via carbon implantation post-fabrication (IPF) and measure ZPL count rates as high as 140 kcts/s under off-resonant excitation, more than four times higher than the state of the art. The increase in the flux of coherent photons is achieved by means of Purcell-enhancement, increasing the fraction of photons emitted into the ZPL from $\sim 2.6\%$ to 48% with an overall Purcell-factor of 1.9. Furthermore, by efficient suppression of the resonant excitation, we successfully measure resonance fluorescence from an NV. This is the first demonstration up to date of NV resonance fluorescence with a signal-to-background ratio higher than 1 that does not rely on temporal filtering. We extract an NV linewidth of 159.0 MHz, confirming the results shown in Chapter 4 and demonstrating once again that carbon IPF yields narrow-linewidth NVs even in microfabricated thin diamond. At our maximum available power, we measure a mean resonance fluorescence count rate of 43 kcts/s. Projecting the current system efficiency to applications relying on double-click protocols for spin-spin entanglement, our platform would increase the entanglement success probability by more than an order of magnitude, and by more than two orders of magnitude with feasible system improvements. The resonant readout, together with the narrow NV linewidths and the associated reduced experimental overhead, establishes the NV-cavity system as an attractive photonic interface and opens up its use in a wide range of applications in the area of quantum communication.

5.2 Introduction

The NV center in diamond, possessing a direct link between its long-lived spin state^{36,37,119} and a photon³⁸, with convenient spin state manipulation via microwaves and optical spin initialization and readout^{43,144}, is an attractive spin qubit. How-

ever, its optical properties result in a low flux of useful photonic qubits for quantum communication^{11,54}. A way to increase the coherent photon flux is to place an NV-containing diamond membrane inside an open microcavity^{58,60–64} – a platform enabling efficient mode-matching to external optics and tuning of the cavity resonance to the emitter, as well as funneling of the emission into the cavity mode. Compared to other photonic structures designed to increase the photon flux such as SILs^{145,146}, the open microcavity has the advantage of increasing the fraction of coherent emission. Compared to photonic crystal cavities (PCCs)^{297,298}, the advantage is the minimal required diamond microfabrication^{58,147,259,268–270}, preserving the bulk-like properties of the emitters to a large extent.

The open microcavity as a spin-photon interface presents certain challenges: a balance has to be found between the maximal thickness of the diamond structure (preserving the optical properties of the emitter) and the maximal Purcell-enhancement (generally decreasing with the diamond thickness). Furthermore, the diamond surface roughness introduces scattering losses and makes it difficult to achieve optimal cavity performance^{172,259,269,270,299,300}. Operating in a diamond-in-cavity configuration at room temperature, a cavity finesse of at most 17 000¹⁴⁷ has been achieved. The transition to cryogenic temperatures (~ 4 K) generally leads to reduced cavity performance, with the best implementation so far yielding a finesse of 5 300⁵⁸. Until now, NV-cavity systems have been used to demonstrate Purcell-enhancement of the NV emission^{58,61–63,259}, but have fallen short in efficiently extracting the emitted photons.

An additional challenge is to achieve ZPL readout under resonant excitation: in any quantum entanglement operation, only coherent photons can be employed as photonic qubits. So far, efficient resonant excitation and readout of NVs has been made possible via temporal filtering and polarization-based suppression of the excitation light, using a SIL for increased collection efficiency^{11,12,54,155}, or via coherent scattering at low laser powers³⁰¹.

In this work, we use a low-charge-noise NV created via carbon IPF and couple its emission to a high-finesse cavity at low temperature. Shortening of the emitter's radiative lifetime gives evidence of a Purcell-enhancement. Under off-resonant excitation, we record ZPL count rates far surpassing the current state-of-the-art photonic interfaces based on SILs. Finally, polarization-based suppression of the resonant excitation light enables resonance fluorescence on a cavity-coupled NV to be detected without relying on temporal filtering, establishing the platform as an efficient photonic interface for quantum applications.

5.3 Experimental setup

To enhance the flux of useful photons from an NV, we use an open, Fabry-Perot-type plano-concave microcavity. We incorporate ~ 2 μm thick diamond membranes with NVs made via carbon IPF and operate the system at room temperature and at low (~ 4 K) temperature.

5.3.1 Cavity assembly

The open microcavity consists of a planar bottom mirror and a concave top mirror. We excite and collect through the top mirror, which is designed to be the preferential direction of photon leakage by having a higher, approximately 10 times, transmission compared to the bottom mirror. Figure 5.1a shows the cavity assembly.

The bottom mirror rests on a stack of cryogenic piezo-driven nanopositioners (attocube, ANPx51, ANPx51 and ANPz51), enabling three-axis positioning of the bottom mirror with respect to the top mirror. The stack is placed in a small home-built titanium cage. The top mirror, attached to a titanium frame, is fixed to the small titanium cage with spacers made out of indium. Once the mirrors are positioned within a few wavelength's distance from each other, interference of incoming light gives rise to Newton rings. This repeating concentric pattern of dark and light fringes is centered around the point of contact between the mirrors, and so by centering this pattern, the tilt of the top mirror can be adjusted and the parallelity of the two mirrors improved. Another stack of nanopositioners with a larger range of motion (attocube, ANPx101, ANPx101 and ANPz101) moves the small titanium cage with respect to the collection and excitation axis.

The entire assembly is placed into a large home-built titanium cage; light is coupled in and out of the cavity through an objective (Microthek, 20x/0.4) mounted at the top of the large cage. The system can be positioned either right below external optics at room temperature, or suspended at the bottom of a non-magnetic steel "skeleton" for cryogenic measurements. The skeleton is inserted into a steel tube which is evacuated and subsequently filled with 25 mbar He exchange gas to ensure good thermalization of the sample. The tube is immersed in liquid helium in a bath cryostat, with optical access possible through a laser window (Thorlabs, WL11050-C11).

The cavity mirrors are made by coating 5-by-5 mm², 525 μm thick SiO₂ substrates with a distributed Bragg reflector (DBR) consisting of alternating λ/4-thick layers of SiO₂ and Ta₂O₅. Both mirrors are terminated with Ta₂O₅ layers, which we refer to as high-index termination (H-termination). In order to be able to reach as short mirror separations as possible, 2.5 μm high mesas are etched into the top mirror, see Fig. 5.1b. This reduces the area of the top and bottom mirror that goes into close contact and so reduces the risk of obstruction due to particles between the mirrors.

On each mesa, a curved surface is made via laser ablation following a previously developed method^{302,303}. This results in multiple useful cavities on each mirror chip. The laser ablation process is based on focusing the output of a CO₂ laser (λ ≈ 10 μm) for 10-100 ms on a low-surface-roughness SiO₂ substrate, upon which thermal evaporation, melting and re-solidification occurs, producing a smooth crater with a roughness of approximately 0.2 nm rms. For a given σ_{sc} rms roughness of the crater surface, scattering losses can be estimated with

$$S \approx \left(\frac{4\pi\sigma_{sc}}{\lambda} \right)^2, \quad (5.1)$$

giving about 16 ppm scattering losses at the NV ZPL wavelength of 637 nm²⁶¹.

We characterize the laser-ablated curved surface on each mesa with a confocal laser scanning microscope (Keyence, VK-X1000). The measured profile, shown in the inset in

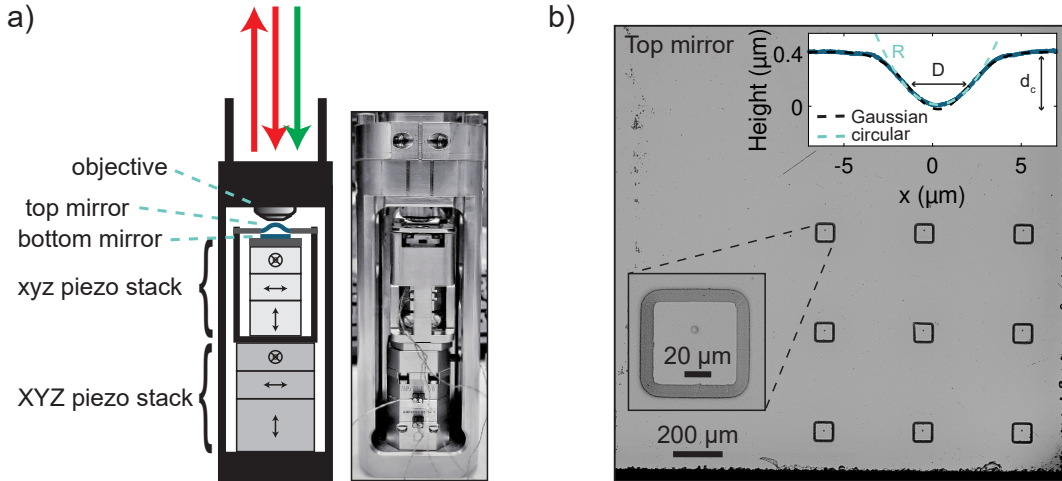


Figure 5.1.: A tunable open microcavity. (a) The cavity assembly. One xyz-piezo actuator stack moves the bottom mirror with respect to the top mirror. Another xyz-piezo actuator stack moves the entire cavity with respect to the objective. (b) A top mirror with 10 mesas, each containing a laser-ablated crater. Inset, bottom left: magnified image of one of the mesas. Inset, top right: a Gaussian and circular fit of the curved crater profile.

Fig. 5.1b, can be approximated by a Gaussian:

$$z(r) = d_c \cdot e^{-r^2/\sigma^2} \quad (5.2)$$

where d_c is the depth of the crater²⁶¹. The full width $1/e$ gives an approximation for the useful mirror diameter D , outside of which clipping losses introduce losses to the cavity performance. Within the clipping radius, the profile is well-approximated by a spherical surface; its radius of curvature (ROC) R defines the mirror curvature. The crater depth, diameter and radius are related via $d_c \approx D^2/8R$. Astigmatism of the CO₂ laser beam leads to a slight asymmetry, or ellipticity (typically around 5%), of the cratered craters²⁶¹. This is one of the factors contributing to the anisotropy of a cavity, resulting in each cavity resonance being split into a linear polarization doublet³⁰⁴.

5.3.2 Diamond sample

We use $\sim 2 \mu\text{m}$ thick diamond platelets with NVs created via carbon IPF. For details regarding the sample fabrication, see Section 4.3. We implant $^{12}\text{C}^+$ at an angle of 7° with an implantation energy of 50 keV and a fluence of $5 \cdot 10^8 \text{ cm}^{-2}$ in order to form NVs at a depth $\approx 66 \text{ nm}$. For H-terminated mirrors, this is the depth corresponding to an intra-cavity field antinode and maximal NV-cavity coupling strength (see Section 2.3.4.3).

Figure 5.2 demonstrates how thin glass capillaries attached to micromanipulators are used to break out and transfer individual diamond platelets from a patterned diamond sample onto a cavity bottom mirror. The broken-out platelets typically show interference fringes indicating poor bonding to the mirror (Fig. 5.2a, top right panel). After laterally translating the structures on the mirror surface until good contact is achieved between the structure and the mirror (demonstrated by the absence of interference fringes), the mirror-diamond interface is wetted with deionized water using one of the capillaries

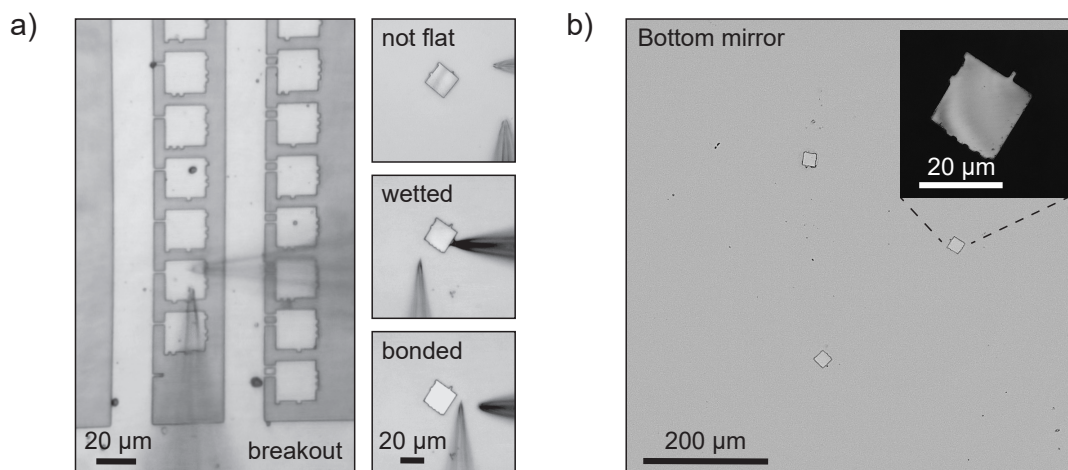


Figure 5.2.: Bonding a diamond platelet to a cavity mirror. (a) Glass capillaries attached to micromanipulators are used to break out diamond platelets and manipulate them on the flat mirror surface until they are bonded. (b) A bottom mirror, with three diamond platelets bonded to it. Inset: magnified image of one of the bonded platelets.

(Fig. 5.2a, center right panel), after which the capillary is retracted. Upon drying of the water (Fig. 5.2a, bottom right panel), the platelet is bonded via van der Waals-forces to the mirror and can no longer be moved using the capillaries. Successful bonding relies on a smooth diamond surface, a smooth mirror surface, and an absence of particles between the diamond and the mirror. Figure 5.2b shows a bottom mirror with three bonded diamond platelets.

5.3.3 Measurement setup

We use a microscope head, schematically illustrated in Fig. 5.3, for measurements at room- and at low temperature. Light is in- and out-coupled from optical fibers using fiber collimators (Schäfter+Kirchhoff, 60FC-L-4-M20L-04 for 532 nm excitation and Schäfter+Kirchhoff, 60FC-SF-4-M20-33 for 637 nm excitation and detection) that are mounted on slip-plate positioners (Thorlabs, SPT1C). The excitation light is filtered depending on the wavelength (Semrock, 530/43 BrightLine HC for 532 nm excitation and Semrock, 630/38 BrightLine HC for 637 nm excitation). A 561 nm long-pass filter (Semrock, 561 LP Edge Basic Longpass Filter) is used in the detection path when the full cavity mode structure is characterized; a 638 nm band-pass filter (Semrock, HC Laser Clean-up MaxLine 638/2,4) is added to exclusively detect ZPL photons and reduce broadband background fluorescence reaching the detector when illuminating with 532 nm light.

Polarization-based extinction of the resonant excitation and alignment of the polarization axis with respect to cavity modes is carried out with a linear polarizer (LP, Thorlabs, LPVISC050), quarter-wave plate (QWP, B. Halle Nachfl. GmbH), half-wave plate (HWP, B. Halle Nachfl. GmbH) and a polarizing beamsplitter (PBS, Thorlabs, PBS25-633). A second PBS is used for imaging by deflecting leakage light onto a CMOS camera (Allied Vision, Guppy Pro F-503 1/2.5"). Broadband illumination is provided by a pigtailed LED (Thorlabs, EP810S04). A dichroic mirror (DM, Semrock, Shortpass Beamsplitter HC 697 SP) separates the broadband illumination from the resonant excitation; another DM

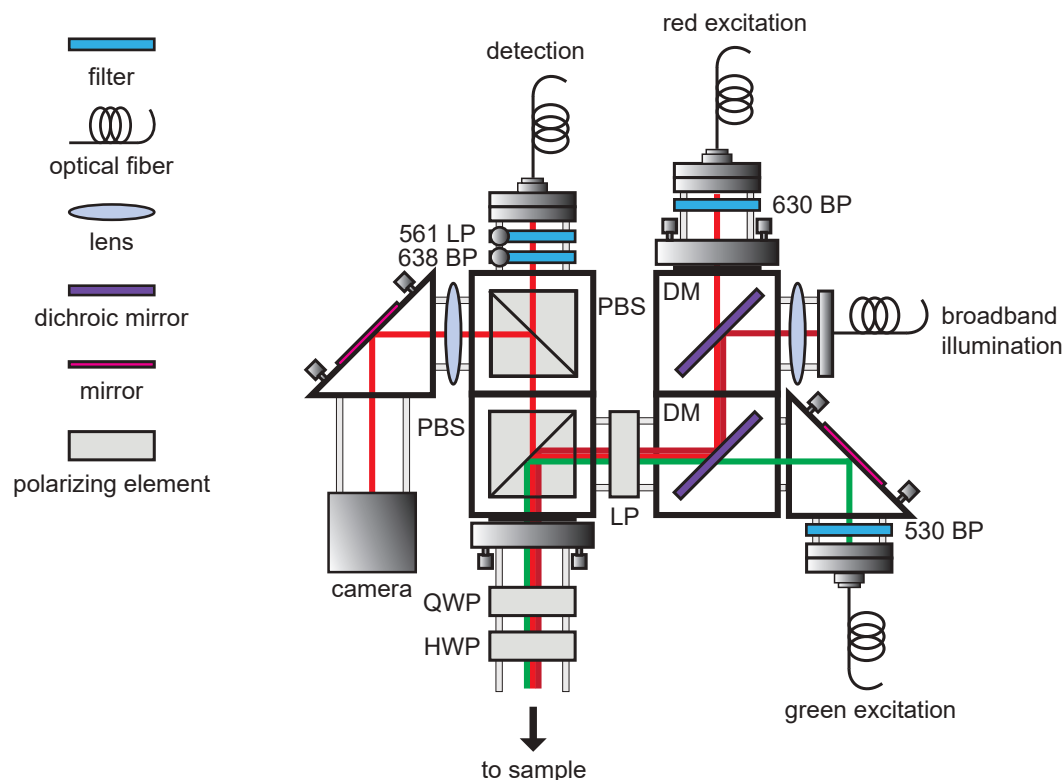


Figure 5.3.: Microscope head allowing for off-resonant green, resonant red and broadband illumination. An LP, PBS and a set of waveplates (QWP and HWP) enable polarization-based extinction of resonant excitation as well as alignment of the excitation polarization axis with respect to the cavity modes and NV dipole.

(Semrock, Shortpass Beamsplitter HC 614 SPUV) separates the green excitation from the red. The full microscope head rests on a tip-tilt stage and is 30 mm-cage compatible.

We use a continuous-wave green laser (Laser Century, GL532N6-2500) or a pulsed supercontinuum source (NKT Photonics, SuperK Extreme EXW-12 or SuperK Fianium FIU-15 PP, operated at 532 nm) for off-resonant excitation. Two tunable red lasers (Newport, Velocity TLB-6704-OI and Toptica Photonics, DL 100/pro), PID-locked to a wavemeter (HighFinesse, Ångstrom WS/U-30U), are used for resonant excitation. The Velocity TLB-6704-OI laser gives a mode-hop-free tuning range of up to 60 GHz between 636 nm and 638 nm and the DL100 Pro laser gives a mode-hop-free tuning range of 2-3 GHz between 632.5 nm and 640 nm. For measurements requiring short durations of interleaved red and green exposure, we use acousto-optic modulators (AOM, Gooch & Housego, AOMO 3200-121) with waveforms provided by an arbitrary waveform generator (AWG, Agilent, 33500B) and monitor the output optical power on photodiodes (PD, Thorlabs, PDA10A2). We use a double-pass AOM configuration in order to achieve high (>60 dB) on/off-ratios in the excitation cycle.

Light collected through the detection path is fiber-coupled and routed either to an avalanche photodiode (APD, Excelitas, SPCM-AQRH-14(15)-FC or SPCM-900-14-FC), PD (Thorlabs, SM05PD1A) or a liquid nitrogen-cooled CCD camera coupled to a grating spectrometer (Princeton Instruments, Acton SP2500). For photon autocorrelation and lifetime measurements, the APD output pulses are sent to a picosecond event timing module (PicoQuant, PicoHarp 300), enabling time-tagging and post-processing of the

data. Tuning of the cavity length is carried out by applying a voltage to the bottom mirror piezo via a low noise, high resolution DAC (Physics Basel, SP 927) used together with a low-noise amplifier (Physics Basel, SP 908). Waveforms for repeatedly sweeping a certain cavity range are generated by another AWG (Keithley, 3390).

Optimal cavity performance at low temperature requires ultra-low mechanical, acoustic and electrical noise. We ensure minimal system vibrations by operating in a super-insulated liquid helium bath cryostat (Precision Cryogenics) and isolate the cavity from mechanical noise by placing the cryostat on a combination of active (TableStable, AVI-200XL/LP) and passive (Newport, VIB320-110180) vibration isolation. We shield the system from acoustic noise by means of a custom-built acoustic enclosure (Accurion).

5.4 Cavity characterization

The main characteristics for the performance of a cavity are the finesse and quality factor (Q-factor), both introduced in Section 2.3.4.1. The finesse can be extracted from the free spectral range $\lambda/2$ and cavity resonance FWHM linewidth Γ_l , both given in units of length, as

$$\mathcal{F} = \frac{\lambda/2}{\Gamma_l}. \quad (5.3)$$

The finesse can also be calculated by expressing the free spectral range and cavity linewidth in units of frequency, but this will not necessarily give the same result as Eq. (5.3) for a cavity with a diamond inside due to the modified mode structure for the coupled system.

The Q-factor can be calculated in units of frequency as

$$Q = \frac{\nu}{\Gamma_\nu} \quad (5.4)$$

denoting the cavity linewidth at frequency ν as Γ_ν (which is related to the cavity loss rate κ via $\Gamma_\nu = \kappa/(2\pi)$).

In order to extract the cavity finesse and Q-factor, we characterize a number of cavity resonances. Under red laser illumination, we apply a sinusoidal displacement to the cavity bottom mirror piezo to repeatedly sweep the cavity length over a certain range, and detect the photons reflected by the cavity on a PD. We use two measurement approaches, referred to as reflection (Fig. 5.4a) and transmission (Fig. 5.4b), to characterize the cavity. Both approaches exploit the fact that light resonant with the cavity acquires a phase shift of π compared to non-resonant light (which is reflected off the top cavity mirror). The interaction of the promptly reflected and the resonant light rotates the global polarization state so that only non-resonant (resonant) light is transmitted to the detector in a reflection (transmission) measurement. This results in a high (low) background signal with dips (peaks) at each cavity resonance in reflection (transmission) (Fig. 5.4c). In a reflection measurement, the shape of the resonance enables optimization of the excitation with respect to the top mirror dimple (misalignment yields a Fano-like lineshape). In a transmission measurement designed to characterize the cavity performance, in the case of non-degenerate orthogonal cavity modes, the HWP needs to be set such that the po-

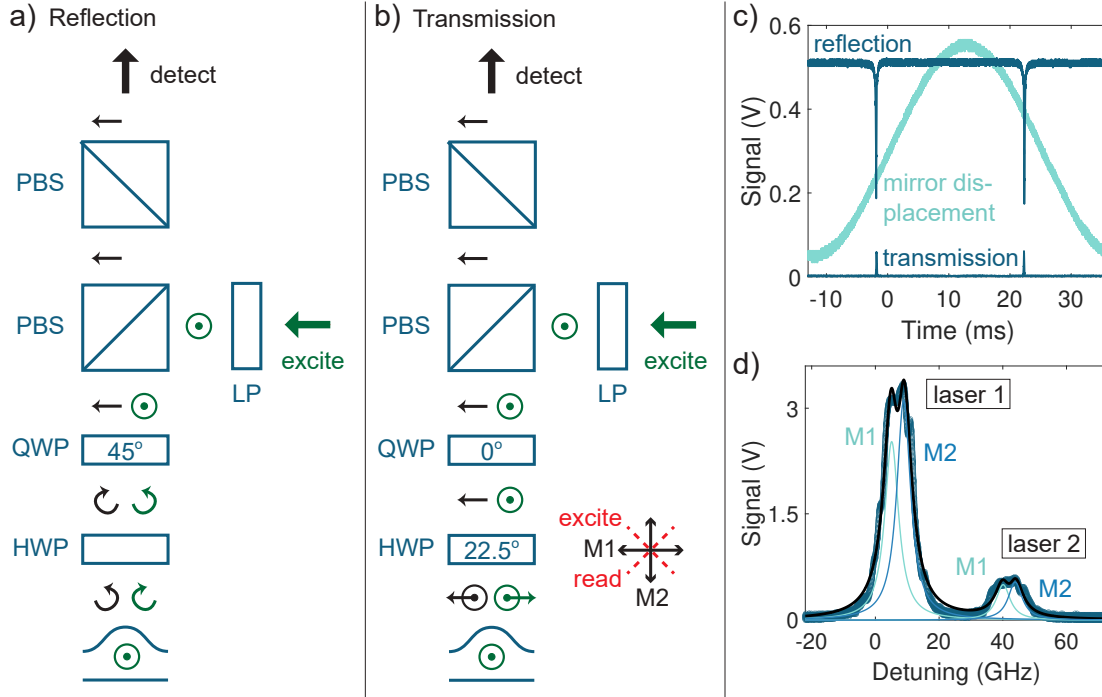


Figure 5.4: Two measurement settings. (a) A reflection measurement. The QWP is set to send circularly polarized light to the cavity. (b) A transmission measurement. The HWP is used to rotate the polarization axis of the incoming linearly polarized light. For optimal excitation and readout, it sets the polarization axis of the incoming light to 45° with respect to each of the cavity modes (M1 and M2). (c) A reflection and transmission signal together with the associated voltage signal applied to change the cavity length. (d) A bare cavity resonance in transmission, measured with two lasers separated by $\nu_{sep} = 30$ GHz. Within each laser resonance, two close-to-degenerate cavity modes (M1 and M2) have been fitted. The fitted FWHM is $\Gamma_\nu = 5.3$ GHz and the mode splitting is $\delta_\nu = 3.8$ GHz.

larization axis of the incoming linearly polarized light lies between the polarizations of the two cavity modes (inset in Fig. 5.4b).

For perfectly degenerate cavity modes, a cavity resonance is described by a single Lorentzian:

$$E(t) = y_0 + A \cdot \frac{\Gamma_t/2}{(\Gamma_t/2)^2 + (t - t_0)^2} \quad (5.5)$$

where y_0 represents the background, A the amplitude, t_0 the center coordinate and Γ_t the full width-half maximum (FWHM) width in units of time. The measured intensity is in this case directly given by the square of the absolute value of the field:

$$I_{deg.}(t) = |E(t)|^2 = E \cdot E^* \quad (5.6)$$

For a certain degree of cavity anisotropy, however, the degeneracy of the cavity modes is lifted. Then, the measured intensity is given not by the sum of the intensities, but the square of the sum of the fields:

$$I_{non-deg.}(t) = |E_{tot.}(t)|^2 = (E_1 + E_2) \cdot (E_1 + E_2)^* \quad (5.7)$$

We denote the FWHM width of each of the non-degenerate modes M1 and M2 by Γ_t , the respective amplitudes by $A_{c,1}$ and $A_{c,2}$, and the mode splitting by δt . We describe the

field from each mode by $E_c(t)$:

$$E_{c,1}(t) = A_{c,1} \cdot \frac{\Gamma_t/2}{\Gamma_t/2 + i(t - t_{0,1})} \quad (5.8)$$

$$E_{c,2}(t) = A_{c,2} \cdot \frac{\Gamma_t/2}{\Gamma_t/2 + i(t - t_{0,2})} \quad (5.9)$$

the square of which gives a Lorentzian. The center coordinates of the two modes are related via $t_{0,1} = t_{0,2} + \delta t$. The measured intensity from a split cavity resonance is then given by

$$I_{meas}(t) = y_0 + (E_{c,1} + E_{c,2}) \cdot (E_{c,1} + E_{c,2})^* \quad (5.10)$$

A fit to a transmission measurement using Eq. (5.10) yields the cavity linewidth Γ_t , the mode splitting δt , and splitting between the resonances t_{sep} in units of time. By simultaneously measuring the transmission signal of two narrow-linewidth lasers, locked to have a known frequency separation ν_{sep} , these parameters can be translated into units of frequency with the conversion factor $\Delta\nu/\Delta t = \nu_{sep}/t_{sep}$ (Fig. 5.4d). This yields the cavity linewidth in frequency,

$$\Gamma_\nu = \Gamma_t \cdot \frac{\Delta\nu}{\Delta t} \quad (5.11)$$

which can be used in Eq. (5.4) to calculate the cavity Q-factor.

In order to calculate the cavity finesse using Eq. (5.3), the cavity linewidth Γ_t needs to be expressed in units of length as Γ_l . For this, the slope $\Delta\nu/\Delta l$ has to be extracted, describing the dependence of a resonance frequency on the cavity length. A way to do this is by sweeping the cavity length over multiple free spectral ranges, exciting background fluorescence with broadband or off-resonant light, and recording the photons leaking out of the cavity on a spectrometer as a function of the bottom mirror displacement. We model this displacement as a function of voltage applied to the piezo actuator with a nonlinear function $D(V)$:

$$D(V) = A \cdot \frac{V}{B - V} \quad (5.12)$$

where A and B are fitting parameters. For small applied voltages, the bottom mirror displacement is linear, while for large applied voltages, the cavity length no longer changes due to the finite range of the piezo actuator.

For a bare cavity, the resulting mode structure is described by

$$\nu = \nu_0 \left(1 + \frac{\Delta m + \frac{2\nu_0}{c}(D(V) - D(V_0))}{m_0 - \frac{2\nu_0}{c}(D(V) - D(V_0))} \right) \quad (5.13)$$

where the resonance frequency ν of a mode with mode number $m = m_0 + \Delta m$ corresponds to an applied voltage V , the resonance frequency ν_0 of a mode with mode number m_0 corresponds to an applied voltage V_0 , and c is the speed of light. More details on Eqs. (5.12) and (5.13) can be found in Section B.1.

For a cavity with a diamond inside, described in Section 2.3.4.2, the mode structure is modified due to the coupling between two cavities: one defined by the bottom mirror and the air-diamond interface, and one defined by the air-diamond interface and the top mirror. Depending on where the highest field intensity is, and whether the field has a

node or an antinode at the diamond-air interface, the resonances can be categorized as air- or diamond-confined for a certain wavelength.

By using a one-dimensional model, assuming lossless mirrors and neglecting the transverse Gaussian extent of the beam as well as the Gouy phase of the cavity mode, the resonance frequencies of the coupled system can be derived as¹⁴⁷

$$\nu \approx \frac{c}{2\pi[L + (n_d - 1)t_d]} \cdot \left\{ \pi m - (-1)^m \cdot \sin^{-1} \left[\frac{n_d - 1}{n_d + 1} \sin \left(\frac{m\pi[L - (n_d + 1)t_d]}{L + (n_d - 1)t_d} \right) \right] \right\} \quad (5.14)$$

Here, m is the mode number, n_d the refractive index of diamond, L the total cavity length (including both the diamond and the air gap), and t_d the thickness of the diamond. More details related to Eq. (5.14) can be found in Section B.2.

From a fit using Eq. (5.13) or Eq. (5.14), the slope $\Delta\nu/\Delta l$ can be extracted. This allows the splitting between the two laser resonances to be expressed in units of length, $l_{sep} = \nu_{sep}/(\Delta\nu/\Delta l)$. This conversion factor can be used together with the known splitting between the laser resonances in time to deduce the conversion factor between length and time, $\Delta l/\Delta t = l_{sep}/t_{sep}$, which ultimately makes it possible to express the width of each cavity resonance in units of length, $\Gamma_l = \Gamma_t \cdot (\Delta l/\Delta t)$. Finally, with Eq. (5.3), the finesse can be calculated.

5.4.1 Cavity characterization at room temperature

We use the concepts described in Section 5.4 to first characterize the performance of a bare cavity at room temperature. We use a top mirror with a transmission of $\lesssim 360$ ppm and a bottom mirror with a transmission of 56 ppm, giving a finesse of $\gtrsim 15\,086$ according to Eq. (2.53) when assuming no absorption and scattering losses. The top mirror crater is characterized using a confocal laser scanning microscope as described in Section 5.3.1, giving a crater radius of curvature of 15 μm , Gaussian FWHM of 4.8 μm , depth of 0.38 μm and asymmetry of 0.9%. Due to polarization-related photon leakage in the microscope head, the spectra for each cavity detuning exhibit a large constant background; we correct for this by subtracting each spectrum from the spectrum taken at the consecutive detuning. The resulting bare cavity mode structure is shown in Fig 5.5a.

The two rightmost resonances exhibit a shallower slope compared to the others, indicating that the two cavity mirrors come into partial contact and give a smaller change in mirror separation for the same applied voltage. We refer to these modes as contact modes. A fit according to Eq. (5.13) yields that the first contact mode, the second-rightmost resonance in the scan, is mode number 6, corresponding to a minimal mirror separation of 1.9 μm according to Eq. (2.56). This agrees well with the maximal precision we can achieve in aligning the mirrors to each other ($\sim \lambda/2$ over $\lesssim 1$ mm, given by the Newton rings described in Section 5.3.1).

After moving a thin diamond platelet into the cavity by laterally translating the bottom mirror, we measure the mode structure of the coupled air-diamond system, seen in Fig. 5.5b. The platelet fabrication process (Section 4.3) typically results in a thickness gradient across the diamond, which enables us to sample both an air- (top panel) and a more diamond-confined mode (bottom panel) for emission at 637 nm on the same structure.

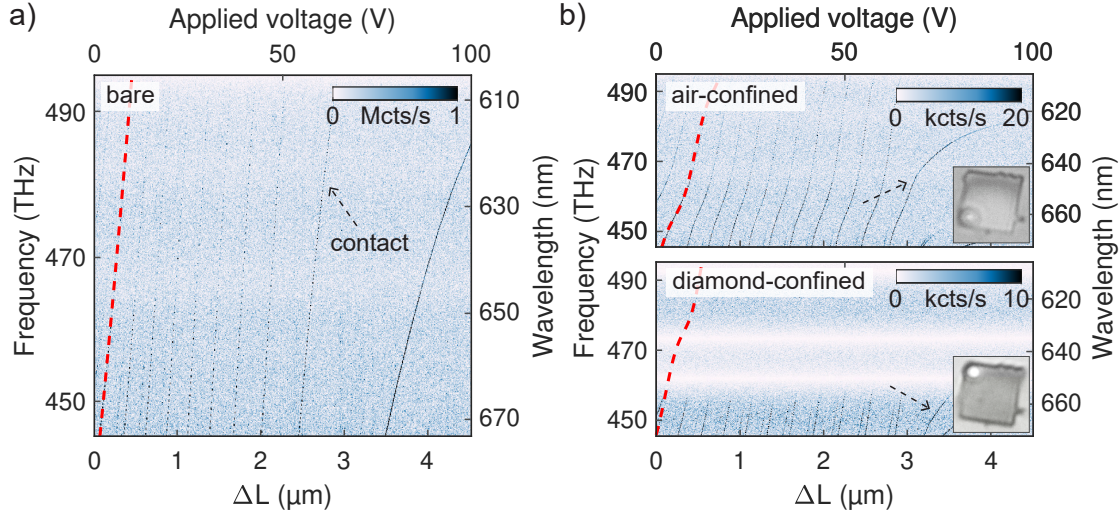


Figure 5.5.: Cavity mode structure at room temperature. Red dashed lines are fits to individual resonances and modes corresponding to contact between the mirrors are indicated by black dashed arrows. Increasing displacement ΔL corresponds to a shorter cavity. (a) Bare cavity mode structure. (b) Mode structure with a diamond membrane inside the cavity. Depending on the location on the diamond, indicated in the insets, the mode at ~ 637 nm can be either air-confined (top) or diamond-confined (bottom). The bright stripes seen in the bottom panel stem from background-subtraction.

From a fit with Eq. (5.14), we obtain a contact mode number of 15 (12) for the air-confined (diamond-confined) mode. This corresponds to a larger minimal mirror separation compared to the bare cavity, expected due to the presence of the diamond. The diamond thickness extracted from the fit is $1.71 \mu\text{m}$ ($1.64 \mu\text{m}$) for the air(diamond)-confined mode.

We calculate the finesse and Q-factor (Fig. 5.7a) of each mode following Section 5.4. The average finesse of the bare cavity is 14 993, which corresponds to only a few ppm losses compared to the lossless finesse assuming a bottom (top) mirror reflectivity of 56 (360) ppm. The air-confined modes yield an average finesse of 9 699, indicating that the insertion of the diamond introduces 231 ppm losses compared to the lossless finesse.

The diamond-confined modes result in a mean finesse of 4 578, corresponding to 956 ppm losses. Approximately 684 ppm of these can be explained by the reduced reflectivity of the bottom mirror upon placing a diamond slab on top it – the H-terminated mirror ($n \approx 2.1$) has a smaller refractive index contrast to diamond ($n \approx 2.41$) compared to air ($n \approx 1$). The remaining additional losses originate from scattering losses at the air-diamond interface: in a diamond-confined mode, the electric field has an antinode at the diamond-air interface, leading to a higher sensitivity to surface roughness compared to an air-confined mode. With present fabrication methods, we expect an rms diamond surface roughness of at best $\sigma_{rms} = 0.3$ nm, with polishing-induced additional long-range variations on the order of $1\text{-}2$ nm⁶⁴. Our results emphasize the difficulty in working in a diamond-confined mode and finding a smooth enough location on the diamond surface to achieve high finesse values.

5.4.2 Cavity characterization at low temperature

In order to be able to selectively enhance individual transitions of NVs, we move on to measure at low temperature (~ 4 K) in a liquid helium bath cryostat. We first characterize the noise environment by using a cavity resonance as a probe. By fixing the cavity length at the flank of a resonance, we obtain a high sensitivity to displacement, and record the noise-induced fluctuations in the cavity length and signal. The extracted power spectral density (PSD) is shown in Fig. 5.6a. Except for resonances corresponding to electrical mains pickup noise close to 50 Hz and 100 Hz, we see peaks around 106 Hz, 113 Hz, 116 Hz, 118 Hz, 122 Hz and 131 Hz. We identify them as resonances of the piezo actuators by applying sinusoidal displacements of these frequencies to the actuators and seeing resonating behavior in the cavity oscillations. The peak around 2.5 kHz is attributed to electrical noise.

Figure 5.6b shows the integrated rms noise amplitude A_{rms} , which for the full measured frequency range of 0-125 kHz amounts to 4.2 pm. This is only a fraction of the FWHM of $\Gamma_l = 41.7$ pm of the cavity resonance in Fig. 5.4d. The measured noise level is comparable to the performance of cavities in a similar cryogenic system³⁰² and low compared to cavities operated in closed-cycle systems, even when considering only the low-noise periods of the cold head cycle^{259,305}. The obtained noise amplitude becomes comparable to the cavity linewidth only for a finesse of $\mathcal{F}_{max} = (\lambda/2)/A_{rms} = 74\,100$, far exceeding the maximum possible finesse given by the specifications of the used mirrors.

We characterize the cavity performance at low temperature in two separate cooldowns that we refer to as cooldown A and cooldown B. We use a bottom mirror with a transmission of 56 ppm and a top mirror with a transmission of 485 ppm. The top mirror crater has a radius of curvature of 11 μm , an asymmetry of 5%, a depth of 0.4 μm and a FWHM of 4.3 μm . The specifications of the top and bottom mirror result in a finesse of 11 607 according to Eq. (2.53) when assuming no absorption and scattering losses. In cooldown

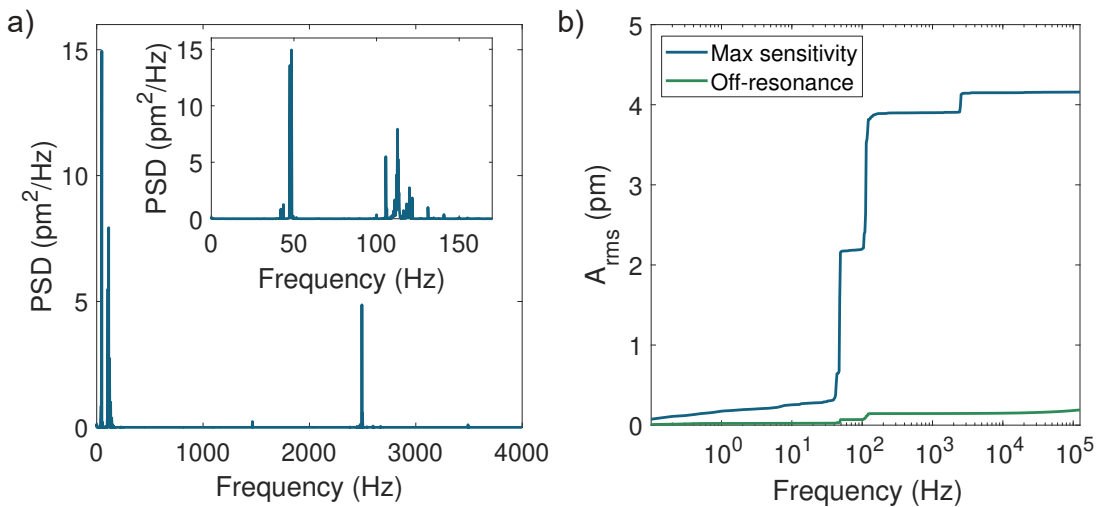


Figure 5.6.: Noise characterization at low temperature. (a) PSD of the noise in the system. Resonances can be seen close to 50 Hz, 100-150 Hz and 2500 Hz. (b) rms amplitude of the noise, giving an integrated value of 4.2 pm over the evaluated frequency range.

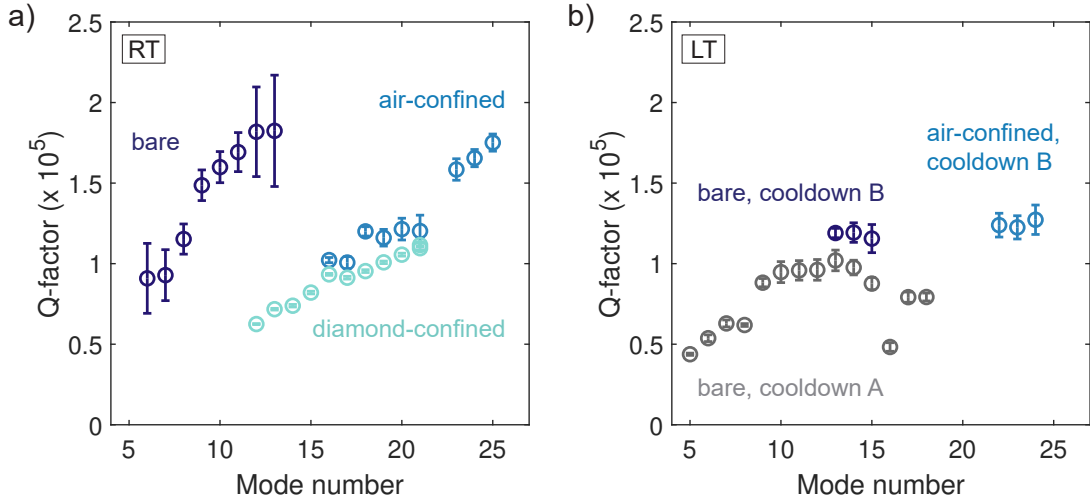


Figure 5.7.: Q-factors at room temperature (RT) and low temperature (LT). (a) Q-factors at RT for the configurations shown in Fig. 5.5. (b) Q-factors at LT in two different cooldowns.

B, a thin diamond membrane is incorporated into the cavity.

The Q-factors of individual resonances in the two cooldowns are presented in Fig. 5.7b. We measure an average bare cavity finesse of 6975 in cooldown A and of 8460 in cooldown B, illustrating how clipping losses (in this case, contributing for mode numbers of 14 and higher) can reduce the bare cavity finesse by more than 20%. In cooldown B, we operate in an air-confined mode at 637 nm and extract a diamond thickness of 2.0 μm and average finesse of 7937. In both cooldowns, we measure mean cavity mode splittings between 2 and 4 GHz.

We exchange the top- and bottom mirror for different mirrors with the same specifications (485 and 56 ppm transmission, respectively), and bond new diamond platelets to the bottom mirror. The radius of curvature of the top mirror crater is 14 μm and it has an asymmetry of 2.9%, depth of 0.3 μm and FWHM of 4.0 μm . We characterize the mode structure on and off the diamond, this time using a narrow-band 532 nm laser to excite background fluorescence within the cavity, in what we refer to as cooldown C. The advantage of using green excitation is that it is not filtered by the DMs used in the microscope head, resulting in a wider frequency range for which the mode structure can be detected. In addition, it results in less polarization-based leakage in the microscope head compared to broadband excitation. The results are shown in Fig. 5.8. The superimposed fit deviates from the data at the lowest and highest frequencies due to differences in mirror transmission close to the mirror stopbands.

Fitting yields mode numbers ranging from 6-8 for the bare cavity and 15-17 for the cavity with diamond, with an extracted diamond thickness of 1.6 μm . The average finesse of the bare cavity is 8877, indicating 166.8 ppm extra losses compared to the lossless finesse of 11 607. The air-confined mode has an average finesse of 4756, corresponding to 780.1 ppm additional losses and indicating a location on the diamond with increased surface roughness. (On a different location on the same diamond, a higher finesse value of ~ 6700 could be measured.) We obtain a mean cavity mode splitting of 5 GHz for the bare cavity; the resonances for the air-confined mode on the diamond, on the other hand, have an average mode splitting as high as 21.6 GHz. This implies that uniaxial strain in

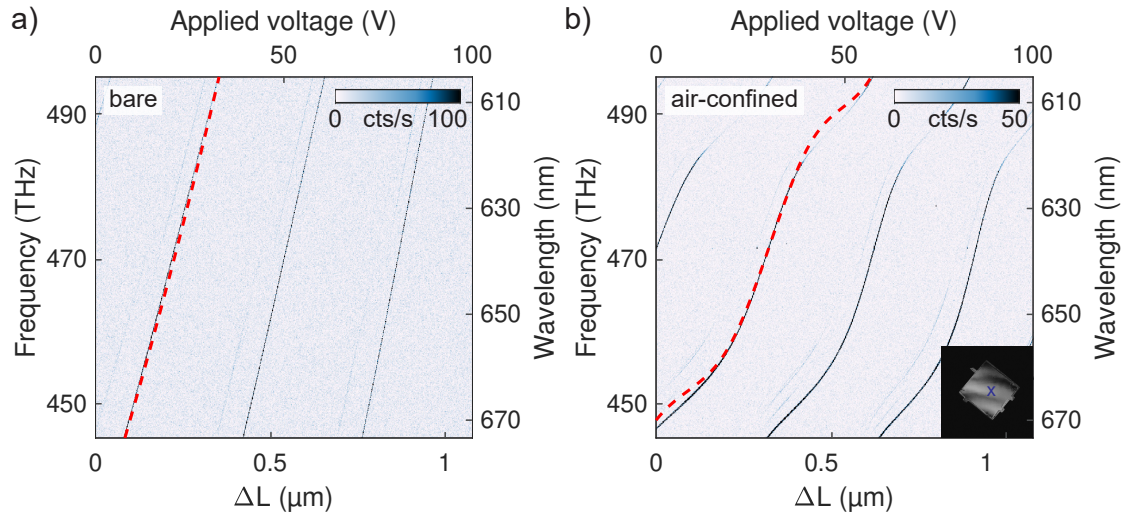


Figure 5.8.: Cavity mode structure at low temperature, measured under 0.4 mW green excitation. Red dashed lines are fits to individual resonances. The smaller range of the piezo actuators at low temperature with respect to room temperature leads to a smaller displacement range for the same applied voltage compared to room temperature. (a) Bare cavity mode structure. (b) Mode structure with a diamond membrane. An air-confined mode is found for operation at ~ 637 nm. The inset shows the diamond membrane, with a blue cross indicating the approximate location of the laser focus.

the diamond membrane, which induces birefringence and splits the fundamental modes of the cavity^{304,306,307}, is the dominant factor for the mode splitting compared to the one given by the crater ellipticity.

Note that slight misalignment of the excitation with respect to the top mirror crater leads to an increased visibility of higher-order transverse modes in Fig. 5.8. Resonant coupling between fundamental longitudinal modes and higher-order transverse modes of the cavity can result in hybridized modes, the wider waists of which lead to clipping losses. For the short cavities that were studied in this work, the effect is negligible, but for certain cavity lengths and specific resonance frequencies the finesse can drop due to this effect²⁶⁵.

5.5 Purcell-enhancement

We now move on to characterizing the coupling between an NV in the diamond membrane and the cavity. In order to detect an NV coupling to the cavity mode, we apply a 5 Hz symmetric saw-tooth ramp to the bottom mirror piezo actuator and sweep a few-hundred-GHz displacement range around a chosen central frequency close to 637 nm. By off-resonantly (532 nm) exciting and recording the resulting signal on a spectrometer, we obtain an accumulated signal consisting of the background fluorescence that is seen in Fig. 5.8. An NV coupling to the cavity mode is identified as a peak in counts within the swept range. After optimizing the relative position of the cavity mode and emitter by tuning the lateral position of the bottom mirror, a signal such as the one shown in Fig. 5.9a is obtained. The spectrally resolved scan has bright spots at two different emis-

sion frequencies, most likely corresponding to the E_x and E_y transition of the same NV, referred to as NV A. Fig. 5.9b shows the corresponding integrated signal, detected on an APD. The data shown in Figs. 5.9a and 5.9b was recorded during cooldown B; in this case, the mode splitting of the cavity could not be resolved.

An NV in a different diamond membrane, used in cooldown C, resulted in the signal shown in Fig. 5.9c. We refer to this NV as NV B. Here, the two intensity maxima are located at the same emission frequency, in contrast to Fig. 5.9a, indicating the coupling of one NV transition to two non-degenerate cavity modes. The absence of a peak corresponding to the other linearly polarized NV transition indicates a higher frequency splitting between the E_x and E_y transitions and so a larger transverse strain level experienced by the NV. The large cavity mode splitting of 21.6 GHz measured at this location on

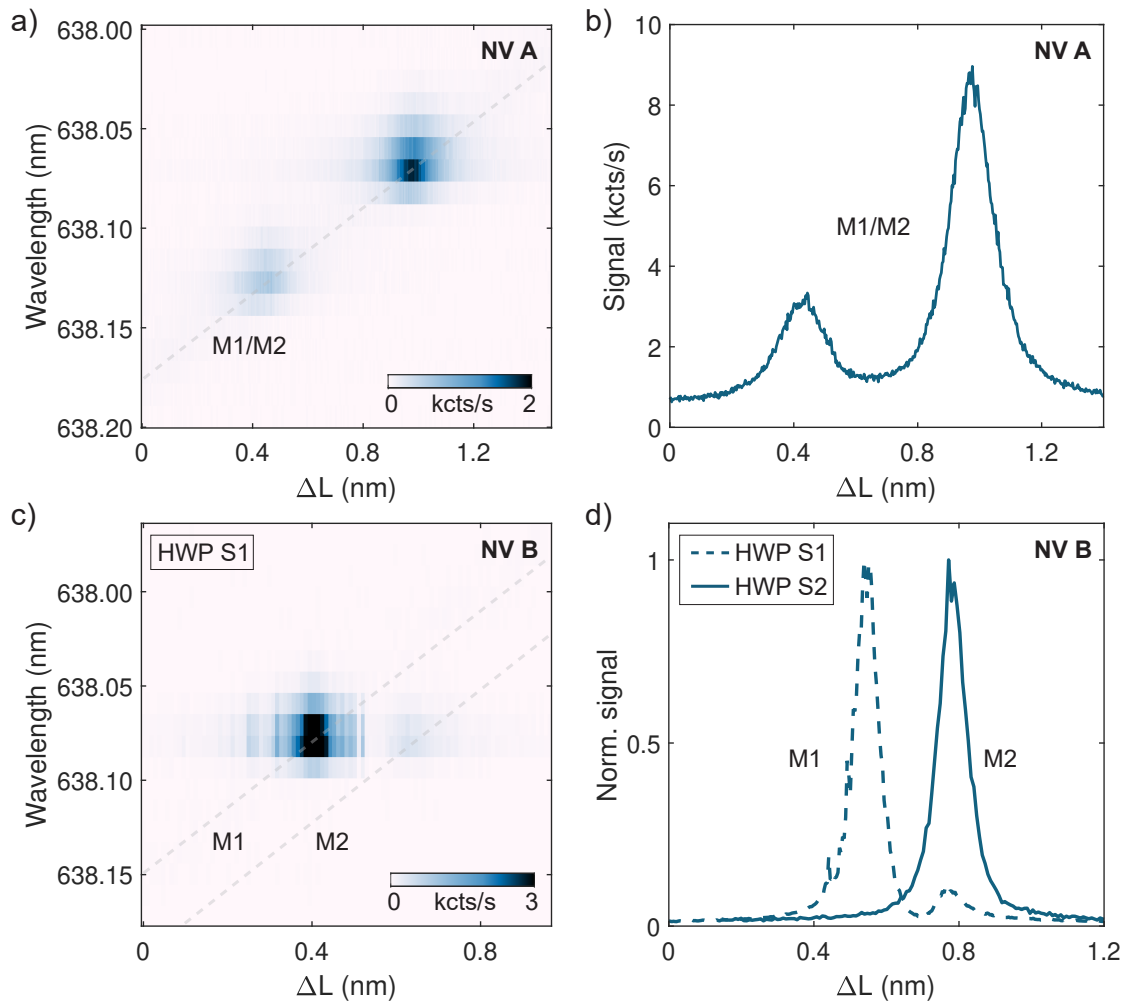


Figure 5.9.: NVs coupling to the modes of a cavity. (a) Spectrally resolved photoluminescence (PL) as a function of cavity length, for the two transitions of NV A coupling to a single degenerate cavity mode M1/M2. (b) Integrated PL as a function of cavity length for NV A. (c) Spectrally resolved PL as a function of cavity length, for a single transition of NV B coupling to the two cavity modes M1 and M2. (d) Integrated PL as a function of cavity length for NV B, for two different HWP settings. The signals have been normalized in order to better illustrate the effect of the HWP on the measured relative intensity of the peaks. The maximum intensity for HWP S1 corresponds to 43.2 kcts/s and for HWP S2 to 11.0 kcts/s, with the difference stemming mainly from a difference in excitation powers.

the diamond is another indication. We operate in mode number 16 (second mode from the right in Fig. 5.8b), with a Q-factor of 42 929 (cavity resonance FWHM of 11.0 GHz) and finesse of 4 334.

We refer to the two orthogonal modes of the cavity as mode M1 and mode M2. The relative intensity of the peaks shown in Fig. 5.9c depends on the alignment of the readout polarization axis with respect to the cavity modes. Two different settings of the HWP, referred to as HWP S1 and HWP S2, give rise to the different results, as shown in Fig. 5.9d. This illustrates the importance of the waveplate alignment for optimal readout in the respective modes.

5.5.1 Lifetime measurements

In the weak coupling regime, Purcell-enhancement is characterized by an increased emitter decay rate and shortened radiative lifetime compared to the 12-14 ns excited-state lifetime reported in literature^{38,40,56,57}. We investigate the Purcell-enhancement of the NVs coupled to the cavity: by tuning the cavity length over the emission frequency of the NV, we tune the coupling strength and so change the effect of the cavity on the NV emission rate. We excite the NV off-resonantly (532 nm) with a pulsed supercontinuum source operating at a pulse rate of 19.5 MHz and power of 0.4 mW and monitor the arrival of PL photons during 60-90 s using a picosecond event-timing module with a time-bin of 512 ps. The excitation power is measured between the bottom of the microscope head and the laser window, meaning that the power reaching the cavity after passing through the window and the objective is lower. In order to avoid a large contribution of background excited by the off-resonant excitation, we use both a 561 nm long-pass and a 638 nm band-pass filter in the detection path. We prevent cavity drifts from affecting the measurement by regularly re-centering the swept cavity range around the NV resonance.

The result of such a measurement on NV B, using the two different HWP settings introduced in Fig. 5.9d, is shown in Fig. 5.10a-b. We extract the radiative lifetime at each cavity detuning by fitting the signal with a single exponential with amplitude A_d and decay rate γ_d to each decay curve, with the radiative lifetime τ_d given by $\tau_d = 1/\gamma_d$.

Fig. 5.10c shows selected decay traces on resonance with cavity mode M1, on resonance with cavity mode M2, and far off-resonance with either mode, for HWP S1. The lifetime decreases to 9.9 ns for mode M1 and to 6.4 ns for mode M2 (corresponding to enhanced decay rates of $\gamma_{d,M1} = \gamma_{Purcell,M1} = 2\pi \cdot 16.1$ MHz and $\gamma_{d,M2} = \gamma_{Purcell,M2} = 2\pi \cdot 24.7$ MHz, respectively), a clear evidence of the Purcell effect. Fig. 5.10d shows similar decay traces but for HWP S2, for which we preferentially collect photons emitted into the more strongly coupled cavity mode M2. This does not affect the Purcell-enhancement in the two modes, only their relative intensity. We extract a similar reduced radiative lifetime of 10.4 ns and 7.0 ns in mode M1 and mode M2.

The fitted signal amplitude and radiative lifetime as a function of cavity detuning for HWP S1 is shown in Fig. 5.10e. The two modes of the cavity are clearly visible, each resulting in a shortening of the NV radiative lifetime. With this HWP setting, the photon collection is optimized for cavity mode M1, while the coupling and lifetime reduction is stronger in mode M2. Fitting the dependence of the signal amplitude on the cavity detuning with two Lorentzian functions with the same width results in a resonance FWHM

of 69 pm. Together with the free spectral range of 281 nm from Fig 5.8b, this yields a finesse of 4066, close to the previously measured finesse of 4334 in this mode. A double-Lorentzian fit of the lifetime modification gives a slightly increased resonance FWHM of 99 pm compared to the signal amplitude curve, indicating a higher sensitivity of this metric to noise. The fit also yields the NV lifetime when the cavity is far-detuned from the NV resonance, $\tau_0 = 12.1$ ns. This corresponds to a decay rate of $\gamma_0 = 2\pi \cdot 13.2$ MHz

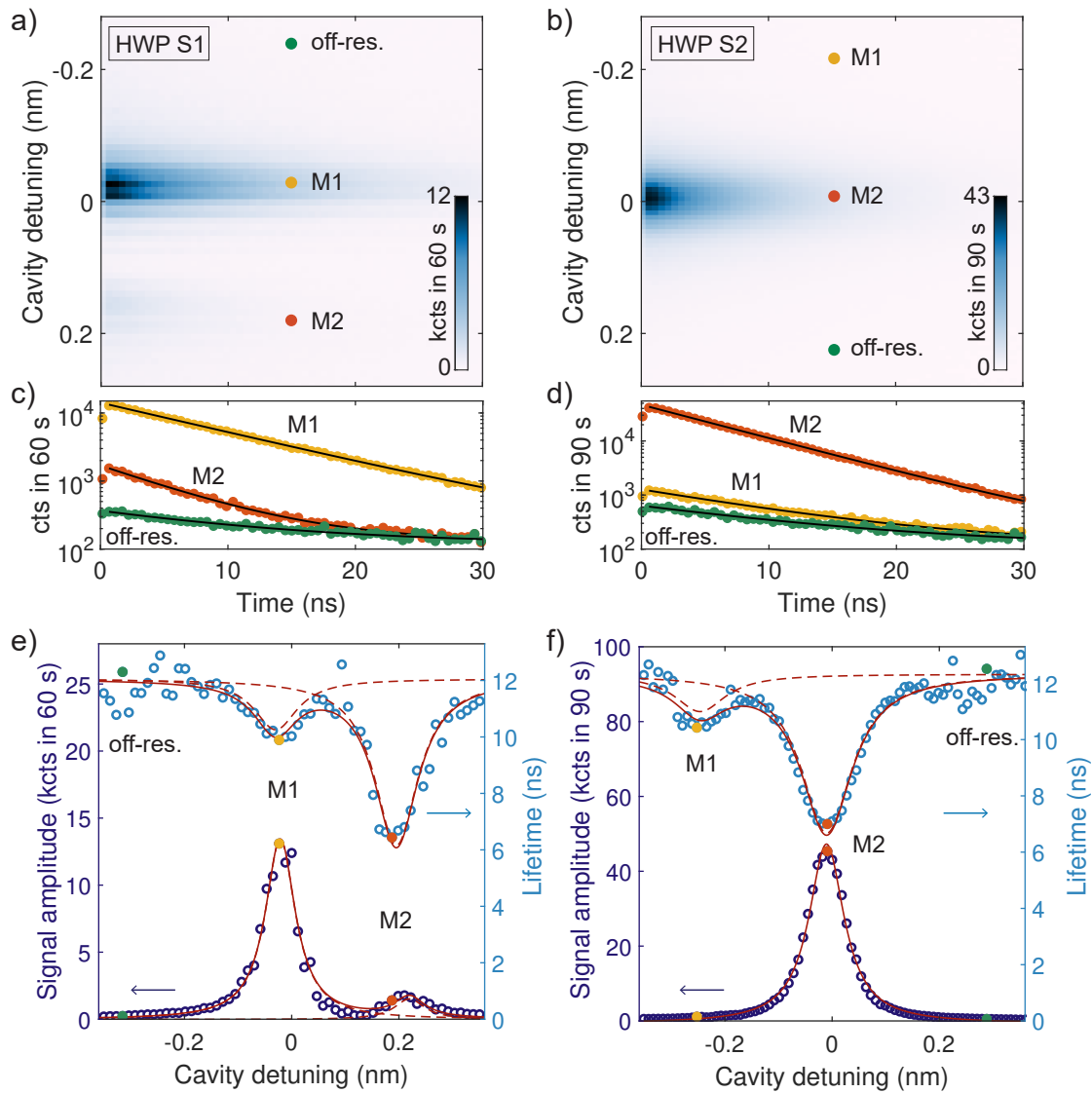


Figure 5.10.: Purcell-enhancement of NV B. (a) ZPL signal decay after an off-resonant excitation pulse as a function of time and cavity detuning for HWP S1. (b) ZPL signal decay after an off-resonant excitation pulse as a function of time and cavity detuning for HWP S2. (c) Selected decay traces for HWP S1, corresponding to mode M1 (yellow), mode M2 (orange) and far off-resonance with either mode (green). (d) Selected decay traces for HWP S2, corresponding to mode M1 (yellow), mode M2 (orange) and far off-resonance with either mode (green). (e) Fitted signal amplitude and radiative lifetime as a function of cavity detuning for HWP S1. The NV couples most efficiently to mode M2, signified by the larger lifetime reduction, but the readout is optimized for mode M1. (f) Fitted signal amplitude and radiative lifetime as a function of cavity detuning for HWP S2. For this HWP setting, the collection is optimized for mode M2, and the two modes are visualized only by their lifetime reduction.

which agrees well with NV excited-state lifetimes reported in literature^{40,56,57}.

The extracted signal amplitude and radiative lifetime for HWP S2 are shown in Fig. 5.10f. Just as in Fig. 5.9d, only a single peak is visible in the dependence of the signal amplitude on the cavity detuning, while the lifetime modification detects both cavity modes. The FWHM of the lifetime modification dip, 116 pm, is again larger compared to the FWHM of the signal amplitude peak, 80 pm, indicating a larger sensitivity of the NV-cavity coupling strength to noise in the system. The presence of a lifetime reduction in both mode M1 and mode M2 indicates a misalignment of the NV optical dipole with respect to both of the orthogonal cavity modes – a crucial requirement to be able to simultaneously excite and detect NV resonance fluorescence in the cavity.

From the cavity-enhanced decay rate, we can quantify the Purcell-enhancement. For a decay rate γ_0 into all decay channels of an NV without the top mirror and a decay rate of $\gamma_{Purcell}$ on resonance with the cavity, the overall Purcell-enhancement is given by Eq. (2.50). We approximate γ_0 with the far-detuned decay rate of $2\pi \cdot 13.2$ MHz and extract an overall Purcell-factor of $F_{P,M1} = 1.2$ and $F_{P,M2} = 1.9$ for mode M1 and mode M2, respectively. Eq. (2.52) gives $\beta_{M1} = 0.180$ and $\beta_{M2} = 0.466$, meaning that the NV-cavity coupling in mode M1 (M2) results in 18.0% (46.6%) of all the photons being emitted into the cavity mode.

Since only a fraction of the total NV emission (the photons emitted into the ZPL) is enhanced by the cavity, even a small overall Purcell-factor implies a significant increase of the fraction of photons emitted into the cavity mode. The Purcell-enhancement of the ZPL alone can be described by Eq. (2.49). Assuming an NV Debye-Waller factor of 2.55%⁵⁸, we obtain a ZPL Purcell-factor of $F_{P,M1}^{ZPL} = 9.6$ and $F_{P,M2}^{ZPL} = 35.2$ for mode M1 and mode M2, respectively. Finally, the fraction of NV photons emitted into the ZPL can be calculated from the obtained values by

$$\alpha_{ZPL} = F_P^{ZPL} \cdot \frac{\xi \gamma_0}{\gamma_{Purcell}} \quad (5.15)$$

yielding a fraction of photons funneled into the ZPL of $\alpha_{ZPL,M1} = 20.0\%$ and $\alpha_{ZPL,M2} = 48.0\%$ for the two cavity modes. The increase in the coherent emission fraction demonstrates one of the advantages of using the open microcavity as a photonic interface to an incoherent emitter such as an NV.

We characterize the cavity enhancement in terms of the coupling strength according to Eq. (2.36) and extract a maximal coupling strength (corresponding to the stronger coupled mode M2) of $g_0 = 2\pi \cdot 178.0$ MHz for a cavity linewidth of $\kappa = 2\pi \cdot 11.0$ GHz and photon loss rate $\gamma = 2\pi \cdot 13.2$ MHz. We assume here that γ is given purely by the emitter decay rate off-resonance with the cavity, neglecting dephasing effects. The obtained values, with $\kappa > g_0 \gg \gamma$, place the interaction in the weak coupling regime of cavity quantum electrodynamics.

5.5.2 Photon autocorrelation measurements

We confirm that the detected photons stem from a single NV by performing photon autocorrelation measurements in a Hanbury Brown-Twiss setup. We excite NV B off-resonantly with a continuous-wave green laser with a power of 1.8 mW and record the

emitted photons on two APDs. Time-resolved PL is recorded using the same picosecond event timing module as for the lifetime measurements, this time correlating the arrival times of the photons on each APD. The result, normalized to the value at long delay times, is shown in Fig. 5.11a. The measurements are carried out with HWP S1 and the cavity detuning set to be on resonance with mode M1.

In order to fit the autocorrelation data, we use a rate equation model assuming a three-level system, with state 1 referring to the NV ground state in $m_s = 0$, state 2 to the excited E_x or E_y state, and state 3 to the singlet levels or neutral charge state of the NV (Fig. 5.11b). The transition rates involved are k_{12} , k_{21} , k_{23} , and k_{31} , with k_{21} being the only radiative one. The autocorrelation function is extracted by comparing the excited-state population at a time t to the excited-state population in steady-state, $g^{(2)}(t) = p_2(t)/p_2(\infty)$. After solving the rate equations defining the three-level system, neglecting the population transfer channels 1 to 3 and 3 to 2, and assuming that the rates transferring population between states 1 and 2 are much higher than the rates related to state 3 (i.e., that $k_{12}, k_{21} \gg k_{23}, k_{31}$), the expression for the second-order correlation function is³⁰⁸

$$g_{ideal}^{(2)}(t) = 1 - \beta e^{-\gamma_1 t} + (\beta - 1)e^{-\gamma_2 t} \quad (5.16)$$

where the parameters β , γ_1 and γ_2 are given by the individual transition rates via³⁰⁸

$$\beta = 1 + \frac{k_{12}k_{23}}{k_{31}(k_{12} + k_{21})} \quad (5.17)$$

$$\gamma_1 = k_{12} + k_{21} \quad (5.18)$$

$$\gamma_2 = k_{31} + \frac{k_{12}k_{23}}{k_{12} + k_{21}} \quad (5.19)$$

The experimental data deviates from $g_{ideal}^{(2)}(t)$ due to incoherent background light collected by the two APDs, leading to a non-zero antibunching dip. We therefore describe

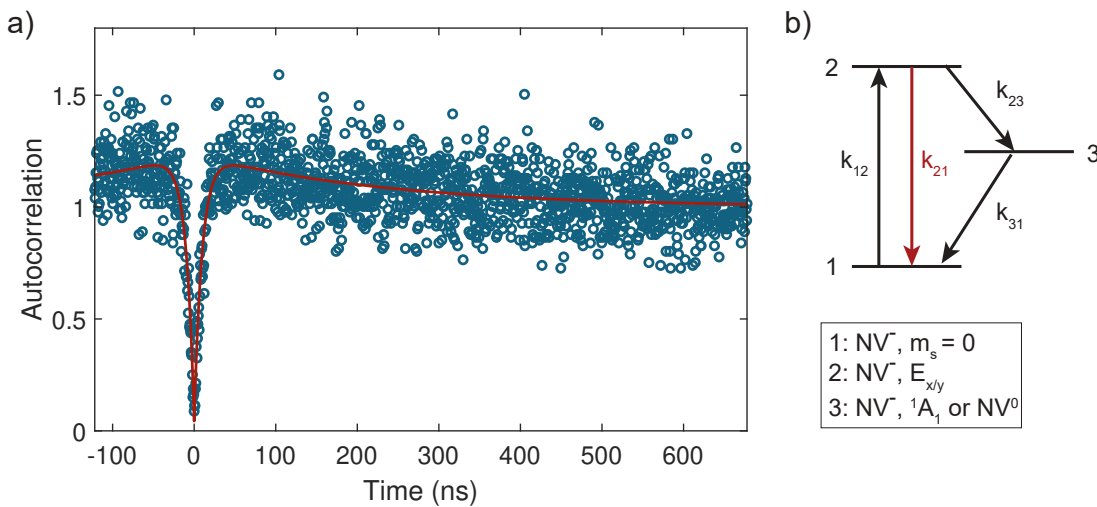


Figure 5.11.: Photon autocorrelation measurement. (a) $g^{(2)}(t)$ on resonance with cavity mode M1. The antibunching dip value of < 0.5 implies a single-photon emitter. (b) A three-level system used to model the autocorrelation data. State 3 represents a "dark" state, which in the case of a negatively charged NV can correspond either to the singlet state or NV⁰.

our data with a corrected correlation function according to

$$g^{(2)}(t) = \rho^2 g_{ideal}^{(2)}(t) + 1 - \rho^2 \quad (5.20)$$

where $\rho = S/(S + B)$ contains the relative contribution of the NV fluorescence signal S and the spurious incoherent background B ³⁰⁸. We leave the transition rates k_{12} , k_{21} , k_{23} , and k_{31} as well as the correction factor ρ as free fitting parameters.

The fit yields $k_{12} = 2.5$ MHz, $k_{21} = 101.2$ MHz (with $k_{21}/(2\pi)$ giving an overall Purcell factor of $F_p = 1.2$, matching what was obtained from the lifetime measurements on mode M1 in Section 5.5.1), $k_{23} = 32.0$ MHz, $k_{31} = 3.8$ MHz, $\rho = 0.98$ and $g^{(2)}(0) = 0.04$. The antibunching dip with a value of $g^{(2)}(0) < 0.5$ is a clear signature of single photon emission. Bunching behavior is seen for delays slightly larger than 0, confirming the presence of a "dark" state (level 3 in the rate equation model).

5.6 Resonance fluorescence from an NV in a cavity

In the coupled NV-cavity system, the photon flux into the ZPL is Purcell-enhanced by the cavity at the cost of reduced photon emission into the PSB. Furthermore, only photons emitted into modes within the cavity stopband are efficiently funneled out of the cavity. PSB-based readout of the NV spin state thus becomes inefficient. In order to exploit the advantages of the increased photon flux achieved with the cavity platform, and in order to make it useful in a quantum entanglement protocol^{11,12,54,155}, ZPL-readout therefore has to be achieved. With resonant readout comes the challenge of preventing excitation laser photons from leaking into the detection path. This difficulty, together with the small fraction of ZPL photons, has so far prevented the observation of resonance fluorescence from NVs with a signal-to-background ratio above 1 without relying on temporal filtering^{54,259,301}.

5.6.1 Measurement sequence and laser suppression

An established scheme to filter out resonant excitation light is by polarization-based laser suppression in a dark-field microscope. In such a microscope, light passes through a linear polarizer, is reflected off a surface, and is suppressed by means of a second linear polarizer, perpendicular to the first. This arrangement, when implemented in a confocal, diffraction-limited configuration, enables extinction ratios much higher than what is given by the specifications of the polarizers³⁰⁹.

The cross-polarization scheme has been used to detect resonance fluorescence from solid-state quantum dots (QDs)^{30,310}, reaching attenuations exceeding 7 orders of magnitude³¹¹, and has been employed in state-of-the-art demonstrations of QD-based

ⁱRef. 54 uses a SIL for improved collection efficiency, employs a time window to filter out residual laser pulses after a cross-polarization scheme, and achieves a signal-to-background ratio of at least 10. Ref. 259 uses a fiber-based open microcavity together with cross-polarization and temporal filtering and achieves a signal-to-background ratio below 1. Ref. 301 does not rely on temporal filtering and instead demonstrates coherent scattering at low laser powers. The resulting contrast is less than a percent.

single-photon sources³¹². Owing to working with only one color of excitation, focusing and collection of light can in the case of QDs often be done using a single, aberration-corrected lens; in the case of an NV, however, an objective is required due to working with two widely different excitation wavelengths. At low temperature, the performance of the objective typically deteriorates, introducing additional aberrations and making it difficult to achieve as high extinction ratios as for QDs. Furthermore, the small optical dipole moment of the NV leads to a lower signal-to-laser ratio in comparison. Nevertheless, owing to the enhancement of the intra-cavity field by a factor of up to the finesse, resonant excitation of the NV inside the cavity is more efficient compared to in free space. This, together with the cross-polarization scheme, enables us to measure resonance fluorescence without having to rely on temporal filtering. Excitation is performed with the polarization axis set along cavity mode M1, using the spectral tail of the mode to excite the NV. Readout is performed with the polarization axis set along cavity mode M2. In this configuration, we achieve extinction ratios of up to 5 orders of magnitude.

We apply interleaved green and red pulses at a rate of either 161 kHz or 30 kHz (with a green-to-red duty cycle of 24-to-69% and 5-to-93%, respectively) and use the same picosecond event timing module as for the lifetime and photon autocorrelation measurements to assign each detected photon to either the green (PL) or red (resonance fluorescence) pulse window. The off-resonant green excitation, typically 0.2-0.4 mW, is used to restore the negative charge state of the NV and initialize it in the ground state spin sub-level $m_s = 0$. In order to maintain the wanted NV-cavity detuning during measurements, we regularly sweep the cavity across the NV resonance under green excitation and correct the applied voltage to the bottom mirror piezo actuator. The recentering is repeated at a rate based on the drift rate of the cavity, typically every ten minutes.

The external optics are set as for a cavity transmission measurement (described in Section 5.4 and visualized in Fig. 5.4b), but with the HWP fast or slow axis aligned to one of the cavity modes. We use two different detection channels. One is the reflection channel, in which the photons that are reflected off the cavity are detected in the excitation arm of the microscope head. Another is the laser suppression channel, corresponding to the usual detection path. In an ideal cross-polarization scheme, the resonant laser light is suppressed (as only one cavity mode is excited and the other, orthogonal, cavity mode is read out), and only the photons emitted by an NV inside the cavity are detected in this channel. In order for the NV to be excited *and* not be suppressed by the cross-polarization scheme, its two linear orthogonal dipoles E_x and E_y have to be slightly misaligned with respect to the two cavity modes. The measurements in Section 5.5.1 confirm such a misalignment for NV B, since coupling of the NV to both cavity modes is observed.

We sweep the cavity length and frequency of the resonant laser across the NV resonance while recording the photons emitted during the green and red excitation. The data recorded during the green excitation is shown in Fig. 5.12a, demonstrating that the cavity (M1) remains centered at the NV resonance throughout the measurement. Figure 5.12b shows the counts in the reflection channel, measured with a resonant excitation power of 50 nW and integration time per frequency setpoint of 10 s. We can see the expected dip in signal once the cavity resonance frequency matches that of the resonant laser. As the measurement is based on excitation and readout along the same polarization axis, only one of the cavity modes (in this case mode M1) is probed. The laser suppression measurement, shown in Fig. 5.12c, instead visualizes both cavity modes due to the residual

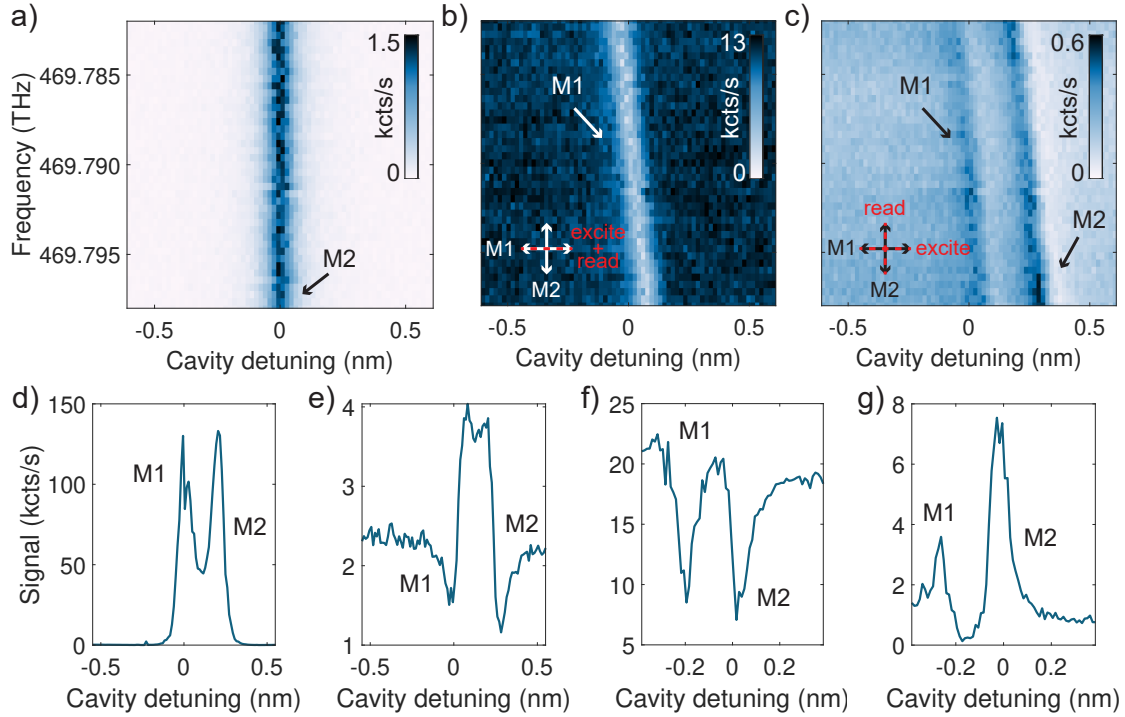


Figure 5.12.: Measurement sequence and suppression of resonant excitation. (a) Counts as a function of cavity detuning under off-resonant excitation. (b) Counts in the reflection channel as a function of cavity detuning and resonant excitation frequency. The inset shows how the same cavity mode is excited and read-out. (c) Counts in the laser suppression channel as a function of cavity detuning and resonant excitation frequency. The inset shows how one of the cavity modes is excited and the other one is read out. (d)-(g) Counts in a the laser suppression channel as a function of cavity detuning for different relative QWP/HWP orientations. (d)-(e) were measured with 100 nW and (f)-(g) with 10 nW red excitation power.

leakage of laser photons.

Figure 5.12d-g illustrates the difficulty in successfully suppressing the resonant laser light. The subfigures correspond to four different relative QWP/HWP orientations, differing only by a fraction of a degree, demonstrating that small changes in the wave plate orientation changes the laser suppression by orders of magnitude. In each of the measurements, both of the two unsuppressed cavity resonances can be seen, with the relative intensities depending on the exact QWP/HWP setting. The laser suppression needs to be optimized by tuning both the HWP and the QWP, most probably due to deviations from the design specifications in the phase shift imposed by the wave plates.

5.6.2 Resonance fluorescence

In the measurement shown in Fig. 5.12a-c, the crossing between the cavity mode and the NV resonance occurs for mode M1. As seen in Fig. 5.10e and Fig. 5.10f, the NV-cavity coupling strength is stronger in mode M2. In order to explore the maximal possible coupling, we therefore shift the frequency range of the resonant laser to lower frequencies and optimize the laser suppression for mode M2. The result of a repeated cavity- and laser-sweep is shown in Fig. 5.13. We use an off-resonant excitation power of 0.3 mW,

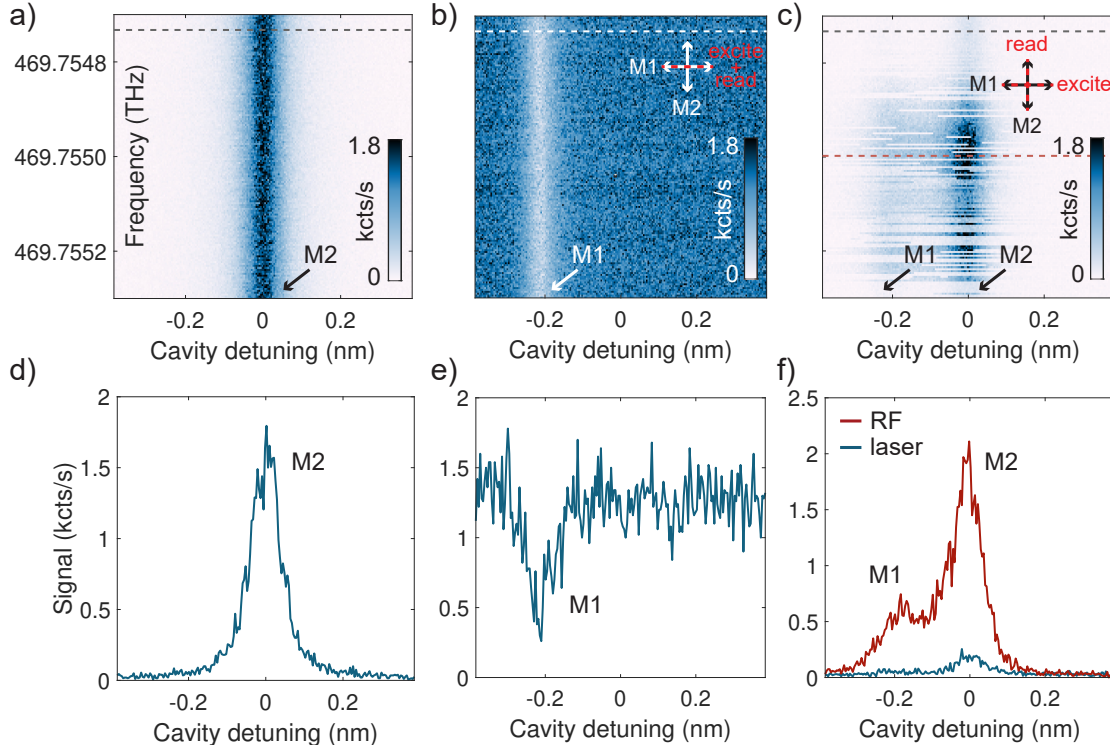


Figure 5.13.: Measuring resonance fluorescence. (a) Counts as a function of cavity detuning under off-resonant excitation. (b) Counts in the reflection channel as a function of cavity detuning and resonant excitation frequency. Note the smaller laser scanning range compared to Fig. 5.12. (c) Counts in the laser suppression channel as a function of cavity detuning and resonant excitation frequency. Where the cavity and NV resonance overlap, NV resonance fluorescence is detected. (d) Linecut along the gray dashed line in (a), showing the cavity-enhanced NV emission under off-resonant excitation. (e) Linecut along the gray dashed line in (b), showing the dip in signal corresponding to cavity mode M1. (f) Linecuts along the dashed lines in (c), showing the unsuppressed excitation light as well as the resonance fluorescence (RF) signal.

a resonant excitation power of 0.5 nW, and an integration time of 0.2 ns per frequency point. At the crossing between the NV resonance and the cavity resonance, we detect resonance fluorescence (Fig. 5.13c,f).

The resonance fluorescence signal includes several interesting features. With the HWP fast or slow axis aligned to M1, we excite in mode M1 and read out in mode M2, yielding the expected resonance fluorescence signal in mode M2. However, a weaker resonance fluorescence signal can be seen also in mode M1, stemming from the partial spectral overlap between mode M1 and mode M2. The resonance fluorescence furthermore features a “switching” behavior, better illustrated in a repeated measurement shown in Fig. 5.14. There, we lock the cavity at zero detuning from the NV resonance and only tune the resonant excitation frequency. We use an off-resonant excitation power of 0.4 mW and a resonant excitation power of 0.1-0.3 nW.

Fig. 5.14a shows a resonance fluorescence signal measured with an integration time of 1 s per laser frequency setpoint. A single peak surrounded by a few additional scattered data points is observed. In Fig. 5.14b, for the same measurement but with a longer integration time of 18 s per frequency setpoint, a second peak can be seen.

As our measurement includes a regular off-resonant repump pulse, the charge environment of the NV is periodically re-shuffled. This is a well-known phenomenon in

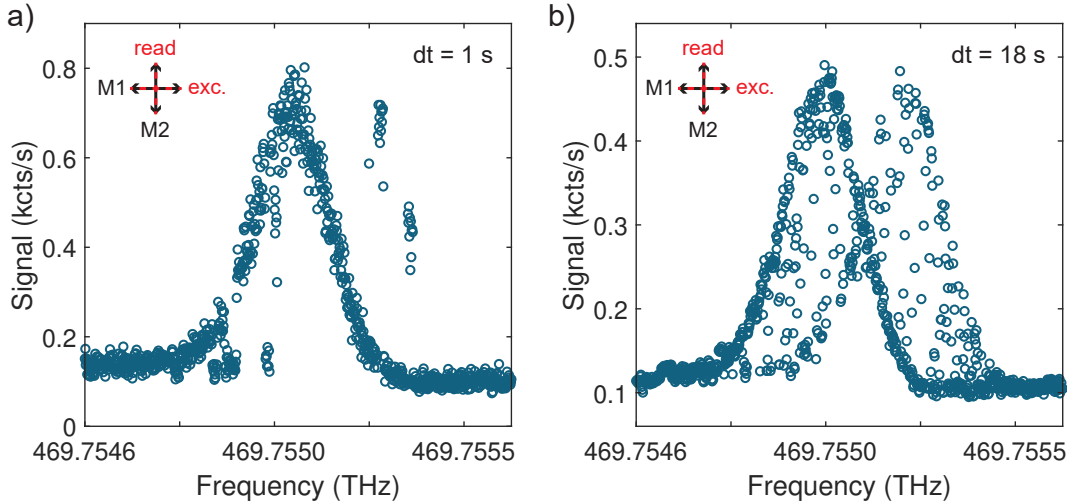


Figure 5.14.: A shifting resonance fluorescence signal. (a) Resonance fluorescence detected at zero cavity detuning with an integration time of 1 s per frequency setpoint. (b) Resonance fluorescence detected at zero cavity detuning with an integration time of 18 s per frequency setpoint, showing a Stark-induced shifting of the resonance depending on the state of a nearby charge trap.

PLE measurements, where it leads to Stark shifts of the ZPL line and extrinsic linewidth broadening (see Section 2.1.2.2). A plausible explanation for the switching behavior seen in the resonance fluorescence is therefore a close-lying charge trap. A single trap with two states, corresponding to the trap being “loaded” with an additional charge or not, leads to two distinct NV ZPL emission frequencies depending on the state of the trap. Depending on the timescale of the measurement and the trap-induced shifting of the emission line, only a few (Fig. 5.14a) or many (Fig. 5.14b) shifts are recorded during a laser scan.

We repeatedly measure the resonance fluorescence signal with a shorter integration time of 0.1 s per frequency setpoint (Fig. 5.15a) and create a histogram of the resulting intensity according to frequency and count rate (Fig. 5.15b). By assuming Gaussian distributions for the counts during repeated measurements, each data point can be attributed to one or the other state with a certain probability. The result of such an attribution is shown in Fig. 5.15c. Assuming the same width for both resonances yields a Lorentzian FWHM linewidth of 159.0 MHz. This agrees well with previously measured linewidths on samples made via carbon IPF (see Section 4.4.3) and confirms that the method can be used to create narrow-linewidth NVs even in diamond microstructures as thin as 1.6 μm . The fit furthermore yields a signal-to-background ratio of 14.0 (corresponding to a contrast of 93.3%), a first demonstration of resonance fluorescence with a signal-to-background ratio exceeding 1 measured without relying on temporal filtering^{54,259,301}.

The splitting between the states of 170.6 MHz gives an upper bound on the distance to the nearby charge trap of 230.5 nm, assuming maximal field projection onto the probed NV dipole and a linear absolute Stark shift of 6.3 GHz/MV m^{-1} according to Ref. 40. Without measuring a resonance fluorescence signal with a similar shifting behavior for the other linearly polarized NV transition, we can only calculate an upper estimate for the distance to the trap.

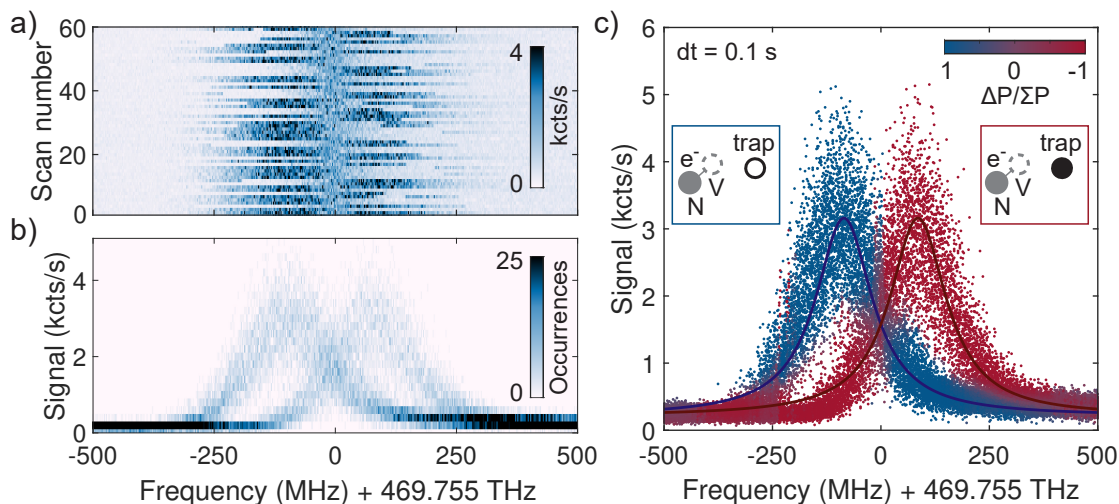


Figure 5.15.: Attributing the resonance fluorescence signal to two different charge environment settings. (a) Repeated scans of the resonance fluorescence signal, using a green excitation power of 0.2 mW, a red excitation power of 0.1 nW and an integration time of 0.1 s per frequency set-point. The peak intensity shifts between the left and the right state. (b) A histogram according to frequency (bin width 2.2 MHz) and count rate (bin width 20 cts/s) of the measurement in (a). (c) Fitting two Lorentzians to the measured resonance fluorescence signal and attributing each data point to either the left state (blue) or the right state (red) with a certain probability, mapped by the color scheme. The insets show a suggested mechanism for the spectral shift: a nearby charge trap being loaded and unloaded due to the green repump.

5.6.3 Power-dependent dynamics

We explore the power dependence of the resonance fluorescence signal, by interleaving the green and red excitation at a constant rate of 30 kHz and relative duty cycle of 5-to-93%, and varying the respective powers. We start by tuning the green excitation power, keeping the red power constant at 5.5 nW. We sum the counts collected during 300 resonant excitation pulses, giving a total integration time of 9.3 ms. Due to the Stark-induced shifting between two emission frequencies, a long time trace taken at resonance with one of the peaks shows an “on/off” behavior, shown in Fig. 5.16a-d. When the nearby trap is in a certain charge state, the NV is on resonance with the laser, and the recorded resonance fluorescence counts are high. Once the charge trap is loaded or unloaded, the NV ZPL frequency is Stark-shifted such that it is off-resonance with the laser, and the count rate drops.

By creating a histogram of the count rates, a certain count rate can be attributed to the NV being on- or off-resonance with the resonant laser. We fit three Gaussians, corresponding to the on-resonance case, the off-resonance case, and laser background, to the histogram; the results are shown in Fig. 5.16f-i. At low green power (Fig. 5.16f), the switching between the on- and off-resonance case happens at a low rate. As the green power is increased, the shifting rate increases (Fig. 5.16g-h). As one approaches off-resonant powers above 3 mW (Fig. 5.16i), the switching occurs at such a high rate that the count rate within a counting interval averages to the mean of the on-resonance and the off-resonance case. This corresponds to an increase in the rate of the loading and unloading of the nearby charge trap with increasing green power. Note that the probability

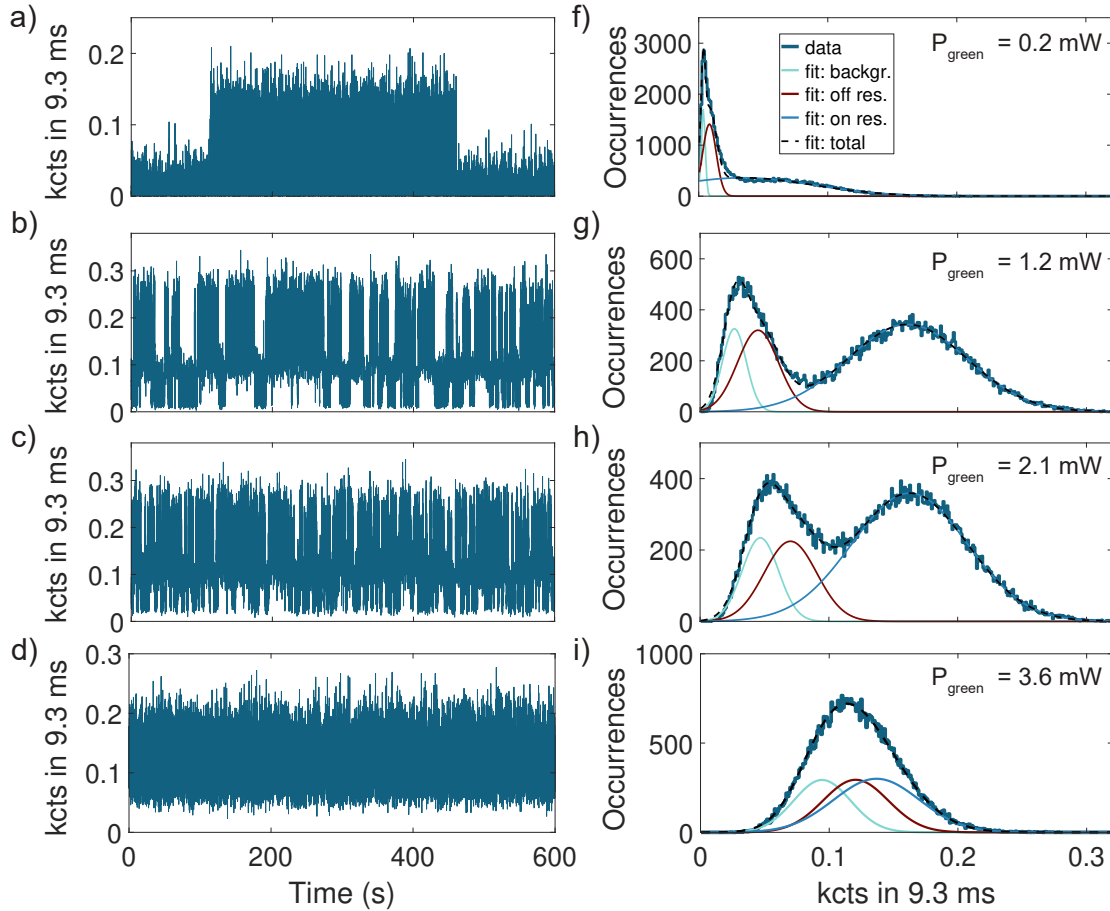


Figure 5.16.: Time-resolved resonance fluorescence as a function of the green excitation power. (a)-(d) ZPL count rate as a function of time, with the red laser locked at 469.755 THz at a power of 5.5 nW. The green excitation power is 0.2 mW in (a), 1.2 mW in (b), 2.1 mW in (c) and 3.6 mW in (d). (f)-(i) Histograms of the count rates measured in (a)-(d), fitted with three distributions to attribute each count rate to laser background (low count rate), to the NV being off-resonance with the laser (intermediate count rate), or to the NV being on resonance with the laser (high count rate).

of the NV transition being on or off resonance with the laser is approximately equal and independent of the green power.

We perform the same measurement, but instead keeping a constant green excitation power of 0.2 mW and varying the red power. The result, shown in Fig. 5.17, shows a different behavior than the green power dependence: a higher resonant excitation power does not significantly affect the rate of switching between the two states, but rather leads to a higher average count rate. The probability of the transition being on or off resonance with the laser is approximately equal and independent of the red power. We note that the resonance fluorescence signal stays high (the NV ZPL stays on resonance with the laser) for durations reaching several minutes, indicating a long stability even under the regular green repump. For the highest available resonant power of 300 nW, the drive is strong enough to address both states, which can be seen via the apparent absence of switching between the states in Fig. 5.17d and the presence of both the on-resonance and the off-resonance distributions in Fig. 5.17i.

After assigning each data point to either laser background or the NV being on- or off-

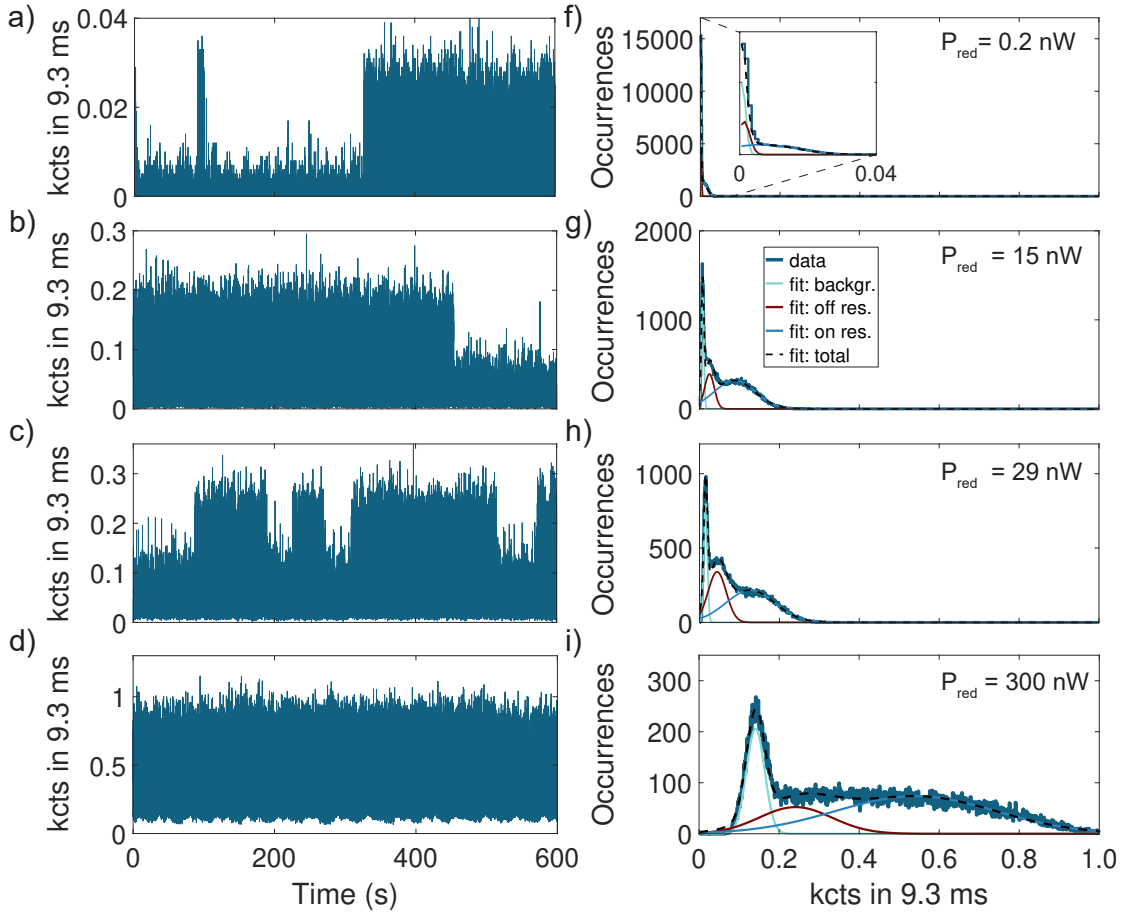


Figure 5.17.: Time-resolved resonance fluorescence as a function of the red excitation power. (a)-(d) ZPL count rate as a function of time, with the red laser locked at 469.755 THz at a power of 0.2 nW in (a), 15 nW in (b), 29 nW in (c) and 300 nW in (d), using a green excitation power of 0.2 mW. (f)-(i) Histograms of the count rates measured in (a)-(d), fitted with three distributions to attribute each count rate to laser background (low count rate), to the NV being off-resonance with the laser (intermediate count rate), or to the NV being on resonance with the laser (high count rate).

resonance with the laser, the data can be post-processed to extract only the photons detected when being on resonance. Figure 5.18 shows the corresponding time evolution of the ZPL photon count rate. The green power dependence in Fig. 5.18a demonstrates that the maximum count rate is unchanged above a certain green power, which is expected since the green excitation serves only for initialization of the NV spin- and charge state. The red power dependence in Fig. 5.18b, on the other hand, shows a clear increase of the average count rate with power. Furthermore, a faster decay of the signal intensity can be seen with increasing power. Part of it could be attributed to a two-photon ionization process, which is known to increase quadratically with the resonant power³¹³. At higher resonant powers, the time evolution shows a non-trivial multi-exponential decay, which leads us to speculate that an additional mechanism, possibly related to the redistribution of population between spin sublevels, is involved in the NV photodynamics.

The charge-trap-related hopping of the ZPL frequency during a measurement such as the one in Fig. 5.14 could be avoided by applying a charge- and spin-state resetting green pulse only at the beginning of the resonant laser sweep. The feasibility of this depends

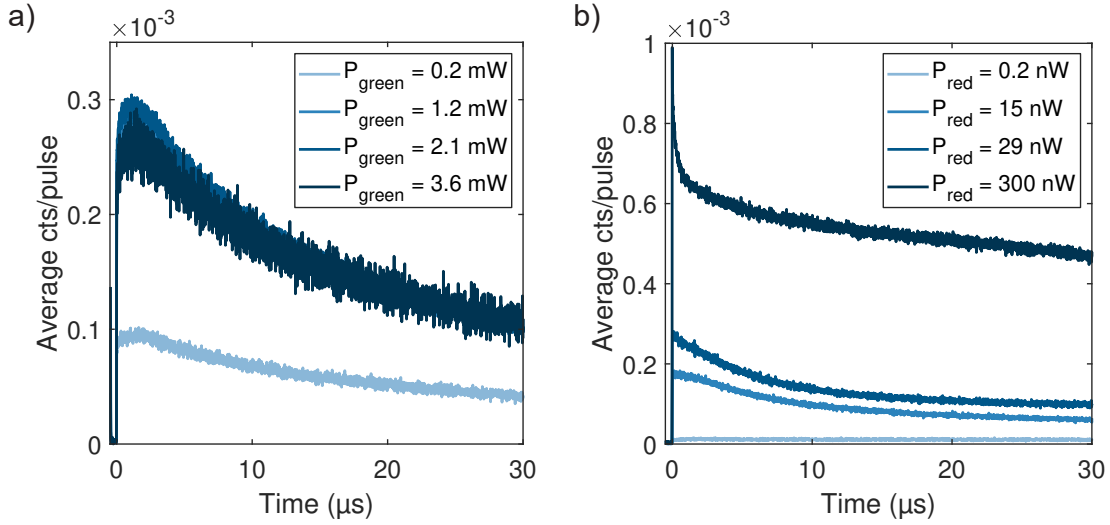


Figure 5.18.: Ionization as a function of power. (a) ZPL counts on resonance with the laser as a function of time, with the resonant laser locked at 469.755 THz with a power of 5.5 nW. Time traces are shown for increasing green excitation powers (0.2 mW, 1.2 mW, 2.1 mW, and 3.6 mW). (b) ZPL counts on resonance with the laser as a function of time, with the resonant laser locked at 469.755 THz and the green excitation power kept at 0.2 mW. Time traces are shown for increasing red excitation powers (0.2 nW, 15 nW, 29 nW, and 300 nW).

on the ionization rate and signal-to-noise ratio in the measured RF signal.

5.6.4 Saturation curves and system efficiency

We move on to determine the saturation behavior of the cavity-enhanced signal. We first study the power dependence of the photon count rates recorded during the green pulse window (compare with the signal shown in Fig. 5.13a,d). The data was collected during the measurement that is presented in Figs. 5.16, 5.17 and 5.18. The resulting saturation curve is shown in Fig. 5.19a.

We model the NV as a two-level system that loses coherence quickly compared to the pulse duration when driven resonantly, and describe the incomplete initialization into NV^- , $m_s = 0$ by the green excitation via an initialization power P_{init} . The resulting expression for the count rate as a function of power is

$$C(P) = C_{sat,green} \cdot \left(0.2 + 0.8 \cdot \frac{P}{P + P_{init}} \right) \cdot \frac{P}{P + P_{sat,green}} \quad (5.21)$$

where $C_{sat,green}$ is the saturation count rate and $P_{sat,green}$ the saturation power. Here, we have assumed a maximal spin-polarization degree of 80%³⁸. The fit yields a saturation count rate of 756 kcts/s, saturation power of 15.3 mW and initialization power of 0.2 mW. The data is also well-described by a linear fit, indicating operation far from saturation. Measurements with even higher green powers typically led to gradual NV bleaching.

We compare the obtained ZPL count rates with ZPL count rates obtained in free-space, without the cavity, typically corresponding to approximately 0.7 kcts/s on a spectrometer for a green power of 0.5 mW. In the cavity, we measure a 30 times higher count rate

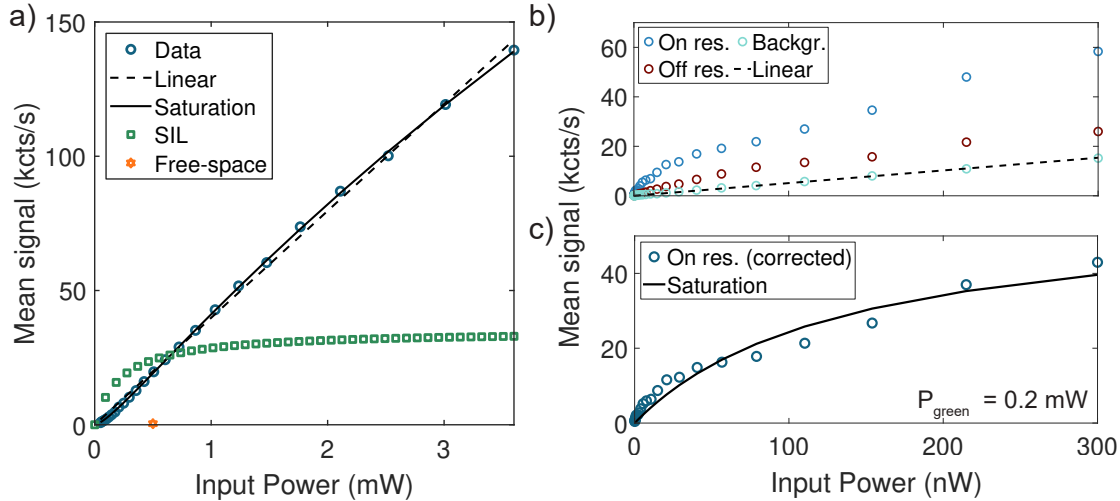


Figure 5.19.: Saturation behavior - mean intensity. (a) ZPL counts during the green pulse as a function of the green excitation power. The red power is kept constant at 5.5 nW. The data is well-described by a linear fit, indicating operation far from saturation. Fitting a saturation curve yields a saturation count rate of 756 kcts/s. The state-of-the-art count rates recorded with a FIB-SIL, extracted from Ref. 54, as well as a typical count rate in free-space without the cavity (~ 0.7 kcts/s) are inserted for comparison. (b) ZPL counts during the red pulse for the on- and off-resonance case, as a function of the red excitation power. The green power is kept constant at 0.2 mW. (c) Background-subtracted saturation curve, with a fit yielding a saturation count rate of 57.5 kcts/s.

for the same excitation power. Moreover, we compare our results to the state-of-the-art count rates obtained for a SIL used together with adaptive optics, corresponding to 32.9 kcts/s at saturation⁵⁴. Our count rate of 140.0 kcts/s at the maximum used green power of 3.6 mW exceeds this value by a factor of 4.3. Note that this factor is a lower bound, since we are operating relatively far from saturation. This emphasizes the excellent performance of the coupled NV-cavity system, and its advantage over the SIL in terms of the attainable coherent photon flux.

We now study the power dependence of the photon count rates recorded during the red pulse window (compare with the signal shown in Fig. 5.14). The dependence on the resonant excitation power, after extracting the average signal during time traces such as the ones shown in Fig. 5.18, is shown in Fig. 5.19b. The result after correcting for laser background is shown in Fig. 5.19c. The power dependence can be fitted without including the initialization power needed to describe the green excitation via

$$C(P) = C_{sat,red} \cdot \frac{P}{P + P_{sat,red}} \quad (5.22)$$

With this, we obtain a saturation count rate of 57.5 kcts/s and a saturation power of 135.6 nW. The count rate measured with our maximum used red power of 300 nW is 43.0 kcts/s. The count rate saturates at lower powers due to ionization increasing with power.

To exclude the effect of ionization and represent better the case of pulsed excitation, we extract the peak count rate for each power, and fit a new saturation curve. The result is shown in Fig. 5.20a, yielding a saturation count rate of 101.4 kcts/s and a saturation power of 86.8 nW. The peak count rate measured with our maximum red power of

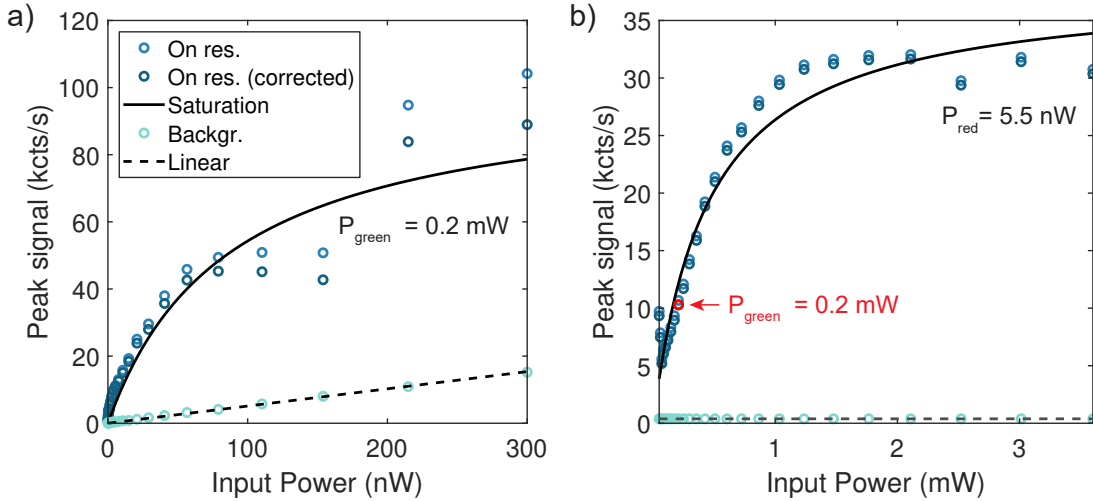


Figure 5.20.: Saturation behavior - peak intensity. (a) ZPL counts during the red pulse for the on-resonance state, as a function of the red excitation power. The green power is kept constant at 0.2 mW. A fit to the background-corrected counts yields a saturation count rate of 101.4 kcts/s. Data points corresponding to higher resonant input power deviate from the expected saturation curve, most probably due to issues with the signal attribution to the on-resonance or off-resonance case for these powers. (b) ZPL counts during the red pulse for the on-resonance state, as a function of the green excitation power, corrected for background. The red power is kept constant at 5.5 nW. A fit yields a saturation count rate of 38.0 kcts/s. The data point corresponding to the green power used for the saturation curves in Fig. 5.19b-c and Fig. 5.20a is indicated in red.

300 nW is 89.0 kcts/s.

Finally, the green excitation influences not only the counts in the ZPL under off-resonant excitation, but also the resonance fluorescence count rate, since it affects the degree of polarization into NV^- , $m_s = 0$. Fig. 5.20b shows the dependence of the peak resonance fluorescence counts on the green power, with a fit (excluding the first two data points) yielding a saturation count rate of 38.0 kcts/s and a saturation power of 0.4 mW. We see that, at the cost of faster spectral shifting of the resonance, we can excite the NV more efficiently and extract even higher count rates by increasing the green power.

The obtained count rates are limited by losses in the system. As the measured NV is at a location on the diamond with a finesse of 4334, there are 908.7 ppm additional losses compared to the specifications of the used mirrors. This corresponds to $\kappa_{top} = 2\pi \cdot 3.7$ GHz for $\kappa = 2\pi \cdot 11.0$ GHz according to Eq. (2.62). With $F_p = 1.9$ and $\beta = 0.466$, this results in a total system efficiency of $\eta_{tot} = 15.6\%$ according to Eqs. (2.63) and (2.64). As locations on the same diamond structure with a better finesse of 6700 were measured, finding an NV at such a location with the same coupling to the cavity would increase the overall Purcell-factor to $F_p = 2.4$ ($\kappa = 2\pi \cdot 7.1$ GHz) and the total system efficiency to $\eta_{tot} = 29.7\%$ ($\beta = 0.576$, $\kappa_{top} = 2\pi \cdot 3.7$ GHz). If the bare-cavity finesse of 8877 could be achieved also on the diamond, a total efficiency of up to $\eta_{tot} = 44.0\%$ ($F_p = 2.8$, $\beta = 0.643$, $\kappa = 2\pi \cdot 5.3$ GHz, $\kappa_{top} = 2\pi \cdot 3.7$ GHz) could be achieved.

Once a photon is emitted from the cavity, it needs to pass through an objective, laser window, optics in the microscope head, fiber-coupler and fiber before being detected by an APD. With a poor objective transmission of 0.45 at low temperature, combined transmission of 0.66 of the external optics, and an APD detection efficiency of 0.68, we can use the maximum rate under off-resonant excitation of 140.0 kcts/s to calculate an effective

NV ZPL photon emission rate into the cavity mode of 4.5 Mcts/s and an overall setup efficiency of 3.1%. Using a cryo-compatible objective with a transmission of 0.8 and operating at a lower-loss location on the diamond would increase the detected count rate to 475.0 kcts/s, corresponding to an improved detection efficiency of 10.6%. Achieving the bare cavity finesse would increase these numbers to 703.1 kcts/s and 15.8%, respectively.

5.7 Conclusions and outlook

In conclusion, we have implemented an efficient coupled NV-cavity system that we successfully operate in a cryogenic environment, achieving a low integrated mechanical noise floor of 4.3 pm and measuring finesse values of up to ~ 8900 in the bare cavity and ~ 7900 on a diamond platelet. We demonstrate Purcell-enhancement of NVs under off-resonant excitation, reaching Purcell-factors of up to 1.9. This translates into 48.0% of the photons emitted into the ZPL, an improvement by a factor of 18 compared to the NV Debye-Waller factor of 2.55%⁵⁸. Under off-resonant excitation, we record ZPL count rates surpassing the current state-of-the-art photonic interfaces based on SILs⁵⁴ by a factor of 4.3, reaching 140 kcts/s away from saturation. Our work represents crucial progress in not only shortening the NV radiative lifetime with a cavity, but also efficiently extracting and detecting the increased flux of coherent photons.

For the first time for an NV in diamond, we successfully use resonant excitation and ZPL readout to measure resonance fluorescence with a signal-to-background ratio higher than 1 without relying on temporal filtering. We measure a maximum mean resonance fluorescence count rate of 43.0 kcts/s. The resonance fluorescence signal yields an extrinsically broadened NV linewidth of 159.0 MHz, emphasizing the high-quality NVs created via carbon IPF even in a 1.6 μm thin diamond membrane. This is further demonstrated by the charge-trap-related hopping behavior of the resonance fluorescence signal between two ZPL emission frequencies: the fact that a distinct shift between two states can be resolved indicates a low density of charge traps in the vicinity of the NV.

Projecting the current system efficiency to applications relying on photon-photon entanglement using the Barrett-Kok protocol¹⁵⁸ would result in entanglement rates increased by more than an order of magnitude compared to the state of the art. With feasible system improvements, such as the use of a cryo-compatible objective and measuring at a lower-loss location on the same diamond membrane, the rates would increase by more than two orders of magnitude. The resonant readout and narrow NV linewidths achieved in this work makes the cavity platform an extremely attractive building block in any quantum entanglement protocol based on NVs^{11,12,54,155}.

6

CONCLUSIONS

This work set out to overcome some of the disadvantages of an NV in diamond as a source of photonic qubits. The inefficient photon extraction out of the host material, the small fraction of coherent emission, the long radiative lifetime, as well as the broadened ZPL linewidths in microstructured diamond all impose limitations on experimental implementations of the NV as a node in a quantum network.

Here, ways to tackle all of the above-mentioned problems have been presented. Two improved methods for NV formation were developed – laser writing and carbon IPF – and were shown to result in narrow extrinsically broadened linewidths, both in bulk and in microstructured, 2-6 μm thick diamond. Laser writing of NVs with as low single-pulse energies as 5.8 nJ was made possible by the use of a t-SIL, which furthermore enabled us to create NVs both close to the diamond surface and deep within the bulk. An estimated 96% of the created NVs exhibited an extrinsically broadened linewidth below 150 MHz, being an exceptionally high probability of generating narrow-linewidth NVs compared to the usual method of NV formation based on the implantation of nitrogen^{108,127,130}. Even after etching a laser-written diamond down to 6 μm thickness, a median linewidth as low as 122 MHz could be measured. Carbon IPF, a method in which carbon was implanted directly into thin diamond microstructures to form NVs, resulted in 48% of the NVs having an extrinsically broadened linewidth below 150 MHz in structure thicknesses down to 1.9 μm . In both of the presented NV formation methods, the measured linewidths indicate an on average lower charge-noise level and reduced spectral diffusion compared to other approaches. Importantly, the large fraction of NVs exhibiting a narrow optical linewidth makes both laser writing and carbon IPF excellent candidates for applications based on spin-photon entanglement, as it is greatly beneficial to perform experiments with minimal pre-selection of NVs.

In order to increase the NV coherent photon flux, diamond platelets with NVs created via carbon IPF were incorporated into an open microcavity to make use of the Purcell-enhancement. The microcavity allowed full spectral tunability and increased both the collection efficiency, the fraction of coherent emission, and the flux of ZPL photons. The system was successfully operated at cryogenic temperatures, achieving finesse values reaching ~ 7900 . ZPL count rates 30 times higher compared to NVs located outside the cavity were detected under off-resonant excitation. An overall Purcell-enhancement of up to 1.9 was measured, corresponding to more than 46% of the photons emitted into the ZPL, to be compared to the NV Debye-Waller factor of 2.55%⁵⁸. The achieved count rates under off-resonant excitation, reaching 140 kcts/s even far from saturation, surpass the current state-of-the-art photonic interfaces based on SILs⁵⁴ by a factor of 4.3. Finally, for the first time for an NV in diamond, resonant excitation and ZPL readout was used

to successfully measure NV resonance fluorescence with a signal-to-background ratio higher than 1 without relying on temporal filtering.

Projecting the current system efficiency to applications relying on two-mode interference and assuming the use of the Barrett-Kok protocol¹⁵⁸ would result in entanglement rates increased by more than an order of magnitude. With feasible system improvements, such as using a better suited low-temperature objective and sampling a lower-intrinsic-loss area on the diamond platelet, one could envision increasing the entanglement rates by more than two orders of magnitude. The low-charge-noise NVs, the resonant readout and the high coherent photon flux together make the NV-cavity platform an extremely attractive spin-photon interface, and paves the way for using it in a wide range of applications in the area of quantum communication.

7

OUTLOOK

In this work, progress on a number of topics related to the use of NVs for quantum applications has been described. There are a number of further directions to be explored.

The creation of NVs at specified locations inside diamond opens up exciting possibilities. With improved positioning accuracy, demonstrated in-plane by laser-induced local annealing²²⁷, and with future improvements in the accuracy in depth through delta-doping¹³⁴, laser writing into more complex photonic structures can be realized. The crucial aspect is to maintain the quality of the diamond surface by keeping a low laser intensity at its interface to air. Being able to incorporate low-charge-noise NVs into waveguiding structures such as pillars^{96,97,295} would enable the use of laser-written NVs in NV-based sensing⁹⁵. Laser writing directly into etched diamond platelets^{269,270,285}, with certain progress demonstrated in this work, would make the incorporation of narrowlinewidth NVs into open microcavities possible^{58,60–62,64}. Moreover, laser writing offers promising capabilities such as the creation of three-dimensional NV arrays²⁷⁹ and direct writing of carbon-based electrodes^{280,281}.

Our open microcavity currently operates as an efficient photonic interface to the ZPL photons emitted by an NV. This is an important step towards implementing the system as a coherent spin-photon interface, which in turn is a stepping stone for the ultimate goal of using NVs as nodes in a quantum network. Already now, with the possibility of resonant excitation and readout, the NV and its optical coherence can be explored under resonant excitation. The single-photon indistinguishability could be measured in a Hong-Ou-Mandel experiment and pulsed resonant excitation could be used to extract the optical T_2 and T_2^* time. A different NV would most probably not have the charge-trap-related hopping behavior measured here, reducing the amount of post-processing needed to filter out the counts on resonance.

Looking forward, the most relevant system improvements on a short timescale are related to the overall efficiency of the system. One of the main limitations of the system is the surface quality of the diamond platelet. Finding a different NV with the same coupling strength but positioned at a lower-loss location in the diamond would increase the system efficiency from 15.8% to 30.1%. The overall surface quality could be improved with a new, commercially available diamond polishing method, resulting in less than 0.1 nm rms surface roughness³¹⁴. Interface-related losses could be mitigated further by depositing a thin oxide layer of SiO_2 on the top surface of the diamond via atomic-layer deposition (ALD)²⁶⁴. This would reduce the refractive index contrast between the air and the diamond, decreasing the sensitivity to scattering losses at the interface, and possibly also result in a smoother interface to the air³¹⁵. Reduced surface scattering would enable operation in a diamond-confined mode, which typically gives a higher Purcell-

enhancement owing to the greater electric field strength at the location of the NV.

Higher Purcell-factors could also be reached by working with a thinner diamond platelet. In the compromise between maintaining bulk-like NV optical properties and achieving a high Purcell-enhancement, we have worked with $\sim 2 \mu\text{m}$ thick diamonds with NVs created via carbon IPF. Showing no trend of increasing NV linewidths with decreasing structure thickness, carbon IPF is a promising method for working with even thinner diamonds. The spectral diffusion can further be mitigated by using a laser resonant with NV^0 to stabilize the negative charge state³¹³. A recent method achieving increased NV optical coherence with careful surface treatment and oxygen annealing could be greatly beneficial for our system, provided the approach results in narrower NV linewidths¹³². Another compelling technique, only employed for SnVs until now, uses blue illumination to saturate the charge environment and reduce the charge noise¹⁹¹.

The achievable count rates depend not only on the properties of the emitter, but also on the performance of the cavity. A way to achieve higher cavity outcoupling efficiencies is to use a low-index-terminated (L-terminated) bottom mirror, with SiO_2 as the top DBR layer instead of Ta_2O_5 . This gives an increased reflectivity with respect to diamond and an increase in the Purcell-enhancement, with a higher leakage of photons through the top mirror as a consequence. For optimal coupling and a field antinode at the location of the NV, L-terminated bottom mirrors would require positioning of the NV at $\lambda/2$ distance from the bottom mirror. The use of L-terminated mirrors would furthermore set higher requirements on the diamond surface quality, as there would be a field antinode on either one or both diamond surfaces depending on the type of mode.

Finally, the excitation and detection efficiency of the system depends also on the external optics. The suppression of the resonant excitation laser could be improved by using a more dedicated aberration-corrected system for focusing and collecting at low temperature. This would increase the signal-to-noise ratio and make it possible to detect weaker resonance fluorescence signals, hopefully mapping more of the low-temperature excited-state structure of the NV.

The coupled NV-cavity system can be used as a spin-photon interface. High-fidelity spin-state control could be realized inside the cavity by incorporating MW striplines²⁶⁸, as long as MW-induced heating and cavity drift can be mitigated. We have performed proof-of-principle tests of a MW stripline created via photolithography and lift-off on a flat cavity mirror substrate. The results are shown in Fig. 7.1. For NVs positioned right above the stripline, we record Rabi frequencies between 8 and 12 MHz, corresponding to a π -pulse length between 38 and 61 ns. For an NV as far as $110 \mu\text{m}$ from the stripline, we record a Rabi frequency of 2.6 MHz. This is within the diamond positioning accuracy achieved using micromanipulators. Implementing an additional lead would allow for electric-field tuning of the NV emission frequency⁴¹.

Ultimately, spin-spin entanglement between remote NVs using previously developed protocols^{41,54,158} should be possible. Applying quantum frequency conversion to convert the ZPL photons to telecom wavelengths^{160,316,317} would reduce the photon losses in optical fibers and remove the need for electric-field tuning of the NV emission. As the cavity increases the coherent photon flux and thereby the entanglement success probability, it is also beneficial for the use of NVs as quantum repeaters, distributing entanglement over even larger distances^{318–320}.

Finally, we can discuss the general applicability of our system. Focusing on defects

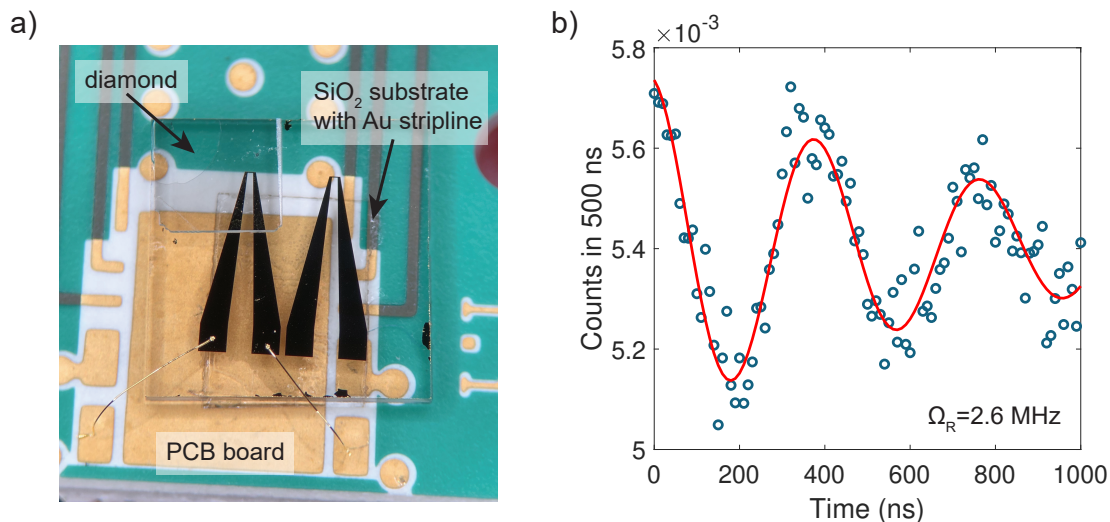


Figure 7.1.: A MW stripline for NV spin-state manipulation. (a) A high-NV-density diamond is placed above a gold stripline, fabricated on a silica substrate and wire-bonded to a PCB. (b) Spin Rabi oscillations with a frequency of 2.6 MHz, measured on an NV 110 μm away from the stripline.

in diamond and comparing with recent progress demonstrated on the incorporation of GeV and SiV⁻ into open microcavities^{172,187,299}, we can conclude that by changing the DBR coating of the mirrors to adjust for a different emission wavelength, we could easily adapt our system also to other color centers. With the wide applicability of the cavity platform, the results demonstrated in this work pave the way for faster and more efficient long-distance quantum communication based on defects in diamond.

A

SIMULATING THE EXTENT OF A LASER FOCUS VIA RAY TRACING

Focusing light from a low-refractive index material such as air into a high-refractive index material such as diamond through a planar interface introduces spherical aberrations. The aberrations increase the extent of the focus inside the diamond compared to the diffraction limit, introduced in Section 2.2.5.1. In this section, we use ray tracing to calculate the increased extent of the focus due to spherical aberrations. Ray tracing is a simplification, as it does not take into account the temporal extent or spatial intensity variation of a beam, but nevertheless provides a good approximation of the spatial extent of the focus.

A.1 Focusing without a SIL

We first consider individual rays impinging on a flat interface between a region with refractive index n_1 , assumed to be air, and a region with refractive index n_2 , with $n_2 > n_1$. To focus light not at the interface between the materials, but within the material with refractive index n_2 , either the focusing optics has to be moved down a distance d^* , or the interface between the two materials has to be moved up a distance d^* . The physical result will be the same in both cases.

In Fig. A.1a, no SIL is used to focus the light. The angle of the incoming ray is set by θ_1 ; its maximal value, $\theta_{1,max}$, is given by the focusing numerical aperture (NA):

$$\text{NA} = \sin(\theta_{1,max}) \quad (\text{A.1})$$

We use Snell's law to calculate the angle of refraction θ_2 within the high-index material:

$$n_1 \sin(\theta_1) = n_2 \sin(\theta_2) \quad (\text{A.2})$$

which gives, for $n_1 = 1$,

$$\theta_2 = \arcsin\left(\frac{\sin(\theta_1)}{n_2}\right) \quad (\text{A.3})$$

We turn to the triangles in panels 1 and 2 in Fig. A.1a, which give

$$x_1 = d^* \tan(\theta_1) \quad (\text{A.4})$$

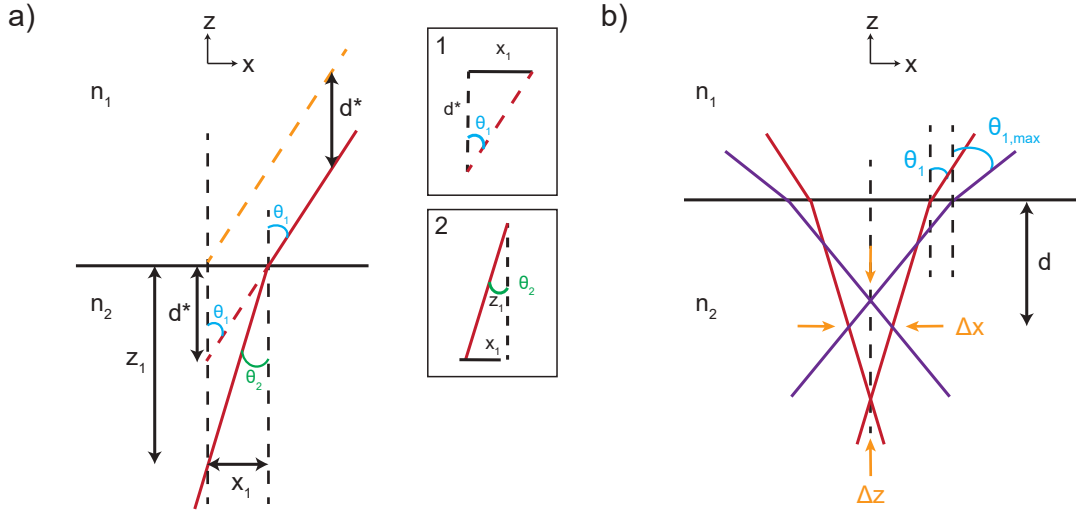


Figure A.1.: Ray tracing at the interface between two materials. (a) Directly focusing light from a material with refractive index n_1 into a material with refractive index n_2 . The distance d^* is defined as the distance which the interface between the two materials has been moved closer with respect to the focusing optics. (b) Spherical aberrations lead to an extended focus both across (Δx) and along (Δz) the optical axis. The focusing depth d is defined as the distance from the point of minimum Δx to the interface between the two materials.

and

$$z_1 = \frac{x_1}{\tan(\theta_2)} \quad (\text{A.5})$$

with x_1 defined as the distance between the point at which a ray hits the interface between the two materials and the optical axis. z_1 is the depth within the high-index material at which the ray defined by x_1 crosses the optical axis.

We define Δx as the in-plane focal spread and Δz as the focal spread along the optical axis. We further introduce the focusing depth d , which is the distance from the point of minimum Δx to the diamond surface. See Fig. A.1b. Note that d differs from the distance d^* .

We now define the focal spread *along* the optical axis as

$$\Delta z = \lim_{\theta_1 \rightarrow 0} [z_1(\theta_{1,max}) - z_1(\theta_1)] \quad (\text{A.6})$$

In order to derive the focal spread *across* the optical axis, we describe a point x along the refracted beam as a function of the depth z as

$$x = -\frac{x_1}{z_1}z + x_1 \quad (\text{A.7})$$

where the location of minimal spread Δx is given by the z that satisfies

$$x(\theta_{1,max}) = -x(\theta_1) \quad (\text{A.8})$$

for $\theta_1 \in [0, \theta_{1,max}]$. We denote this value of z as z_{cross} and the corresponding absolute value of x given by Eq. (A.7) as x_{cross} . Then, the spread across the optical axis is given by

$$\Delta x = 2 \cdot \max(x_{cross}) \quad (\text{A.9})$$

The resulting focal volume is calculated as the volume of a spheroid by

$$V = \frac{4\pi}{3} \left(\frac{\Delta x}{2} \right)^2 \frac{\Delta z}{2} = \frac{(\Delta x)^2 \cdot \Delta z}{2} \quad (\text{A.10})$$

Finally,

$$A = \pi x_1^2 \quad (\text{A.11})$$

gives the extent of the beam, or the exposed area, at the interface between the low-refractive-index region and the high-refractive-index region.

A.2 Focusing with an h-SIL

We now turn to the case of focusing through a hemispherical SIL, or h-SIL, as shown in Fig. A.2a. The surrounding medium is again assumed to be air, $n_1 = 1$, the h-SIL has a refractive index $n_2 > n_1$, and the material into which the rays are focused has a refractive index of $n_3 > n_2$. In order to be able to express Δx and Δz , a few more angles have to be considered compared to the case of focusing without a SIL.

The triangle in panel 1 in Fig. A.2a gives an expression for the angle α , defined as the angle between a ray impinging on the SIL surface and the normal of that surface.

$$\frac{r}{\sin(\theta_1)} = \frac{d^*}{\sin \alpha} \quad (\text{A.12})$$

$$\alpha = \arcsin \left(\frac{d^* \sin(\theta_1)}{r} \right) \quad (\text{A.13})$$

r is the radius of the SIL and d^* is defined as before. Snell's law gives

$$\theta_2 = \arcsin \left(\frac{\sin(\alpha)}{n_2} \right) \quad (\text{A.14})$$

The triangle in panel 2 yields

$$\frac{x_1}{\sin(\alpha - \theta_2)} = \frac{r}{\sin(\gamma)} \quad (\text{A.15})$$

which results in

$$x_1 = \frac{r \sin(\alpha - \theta_2)}{\sin(\gamma)} \quad (\text{A.16})$$

The angle γ can be expressed in terms of θ_1 and θ_2 via $\gamma = \pi - \delta - \alpha + \theta_2 = \pi/2 + \theta_1 + \theta_2$. The triangle in panel 3 gives $\pi/2 - \lambda = \pi - \theta_2 - \tau = \pi/2 - \theta_2 - \theta_1$, which results in $\lambda = \theta_1 + \theta_2$. This enables us to express the last angle of refraction, θ_3 , via Snell's law:

$$n_2 \sin(\lambda) = n_3 \sin(\theta_3) \quad (\text{A.17})$$

$$\theta_3 = \arcsin \left(\frac{n_2 \sin(\lambda)}{n_3} \right) \quad (\text{A.18})$$

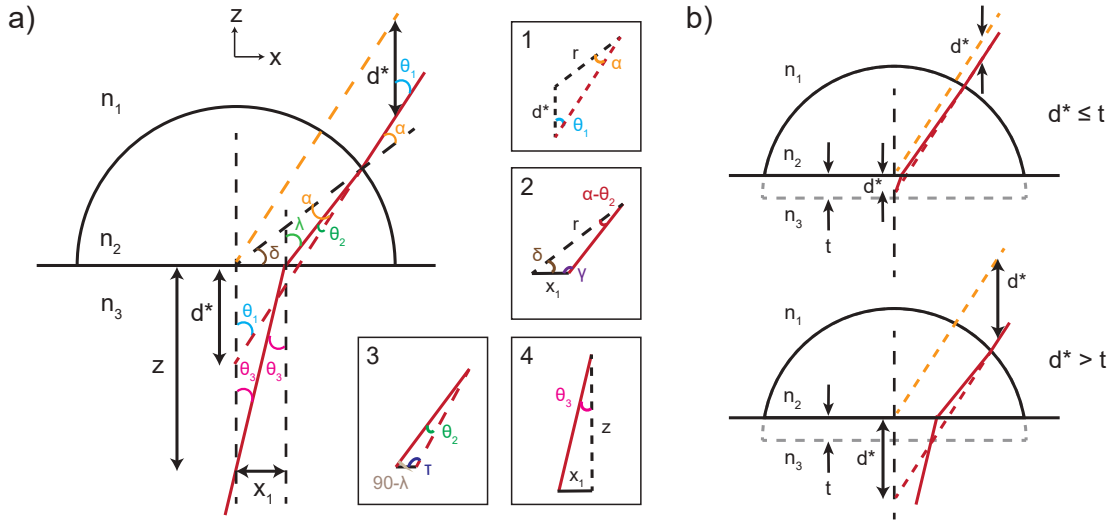


Figure A.2.: Ray tracing in the case of a SIL. (a) Focusing light from a material with refractive index n_1 into a material with refractive index n_3 through a SIL with refractive index n_2 . (b) The two cases of focusing through a t-SIL: lowering the focus a distance d^* smaller than or equal to the SIL truncation t , or lowering the focus a distance d^* larger than the truncation t .

from which, using the triangle in panel 4, we get an expression for the depth z :

$$z = \frac{x_1}{\tan(\theta_3)} \quad (\text{A.19})$$

Finally, we get the extent of the focus Δz along the optical axis by using Eq. (A.6).

We describe a point x along the refracted beam within the material with refractive index n_3 :

$$x = -z \tan(\theta_3) + x_1 \quad (\text{A.20})$$

Just as for focusing without a SIL, the extent of the focus Δx across the optical axis is then given by Eq. (A.9), with x_{cross} given according to Eq. (A.20) by the value of z that satisfies Eq. (A.8).

The exposed area on the $n_2 - n_3$ interface is calculated using Eq. (A.11), with x_1 given by Eq. (A.16). The focal volume is calculated with Eq. (A.10).

A.3 Focusing with a t-SIL

Focusing through a truncated h-SIL, a t-SIL, is similar to the case of focusing through an h-SIL, but involves two regimes – focusing at a depth d^* smaller than or equal to the truncation t of the SIL, and focusing at a depth d^* larger than the truncation. Both cases are illustrated in Fig. A.2b.

The spherical aberrations in the case of a t-SIL are calculated in the same way as for an h-SIL, except for slightly adjusted expressions for the angles α and λ and the distance x_1 :

$$\alpha = \arcsin\left(\frac{|t - d^*| \sin(\theta_1)}{r}\right) \quad (\text{A.21})$$

$$\lambda = \begin{cases} \theta_1 + \theta_2 - \alpha & \text{if } d^* \leq t \\ \theta_1 - \theta_2 + \alpha & \text{if } d^* > t \end{cases} \quad (\text{A.22})$$

$$x_1 = \begin{cases} \frac{(t \sin(\lambda) - r \sin(\theta_2))}{\sin(\pi/2 - \lambda)} & \text{if } d^* \leq t \\ \frac{(t \sin(\lambda) + r \sin(\theta_2))}{\sin(\pi/2 - \lambda)} & \text{if } d^* > t \end{cases} \quad (\text{A.23})$$

The focal spread, focal volume, and exposed area on the surface are calculated using Eq. (A.9), Eq. (A.6), Eq. (A.10) and Eq. (A.11) following the approach for the h-SIL.

B

THE DIAMOND-CAVITY MODE STRUCTURE

A way to extract the mode number and cavity length for a specific cavity resonance is by fitting the cavity mode structure. The mode structure can in turn be measured by sweeping the cavity length over multiple free spectral ranges under green illumination and recording the light leaking out of the cavity as a function of wavelength. In this section, we qualitatively express the mode structure of a bare cavity and a cavity with a diamond membrane using one-dimensional models.

B.1 Bare cavity

For a bare cavity, the cavity length at resonance is given by $l_{cav} = m \frac{\lambda_r}{2}$, with λ_r being the resonance wavelength and m an integer. The FSR in length is given by the difference in the cavity length between consecutive modes:

$$\Delta d_{m,m-1} = m \frac{\lambda_r}{2} - (m-1) \frac{\lambda_r}{2} = \frac{\lambda_r}{2} = \frac{c}{2\nu_r} \quad (\text{B.1})$$

where ν_r is the resonance frequency and c the speed of light. This leads to the difference in cavity length between any two modes being

$$\Delta d_{\Delta m} = \Delta m \frac{c}{2\nu} \quad (\text{B.2})$$

where Δm is the integer difference in the mode number between the modes in question.

Within a mode, the difference in cavity length for two wavelengths λ_1 and λ_2 is given by

$$\Delta d_{\lambda_1, \lambda_2} = m \frac{\lambda_1}{2} - m \frac{\lambda_2}{2} = \frac{m}{2} \left(\frac{c}{\nu_1} - \frac{c}{\nu_2} \right) = \frac{mc}{2} \left(\frac{\nu_2 - \nu_1}{\nu_2 \nu_1} \right) \quad (\text{B.3})$$

which can be re-expressed as

$$\Delta d_{\Delta \nu} = \frac{mc}{2\nu_0} \left(\frac{-\Delta \nu}{\Delta \nu + \nu_0} \right) \quad (\text{B.4})$$

where $\Delta \nu = \nu_1 - \nu_2$. With this, any difference in the cavity length can be derived as the

sum of Eq. (B.2) and Eq. (B.4),

$$\Delta d = \Delta d_{\Delta\nu} + \Delta d_{\Delta m} = \frac{c}{2\nu_0} \left(\Delta m - (m_0 + \Delta m) \frac{\Delta\nu}{\Delta\nu + \nu_0} \right) \quad (\text{B.5})$$

where the mode number is expressed as $m = m_0 + \Delta m$.

We model the displacement of the bottom mirror as a function of voltage applied to the piezo actuator it rests on with a nonlinear function $D(V)$:

$$D(V) = A \frac{V}{B - V} \quad (\text{B.6})$$

where A and B are fitting parameters. The difference in cavity length is connected to the piezo displacement via

$$\Delta d = -(D(V) - D(V_0)) \quad (\text{B.7})$$

since applying a higher voltage on the piezo actuator leads to a shorter cavity. With the given expression for the piezo nonlinearity, this models the change in cavity length: for small applied voltages, the displacement of the bottom mirror is linear, while for large applied voltages (approaching the maximum possible displacement of the piezo actuator) the cavity length does not change much. By setting Eq. (B.5) and Eq. (B.7) equal and solving for $\Delta\nu$, we obtain an expression for the bare cavity mode structure:

$$\Delta\nu = \nu_0 \frac{\Delta m + \frac{2\nu_0}{c} (D(V) - D(V_0))}{m_0 - \frac{2\nu_0}{c} (D(V) - D(V_0))} \quad (\text{B.8})$$

Here, the resonance frequency ν of a mode with mode number $m = m_0 + \Delta m$ corresponds to an applied voltage V , the resonance frequency ν_0 of a mode with mode number m_0 corresponds to an applied voltage V_0 , and c is the speed of light.

B.2 Cavity with diamond

For a cavity with a thin diamond slab inside, one can use a simple one-dimensional model to describe the mode structure, following Ref. 147. The model is an approximation, as it neglects the transverse Gaussian extent of the beam as well as the Gouy phase of the cavity mode. It furthermore works under the assumption of lossless mirrors. With high-index-terminated mirrors, giving a π phase shift upon reflection, the model resonance frequencies are given by solutions to the transcendental equation

$$(1 + n_d) \sin \left(\frac{2\pi\nu}{c} [L + t_d(n_d - 1)] \right) = (1 - n_d) \sin \left(\frac{2\pi\nu}{c} [L - t_d(n_d + 1)] \right) \quad (\text{B.9})$$

which yields resonances every $\frac{c}{2\nu}$ in cavity length, just as for the case of a bare cavity. Here, n_d is the refractive index and t_d the thickness of the diamond slab and L the total cavity length (including both the diamond and the air gap).

For large mode numbers, one can write ν in terms of its deviation $\delta\nu$ from an integer

multiple m of the average free spectral range:

$$\nu = \delta\nu + \frac{mc/2}{L + (n_d - 1)t_d} \quad (\text{B.10})$$

Neglecting $\delta\nu$ on the right-hand side of Eq.(B.9), one finally gets

$$\nu \approx \frac{c}{2\pi[L + (n_d - 1)t_d]} \cdot \left\{ \pi m - (-1)^m \cdot \sin^{-1} \left[\frac{n_d - 1}{n_d + 1} \sin \left(\frac{m\pi[L - (n_d + 1)t_d]}{L + (n_d - 1)t_d} \right) \right] \right\} \quad (\text{B.11})$$

for the fundamental mode frequencies. Again, we translate the total cavity length into the bottom mirror displacement via $L = L_0 + \Delta d$, with Δd given by Eq. (B.7) and L_0 by

$$L_0 = m_0 \cdot \frac{c}{2\nu_0} + t_d - n_d t_d \quad (\text{B.12})$$

so that it corresponds to the cavity length for mode m_0 .

BIBLIOGRAPHY

1. Licklider, J. C. R. & Taylor, R. W. The Computer as a Communication Device. *Science and Technology* **76**, 21–31 (1968).
2. Abbate, J. *Inventing the Internet* (MIT Press, 1999).
3. Hauben, M. Behind the Net: The Untold Story of the ARPANET and Computer Science (Chapter 7). *First Monday* **3** (1998).
4. Elliott, C. *et al.* Current status of the DARPA Quantum Network in *Quantum Information and Computation III* **5815** (2005), 138–149.
5. Peev, M. *et al.* The SECOQC quantum key distribution network in Vienna. *New Journal of Physics* **11**, 75001 (2009).
6. Peng, C. Z. *et al.* Metropolitan all-pass and inter-city quantum communication network. *Optics Express* **18**, 27217–27225 (2010).
7. Sasaki, M. *et al.* Field test of quantum key distribution in the Tokyo QKD Network. *Optics Express* **19**, 10387–10409 (2011).
8. Stucki, D. *et al.* Long-term performance of the SwissQuantum quantum key distribution network in a field environment. *New Journal of Physics* **13**, 123001 (2011).
9. Joshi, S. K. *et al.* A trusted node-free eight-user metropolitan quantum communication network. *Science Advances* **6**, eaba0959 (2020).
10. Chen, T. Y. *et al.* Implementation of a 46-node quantum metropolitan area network. *npj Quantum Information* **7**, 134 (2021).
11. Pompili, M. *et al.* Realization of a multinode quantum network of remote solid-state qubits. *Science* **372**, 259–264 (2021).
12. Hermans, S. L. N. *et al.* Qubit teleportation between non-neighbouring nodes in a quantum network. *Nature* **605**, 663–668 (2022).
13. Wehner, S., Elkouss, D. & Hanson, R. Quantum internet: A vision for the road ahead. *Science* **362**, eaam9288 (2018).
14. Clarke, J. & Wilhelm, F. K. Superconducting quantum bits. *Nature* **453**, 1031–1042 (2008).
15. Devoret, M. H. & Schoelkopf, R. J. Superconducting Circuits for Quantum Information: An Outlook. *Science* **339**, 1169–1174 (2013).
16. Ritter, S. *et al.* An elementary quantum network of single atoms in optical cavities. *Nature* **484**, 195–200 (2012).
17. Saffman, M. Quantum computing with atomic qubits and Rydberg interactions: Progress and challenges. *Journal of Physics B: Atomic, Molecular and Optical Physics* **49**, 202001 (2016).
18. Duan, L. M. & Monroe, C. Colloquium: Quantum networks with trapped ions. *Reviews of Modern Physics* **82**, 1209–1224 (2010).
19. Schindler, P. *et al.* A quantum information processor with trapped ions. *New Journal of Physics* **15**, 123012 (2013).

20. Bruzewicz, C. D., Chiaverini, J., McConnell, R. & Sage, J. M. Trapped-ion quantum computing: Progress and challenges. *Applied Physics Reviews* **6**, 021314 (2019).
21. Matthews, J. C., Politi, A., Stefanov, A. & O'Brien, J. L. Manipulation of multi-photon entanglement in waveguide quantum circuits. *Nature Photonics* **3**, 346–350 (2009).
22. Crespi, A. *et al.* Integrated photonic quantum gates for polarization qubits. *Nature Communications* **2**, 566 (2011).
23. Zhong, H. S. *et al.* Quantum computational advantage using photons. *Science* **370**, 1460–1463 (2020).
24. Koppens, F. H. *et al.* Driven coherent oscillations of a single electron spin in a quantum dot. *Nature* **442**, 766–771 (2006).
25. Pla, J. J. *et al.* A single-atom electron spin qubit in silicon. *Nature* **489**, 541–544 (2012).
26. Maurand, R. *et al.* A CMOS silicon spin qubit. *Nature Communications* **7**, 13575 (2016).
27. Warburton, R. J. Single spins in self-assembled quantum dots. *Nature Materials* **12**, 483–493 (2013).
28. Kroutvar, M. *et al.* Optically programmable electron spin memory using semiconductor quantum dots. *Nature* **432**, 81–84 (2004).
29. Press, D., Ladd, T. D., Zhang, B. & Yamamoto, Y. Complete quantum control of a single quantum dot spin using ultrafast optical pulses. *Nature* **456**, 218–221 (2008).
30. Zhai, L. *et al.* Low-noise GaAs quantum dots for quantum photonics. *Nature Communications* **11**, 4745 (2020).
31. Childress, L. & Hanson, R. Diamond NV centers for quantum computing and quantum networks. *MRS Bulletin* **38**, 134–138 (2013).
32. Awschalom, D. D., Hanson, R., Wrachtrup, J. & Zhou, B. B. Quantum technologies with optically interfaced solid-state spins. *Nature Photonics* **12**, 516–527 (2018).
33. Kimble, H. J. The quantum internet. *Nature* **453**, 1023–1030 (2008).
34. Wolfowicz, G. *et al.* Quantum guidelines for solid-state spin defects. *Nature Reviews Materials* **6**, 1191–1191 (2021).
35. Gruber, A. *et al.* Scanning confocal optical microscopy and magnetic resonance on single defect centers. *Science* **276**, 2012–2014 (1997).
36. Maurer, P. C. *et al.* Room-Temperature Quantum Bit Memory Exceeding One Second. *Science* **336**, 1283–1286 (2012).
37. Abobeih, M. H. *et al.* One-second coherence for a single electron spin coupled to a multi-qubit nuclear-spin environment. *Nature Communications* **9**, 2552 (2018).
38. Doherty, M. W. *et al.* The nitrogen-vacancy colour centre in diamond. *Physics Reports* **528**, 1–45 (2013).
39. Radko, I. P. *et al.* Determining the internal quantum efficiency of shallow-implanted nitrogen-vacancy defects in bulk diamond. *Optics Express* **24**, 27715–27725 (2016).

40. Tamarat, P. *et al.* Stark shift control of single optical centers in diamond. *Physical Review Letters* **97**, 083002 (2006).
41. Bernien, H. *et al.* Two-photon quantum interference from separate nitrogen vacancy centers in diamond. *Physical Review Letters* **108**, 043604 (2012).
42. Neumann, P. *et al.* Single-shot readout of a single nuclear spin. *Science* **329**, 542–544 (2010).
43. Robledo, L. *et al.* High-fidelity projective read-out of a solid-state spin quantum register. *Nature* **477**, 574–578 (2011).
44. Taminiau, T. H. *et al.* Detection and control of individual nuclear spins using a weakly coupled electron spin. *Physical Review Letters* **109**, 137602 (2012).
45. Bradley, C. E. *et al.* A Ten-Qubit Solid-State Spin Register with Quantum Memory up to One Minute. *Physical Review X* **9**, 31045 (2019).
46. Itoh, K. M. & Watanabe, H. Isotope engineering of silicon and diamond for quantum computing and sensing applications. *MRS Communications* **4**, 143–157 (2014).
47. Meijer, J. *et al.* Generation of single color centers by focused nitrogen implantation. *Applied Physics Letters* **87**, 261909 (2005).
48. Rabeau, J. R. *et al.* Implantation of labelled single nitrogen vacancy centers in diamond using ^{15}N . *Applied Physics Letters* **88**, 023113 (2006).
49. Chen, Y. C. *et al.* Laser writing of coherent colour centres in diamond. *Nature Photonics* **11**, 77–80 (2017).
50. Rondin, L. *et al.* Magnetometry with nitrogen-vacancy defects in diamond. *Reports on Progress in Physics* **77**, 056503 (2014).
51. Chen, E. H. *et al.* High-sensitivity spin-based electrometry with an ensemble of nitrogen-vacancy centers in diamond. *Physical Review A* **95**, 053417 (2017).
52. Block, M. *et al.* Optically Enhanced Electric Field Sensing Using Nitrogen-Vacancy Ensembles. *Physical Review Applied* **16**, 024024 (2021).
53. Toyli, D. M., De Las Casas, C. F., Christle, D. J., Dobrovitski, V. V. & Awschalom, D. D. Fluorescence thermometry enhanced by the quantum coherence of single spins in diamond. *PNAS* **110**, 8417–8421 (2013).
54. Hensen, B. *et al.* Loophole-free Bell inequality violation using electron spins separated by 1.3 kilometres. *Nature* **526**, 682–686 (2015).
55. Stoneham, A. M. *Theory of Defects in Solids: Electronic Structure of Defects in Insulators and Semiconductors* (Oxford University Press, Oxford, 1975).
56. Batalov, A. *et al.* Temporal coherence of photons emitted by single nitrogen-vacancy defect centers in diamond using optical rabi-oscillations. *Physical Review Letters* **100**, 077401 (2008).
57. Robledo, L., Bernien, H., Sar, T. V. D. & Hanson, R. Spin dynamics in the optical cycle of single nitrogen-vacancy centres in diamond. *New Journal of Physics* **13**, 025013 (2011).

58. Riedel, D. *et al.* Deterministic enhancement of coherent photon generation from a nitrogen-vacancy center in ultrapure diamond. *Physical Review X* **7**, 20932–20943 (2017).
59. Kambs, B. & Becher, C. Limitations on the indistinguishability of photons from remote solid state sources. *New Journal of Physics* **20**, 115003 (2018).
60. Barbour, R. J. *et al.* A tunable microcavity. *Journal of Applied Physics* **110**, 053107 (2011).
61. Albrecht, R., Bommer, A., Deutsch, C., Reichel, J. & Becher, C. Coupling of a single nitrogen-vacancy center in diamond to a fiber-based microcavity. *Physical Review Letters* **110**, 243602 (2013).
62. Johnson, S. *et al.* Tunable cavity coupling of the zero phonon line of a nitrogen-vacancy defect in diamond. *New Journal of Physics* **17**, 122003 (2015).
63. Kaupp, H. *et al.* Purcell-Enhanced Single-Photon Emission from Nitrogen-Vacancy Centers Coupled to a Tunable Microcavity. *Physical Review Applied* **6**, 054010 (2016).
64. Flågan, S. *et al.* A diamond-confined open microcavity featuring a high quality-factor and a small mode-volume. *Journal of Applied Physics* **131**, 113102 (2022).
65. Field, J. E. The mechanical and strength properties of diamond. *Reports on Progress in Physics* **75**, 126505 (2012).
66. Konov, V. I. Laser in micro and nanoprocessing of diamond materials. *Laser and Photonics Reviews* **6**, 739–766 (2012).
67. Angus, J. C. Diamond synthesis by chemical vapor deposition: The early years. *Diamond and Related Materials* **49**, 77–86 (2014).
68. Schwander, M. & Partes, K. A review of diamond synthesis by CVD processes. *Diamond and Related Materials* **20**, 1287–1301 (2011).
69. Breeding, C. & Shigley, J. The "type" classification system of diamonds and its importance in gemology. *Gems and Gemology* **45**, 96–111 (2009).
70. *The Element Six CVD Diamond Handbook* (Element Six, 2021).
71. Loubser, J. H. N.; Van Wyk, J. A. Optical spin-polarisation in a triplet state in irradiated and annealed type 1b diamonds. *Diamond Research* **11**, 11–14 (1977).
72. Loubser, J. H. & Van Wyk, J. A. Electron spin resonance in the study of diamond. *Reports on Progress in Physics* **41**, 1201–1248 (1978).
73. Mita, Y. Change of absorption spectra in type-1b diamond with heavy neutron irradiation. *Physical Review B - Condensed Matter and Materials Physics* **53**, 11360–11364 (1996).
74. Davies, G. Dynamic Jahn-Teller distortions at trigonal optical centres in diamond. *Journal of Physics C: Solid State Physics* **12**, 2551–2566 (1979).
75. Du Preez, L. *Electron paramagnetic resonance and optical investigations of defect centres in diamond* PhD thesis (University of the Witwatersrand, 1965).
76. Rogers, L. J., Armstrong, S., Sellars, M. J. & Manson, N. B. Infrared emission of the NV centre in diamond: Zeeman and uniaxial stress studies. *New Journal of Physics* **10**, 103024 (2008).

77. Acosta, V. M., Jarmola, A., Bauch, E. & Budker, D. Optical properties of the nitrogen-vacancy singlet levels in diamond. *Physical Review B - Condensed Matter and Materials Physics* **82**, 2–5 (2010).
78. Collins, A. T. The Fermi level in diamond. *Journal of Physics Condensed Matter* **14**, 3743–3750 (2002).
79. Fuchs, G. D. *et al.* Excited-state spectroscopy using single spin manipulation in diamond. *Physical Review Letters* **101**, 117601 (2008).
80. Neumann, P. *et al.* Excited-state spectroscopy of single NV defects in diamond using optically detected magnetic resonance. *New Journal of Physics* **11**, 013017 (2009).
81. Gali, A., Fyta, M. & Kaxiras, E. Ab initio supercell calculations on nitrogen-vacancy center in diamond: Electronic structure and hyperfine tensors. *Physical Review B - Condensed Matter and Materials Physics* **77**, 155206 (2008).
82. Maze, J. R. *et al.* Properties of nitrogen-vacancy centers in diamond: the group theoretic approach. *New Journal of Physics* **13**, 25025 (2011).
83. Van Oort, E. & Glasbeek, M. Electric-field-induced modulation of spin echoes of N-V centers in diamond. *Chemical Physics Letters* **168**, 529–532 (1990).
84. Batalov, A. *et al.* Low Temperature Studies of the Excited-State Structure of Negatively Charged Nitrogen-Vacancy Color Centers in Diamond. *Physical Review Letters* **102**, 195506 (2009).
85. Tamarat, P. *et al.* Spin-flip and spin-conserving optical transitions of the nitrogen-vacancy centre in diamond. *New Journal of Physics* **10**, 045004 (2008).
86. Happacher, J. *et al.* Low-Temperature Photophysics of Single Nitrogen-Vacancy Centers in Diamond. *Physical Review Letters* **128**, 177401 (2022).
87. Ernst, S., Scheidegger, P. J., Diesch, S., Lorenzelli, L. & Degen, C. L. Temperature dependence of photoluminescence intensity and spin contrast in nitrogen-vacancy centers. *arXiv:2301.05091* (2023).
88. Happacher, J. *et al.* Temperature Dependent Photophysics of Single NV Centers in Diamond. *arXiv:2302.00011* (2023).
89. Baier, S. *et al.* Orbital and Spin Dynamics of Single Neutrally-Charged Nitrogen-Vacancy Centers in Diamond. *Physical Review Letters* **125**, 193601 (2020).
90. Davies, G. The Jahn-Teller effect and vibronic coupling at deep levels in diamond. *Reports on Progress in Physics* **44**, 787–830 (1981).
91. Manson, N. B., Harrison, J. P. & Sellars, M. J. Nitrogen-vacancy center in diamond: Model of the electronic structure and associated dynamics. *Physical Review B - Condensed Matter and Materials Physics* **74**, 104303 (2006).
92. Gupta, A., Hacquebard, L. & Childress, L. Efficient signal processing for time-resolved fluorescence detection of nitrogen-vacancy spins in diamond. *Journal of the Optical Society of America B* **33**, B28–B34 (2016).
93. Felton, S. *et al.* Hyperfine interaction in the ground state of the negatively charged nitrogen vacancy center in diamond. *Physical Review B - Condensed Matter and Materials Physics* **79**, 075203 (2009).

94. Chernobrod, B. M. & Berman, G. P. Spin microscope based on optically detected magnetic resonance. *Journal of Applied Physics* **97**, 014903 (2005).
95. Maletinsky, P. *et al.* A robust scanning diamond sensor for nanoscale imaging with single nitrogen-vacancy centres. *Nature Nanotechnology* **7**, 320–324 (2012).
96. Hedrich, N., Rohner, D., Batzer, M., Maletinsky, P. & Shields, B. J. Parabolic Diamond Scanning Probes for Single-Spin Magnetic Field Imaging. *Physical Review Applied* **14**, 064007 (2020).
97. Rohner, D. *et al.* (111)-Oriented, Single Crystal Diamond Tips for Nanoscale Scanning Probe Imaging of Out-of-Plane Magnetic Fields. *Applied Physics Letters* **115**, 192401 (2019).
98. Thiel, L. *et al.* Probing magnetism in 2D materials at the nanoscale with single-spin microscopy. *Science* **364**, 973–976 (2019).
99. Palm, M. L. *et al.* Imaging of Submicroampere Currents in Bilayer Graphene Using a Scanning Diamond Magnetometer. *Physical Review Applied* **17**, 054008 (2022).
100. Hedrich, N. *et al.* Nanoscale mechanics of antiferromagnetic domain walls. *Nature Physics* **17**, 574–577 (2021).
101. Steiner, M., Neumann, P., Beck, J., Jelezko, F. & Wrachtrup, J. Universal enhancement of the optical readout fidelity of single electron spins at nitrogen-vacancy centers in diamond. *Physical Review B - Condensed Matter and Materials Physics* **81**, 035205 (2010).
102. Waldherr, G. *et al.* Dark states of single nitrogen-vacancy centers in diamond unraveled by single shot NMR. *Physical Review Letters* **106**, 157601 (2011).
103. Manson, N. B. & Harrison, J. P. Photo-ionization of the nitrogen-vacancy center in diamond. *Diamond and Related Materials* **14**, 1705–1710 (2005).
104. Treussart, F. *et al.* Photoluminescence of single colour defects in 50 nm diamond nanocrystals. *Physica B: Condensed Matter* **376-377**, 926–929 (2006).
105. Beha, K., Batalov, A., Manson, N. B., Bratschitsch, R. & Leitenstorfer, A. Optimum photoluminescence excitation and recharging cycle of single nitrogen-vacancy centers in ultrapure diamond. *Physical Review Letters* **109**, 097404 (2012).
106. Dhomkar, S., Jayakumar, H., Zangara, P. R. & Meriles, C. A. Charge Dynamics in near-Surface, Variable-Density Ensembles of Nitrogen-Vacancy Centers in Diamond. *Nano Letters* **18**, 4046–4052 (2018).
107. Fu, K. M. C. *et al.* Observation of the dynamic Jahn-Teller effect in the excited states of nitrogen-vacancy centers in diamond. *Physical Review Letters* **103**, 256404 (2009).
108. Chu, Y. *et al.* Coherent optical transitions in implanted nitrogen vacancy centers. *Nano Letters* **14**, 1982–1986 (2014).
109. Bernien, H. *et al.* Heralded entanglement between solid-state qubits separated by three metres. *Nature* **497**, 86–90 (2013).
110. Acosta, V. M. *et al.* Dynamic stabilization of the optical resonances of single nitrogen-vacancy centers in diamond. *Physical Review Letters* **108**, 206401 (2012).
111. Loudon, R. *The quantum theory of light* (OUP Oxford, 2000).

112. Myers, B. A., Ariyaratne, A. & Jayich, A. C. Double-Quantum Spin-Relaxation Limits to Coherence of Near-Surface Nitrogen-Vacancy Centers. *Physical Review Letters* **118**, 197201 (2017).
113. Redman, D. A., Brown, S., Sands, R. H. & Rand, S. C. Spin dynamics and electronic states of N-V centers in diamond by EPR and four-wave-mixing spectroscopy. *Physical Review Letters* **67**, 3420–3423 (1991).
114. Norambuena, A. *et al.* Spin-lattice relaxation of individual solid-state spins. *Physical Review B* **97**, 094304 (2018).
115. Balasubramanian, G. *et al.* Ultralong spin coherence time in isotopically engineered diamond. *Nature Materials* **8**, 383–387 (2009).
116. Acosta, V. M. *et al.* Diamonds with a high density of nitrogen-vacancy centers for magnetometry applications. *Physical Review B - Condensed Matter and Materials Physics* **80**, 115202 (2009).
117. Mizuochi, N. *et al.* Coherence of single spins coupled to a nuclear spin bath of varying density. *Physical Review B - Condensed Matter and Materials Physics* **80**, 041201 (2009).
118. Herbschleb, E. D. *et al.* Ultra-long coherence times amongst room-temperature solid-state spins. *Nature Communications* **10**, 3766 (2019).
119. Bar-Gill, N., Pham, L. M., Jarmola, A., Budker, D. & Walsworth, R. L. Solid-state electronic spin coherence time approaching one second. *Nature Communications* **4**, 1743 (2013).
120. Yamamoto, T. *et al.* Extending spin coherence times of diamond qubits by high-temperature annealing. *Physical Review B - Condensed Matter and Materials Physics* **88**, 075206 (2013).
121. Davies, G., Lawson, S. C., Collins, A. T., Mainwood, A. & Sharp, S. J. Vacancy-related centers in diamond. *Physical Review B* **46**, 13157–13170 (1992).
122. Deák, P., Aradi, B., Kaviani, M., Frauenheim, T. & Gali, A. Formation of NV centers in diamond: A theoretical study based on calculated transitions and migration of nitrogen and vacancy related defects. *Physical Review B - Condensed Matter and Materials Physics* **89**, 075203 (2014).
123. Lomer, J. N. & Wild, A. M. A. Electron spin resonance in electron irradiated diamond annealed to high temperatures. *Radiation Effects* **17**, 37–44 (1973).
124. Naydenov, B. *et al.* Increasing the coherence time of single electron spins in diamond by high temperature annealing. *Applied Physics Letters* **97**, 242511 (2010).
125. Pezzagna, S., Naydenov, B., Jelezko, F., Wrachtrup, J. & Meijer, J. Creation efficiency of nitrogen-vacancy centres in diamond. *New Journal of Physics* **12**, 065017 (2010).
126. Lekavicius, I., Oo, T. & Wang, H. Diamond Lamb wave spin-mechanical resonators with optically coherent nitrogen vacancy centers. *Journal of Applied Physics* **126**, 214301 (2019).
127. Kasperczyk, M. *et al.* Statistically modeling optical linewidths of nitrogen vacancy centers in microstructures. *Physical Review B* **102**, 75312 (2020).

128. Ruf, M. *et al.* Optically coherent nitrogen-vacancy centers in micrometer-thin etched diamond membranes. *Nano Letters* **19**, 3987–3992 (2019).
129. Junk, G. & Svec, H. J. The absolute abundance of the nitrogen isotopes in the atmosphere and compressed gas from various sources. *Geochimica et Cosmochimica Acta* **14**, 234–243 (1958).
130. Van Dam, S. B. *et al.* Optical coherence of diamond nitrogen-vacancy centers formed by ion implantation and annealing. *Physical Review B* **99**, 161203 (2019).
131. Chakravarthi, S., Pederson, C., Kazi, Z., Ivanov, A. & Fu, K. M. C. Impact of surface and laser-induced noise on the spectral stability of implanted nitrogen-vacancy centers in diamond. *Physical Review B* **104**, 1–8 (2021).
132. Sangtawesin, S. *et al.* Origins of Diamond Surface Noise Probed by Correlating Single-Spin Measurements with Surface Spectroscopy. *Physical Review X* **9**, 1–17 (2019).
133. McLellan, C. A. *et al.* Patterned Formation of Highly Coherent Nitrogen-Vacancy Centers Using a Focused Electron Irradiation Technique. *Nano Letters* **16**, 2450–2454 (2016).
134. Ohno, K. *et al.* Engineering shallow spins in diamond with nitrogen delta-doping. *Applied Physics Letters* **101**, 082413 (2012).
135. Ishikawa, T. *et al.* Optical and spin coherence properties of nitrogen-vacancy centers placed in a 100 nm thick isotopically purified diamond layer. *Nano Letters* **12**, 2083–2087 (2012).
136. Smith, J. M., Meynell, S. A., Bleszynski Jayich, A. C. & Meijer, J. Colour centre generation in diamond for quantum technologies. *Nanophotonics* **8**, 1889–1906 (2019).
137. Gao, S. *et al.* Laser-induced color centers in crystals. *Optics and Laser Technology* **146**, 107527 (2022).
138. Kononenko, V. V. *et al.* Nitrogen-vacancy defects in diamond produced by femtosecond laser nanoablation technique. *Applied Physics Letters* **111**, 081101 (2017).
139. Berzins, A., Grube, H., Sprugis, E., Vaivars, G. & Fescenko, I. Impact of Helium Ion Implantation Dose and Annealing on Dense Near-Surface Layers of NV Centers. *Nanomaterials* **12**, 1–13 (2022).
140. Kleinsasser, E. E. *et al.* High density nitrogen-vacancy sensing surface created via He⁺ ion implantation of ¹²C diamond. *Applied Physics Letters* **108**, 202401 (2016).
141. De Oliveira, F. F. *et al.* Toward Optimized Surface δ -Profiles of Nitrogen-Vacancy Centers Activated by Helium Irradiation in Diamond. *Nano Letters* **16**, 2228–2233 (2016).
142. Huang, Z. *et al.* Diamond nitrogen-vacancy centers created by scanning focused helium ion beam and annealing. *Applied Physics Letters* **103**, 081906 (2013).
143. Alghannam, F. & Hemmer, P. Engineering of Shallow Layers of Nitrogen Vacancy Colour Centres in Diamond Using Plasma Immersion Ion Implantation. *Scientific Reports* **9**, 5870 (2019).

144. Robledo, L., Bernien, H., Van Weperen, I. & Hanson, R. Control and coherence of the optical transition of single nitrogen vacancy centers in diamond. *Physical Review Letters* **105**, 1–4 (2010).
145. Hadden, J. P. *et al.* Strongly enhanced photon collection from diamond defect centers under microfabricated integrated solid immersion lenses. *Applied Physics Letters* **97**, 241901 (2010).
146. Jamali, M. *et al.* Microscopic diamond solid-immersion-lenses fabricated around single defect centers by focused ion beam milling. *Review of Scientific Instruments* **85**, 123703 (2014).
147. Janitz, E. *et al.* Fabry-Perot microcavity for diamond-based photonics. *Physical Review A - Atomic, Molecular, and Optical Physics* **92**, 1–11 (2015).
148. Gurudev Dutt, M. V. Quantum Register Based on Individual Electronic and Nuclear Spin Qubits in Diamond. *Science* **316**, 1312–1316 (2007).
149. Dréau, A., Maze, J. R., Lesik, M., Roch, J. F. & Jacques, V. High-resolution spectroscopy of single NV defects coupled with nearby ^{13}C nuclear spins in diamond. *Physical Review B - Condensed Matter and Materials Physics* **85**, 134107 (2012).
150. Jelezko, F., Gaebel, T., Popa, I., Gruber, A. & Wrachtrup, J. Observation of Coherent Oscillations in a Single Electron Spin. *Physical Review Letters* **92**, 076401 (2004).
151. Neumann, P. *et al.* Multipartite entanglement among single spins in diamond. *Science* **323**, 1326–1329 (2009).
152. Kolkowitz, S., Unterreithmeier, Q. P., Bennett, S. D. & Lukin, M. D. Sensing distant nuclear spins with a single electron spin. *Physical Review Letters* **109**, 137601 (2012).
153. Taminiau, T. H., Cramer, J., Van Der Sar, T., Dobrovitski, V. V. & Hanson, R. Universal control and error correction in multi-qubit spin registers in diamond. *Nature Nanotechnology* **9**, 171–176 (2014).
154. Togan, E. *et al.* Quantum entanglement between an optical photon and a solid-state spin qubit. *Nature* **466**, 730–734 (2010).
155. Tchegotareva, A. *et al.* Entanglement between a Diamond Spin Qubit and a Photonic Time-Bin Qubit at Telecom Wavelength. *Physical Review Letters* **123**, 063601 (2019).
156. Legero, T., Wilk, T., Kuhn, A. & Rempe, G. Time-resolved two-photon quantum interference. *Applied Physics B: Lasers and Optics* **77**, 797–802 (2003).
157. Legero, T., Wilk, T., Kuhn, A. & Rempe, G. Characterization of Single Photons Using Two-Photon Interference. *Advances In Atomic, Molecular, and Optical Physics* **53**, 253–289 (2006).
158. Barrett, S. D. & Kok, P. Efficient high-fidelity quantum computation using matter qubits and linear optics. *Physical Review A - Atomic, Molecular, and Optical Physics* **71**, 060310 (2005).
159. Humphreys, P. C. *et al.* Deterministic delivery of remote entanglement on a quantum network. *Nature* **558**, 268–273 (2018).

160. Dréau, A., Tchegotareva, A., Mahdaoui, A. E., Bonato, C. & Hanson, R. Quantum Frequency Conversion of Single Photons from a Nitrogen-Vacancy Center in Diamond to Telecommunication Wavelengths. *Physical Review Applied* **9**, 064031 (2018).
161. Janitz, E., Bhaskar, M. K. & Childress, L. Cavity quantum electrodynamics with color centers in diamond. *Optica* **7**, 1232 (2020).
162. Rogers, L. J. *et al.* Multiple intrinsically identical single-photon emitters in the solid state. *Nature Communications* **5**, 4739 (2014).
163. Bradac, C., Gao, W., Forneris, J., Trusheim, M. E. & Aharonovich, I. Quantum nanophotonics with group IV defects in diamond. *Nature Communications* **10**, 5625 (2019).
164. Mukherjee, S. *et al.* A telecom O-band emitter in diamond. *Nano Letters* **23**, 2557–2562 (2023).
165. MacHielse, B. *et al.* Quantum Interference of Electromechanically Stabilized Emitters in Nanophotonic Devices. *Physical Review X* **9**, 1–10 (2019).
166. Ciccarino, C. J. *et al.* Strong spin–orbit quenching via the product Jahn–Teller effect in neutral group IV qubits in diamond. *npj Quantum Materials* **5**, 75 (2020).
167. Hepp, C. *et al.* Electronic structure of the silicon vacancy color center in diamond. *Physical Review Letters* **112**, 036405 (2014).
168. Li, K., Zhou, Y., Rasmita, A., Aharonovich, I. & Gao, W. B. Nonblinking Emitters with Nearly Lifetime-Limited Linewidths in CVD Nanodiamonds. *Physical Review Applied* **6**, 024010 (2016).
169. Jantzen, U. *et al.* Nanodiamonds carrying silicon-vacancy quantum emitters with almost lifetime-limited linewidths. *New Journal of Physics* **18**, 073036 (2016).
170. Evans, R. E., Sipahigil, A., Sukachev, D. D., Zibrov, A. S. & Lukin, M. D. Narrow-Linewidth Homogeneous Optical Emitters in Diamond Nanostructures via Silicon Ion Implantation. *Physical Review Applied* **5**, 044010 (2016).
171. Benedikter, J. *et al.* Cavity-Enhanced Single-Photon Source Based on the Silicon-Vacancy Center in Diamond. *Physical Review Applied* **7**, 024031 (2017).
172. Häußler, S. *et al.* Diamond photonics platform based on silicon vacancy centers in a single-crystal diamond membrane and a fiber cavity. *Physical Review B* **99**, 165310 (2019).
173. Marseglia, L. *et al.* Bright nanowire single photon source based on SiV centers in diamond. *Optics Express* **26**, 80 (2018).
174. Sipahigil, A. *et al.* An integrated diamond nanophotonics platform for quantum-optical networks. *Science* **354**, 847–850 (2016).
175. Wan, N. H. *et al.* Large-scale integration of artificial atoms in hybrid photonic circuits. *Nature* **583**, 226–231 (2020).
176. Jelezko, F. & Wrachtrup, J. Single defect centres in diamond: A review. *physica status solidi (a)* **203**, 3207–3225 (2006).
177. Becker, J. N. *et al.* All-Optical Control of the Silicon-Vacancy Spin in Diamond at Millikelvin Temperatures. *Physical Review Letters* **120**, 053603 (2018).

178. Sukachev, D. D. *et al.* Silicon-Vacancy Spin Qubit in Diamond: A Quantum Memory Exceeding 10 ms with Single-Shot State Readout. *Physical Review Letters* **119**, 223602 (2017).
179. Green, B. L. *et al.* Neutral Silicon-Vacancy Center in Diamond: Spin Polarization and Lifetimes. *Physical Review Letters* **119**, 096402 (2017).
180. Green, B. L. *et al.* Electronic structure of the neutral silicon-vacancy center in diamond. *Physical Review B* **99**, 161112 (2019).
181. Zhang, Z. H., Edmonds, A. M., Palmer, N., Markham, M. L. & De Leon, N. P. Neutral Silicon-Vacancy Centers in Diamond via Photoactivated Itinerant Carriers. *Physical Review Applied* **19**, 034022 (2023).
182. Zhang, Z. H. *et al.* Neutral Silicon Vacancy Centers in Undoped Diamond via Surface Control. *Physical Review Letters* **13**, 166902 (2023).
183. D'Haenens-Johansson, U. F. *et al.* Optical properties of the neutral silicon split-vacancy center in diamond. *Physical Review B - Condensed Matter and Materials Physics* **84**, 245208 (2011).
184. Bhaskar, M. K. *et al.* Quantum Nonlinear Optics with a Germanium-Vacancy Color Center in a Nanoscale Diamond Waveguide. *Physical Review Letters* **118**, 223603 (2017).
185. Siyushev, P. *et al.* Optical and microwave control of germanium-vacancy center spins in diamond. *Physical Review B* **96**, 081201 (2017).
186. Bray, K. *et al.* Single Crystal Diamond Membranes and Photonic Resonators Containing Germanium Vacancy Color Centers. *ACS Photonics* **5**, 4817–4822 (2018).
187. Høy Jensen, R. *et al.* Cavity-Enhanced Photon Emission from a Single Germanium-Vacancy Center in a Diamond Membrane. *Physical Review Applied* **13**, 064016 (2020).
188. Chen, D. *et al.* Optical Gating of Resonance Fluorescence from a Single Germanium Vacancy Color Center in Diamond. *Physical Review Letters* **123** (2019).
189. Chen, Y. H., Stearn, S., Vella, S., Horsley, A. & Doherty, M. W. Optimisation of diamond quantum processors. *New Journal of Physics* **22**, 093068 (2020).
190. Trusheim, M. E. *et al.* Transform-Limited Photons from a Coherent Tin-Vacancy Spin in Diamond. *Physical Review Letters* **124** (2020).
191. Görlitz, J. *et al.* Coherence of a charge stabilised tin-vacancy spin in diamond. *npj Quantum Information* **8**, 45 (2022).
192. Rugar, A. E. *et al.* Quantum Photonic Interface for Tin-Vacancy Centers in Diamond. *Physical Review X* **11**, 1–7 (2021).
193. Arjona Martínez, J. *et al.* Photonic Indistinguishability of the Tin-Vacancy Center in Nanostructured Diamond. *Physical Review Letters* **129**, 173603 (2022).
194. Rugar, A. E., Dory, C., Sun, S. & Vučković, J. Characterization of optical and spin properties of single tin-vacancy centers in diamond nanopillars. *Physical Review B* **99**, 205417 (2019).
195. Trusheim, M. E. *et al.* Lead-related quantum emitters in diamond. *Physical Review B* **99**, 075430 (2019).

196. Muhonen, J. T. *et al.* Storing quantum information for 30 seconds in a nanoelectronic device. *Nature Nanotechnology* **9**, 986–991 (2014).
197. Falk, A. L. *et al.* Polytype control of spin qubits in silicon carbide. *Nature Communications* **4**, 1819 (2013).
198. Christle, D. J. *et al.* Isolated electron spins in silicon carbide with millisecond coherence times. *Nature Materials* **14**, 160–163 (2015).
199. Widmann, M. *et al.* Coherent control of single spins in silicon carbide at room temperature. *Nature Materials* **14**, 164–168 (2015).
200. Klimov, P. V., Falk, A. L., Christle, D. J., Dobrovitski, V. V. & Awschalom, D. D. Quantum entanglement at ambient conditions in a macroscopic solid-state spin ensemble. *Science Advances* **1**, 1–8 (2015).
201. Christle, D. J. *et al.* Isolated spin qubits in SiC with a high-fidelity infrared spin-to-photon interface. *Physical Review X* **7**, 021046 (2017).
202. Simin, D. *et al.* Locking of electron spin coherence above 20 ms in natural silicon carbide. *Physical Review B* **95**, 161201 (2017).
203. Nagy, R. *et al.* Quantum Properties of Dichroic Silicon Vacancies in Silicon Carbide. *Physical Review Applied* **9**, 034022 (2018).
204. Koehl, W. F., Buckley, B. B., Heremans, F. J., Calusine, G. & Awschalom, D. D. Room temperature coherent control of defect spin qubits in silicon carbide. *Nature* **479**, 84–87 (2011).
205. Yang, L. P. *et al.* Electron spin decoherence in silicon carbide nuclear spin bath. *Physical Review B - Condensed Matter and Materials Physics* **90**, 241203 (2014).
206. Seo, H. *et al.* Quantum decoherence dynamics of divacancy spins in silicon carbide. *Nature Communications* **7**, 12935 (2016).
207. De Las Casas, C. F. *et al.* Stark tuning and electrical charge state control of single divacancies in silicon carbide. *Applied Physics Letters* **111**, 262403 (2017).
208. Radulaski, M. *et al.* Photonic crystal cavities in cubic (3C) polytype silicon carbide films. *Optics Express* **21**, 32623 (2013).
209. Calusine, G., Politi, A. & Awschalom, D. D. Cavity-Enhanced Measurements of Defect Spins in Silicon Carbide. *Physical Review Applied* **6**, 014019 (2016).
210. Könz, F. *et al.* Temperature and concentration dependence of optical dephasing, spectral-hole lifetime, and anisotropic absorption in Eu³⁺:Y₂SiO₅. *Physical Review B - Condensed Matter and Materials Physics* **68**, 085109 (2003).
211. Zhong, M. *et al.* Optically addressable nuclear spins in a solid with a six-hour coherence time. *Nature* **517**, 177–180 (2015).
212. Zhong, T. *et al.* Nanophotonic rare-earth quantum memory with optically controlled retrieval. *Science* **357**, 1392–1395 (2017).
213. Zhong, T. *et al.* Optically Addressing Single Rare-Earth Ions in a Nanophotonic Cavity. *Physical Review Letters* **121**, 183603 (2018).
214. Dibos, A. M., Raha, M., Phenicie, C. M. & Thompson, J. D. Atomic Source of Single Photons in the Telecom Band. *Physical Review Letters* **120**, 243601 (2018).

215. Ourari, S. *et al.* Indistinguishable telecom band photons from a single erbium ion in the solid state. *arXiv:2301.03564* (2023).
216. Gattass, R. R. & Mazur, E. Femtosecond laser micromachining in transparent materials. *Nature Photonics* **2**, 219–225 (2008).
217. Mao, S. S. *et al.* Dynamics of femtosecond laser interactions with dielectrics. *Applied Physics A: Materials Science and Processing* **79**, 1695–1709 (2004).
218. Schaffer, C. B., Brodeur, A. & Mazur, E. Laser-induced breakdown and damage in bulk transparent materials induced by tightly focused femtosecond laser pulses. *Measurement Science and Technology* **12**, 1784–1794 (2001).
219. Keldysh, L. Ionization in the field of a strong electromagnetic wave. *Journal of Experimental and Theoretical Physics* **20**, 1307–1314 (1965).
220. Stuart, B. *et al.* Nanosecond-to-femtosecond laser-induced breakdown in dielectrics. *Physical Review B - Condensed Matter and Materials Physics* **53**, 1749–1761 (1996).
221. Thornber, K. K. Applications of scaling to problems in high-field electronic transport. *Journal of Applied Physics* **52**, 279–290 (1981).
222. Griffiths, B. *et al.* Microscopic processes during ultrafast laser generation of Frenkel defects in diamond. *Physical Review B* **104**, 174303 (2021).
223. Clark, J. K. & Walker, J. The neutral vacancy in diamond. *Proceedings of the Royal Society of London. Series A, Mathematical and Physical Sciences* **334**, 241–257 (1973).
224. Bourgoïn, J. C. & Massarani, B. Threshold energy for atomic displacement in diamond. *Physical Review B* **14**, 3690–3694 (1976).
225. Salustro, S., Noël, Y., Zicovich-Wilson, C. M., Olivero, P. & Dovesi, R. The $v + i$ defects in diamond: An ab initio investigation of the electronic structure, of the Raman and IR spectra, and of their possible recombination. *Journal of Chemical Physics* **145**, 184701 (2016).
226. Pimenov, S. M., Khomich, A. A., Neuenschwander, B., Jäggi, B. & Romano, V. Picosecond-laser bulk modification induced enhancement of nitrogen-vacancy luminescence in diamond. *Journal of the Optical Society of America B* **33**, B49–B55 (2016).
227. Chen, Y.-C. *et al.* Laser writing of individual nitrogen-vacancy defects in diamond with near-unity yield. *Optica* **6**, 662 (2019).
228. Kurita, T. *et al.* Efficient generation of nitrogen-vacancy center inside diamond with shortening of laser pulse duration. *Applied Physics Letters* **113**, 211102 (2018).
229. Liu, Y. *et al.* Fabrication of nitrogen vacancy color centers by femtosecond pulse laser illumination. *Optics Express* **21**, 12843 (2013).
230. Kononenko, V. V., Vlasov, I. I., Zavedeev, E. V., Khomich, A. A. & Konov, V. I. Correlation between surface etching and NV centre generation in laser-irradiated diamond. *Applied Physics A* **124**, 226 (2018).
231. Robitaille, A., Boulais, É. & Meunier, M. Mechanisms of plasmon-enhanced femtosecond laser nanoablation of silicon. *Optics Express* **21**, 9703 (2013).

232. Rong, Y. *et al.* Bright near-surface silicon vacancy centers in diamond fabricated by femtosecond laser ablation. *Optics Letters* **44**, 3793 (2019).
233. Wang, X. J., Fang, H. H., Sun, F. W. & Sun, H. B. Laser Writing of Color Centers. *Laser and Photonics Reviews* **16**, 2100029 (2022).
234. Saleem, U. *et al.* Light emission from localised point defects induced in GaN crystal by a femtosecond-pulsed laser. *Optical Materials Express* **8**, 2703 (2018).
235. Buividas, R. *et al.* Photoluminescence from voids created by femtosecond-laser pulses inside cubic-BN. *Optics Letters* **40**, 5711 (2015).
236. Castelletto, S. *et al.* Photoluminescence in hexagonal silicon carbide by direct femtosecond laser writing. *Optics Letters* **43**, 6077 (2018).
237. Castelletto, S. *et al.* Color centers enabled by direct femto-second laser writing in wide bandgap semiconductors. *Nanomaterials* **11**, 1–17 (2021).
238. Chen, Y. C. *et al.* Laser Writing of Scalable Single Color Centers in Silicon Carbide. *Nano Letters* **19**, 2377–2383 (2019).
239. Gao, X. *et al.* Femtosecond Laser Writing of Spin Defects in Hexagonal Boron Nitride. *ACS Photonics* **8**, 994–1000 (2021).
240. Voitovich, A. P. *et al.* Luminescent properties of radiation induced defects in sodium and magnesium fluorides nanocrystals. *Journal of Luminescence* **201**, 57–64 (2018).
241. Dickinson, J. T., Langford, S. C., Avanesyan, S. M. & Orlando, S. Color center formation in KCl and KBr single crystals with femtosecond laser pulses. *Applied Surface Science* **253**, 7874–7878 (2007).
242. Courrol, L. C. *et al.* Production of stabilized color centers in YLiF₄ crystals by high-intensity ultrashort laser pulses. *Journal of the Optical Society of America B* **22**, 2560 (2005).
243. Courrol, L. C. *et al.* Study of color centers produced in thulium doped YLF crystals irradiated by electron beam and femtosecond laser pulses. *Optics Communications* **270**, 340–346 (2007).
244. Wang, X. *et al.* Valence state change and defect centers induced by infrared femtosecond laser in Yb:YAG crystals. *Journal of Applied Physics* **117**, 153104 (2015).
245. Yang, J. Y., Ma, H. L., Ma, G. H., Lu, B. & Ma, H. Phase transformation at the surface of TiO₂ single crystal irradiated by femtosecond laser pulse. *Applied Physics A: Materials Science and Processing* **88**, 801–804 (2007).
246. Jamshidi-Ghaleh, K., Lotfi, E. S. & Masalehdan, H. Darkening enhancement in SK3 glass with quartz under irradiation of femtosecond laser pulses. *Optics and Lasers in Engineering* **49**, 605–608 (2011).
247. Huang, Z. *et al.* Photolithographic Patterning of Organic Color-Centers. *Advanced Materials* **32**, 1906517 (2020).
248. Hou, S. *et al.* Localized emission from laser-irradiated defects in 2D hexagonal boron nitride. *2D Materials* **5**, 015010 (2018).

249. Gan, L. *et al.* Large-Scale, High-Yield Laser Fabrication of Bright and Pure Single-Photon Emitters at Room Temperature in Hexagonal Boron Nitride. *ACS Nano* **16**, 14254–14261 (2022).
250. Born, M.; Wolf, E. *Principles of Optics* 7th ed. (Cambridge University Press, Cambridge, 1999).
251. Serrels, K. A. *et al.* Solid immersion lens applications for nanophotonic devices. *Journal of Nanophotonics* **2**, 021854 (2008).
252. Salter, P. S. & Booth, M. J. Adaptive optics in laser processing. *Light: Science and Applications* **8**, 110 (2019).
253. Serrels, K. A., Ramsay, E., Warburton, R. J. & Reid, D. T. Nanoscale optical microscopy in the vectorial focusing regime. *Nature Photonics* **2**, 311–314 (2008).
254. Mansfield, S. M. & Kino, G. S. Solid immersion microscope. *Applied Physics Letters* **57**, 2615–2616 (1990).
255. Jaynes, E. T. & Cummings, F. W. Comparison of Quantum and Semiclassical Radiation Theories with Application to the Beam Maser. *Proceedings of the IEEE* **51**, 89–109 (1963).
256. Shore, B. W. & Knight, P. L. The Jaynes–Cummings model. *Journal of Modern Optics* **40**, 1195–1238 (1993).
257. Gerry, C. & Knight, P. *Introductory Quantum Optics* (Cambridge University Press, Cambridge, 2004).
258. Fox, M. Quantum Optics - An Introduction [Master Series]. *Oxford University Press* **53**, 397 (2006).
259. Ruf, M., Weaver, M. J., Van Dam, S. B. & Hanson, R. Resonant Excitation and Purcell Enhancement of Coherent Nitrogen-Vacancy Centers Coupled to a Fabry-Perot Microcavity. *Physical Review Applied* **15**, 024049 (2021).
260. Purcell, E. M. Spontaneous Emission Probabilities at Radio Frequencies. *Physical Review* **69**, 681 (1946).
261. Hunger, D. *et al.* A fiber Fabry-Perot cavity with high finesse. *New Journal of Physics* **12**, 065038 (2010).
262. Nagourney, W. G. *Quantum electronics for atomic physics* (Oxford University Press, 2010).
263. Byrnes, S. J. Multilayer optical calculations. *arXiv:1603.02720* (2016).
264. Van Dam, S. B., Ruf, M. & Hanson, R. Optimal design of diamond-air microcavities for quantum networks using an analytical approach. *New Journal of Physics* **20**, 115004 (2018).
265. Benedikter, J. *et al.* Transverse-mode coupling and diffraction loss in tunable Fabry-Pérot microcavities. *New Journal of Physics* **17**, 053051 (2015).
266. Cui, G. & Raymer, M. G. Quantum efficiency of single-photon sources in the cavity-QED strong-coupling regime. *Optics Express* **13**, 9660–9665 (2005).

267. Jelezko, F. *et al.* Observation of coherent oscillation of a single nuclear spin and realization of a two-qubit conditional quantum gate. *Physical Review Letters* **93**, 130501 (2004).
268. Bogdanović, S. *et al.* Robust nano-fabrication of an integrated platform for spin control in a tunable microcavity. *APL Photonics* **2**, 126101 (2017).
269. Heupel, J. *et al.* Fabrication and characterization of single-crystal diamond membranes for quantum photonics with tunable microcavities. *Micromachines* **11**, 1080 (2020).
270. Heupel, J. *et al.* Fabrication of High-Quality Thin Single-Crystal Diamond Membranes with Low Surface Roughness. *Physica Status Solidi (A) Applications and Materials Science*, 2200465 (2022).
271. Campbell, B. & Mainwood, A. Radiation damage of diamond by electron and gamma irradiation. *Physica Status Solidi (A) Applied Research* **181**, 99–107 (2000).
272. Tu, R., Johnson & Cheng, S. *Ray Optics Simulation, phydemo.app/ray-optics/*
273. Konov, V. I. Laser in micro and nanoprocessing of diamond materials. *Laser and Photonics Reviews* **6**, 739–766 (2012).
274. Riedel, D. *et al.* Low-loss broadband antenna for efficient photon collection from a coherent spin in diamond. *Physical Review Applied* **2**, 064011 (2014).
275. Hu, X. J., Dai, Y. B., Li, R. B., Shen, H. S. & He, X. C. The diffusion of vacancies near a diamond (001) surface. *Solid State Communications* **122**, 45–48 (2002).
276. Onoda, S. *et al.* Diffusion of Vacancies Created by High-Energy Heavy Ion Strike Into Diamond. *Physica Status Solidi (A) Applications and Materials Science* **214**, 1700160 (2017).
277. Chu, Y., Markham, M., Twitchen, D. J. & Lukin, M. D. All-optical control of a single electron spin in diamond. *Physical Review A - Atomic, Molecular, and Optical Physics* **91**, 021801 (2015).
278. Aslam, N., Waldherr, G., Neumann, P., Jelezko, F. & Wrachtrup, J. Photo-induced ionization dynamics of the nitrogen vacancy defect in diamond investigated by single-shot charge state detection. *New Journal of Physics* **15**, 013064 (2013).
279. Stephen, C. J. *et al.* Deep Three-Dimensional Solid-State Qubit Arrays with Long-Lived Spin Coherence. *Physical Review Applied* **12**, 2–9 (2019).
280. De Feudis, M. *et al.* Diamond graphitization by laser-writing for all-carbon detector applications. *Diamond and Related Materials* **75**, 25–33 (2017).
281. Kononenko, V. V. *et al.* Highly oriented graphite produced by femtosecond laser on diamond. *Applied Physics Letters* **114**, 251903 (2019).
282. Hadden, J. P. *et al.* Integrated waveguides and deterministically positioned nitrogen vacancy centers in diamond created by femtosecond laser writing. *Optics Letters* **43**, 3586 (2018).
283. Sotillo, B. *et al.* Visible to infrared diamond photonics enabled by focused femtosecond laser pulses. *Micromachines* **8**, 60 (2017).

284. Coccia, G. *et al.* Femtosecond laser writing of integrated photonic circuits in diamond. *EPJ Web of Conferences* **255**, 12006 (2021).
285. Challier, M. *et al.* Advanced fabrication of single-crystal diamond membranes for quantum technologies. *Micromachines* **9**, 148 (2018).
286. Degen, C. L., Reinhard, F. & Cappellaro, P. Quantum sensing. *Reviews of Modern Physics* **89**, 1–39 (2017).
287. Faraon, A., Santori, C., Huang, Z., Acosta, V. M. & Beausoleil, R. G. Coupling of nitrogen-vacancy centers to photonic crystal cavities in monocrystalline diamond. *Physical Review Letters* **109**, 033604 (2012).
288. Li, L. *et al.* Coherent spin control of a nanocavity-enhanced qubit in diamond. *Nature Communications* **6**, 6173 (2015).
289. Chakravarthi, S., Pederson, C., Kazi, Z., Ivanov, A. & Fu, K. M. C. Impact of surface and laser-induced noise on the spectral stability of implanted nitrogen-vacancy centers in diamond. *Physical Review B* **104**, 085425 (2021).
290. Orphal-Kobin, L. *et al.* Optically Coherent Nitrogen-Vacancy Defect Centers in Diamond Nanostructures. *Physical Review X* **13**, 011042 (2023).
291. Lekavicius, I., Oo, T. & Wang, H. Diamond Lamb wave spin-mechanical resonators with optically coherent nitrogen vacancy centers. *Journal of Applied Physics* **126**, 214301 (2019).
292. Naydenov, B. *et al.* Enhanced generation of single optically active spins in diamond by ion implantation. *Applied Physics Letters* **96**, 163108 (2010).
293. Schwartz, J., Aloni, S., Ogletree, D. F. & Schenkel, T. Effects of low-energy electron irradiation on formation of nitrogen-vacancy centers in single-crystal diamond. *New Journal of Physics* **14**, 043024 (2012).
294. Kim, E., Acosta, V. M., Bauch, E., Budker, D. & Hemmer, P. R. Electron spin resonance shift and linewidth broadening of nitrogen-vacancy centers in diamond as a function of electron irradiation dose. *Applied Physics Letters* **101**, 082410 (2012).
295. Appel, P. *et al.* Fabrication of all diamond scanning probes for nanoscale magnetometry. *Review of Scientific Instruments* **87**, 063703 (2016).
296. Barfuss, A., Teissier, J., Neu, E., Nunnenkamp, A. & Maletinsky, P. Strong mechanical driving of a single electron spin. *Nature Physics* **11**, 820–824 (2015).
297. Barclay, P. E., Fu, K.-M., Santori, C. & Beausoleil, R. G. Hybrid photonic crystal cavity and waveguide for coupling to diamond NV-centers. *Optics Express* **17**, 9588–9601 (2009).
298. Faraon, A., Santori, C., Huang, Z., Acosta, V. M. & Beausoleil, R. G. Coupling of nitrogen-vacancy centers to photonic crystal cavities in monocrystalline diamond. *Physical Review Letters* **109**, 033604 (2012).
299. Salz, M. *et al.* Cryogenic platform for coupling color centers in diamond membranes to a fiber-based microcavity. *Applied Physics B: Lasers and Optics* **126**, 1–9 (2020).
300. Flågan, S. *et al.* A diamond-confined open microcavity featuring a high quality-factor and a small mode-volume. *Journal of Applied Physics* **131**, 113102 (2022).

301. Tran, T. H., Siyushev, P., Wrachtrup, J. & Gerhardt, I. Extinction of light and coherent scattering by a single nitrogen-vacancy center in diamond. *Physical Review A* **95**, 053831 (2017).
302. Greuter, L. *et al.* A small mode volume tunable microcavity: Development and characterization. *Applied Physics Letters* **105**, 121105 (2014).
303. Najer, D., Renggli, M., Riedel, D., Starosielec, S. & Warburton, R. J. Fabrication of mirror templates in silica with micron-sized radii of curvature. *Applied Physics Letters* **110**, 011101 (2017).
304. Uphoff, M., Brekenfeld, M., Rempe, G. & Ritter, S. Frequency splitting of polarization eigenmodes in microscopic Fabry-Perot cavities. *New Journal of Physics* **17**, 013053 (2015).
305. Fontana, Y., Zifkin, R., Janitz, E., Rodríguez Rosenblueth, C. D. & Childress, L. A mechanically stable and tunable cryogenic Fabry-Pérot microcavity. *Review of Scientific Instruments* **92**, 053906 (2021).
306. Lang, A. R. Causes of birefringence in diamond. *Nature* **213**, 248–251 (1967).
307. Howell, D. Strain-induced birefringence in natural diamond: a review. *European Journal of Mineralogy* **24**, 575–585 (2012).
308. Berthel, M. *et al.* Photophysics of single nitrogen-vacancy centers in diamond nanocrystals. *Physical Review B - Condensed Matter and Materials Physics* **91**, 035308 (2015).
309. Benelajla, M., Kammann, E., Urbaszek, B. & Karrai, K. Physical Origins of Extreme Cross-Polarization Extinction in Confocal Microscopy. *Physical Review X* **11**, 21007 (2021).
310. Vamivakas, A. N., Zhao, Y., Lu, C. Y. & Atatüre, M. Spin-resolved quantum-dot resonance fluorescence. *Nature Physics* **5**, 198–202 (2009).
311. Kuhlmann, A. V. *et al.* A dark-field microscope for background-free detection of resonance fluorescence from single semiconductor quantum dots operating in a set-and-forget mode. *Review of Scientific Instruments* **84**, 073905 (2013).
312. Tomm, N. *et al.* A bright and fast source of coherent single photons. *Nature Nanotechnology* **16**, 399–403 (2021).
313. Siyushev, P. *et al.* Optically controlled switching of the charge state of a single nitrogen-vacancy center in diamond at cryogenic temperatures. *Physical Review Letters* **110**, 167402 (2013).
314. *Almax easyLab, Quantum polishing services, almax-easylab.com/QuantumPolishing.aspx*
315. Lau, W. S. *et al.* Surface smoothing effect of an amorphous thin film deposited by atomic layer deposition on a surface with nano-sized roughness. *AIP Advances* **4**, 027120 (2014).
316. Zaske, S. *et al.* Visible-to-telecom quantum frequency conversion of light from a single quantum emitter. *Physical Review Letters* **109**, 147404 (2012).
317. Stolk, A. J. *et al.* Telecom-Band Quantum Interference of Frequency-Converted Photons from Remote Detuned NV Centers. *PRX Quantum* **3**, 020359 (2022).

318. Childress, L., Taylor, J. M., Sørensen, A. S. & Lukin, M. D. Fault-tolerant quantum communication based on solid-state photon emitters. *Physical Review Letters* **96**, 96–99 (2006).
319. Kalb, N., Humphreys, P. C., Slim, J. J. & Hanson, R. Dephasing mechanisms of diamond-based nuclear-spin memories for quantum networks. *Physical Review A* **97**, 062330 (2018).
320. Rozpedek, F. *et al.* Parameter regimes for a single sequential quantum repeater. *Quantum Science and Technology* **3**, 034002 (2018).

ACKNOWLEDGEMENTS

Most of the chapters in this thesis describe results – this one does not. But it is just as important, because none of this work would have existed, if not for a number of people that I would like to mention here.

First and foremost, I would like to thank the ones who made my PhD possible in the first place – professor Richard Warburton and professor Patrick Maletinsky. I guess it all started with a nervous exchange student from Sweden taking a lecture in quantum optics – little did I know that I would end up doing a PhD in that exact subject. I am grateful to you both for offering me this opportunity, and for letting me work on such an exciting topic in between your two worlds. Richard, thank you for your kind way, your encouraging words, and your scientific advice. It has been a pleasure to discuss results, measurement issues and plans with you. Patrick, thank you for always being excited to hear the latest news from the lab, and for always making time for a quick chat or discussion. Thank you for being direct, for being curious, and for always caring when it mattered. Thank you also to my external referee Lily Childress, for taking the time to read this thesis and evaluate my work. I highly value your feedback.

Next, I would like to thank my first post doc on this project, Tomek Jakubczyk. He taught me everything a first-year PhD student needs to know, in a wonderfully pedagogic and engaged way. We spent endless hours together in the noise and darkness of the laser writing lab, trying to get things to work, and ended up with results better than expected in many ways. I admire your dedication to research, your curiosity, your endless reserve of ideas, and wish I could at least remotely be the same at some point.

My second post doc, Yannik Fontana, taught me close to everything there is to know about optical cavities (and a lot of other things). Thank you for your dedication to the project, your patience with me, and your help. Whether in the lab or on a snowy mountain, I am grateful for you being there and encouraging me when things went wrong (and for not laughing too much at my lack of off-piste skills). Thank you for enduring my techno playlist and my occasional need for “putting stuff into order” in the lab. Thank you for the steady supply of cat-related memes, for making tedious tasks fun, and for sharing so much of your knowledge with me. I am lucky to have shared the last two and a half years of my PhD with you.

I have also had the pleasure to work with another post doc, Brendan Shields. Thank you, Brendan, for the tips and tricks you provided on all aspects of sample fabrication (especially, but not only, on making diamond platelets). I have always admired your calm and steady approach to any problem and I am honored to have had the possibility to work with you.

Thank you to the rest of the diamond cavity team: Sigurd Flågan (who introduced me to the world of linewidth measurements and who always supported me on yr.no being the best weather site), Andrea Corazza (who will keep the fire burning in the diamond-cavity, be it with NVs or SiVs), Toni Berger (who spent his bachelor’s project making microwave striplines with us, and who the Nano-Photonics group is lucky to keep for a bit longer), and Marie Gruet (who did her master’s thesis in our lab and was almost too fast in successfully finishing tasks, including assembling two double-pass AOM setups).

During my PhD, I was responsible for the ICP-RIE of the department. It has been a

pleasure to share this job with Josh Zuber. Thank you for making the duty feels less like a duty, and for spending all those hours cleaning the inside of the reactor chamber while breathing in the pleasant isopropanol-infused air together.

Speaking of instruments, the laser writing project would not have been possible without the Spectra Physics femtosecond laser. Thank you to professor Ilaria Zardo for letting us use it in our experiments and for providing us with space in the lab. Thank you to Marta De Luca and Begoña Abad, who were always ready to help with debugging and giving tips on maintaining the optimal laser performance.

A PhD in experimental physics contains endless hours in the lab, some successes, and lots of disappointments and frustration. Mine is no exception. Nevertheless, it was made easier to endure thanks to the great people that shared it with me, in- and outside of the lab. Thank you, Natasha Tomm, for our sushi-, cocktail- and movie nights, and for sharing many happy and sad moments with me. Thank you, Nadia Antoniadis, for being the best skiing buddy, traveling roommate and office mate for such a long time. Thank you, Märta Tschudin, for our take-away-and-tea-evenings, and for welcoming me during those far-away exchange months in Basel. Thank you, Jodok Happacher, for introducing me to the world of Wes Anderson. Thank you, Lukas Sponfeldner and Simon Geyer, for doing burpees and stair runs with me and Nadia every Monday and Thursday for almost three years now (and a special thank you to the Dreirosen Crossfit Group for keeping me sane during these years!). Without you, I would also not know the lyrics to such an amount of German and Swiss schlager songs. Thank you, Malwina Marczak, for sharing my love for weird memes and Vines. Thank you, Clemens Spinnler and Nam Nguyen, for arranging amazing fondues, game nights, and barbecues.

Together with the already mentioned people, and current and former members of the Nano-Photonics Group and of the Quantum Sensing Group – Nadine Leisgang, Mark Hogg, Liang Zhai, Marcel Erbe, Matthias Löbl, Jonas Roch, Daniel Najer, Sebastien Leni, Willy Stehl, Andreas Kuhlmann, Thibaud Ruelle, Alisa Javadi, Rafael Eggli, Rahel Kaiser, Kai Wagner, David Broadway, Juanita Bocquel, Tobias Sjölander, Minghao Li, Silvia Ruffieux, Patrick Reiser, Samuel Treves, Beat Bürgler, Natascha Hedrich, Paul Lehmann, Debarghya Dutta, Carolin Schrader, Mara Batzer, Lucas Thiel, Mark Kasperczyk, Dominik Rohner, Clément Pellet-Mary, Marcel.li Grimau and Johannes Kölbl – we have had great Friday beers, group hikes, barbecues and skiing days. Thank you for truly letting me feel as a part of two groups – by having double the fun, but also double the scientific exchange and advice.

Thank you to Yannik, Josh, Tomek, Nadia, Christof, Simon and Nam for giving input on various chapters of this thesis. It has helped immensely to have a second (and less stressed) opinion, and improved the quality of this work.

The Department of Physics at University of Basel would not work the same way if it weren't for its mechanical workshop, electronics workshop, technicians, and administration. So thank you, Sascha Martin, Patrick Stöcklin, Stefan Gentsch and team, for providing us with world-class parts and components, often knowing better than us what exactly we needed to improve our setups. Thank you, Michael Steinacher and team, for providing us with a low-noise DAC (and a wide range of other instruments and components) without which our cavity would never have performed as well as it did. Thank you, Dominik Sifrig, for punctually providing the liquid helium needed for our experiments. Thank you, Laurent Marot, Arnold Lücke, and Gerard Gadea Diez, for mak-

ing sure that the department is safe and that our cleanroom equipment is working as it should. And thank you, Jennifer Kern, Germaine Weaver, Barbara Kammermann, Astrid Kalt, Christian Wölfle and Mile Mirkovic, for running this department so smoothly from the administrative side.

By now, I have spent more than six years in Switzerland. What started with an exchange year turned into a lot more... There are many dear friends that I left behind in Sweden. A special mention goes out to Linnea Olsson, Daniel Fransson and Deimante Neimantaite for always supporting me, and for always making time for me when I visited back home. Tack för att ni finns!

Thank you, Christof, for letting me share both my worries and my happiness and excitement with you. Thank you for the encouraging Skype calls, for the travels back and forth in Europe, for the care, and for always making me forget about work for a bit when I was stressed. It has meant, and means, the world to me.

And, last but not least, mum and dad. Thank you for believing in me. Thank you for making it possible for me to be where I am today, and for being there for me no matter what I choose to do or where I choose to live. Thank you.

Viktoria Yurgens
Basel, March 2023

LIST OF PUBLICATIONS

- V. Yurgens, A. Corazza, J. A. Zuber, M. Gruet, M. Kasperczyk, B. J. Shields, R. J. Warburton, Y. Fontana, and P. Maletinsky. Spectrally stable nitrogen-vacancy centers in diamond formed by carbon implantation into thin microstructures. *Applied Physics Letters* **121**, 234001 (2022).
- V. Yurgens, J. A. Zuber, S. Flågan, M. De Luca, B. J. Shields, I. Zardo, P. Maletinsky, R. J. Warburton, and T. Jakubczyk. Low-charge-noise nitrogen-vacancy centers in diamond created using laser writing with a solid-immersion lens. *ACS Photonics* **8**, 1726–1734 (2021).
- M. Kasperczyk, J. A. Zuber, A. Barfuss, J. Kölbl, V. Yurgens, S. Flågan, T. Jakubczyk, B. Shields, R. J. Warburton, and P. Maletinsky. Statistically modeling optical linewidths of nitrogen vacancy centers in microstructures. *Physical Review B* **102**, 075312 (2020).

Publications in preparation:

- V. Yurgens^{*}, Y. Fontana^{*}, A. Corazza, B. J. Shields, P. Maletinsky, and R. J. Warburton. Resonance fluorescence from a low-noise diamond nitrogen-vacancy center in an open microcavity (2023). *In preparation*.
- V. Yurgens, J. Happacher, J. Bocquel, Y. Fontana, T. Jakubczyk, R. J. Warburton, and P. Maletinsky. Low strain and low charge noise in laserwritten nitrogen-vacancy centers in diamond (2023). *In preparation*.

Publications prior to PhD:

- V. Yurgens, F. Koch, M. Scheel, T. Weitkamp, and C. David. Measurement and compensation of misalignment in double-sided hard X-ray Fresnel zone plates. *Journal of Synchrotron Radiation* **27**, 583–589 (2020).
- M. Scheel, J. Perrin, F. Koch, V. Yurgens, V. Le Roux, J. L. Giorgetta, K. Desjardins, C. Meneglier, S. Zhang, C. Engblom, Y.-M. Abiven, G. Cauchon, C. Bourgoïn, A. Lestrade, T. Moreno, F. Polack, C. David, and T. Weitkamp. Toward hard X-ray transmission microscopy at the ANATOMIX beamline of Synchrotron SOLEIL. *Microscopy and Microanalysis* **24**, 246–247 (2018).

^{*} Equal contribution.

CURRICULUM VITAE

Education

2019-2023 **PhD Experimental Physics**

University of Basel, Switzerland

Thesis: *Cavity-enhancement of a low-noise single-photon emitter in diamond*

Advisors: Prof. Richard J. Warburton, Prof. Patrick Maletinsky

2016-2019 **MSc Nanotechnology**

Chalmers University of Technology, Gothenburg, Sweden

Thesis: *Fabrication of double-sided Fresnel zone plates and absolute measurements of their diffraction efficiency in an X-ray-tube-based setup* (performed at the Laboratory for Micro and Nanotechnology, Paul Scherrer Institute, Villigen, Switzerland)

Advisors: Dr. Christian David, Prof. Jörgen Bengtsson, Prof. Åsa Haglund

2016-2017 **Exchange studies**

University of Basel, Switzerland

2013-2016 **BSc Engineering Physics**

Chalmers University of Technology, Gothenburg, Sweden

Thesis: *Ultrafast polarization shifter for 3D-viewing – design, construction and characterization of an optical component based on an antiferroelectric liquid crystal*

Advisor: Prof. Per Rudquist